Studies of Neutron Flux Suppression from a γ-ray Source and The GERDA Calibration System

Dissertation

zur
Erlangung der naturwissenschaftlichen Doktorwürde
(Dr. sc. nat.)

vorgelegt der
Mathematisch-naturwissenschaftlichen Fakultät
der
Universität Zürich

von
Michał Tarka
aus
Polen

Promotionskomitee

Prof. Dr. Laura Baudis (Vorsitz)
Dr. Marc Schumann
Dr. Alfredo F. Ferella

Zürich 2012

Zusammenfassung

GERDA (GERmanium Detector Array) ist ein niedrig-Untergrund Experiment zum Nachweis des neutrinolosen Doppel-Beta-Zerfalls ($0\nu\beta\beta$) in dem ^{76}Ge Isotop. Der Prozess des $0\nu\beta\beta$-Zerfalls ist bis heute die einzige bekannte Methode um die Majorana-Natur des Neutrinos nachzuweisen. Des Weiteren, würde eine Bestimmung der Zerfallsrate Rückschlüsse auf die effektive Neutrinomasse erlauben. Die untere Grenze fuer die $0\nu\beta\beta$ Zerfallsrate von ^{76}Ge liegt derzeit bei $T^{0\nu}_{1/2} > 10^{25}$ Jahren. Zerfallsraten dieser Grössenordnung erfordern sehr lange Messzeiten und extrem niedrige Untergrundraten. Diese sind nur in Untergrundlabors gegeben. Das GERDA Experiment wurde am Laboratori Nazionali del Gran Sasso (LNGS) in einer Tiefe von ca. 1400 m aufgebaut und wurde im November 2011 in Betrieb genommen. Dabei werden isotopisch angereicherte Germanium Detektoren (mit $\sim 86\%$ ^{76}Ge) verwendet, die in flüssigem Argon betrieben werden. Das Argon dient als Kühlmedium und als zusätzliche Abschirmung gegen externe Strahlung. Ziel in der ersten Phase des Experimentes ist es eine Untergrundrate von unter 10^{-2} Ereignissen/keV/kg/a zu erreichen. In der zweiten Phase ist eine Untergrundrate von unter 10^{-3} Ereignissen/keV/kg/a vorgesehen um die bisher weltweit höchste Sensitivität von $T^{0\nu}_{1/2} > 10^{26}$ Jahren zu erreichen. Die Reduzierung des Untergrundes wird durch passive Abschirmung wie z.B. durch das flüssige Argon gewährleistet und durch aktive Methoden wie sie durch das Myon-Veto oder Pulsform-Analysen gegeben sind.
Wegen ihrer elektrischen Neutralität, nehmen Neutronen bei der Unterdrückung von Untergrund Signalen eine Sonderstellung ein. Insbesondere können Neutronen, die in der direkten Detektorumgebung generiert wurden, kaum unterdrückt werden. Dabei spielen Prozesse wie die spontane Spaltung von ^{238}U oder ^{232}Th sowie (α, n) Reaktionen in leichten Elementen eine zentrale Rolle.
Im ersten Teil dieser Arbeit wird die ^{228}Th Kalibrierungsquelle wie sie in GERDA eingesetzt wird unter den Aspekten der (α, n) induzierten Neutron Emission behandelt. Des Weiteren wird eine Methode zur Unterdrückung des (α, n) Kanals und die Produktion einer Neutron reduzierten ^{228}Th Quelle vorgestellt. Die erreichte Neutronreduzierung wird anschliessend mit Messungen charakterisiert die mit einem ^{3}He und einem LiI(Eu) Detektor durchgeführt wurden. In diesem Zusammenhang wurde auch ein neuer niedrig-Untergrund LiI(Eu) Detektor entwickelt, sowie ein Germanium Detektor zur Charakterisierung der γ Aktivität aufgebaut.
Der zweite Teil der Arbeit beschäftigt sich mit dem Aufbau des Kalibrierungssystems für GERDA unter dem Gesichtspunkt der Hardware und Software Entwicklung. Das System wird charakterisiert und Prozeduren zur System Konfiguration und Fehlerhandhabung behandelt.
Abschliessend werden Messungen der Totschicht und des aktiven Volumens von BEGe (Broad Energy Germanium) Detektoren präsentiert. Diese sollen aufgrund ihrer sehr guten Eigenschaften in der zweiten Phase von GERDA zum Einsatz kommen.

Abstract

GERDA (GERmanium Detector Array) is a low-background experiment, searching for the neutrinoless double beta decay ($0\nu\beta\beta$) of the ^{76}Ge isotope. The process of the $0\nu\beta\beta$ decay is currently the only possible way to test the Majorana nature of neutrinos. Furthermore, a measured decay rate will allow for the determination of the effective neutrino mass. The actual best limit for the $0\nu\beta\beta$ decay rate of ^{76}Ge is given by $T^{0\nu}_{1/2} > 10^{25}$ years. Decay times of such order of magnitudes require long data acquisition periods and extremely low background rates, which are only found in underground laboratories. The GERDA experiment is located at the LNGS (Laboratori Nazionali del Gran Sasso) at a depth of about 1400 m rock overburden and has started in November 2011. The experiment operates isotopically enriched Ge detectors ($\sim$86% ^{76}Ge) which are deployed in liquid argon. The argon acts as a cooling liquid and has furthermore a shielding functionality against external radiation. The goal of phase I of GERDA is to reach a background rate below 10^{-2} counts/keV/kg/year. For the second phase of GERDA, a background rate below 10^{-3} counts/keV/kg/year is envisioned, allowing to reach the worldwide best sensitivity of $T^{0\nu}_{1/2} > 10^{26}$ years. Background reduction can be achieved by passive shielding which is given by liquid argon and water shields and by active techniques like the muon-veto or pulse shape analysis methods.
Given their electric neutrality, neutrons play a special role in background considerations. In particular, neutrons emitted in the direct vicinity of the detector cannot be effectively suppressed. This concerns neutrons emitted by spontaneous fission of ^{238}U or ^{232}Th and (α, n) reactions in low-Z materials.
Because GERDA uses ^{228}Th sources for calibration, the first part of this work discusses the aspects of (α, n)-induced neutron fluxes as they result from a ^{228}Th source. Furthermore, a method to suppress the (α, n) channel is introduced and the production of a neutronflux-reduced ^{228}Th source described. The achieved neutron reduction has been characterized by measurements performed with ^{3}He and LiI(Eu) detectors. In this context, a new high-purity LiI(Eu) detector has also been devoloped and a germanium detector has been setup for γ activity measurements.
The second part of this work discusses the calibration system of GERDA under the aspects of hardware and software development. In addition to the system characterization, procedures are introduced concerning the system configuration and the error handling.
Finally, results of the dead layer and active volume measurements of BEGe detectors will be presented. Given their excellent noise and resolution performance, BEGe detectors will be involved in the second phase of GERDA.

Contents

Chapter 1

Introduction

In the late 19^{th} century, experiments with uraniferous fluorescent crystals on photographic plates led to the discovery of radioactivity by Henri Becquerel. The event triggered an entire chain of discoveries and new technologies in nuclear physics. Maria Sklodowska-Curie and Pierre Curie used an ionization chamber to investigate the newly discovered radiation and found further radioactive elements. Rutherford observed the radiation using a Wilson cloud chamber in the presence of a magnetic field and found three radiation categories:

• α**:** the radiation is positively charged, highly ionizing, and exhibits short ranges in matter.

• γ**:** the rays are electrically neutral, weakly ionizing, and have high absorption lengths in matter.

• β**:** the radiation is characterized by negative charges, its ionization properties are weaker than those of α radiation, and it exhibits absorption lengths in matter higher than α radiation but lower than γ radiation.

Rutherford could identify the α radiation as the emission of positive ${}^4_2He$ ions, γ radiation turned out to be electromagnetic waves with energies higher than X-rays while β radiation could be identified with electrons. In order to explain the origin of the radiation, in 1913 Niels Bohr developed the atomic model which described the atom as consisting of a massive, positively charged nucleus surrounded by negatively charged electrons at discrete energy levels. While, the model allowed to describe the γ emission spectra of simple atoms like the hydrogen, the continuous β spectra shown in figure 1.1 was enigmatic. Because neutrinos were still unknown, the β decay was considered as a two body process and therefore a discrete spectrum was expected. In addition, the process seemed to be inconsistent with energy conservation. In 1931, Pauli introduced a hypothetical light and chargeless particle, called the neutrino, designated as ν. In the first order, introducing the neutrino could save the principle of energy conservation and explain why a continuous spectrum of the β decay is observed. Based on the endpoint considerations of the spectrum, it was obvious that the new particle had either no mass or an extremely low mass. Furthermore,

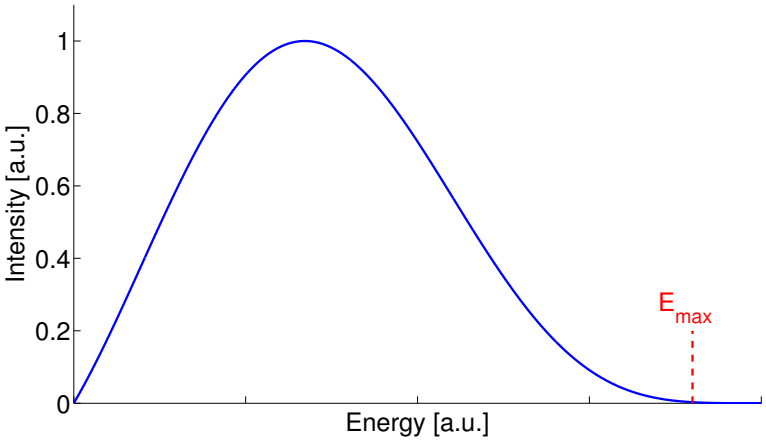

Figure 1.1: Spectrum of the β decay. Its continuous shape could be explained by introducing the neutrino. Energetic considerations, in principle allow determination of the neutrino mass by measuring the exact value of the endpoint.

due to the fact that the neutrino had not been detected at that time, its interaction probability in matter was assumed to be very weak. In 1933 a further particle, the neutron was discovered by James Chadwick. The discovery led finally to a complete picture of the β decay expressed by

$$n \rightarrow p + e^{-} + \overline{\nu}_e \tag{1.1}$$

The initial atomic model from Niels Bohr could only explain the hydrogen spectrum and was further developed by Sommerfeld who introduced additional quantum numbers such as the spin for example. However, the model could not explain the α decay and revealed nothing about the stability conditions of a nucleus. In 1935 Carl Friedrich von Weizsäcker developed the liquid drop model for nuclei, which allowed to consider the nucleus under its binding energy aspects. Later in 1949, a nuclear shell model had been developed by Eugene Paul Wigner, Maria Goeppert-Mayer, and J. Hans. D. Jensen in analogy to the atomic model. It is consistent with quantum physics and introduced nuclear energy levels, nuclear spins, and magnetic momentums of nuclei.

After introducing the neutrino as a hypothetical particle to save the principle of energy conservation, it took another 25 years to prove its existence experimentally by L. Cowan and F. Reines [1]. Although the physical nature and properties of the neutrino could be clarified with the time, leading to its indispensable place within the Standard Model (SM) of particle physics, the question of its mass remains still not fully clarified and is subject to many modern fundamental physics experiments.

1.1 Neutrino masses

Particles and their interactions are described by a physical model called the Standard Model (SM). All known elementary particles can be divided into two groups:

Bosons are the force-transmitting particles with integer spin. Among these particles are the photon, gluon, W^+, W^-, Z^0. The particles are involved in the electromagnetic, strong and weak force exchange. Additional bosons are the hypothetical graviton, carrying the gravitational force, and the Higgs boson, which is responsible for the mass of elementary particles.
Fermions are half-integer-spin particles and are the elementary constituents of matter. The group can be divided into two subgroups - quarks and leptons. Depending on the number and combination of the six quarks, different hadrons (3 quarks) and mesons (2 quarks) are formed in nature. Leptons are divided in three generations, each consisting of

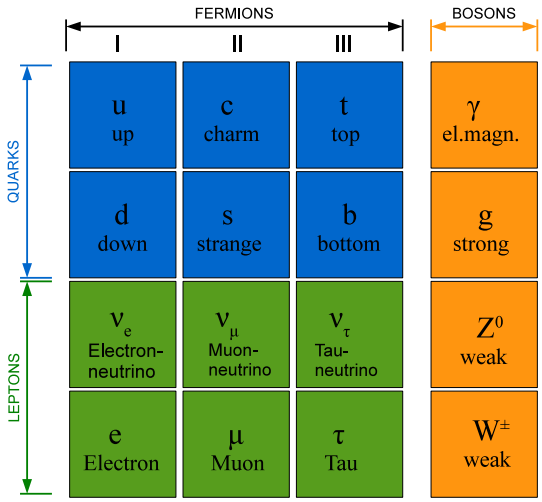

Figure 1.2: Scheme of the Standard Model and its particles. The model contains twelve fundamental particles of matter (fermions) and four force carrying bosons. The bosons are responsible for the electromagnetic, weak and strong interactions. Gravity is not included in the standard model.

an electron e, muon μ and tau τ, which are paired together with a neutrino flavor counterpart ν_e, ν_μ and ν_τ. An overview of the particles involved in the standard model is shown in figure 1.2.

Neutrinos are the lightest known elementary fermions. They do not carry an electrical charge and undergo only weak interactions, which makes them difficult to observe. In the Standard Model, neutrinos are massless, they have three flavor eigenstates and are paired with charged leptons in weak isodoublets. If the neutrino flavor eigenstates participating in the weak interactions differ from the neutrino mass eigenstates, which control the free particle evolution in time, the weak eigenstates $\langle\nu_\alpha|$, with $\alpha = \mathrm{e}, \mu, \tau$ can be expressed as

a linear combination of the three mass states $\langle\nu_i|$, $i = 1, 2, 3$ according to

$$\langle\nu_\alpha| = \sum_i U^*_{\alpha i}|\nu_i\rangle\,, \tag{1.2}$$

where U is a 3x3 unitary neutrino mixing matrix, called the Pontecorvo-Maki-Nakagawa-Sakata (PMNS) matrix. Using the time-dependent Schroedinger equation, expression (1.2) leads to a time or distance dependent neutrino oscillation described by

$$\langle\nu_\alpha(L)| \approx \sum_j U^*_{\alpha j} e^{-i(m_j^2/2E)L}|\nu_j\rangle \tag{1.3}$$

where m_j describes the mass of the j'th eigenstate, L is the travel distance of the neutrino and E is the average energy of all mass eigenstates. After a neutrino with the eigenstate $|\nu_\alpha\rangle$ has travelled a distance L, the probability P to find it in a flavor state $|\nu_\beta\rangle$ can be expressed by

$$P = |\,\langle\nu_\beta|\nu_\alpha(L)\rangle\,|^2\ . \tag{1.4}$$

Neutrino oscillations as described in equation (1.4) imply a violation of the individual lepton number conservation.

Assuming a simplified two-neutrino flavor scenario, the PMNS matrix can be expressed by a 2x2 rotation matrix U,

$$U = \begin{bmatrix} \cos\Theta & \sin\Theta \\ \text{-}\sin\Theta & \cos\Theta \end{bmatrix}, \tag{1.5}$$

where Θ is given by the mixing angle between the mass- and flavor - eigenstates. Additionally, assuming $\Theta \neq 0$, equation (1.4) leads to a non-zero oscillation probability $P(\nu_\alpha \to \nu_\beta)$ if at least one of the mass eigenstates has a non-zero value, as can be expressed by:

$$P(\nu_\alpha \to \nu_\beta) = \sin^2(2\Theta) \cdot \sin^2(\Delta m^2_{12}\frac{L}{4E})\,, \tag{1.6}$$

where Δm^2_{12} is the squared mass difference between two neutrino mass eigenstates. The interpretation of equation (1.6) leads to the conclusion that neutrino oscillations can only take place if they are massive.

In the case of three neutrino flavors, the 3x3 unitary matrix U is parametrized by three angles and three phases

$$U = \begin{bmatrix} 1 & 0 & 0 \\ 0 & c_{23} & s_{23} \\ 0 & -s_{23} & c_{23} \end{bmatrix} \times \begin{bmatrix} c_{13} & 0 & s_{13}e^{-i\delta} \\ 0 & 1 & 0 \\ -s_{13}e^{i\delta} & 0 & c_{13} \end{bmatrix} \times \begin{bmatrix} c_{12} & s_{12} & 0 \\ -s_{12} & c_{12} & 0 \\ 0 & 0 & 1 \end{bmatrix} \times \begin{bmatrix} e^{i\alpha_1/2} & 0 & 0 \\ 0 & e^{i\alpha_2/2} & 0 \\ 0 & 0 & 1 \end{bmatrix}, \tag{1.7}$$

where $s_{ij} = \sin\Theta_{ij}$ and $c_{ij} = \cos\Theta_{ij}$ are defined by the three Euler angles responsible for the mixing. The three parameters δ, α_1 and α_2 are phases that are used to describe the

neutrinos as Dirac or Majorana particles. If neutrinos are Dirac particles, only the Dirac phase δ is physical and responsible for the CP violation in the lepton sector. If neutrinos are Majorana particles, they are their own antiparticles and the two additional phases α_1 and α_2 are observables too.

Summarizing, the observation of neutrino oscillations allow to conclude that neutrinos have mass. Furthermore, knowing their energy and the distance travelled allows only determination of the squared-mass-difference component in equation (1.6). Neutrino oscillation experiments performed in the past already provided the evidence for the massive nature of neutrinos. However, such experiments do not allow to determine the absolute scale of the mass eigenstates. Besides experiments measuring solar and atmospheric neutrinos (e.g. Super-Kamiokande, SNO, IceCube), neutrino generating experiments were performed using reactors (Kamland, Daya Bay, Double Chooz) or accelerators (T2K, Minos e.g.). Experiments with atmospheric or accelerator neutrino oscillations provided information about the $\nu_\mu \rightarrow \nu_\tau$ oscillations, while solar neutrino experiments were consistent with the $\nu_e \rightarrow \nu_\mu$ or $\nu_e \rightarrow \nu_\tau$ oscillations. Combined data analysis leads to a steadily growing precision in the knowledge about the neutrino masses. Data from Kamland and from the observations of solar neutrinos [2] for example, resulted in the determination of the Δm_{12} neutrino mass splitting given by

$$\Delta m^2_{12} = (7.59 \pm 0.21)10^{-5}\text{eV}^2, \tag{1.8}$$

while the MINOS collaboration [3] found a value for the Δm_{32} mass splitting with:

$$\Delta m^2_{32} = (2.32^{+0.12}_{-0.08})10^{-3}\text{eV}^2. \tag{1.9}$$

Besides the mass splittings, all three mixing angles of the PMNS matrix have been measured. Recently, the Daya Bay collaboration found the most precise value for the Θ_{13} angle, with

$$\sin^2\Theta_{13} = 0.092 \pm 0.017 \tag{1.10}$$

as reported in [4]. The full up-to-date knowledge about the neutrino masses and the mixing angles is shown in table 1.1. It allows for two possible mass splitting configurations which are schematically illustrated in figure 1.3 with the masses increasing from bottom to top. The figure also shows the flavor contents of each mass eigenstate. Two neutrino hierarchies are compatible with the existing data:

Normal hierarchy: $m_1 < m_2 < m_3$, $\Delta m^2_{12} \ll \Delta m^2_{23}$

Inverted hierarchy: $m_3 < m_1 < m_2$, $\Delta m^2_{12} \ll \Delta m^2_{13}$

In order to complete the picture of the neutrino masses, the final hierarchy must be determined as well as the mass of the lightest neutrino. While future accelerator experiments could clarify the question of the neutrino hierarchy, double beta decay experiments such

Parameter	Value in $\pm 1\sigma$	Ref.
Δm^2_{21} $[10^{-5}\text{eV}^2]$	$7.59^{+0.2}_{-0.18}$	[5]
Δm^2_{32} $[10^{-3}\text{eV}^2]$	$2.32^{+0.12}_{-0.08}$	[3]
Δm^2_{31} $[10^{-3}\text{eV}^2]$	$2.45^{+0.09}_{-0.09}$ [nh] $-(2.34^{+0.10}_{-0.09})$ [ih]	[5]
$\sin^2\Theta_{12}$	$0.312^{+0.017}_{-0.015}$	[5]
$\sin^2\Theta_{23}$	$0.51^{+0.06}_{-0.06}$ [nh] $0.52^{+0.06}_{-0.06}$ [ih]	[5]
$\sin^2\Theta_{13}$	$0.092^{+0.017}_{-0.017}$	[4]

Table 1.1: Overview of the current knowledge about the neutrino masses and the mixing angles. Values referring to normal and inverted hierarchies are designated as [nh] and [ih] respectively.

as the topic of this thesis could provide information about the effective neutrino mass or about the lightest neutrino. A direct measurement of the latter could for example be realized in close future by the KATRIN experiment [6], which investigates the endpoint of the β decay spectrum of tritium.

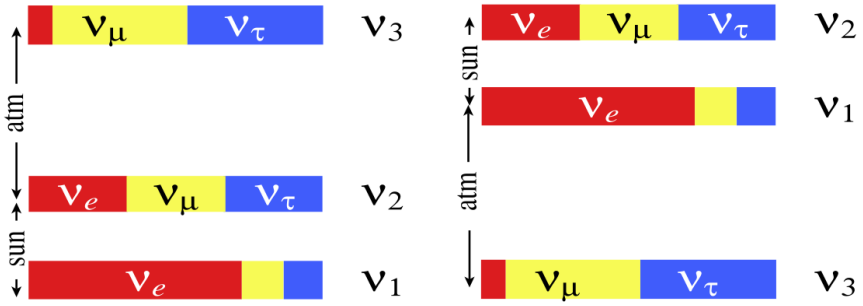

Figure 1.3: Left: Normal neutrino mass hierarchy. The red, yellow and blue bulks denote the flavor content in the mass state ν_i. Right: inverted neutrino mass hierarchy. Both hierarchies are consistent with the current experimental knowledge. Picture taken from [7]

1.2 The Neutrinoless Double Beta Decay ($0\nu\beta\beta$)

Oscillation experiments as outlined in section 1.1 are not able to determine the absolute neutrino mass scale and to distinguish between the two possible mass hierarchies. Furthermore, they tell nothing about the charge conjugation properties of the neutral neutrinos. While charged leptons (Dirac particles) are distinguishable from their charge conjugated antiparticles, Majorana particles are described by fields which remain equal under charge

conjugation $\nu_i^c = \nu_i$ and hence are their own antiparticles. In the standard model, neutrinos are massless Dirac particles and undergo only lepton number conserving processes [8]. However, as neutrino oscillation experiments have shown, neutrinos have a non-zero mass which indicates an incomplete Standard Model description of particle physics. In addition, Majorana neutrinos would allow for observation of processes that violate lepton number conservation.

A process which is considered to enlight the nature of neutrinos and to investigate physics beyond the Standard Model is the double beta decay. In principle, two $\beta\beta$ decay modes are possible which will be outlined below.

The double beta decay ($\beta\beta$) is a rare second order transition between two nuclei with the same atomic number A, in which the nucleus with Z protons decays into a nucleus with $(Z+2)$ protons.

$$(Z, A) \rightarrow (Z+2, A) + e_1^- + e_2^- + \overline{\nu}_{e_1} + \overline{\nu}_{e_2} \tag{1.11}$$

The transition of a ${}^A_Z X$ into a ${}^A_{Z+2} Y$ nucleus can only take place towards a daughter nucleus of lower energy, which is expressed by the Bethe-Weizsäcker formula:

$$E_B({}^A_Z X) = a_1 A - a_2 A^{2/3} - a_3 Z^2 A^{-1/3} - a_4 (N-Z)^2 A^{-1} + \delta \tag{1.12}$$

where a_1, a_2, a_3 are constants and N is the number of neutrons. The pairing term δ is defined for even-even, odd-odd nuclei, and odd atomic number nuclei:

$$\delta(A, Z) = \begin{cases} +\delta_0 & Z,\ N \text{ even, with } A = Z + N \\ 0 & A \text{ odd} \\ -\delta_0 & Z,\ N \text{ odd} \end{cases} \tag{1.13}$$

with

$$\delta_0 = \frac{12}{A^{-3/4}}\,. \tag{1.14}$$

According to expressions (1.12) and (1.13), even-even nuclei are more bound than odd-odd nuclei. Consequently, the binding energy of a nucleus is described by two parabolic distributions in Z as illustrated in figure 1.4. Given by the binding energy of the nucleus, the ($\beta\beta$) transition can only be observed if the single beta transition is energetically forbidden, while on the other side the double beta decay mode is allowed. Such a condition is illustrated in figure 1.4 for the ^{76}Ge isotope. Although the decay through an excited state is possible in principle, typically the decay takes place from the ground state 0^+ of the initial nucleus directly to the ground state of the final nucleus. In total, there are 35 naturally occurring isotopes which can undergo a $\beta\beta$ decay. Although very rare, the two neutrino double beta decay has been observed in several experiments with typical $2\nu\beta\beta$ lifetimes between $10^{18} - 10^{20}$ years as summarized in table 1.2. Because, lepton number and electric charge in the two neutrino double beta decay are conserved, the process is allowed

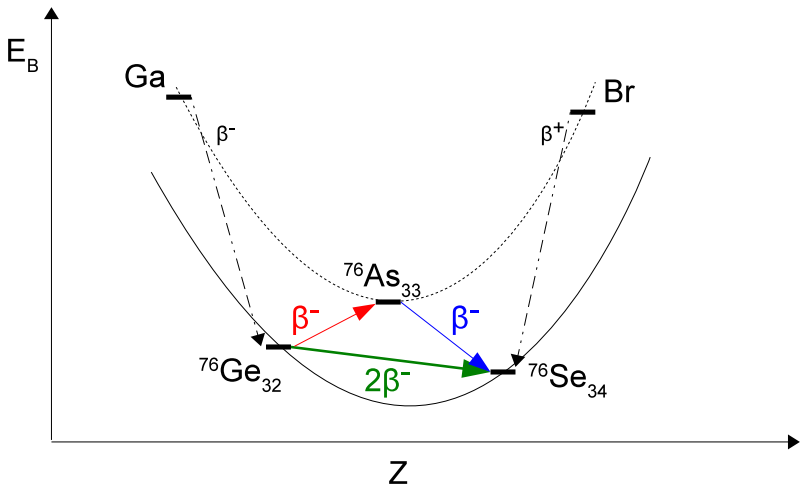

Figure 1.4: Principle of the double beta decay. The single β decay of ^{76}Ge to ^{76}As is energetically forbidden. Because the binding energy of the ^{76}Se is lower than the binding energy of ^{76}Ge, the $\beta\beta$ transition to ^{76}Se is possible.

by the Standard Model of particle physics and was first detected in 1950 in a geochemical experiment [9]. Direct detection took place in 1987 by measuring the double beta decay in ^{82}Se [10]. Besides the two neutrino double beta decay

Isotope	$T^{2\nu}_{1/2}$ [y]	Experiment
^{48}Ca	$(4.4^{+0.6}_{-0.5}) \times 10^{19}$	Irvine TPC [11], TGV [12], NEMO3 [13]
^{76}Ge	$(1.5 \pm 0.1) \times 10^{21}$	PNL-USC-ITEP-YPI [14], IGEX [15], Heidelberg-Moscow [16]
^{82}Se	$(0.92 \pm 0.07) \times 10^{20}$	NEMO3 [17], Irvine TPC [18], NEMO2 [19]
^{96}Zr	$(2.3 \pm 0.2) \times 10^{19}$	NEMO2 [20], NEMO3 [21]
^{100}Mo	$(7.1 \pm 0.4) \times 10^{18}$	NEMO3 [17], NEMO-2 [22], Irvine TPC [23]
^{116}Cd	$(2.8 \pm 0.2) \times 10^{19}$	NEMO3 [13], ELEGANT [24], Solotvina [25], NEMO2 [26]
^{130}Te	$(6.8^{+1.2}_{-1.1}) \times 10^{20}$	CUORICINO [27], NEMO3 [28]
^{136}Xe	$(2.11 \pm 0.21) \times 10^{21}$	EXO-200 [29], KamLAND-Zen [30]
^{150}Nd	$(8.2 \pm 0.9) \times 10^{18}$	Irvine TPC [23], NEMO3 [31]

Table 1.2: Measured $2\nu\beta\beta$ transition half-lifes in nine different isotopes.

$$2\nu\beta\beta : (Z, A) \rightarrow (Z + 2, A) + 2e^- + 2\overline{\nu}_e \tag{1.15}$$

a second decay mode is hypothetically possible. The neutrinoless double beta decay, first proposed by W.H.Furry in 1939 [32],

$$0\nu\beta\beta : (Z, A) \rightarrow (Z + 2, A) + 2e^- \tag{1.16}$$

is possible by assuming the neutrinos to be their own antiparticles. In this case, two electrons and two electron antineutrinos are emitted, but in contrast to the $2\nu\beta\beta$ decay, the two neutrinos can annihilate internally, which results in an emission of only two electrons. The Feynman diagram in figure 1.5 outlines the two channels of double beta decay. In the $2\nu\beta\beta$ mode, two parent neutrons decay simultaneously into two electrons and two antineutrinos by exchanging a pair of W bosons. If the two neutrinos are Majorana particles, they can exchange between the two W bosons, giving rise to an emission of only two electrons on the output channel. Consequently only two electrons are emitted. In the neutrinoless

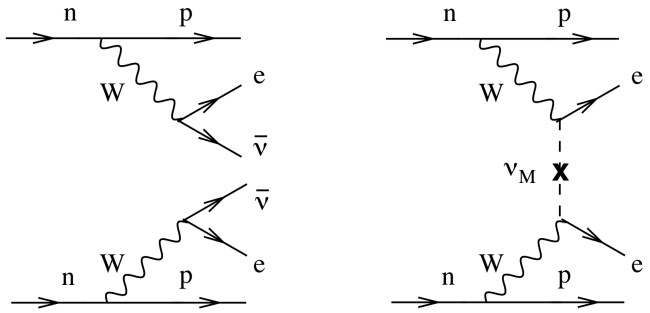

Figure 1.5: Feynman diagrams of the $2\nu\beta\beta$ decay (left) and of the neutrino less $0\nu\beta\beta$ decay, [33].

double beta decay, the lepton number in the initial state is 0, while the lepton number after the decay changes to +2. Therefore, with $\Delta L_{0\nu\beta\beta} = 2$, the $0\nu\beta\beta$ decay process does not conserve the lepton number and is not compatible with the Standard Model.

The kinetic energy of the reaction products in the $0\nu\beta\beta$ is given by the Q-value of the reaction and is shared only by the two electrons if neglecting the nuclear recoil energy. Figure 1.6 shows the continuous spectrum of the $2\nu\beta\beta$ decay in ^{76}Ge with the endpoint given by the Q-value. In contrast to the two neutrino transition, the signature of the $0\nu\beta\beta$ transition must be a sharp peak appearing at the Q-value, with $Q = 2.039$ MeV given for the ^{76}Ge isotope. As has been shown by the Schechter-Valle theorem [35] (Black-Box-Theorem), neutrinoless double beta decay always requires a massive Majorana neutrino independent of the mechanism responsible for the decay. The non-zero mass condition is fulfilled as was shown by neutrino oscillation experiments in the past. The half-life of the $0\nu\beta\beta$ decay can be expressed using Fermi's golden rule [36] by

$$(T^{0\nu}_{1/2})^{-1} = G_{0\nu}(Q, Z) \mid M_{0\nu} \mid^2 \langle m_\nu \rangle^2, \tag{1.17}$$

where $M_{0\nu}$ is the nuclear matrix element (NME) describing the hadronic part of the decay. $G_{0\nu}$(Q,Z) is an integrated kinematic factor (phase space factor) depending on the decay Q-value and the nuclear charge Z, which can be calculated theoretically. Based on different nuclear models, the NME element can also be calculated but with considerable uncertainties. In equation (1.17), $\langle m_\nu \rangle^2$ describes the effective Majorana neutrino mass

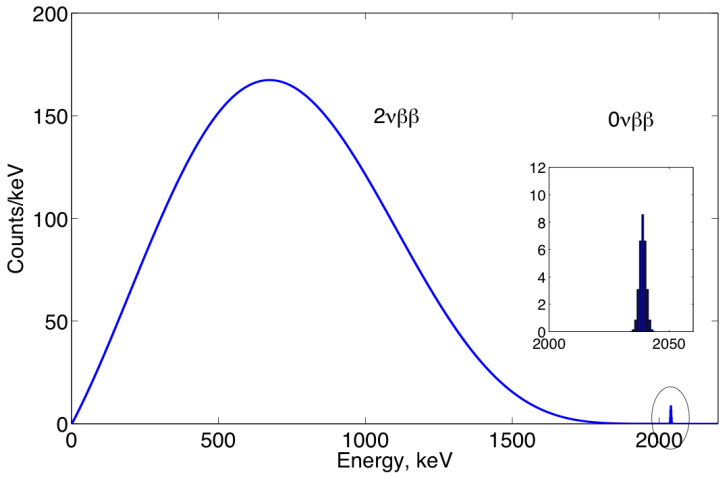

Figure 1.6: Spectrum of the $2\nu\beta\beta$ decay in ^{76}Ge and the sharp signature at the Q-value as expected for the $0\nu\beta\beta$ decay. Figure taken from [34].

expressed by the neutrino mass eigenstates

$$\langle m_\nu \rangle = \mid \sum_{i=1,2,3} m_i U_{ei}^2 \mid, \tag{1.18}$$

where U_{ei} is the unitary matrix defined in equation (1.7) which is responsible for the mixing of the neutrino mass eigenstates to electron neutrinos. Equation (1.17) shows that a non-zero rate for the $0\nu\beta\beta$ decay is observable only for massive Majorana particles. Furthermore, measuring the half-life $T_{1/2}^{0\nu}$ allows for direct conclusions on the effective neutrino mass given by

$$\langle m_\nu \rangle = \frac{6.4 \cdot 10^{12}}{\mid M_{0\nu} \mid \cdot \sqrt{T_{1/2}^{0\nu}[y]}} [\mathrm{eV}]. \tag{1.19}$$

It should be noted that although the Majorana nature of the neutrino can be proven and the effective neutrino mass measured by the observation of $0\nu\beta\beta$ decay, the precision of the measurement is not only given by the experimental conditions but also by the uncertainties of the nuclear models applied in the NME calculations. However, the implications of massive Majorana neutrinos for particle physics are highly intriguing and led to a new generation of $0\nu\beta\beta$ decay experiments. Different configurations have been designed and constructed ranging from separate $0\nu\beta\beta$ sources, solid state detectors, to time projection chambers with the goal to reach the best sensitivity for the neutrinoless double beta decay. In the following, the current status of the neutrinoless double beta decay search will be presented and some of the past, present, and future experiments described.

1.3 Status of the $0\nu\beta\beta$ decay search

The first claim of observing the neutrinoless double beta decay was reported in 2001 by part of the Heidelberg-Moscow experiment (H-M) [37]. The detector consisted of five coaxial, high purity germanium detectors, isotopically enriched in ^{76}Ge up to 86%. Because enriched germanium crystals can be used as the source of $0\nu\beta\beta$ decay and simultaneously be operated as detectors, Ge detectors are the most sensitive experimental setups searching for the neutrinoless double beta decay.
In general, the half-life sensitivity of an experiment improves with increasing lifetime t and the total sensitive mass M. Furthermore, the sensitivity degrades with decreasing detector resolution δE and increasing background B. In enriched germanium detectors, the $\beta\beta$ decay rate scales with an increasing abundance a of the ^{76}Ge isotope and with a decreasing molecular weight W of the source isotope. Considering the detection efficiency ϵ for events at energies equivalent to the Q-value, the total experimental sensitivity can be expressed by

$$T_{1/2}^{0\nu} = \alpha \left(\frac{\epsilon \cdot a}{W}\right) \times \sqrt{\frac{M \times t}{\delta E \times B}} \tag{1.20}$$

as shown in [38] for example. The parameter α is defined for a given signal S to background B ratio and has a value of

$$\alpha \approx 7.3 \times 10^{25}\text{years} \tag{1.21}$$

for $S \approx B$. With 71.7 kg·years of exposure and a background rate of 0.11 keV^{-1}kg^{-1}year^{-1}, the Heidelberg-Moscow experiment found a $0\nu\beta\beta$ half-life range of (0.69-4.18)·10^{25} years within 3σ for the ^{76}Ge decay [39]. The range translates into an effective Majorana neutrino mass of $\langle m_\nu \rangle$ = (0.24-0.58)eV. However, it should be noted that the Heidelberg-Moscow result was claimed only by a part of the collaboration and that the claim is highly controversial to this day. As shown for example in [40], the performed data analysis did not identify three peaks in the region of interest with a higher significance than the 2039 keV peak of the $0\nu\beta\beta$ decay. Furthermore, a null hypothesis analysis has not been performed, and therefore the statistical significance of the peak is not obvious.

Despite the controversial analysis aspects of the Heidelberg-Moscow experiment, the experimental setup was of excellent quality and presented that the conditions required to detect a $0\nu\beta\beta$ signal can be fulfilled with current technology. The claim triggered a chain of projects with the goal to confirm the $0\nu\beta\beta$ claim of the Heidelberg-Moscow experiment with an improved detection sensitivity. In the following, an overview of the current and future experiments searching for the neutrinoless double beta decay will be presented:

IGEX (International Germanium Experiment): The experiment used enriched detectors between 1991 and 2000 and was run in the Homestake gold mine (USA), in the Canfranc Underground Laboratory in Spain, and in the russian Baksan neutrino observatory. In total, the experiment reached an exposure of 8.87 kg·year and reached a comparable sensitivity to the Heidelberg-Moscow experiment. With pulse shape discrimination,

the lowest background ever reached by the experiment was 0.1 counts/(keV·kg·y) with an exposure of 4.65 kg·year [41]. Although the sensitivity reached was close to the Heidelberg-Moscow sensitivity, IGEX could not reject the H-M claim.

CUORICINO: The experiment was setup in the LNGS underground laboratory in Italy and started in 2003. An array of 62 TeO_2 bolometric crystals has been used to search for the $0\nu\beta\beta$ decay of ^{130}Te. With a background of (0.161± 0.006) counts/(keV·kg·y) and five years of exposure [42], the experiments sensitivity was close to the H-M experiment, but could not reject the claim due to uncertainties in the nuclear matrix elements.

NEMO (Neutrino Ettore Majorana Observatory): The experiment was an example for a setup with a separated $0\nu\beta\beta$ source from the detector. The source consists of 20 cylindrical molybdenum foils, enriched in ^{100}Mo with a mass of 10 kg in total. The segmented foils were located in cylindrical plastic scintillators for calorimetry. Furthermore, a magnetic field of 25 Gauss allowed to determine the electrical charge of the tracks observed. NEMO was run between 2003 and 2010 at the Modane Underground Laboratory (LSM) in France and achieved the lowest background level so far of $\sim 10^{-3}$ counts/(keV·kg·y) , [43].

CUORE (Cryogenic Underground Observatory for Rare Events): The experiment is still under construction and is based on the experience from the Cuoricino experiment. The detector will consist of 988 TeO_2 bolometers which will be arranged in 19 towers and operated at (7 -10) mK [44]. Neutron Transmutation Doped (NTD) germanium thermistors will be used to measure the energy deposited in the crystals. The planned total ^{130}Te source mass will be 206 kg, while the total detector mass will be 741 kg. The single tower version of CUORE has been assembled at LNGS in 2011.

EXO (Enriched Xenon Observatory): The experiment uses a time projection chamber (TPC) containing liquid xenon (enriched to 80.6 % in ^{136}Xe) allowing to detect scintillation light and ionization for an effective discrimination efficiency. The first EXO version with natural xenon, EXO-200 contains 200 kg of liquid xenon and has been first assembled in 2010 at WIPP (Waste Isolation Pilot Plant) in the USA with an overburden of 1585 m water equivalent. In order to achieve the goal of being virtually background free, barium tagging is a priority task for EXO especially with regard to a future ton scale experiment. In 2011, first results from the EXO-200 experiment have been published with a measured half-life for the $2\nu\beta\beta$ decay in ^{136}Xe of $T_{1/2} = 2.11\pm0.04$ (stat) ±0.21 (sys)$\times10^{21}$ years [29]. The easy scaleability of liquid xenon which can be used as source and detector simultaneously makes the technology very competitive to solid state detectors.

GERDA (GERmanium Detector Array): GERDA uses naked germanium detectors enriched to 86% in ^{76}Ge and immersed in ultra pure liquid argon. The detectors are assembled in strings which are used to lower the detectors into a stainless steel cryostat. The cryostat is surrounded by an instrumented water shield containing 66 photomultipliers used as a

veto against cosmic muons. Plastic scintillators mounted on top of the detector will be used to increase the discrimination efficiency. GERDA started with phase I in 2010, immersing 17.7 kg of coaxial Ge-detectors which were used in the past by the Heidelberg-Moscow and IGEX experiments. The background measured is (0.07 ± 0.02) counts/(keV·kg·y) [45], which is higher than the background goal of $1{\cdot}10^{-2}$ counts/(keV·kg·y) for the first phase, but lower than the Heidelberg-Moscow and IGEX backgrounds. Although the source of background is not fully understood yet, event discrimination based on pulse shape analysis (PSA) has not been applied so far, and hence a further background reduction will be achieved in near future. In phase II of GERDA, additional p-type Broad Energy detectors will be deployed resulting in a total mass of 35.4 kg. The new detectors are known for an excellent noise and resolution performance and allow for effective PSA discrimination methods. A third phase of GERDA is also foreseen in the future with about one ton of ^{76}Ge material implemented.
More details about GERDA and the BEGe detector technology planned for phase II will be described below in the course of the present work.

MAJORANA: In contrast to the GERDA experiment, MAJORANA will use Ge detectors not immersed in liquid argon, but arranged in an ultra clean vacuum cryostat made of radiopure copper. The first 40 kg demonstrator is under construction at the Deep Underground Science and Engineering Laboratory (DUSEL) in the USA. The demonstrator will contain 20 kg of natural germanium BEGe detectors. The same type of detectors made of enriched germanium is foreseen for the second phase of GERDA. In 2013, the demonstrator is expected to be operational with 12 kg of enriched Ge detectors [46]. The future goal of MAJORANA is a one-ton setup to be realized in an international collaboration.

KamLand-Zen: Like EXO, the KamLand-Zen experiment uses the ^{136}Xe isotope as a source of the $0\nu\beta\beta$ decay. Instead of using a TPC, the xenon gas is dissolved in a liquid scintillator, which allows measurement of the energy of the electrons. It is foreseen to dissolve about 400 kg of ^{136}Xe in the scintillator and up to one ton in the second phase of the experiment. The Xe-loaded liquid scintillator is contained in a transparent balloon, immersed in a second outer volume balloon with liquid scintillator surrounded by photomultipliers. First results for the half-life of the $2\nu\beta\beta$ decay of ^{136}Xe were obtained recently. A measured half-life $T_{1/2} = 2.38{\pm}0.02(\text{stat}) \pm 0.14(\text{sys}){\times}10^{21}$ years has been reported in [30] which is fully consistent with the results obtained by the EXO experiment. The result based on a configuration with 129 kg of ^{136}Xe and an exposure of 77.6 days.

NEXT (Neutrino Experiment with Xenon TPC): the NEXT experiment plans to use the ^{136}Xe isotope as the source and detection medium of $0\nu\beta\beta$ decay. The Xe gas is contained in a TPC under high pressure. The setup allows for a good energy resolution via scintillation light and provides topological information of ionizing event tracks. Both allow for an excellent event discrimination, resulting in an expected background value of $2{\cdot}10^{-4}$ counts/(keV·kg·y) [47]. Commissioning of a 100 kg NEXT configuration at the Canfranc

underground laboratory in Spain is expected in 2013.

SNO+: SNO+ is the successor of the SNO experiment [48], located in the SNOLAB in Canada. The experiment will use liquid scintillator, loaded with 50 kg of the ^{150}Nd isotope. The liquid will be contained in an acrylic, spherical vessel surrounded with photomultipliers. The ^{150}Nd isotope has a calculated decay endpoint of 3.37 MeV, which is above most of the background resulting from natural radioactivity. Based on simulations, a background of 10^{-2} counts/(keV·kg·y) has been predicted for the SNO+ project [49]. Besides the search of neutrinoless double beta decay, the experiment will also perform measurements of low energy solar neutrinos. Commissioning of SNO+ is expected in 2013.

SuperNEMO: SuperNEMO is a further development of the NEMO experiment. Instead of the Mo foils used in NEMO, ^{82}Se will likely be used as the $0\nu\beta\beta$ source. Under consideration are also ^{150}Nd and ^{48}Ca foils. The detector will consist of 20 calorimeter modules, each of them containing a $0\nu\beta\beta$ source foil with a mass of about 5 kg. As its precursor, the new detector configuration will allow for reconstruction of the event trajectories, but furthermore, it is also expected to have better detection efficiency and resolution. Background reduction will be performed by purification methods applied to the foils, resulting in a drastic reduction of the ^{214}Bi, ^{208}Tl and ^{82}Se contents. The first demonstrator will be assembled in the Modane Underground Laboratory and is expected to start in 2013.

Besides the experiments described above, further future projects are under development using, for example, CaF_2 scintillation crystals, CdZnTe semiconductor detectors, or ZnSe crystals. Considering the recent progress in detector technology and background reduction

Experiment	Mass [$kg_{\beta\beta}$]	$T^{0\nu}_{1/2}$ [y]	$m_{\beta\beta}$ [meV]
H-M (claim)	15.2	$(0.69\text{-}4.18)\cdot10^{25}$	240-580
CUORE	206	$8.86\cdot10^{25}$	63
GERDA-I	15.2	$4.49\cdot10^{25}$	252
GERDA-II	30.4	$1.37\cdot10^{26}$	121
EXO200	141	$8.2\cdot10^{25}$	82
KamLAND-Zen	357	$1.32\cdot10^{26}$	65
Majorana	17.2	$7.2\cdot10^{25}$	258

Table 1.3: Sensitivities of experiments for the $0\nu\beta\beta$ half-lifes and the resulting effective neutrino masses. The values are given in 90% CL for an exposure of five years. The first line shows the Heidelberg-Moscow claim for comparison. Data were taken from [50]

techniques, a confirmation or rejection of the Heidelberg-Moscow claim can be expected within a couple of years. As shown in table 1.3 most of the expected half-life sensitivities of already commissioned experiments or near-future experiments will reach the H-M limit after an exposure of 5 years. Depending on the upgrades performed on running detec-

tors, the goal could be reached even earlier. Increasing the sensitive mass, improving the detector resolution, and further background reduction will all increase the sensitivity.

1.4 Germanium detectors in low-background experiments

Due to their excellent energy resolution, detection efficiency, and low threshold energies, germanium detectors cover a broad spectrum of applications mainly in X- and γ-ray detection. The field of operation covers not only areas in applied physics like in medicine or industry, but also fundamental research areas. This entails, for example, fields in spectroscopy, neutron activation, the search for rare signals, screening methods, and background monitoring.

The working principle of Ge detectors is equivalent to this of most semiconductor detectors consisting of two merged volumes, each of them doped with donor and acceptor atoms respectively. Dopants are atoms with at least one more valence electron (donor) or at least one less valence electron (acceptor) in the outer shell than present in the semiconductor atom. Doping changes the energy band structure of a semiconductor by introducing additional discrete energy levels between the valence band and the conductive band. Donor-doped materials are called n-type semiconductors. They are characterized by a low-energy gap between the conductive band and the closest discrete energy level and allow excitation of the electrons into the conductive band with little effort. In the case of germanium, the energy gap is $\sim$0.7 eV which means that electron excitation takes place already at room temperature. It should be considered however, that part of the energy is deposited in phonons in the atomic lattice. Therefore, the average energy needed to produce an electron-hole pair in a germanium crystal at 80 K is 2.95 keV rather than 0.7 eV. Acceptor impurities create a discrete level close to the valence band and introduce an excess of holes in the crystal. In consequence, electrons from the valence band can easily be excited into the extra level, leaving holes behind which are the major charge carriers in p-type semiconductors.

Semiconductor detectors are setup in a diode configuration established via a p-n junction. Figure 1.7 illustrates a p-n junction with a p-type block on the left and the n-type counterpart on the right. Due to the unequal electron concentrations on both sides of the junction, a diffusion current consisting of electrons and holes starts to flow. Electrons diffuse from the n-type area to the p-type area, while holes diffuse in the opposite direction. Since both parts were initially electrical neutral, the diffusion causes a negative net-charge on the p-type side and a positive net charge on the n-type side. In consequence an electrical field builds up, which acts against further diffusion of the charges. Finally, a static equilibrium within the semiconductor is reached with a charge gradient around the junction. The depletion region of a semiconductor is defined as the region in the bulk

characterized by a changing electrical potential. Charges induced in the depletion zone by

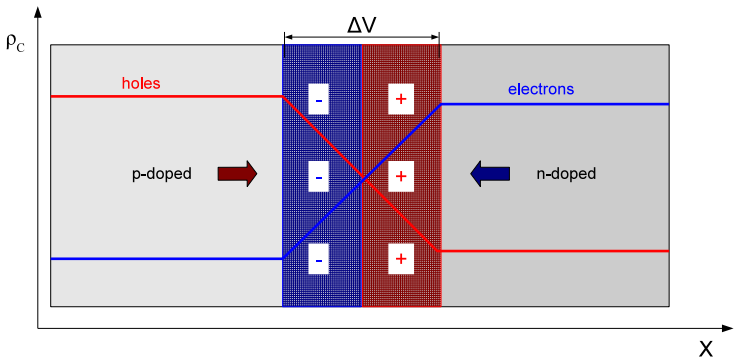

Figure 1.7: Schematic of the charge distribution along a p-n junction. The gradient of the charge density after a diffusion equilibrium has been reached, generates an electrical field which can be used to detect ionization radiation.

ionizing radiation will be accelerated in the electrical field inducing a measurable signal. The p-n junction as illustrated in figure 1.7 can be used as an ionizing radiation detector by measuring a voltage signal on both sides of the block. However, the detection efficiency can be increased drastically by increasing the depletion zone. Applying a positive voltage on the p-side and a negative voltage on the n-side will minimize the depletion zone until the charges recombine and electrical conductivity is established. On the other hand, operating the p-n junction in the reverse bias configuration with a negative voltage on the p-side and a positive voltage on the n-side will increase the depletion zone as shown in figure 1.8 and the p-n configuration will act as an insulator. Because the depletion zone has been increased, the sensitive volume for ionizing radiation has been also increased. Besides the

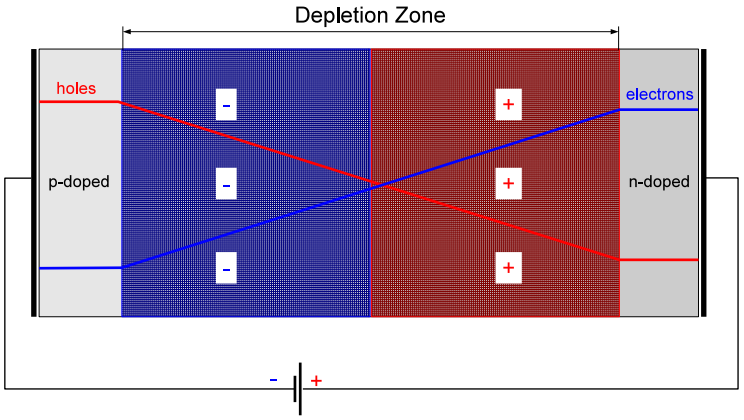

Figure 1.8: Reversed bias voltage applied to a p-n junction for maximizing the depletion zone.

larger sensitive volume, also the charge collection efficiency increases with higher reverse bias voltages. However, the maximal voltage applied is limited by the resistance of the semiconductor, which at some point will break down and start to conduct. Typical voltages

applied to modern germanium detectors are several kV, reaching about 1 mm of depletion per 300 V. The resistivity and hence the maximal bias voltage can be increased using high purity semiconductors.

Germanium crystals are grown in cylinder-shaped ingots. In order to maximize their efficiency, the detectors are typically built in coaxial crystal geometries. Crucial for the final performance of the detector are impurities in the crystal which can act as recombination or trapping centers resulting, for example, in charge trapping, incomplete or delayed charge collection, increased leakage current, and a worsened energy resolution. Furthermore, a reduced bulk resistivity caused by material impurities reduces the breakdown voltage and hence limits the maximal reachable depletion volume. However, intrinsic (ideally pure) semiconductors do not exist in reality. All semiconductors contain impurities of both types p- and n- with acceptor concentrations N_A and donor concentrations N_D, respectively. After a crystal has been grown, the net concentration

$$c_{net} =\mid N_A - N_D \mid \tag{1.22}$$

determines whether the crystal is n-type or p-type. Crystals with equal donor and acceptor concentrations can be considered as intrinsic and are also called compensated materials. As shown for example in [51], the depletion thickness D can be expressed in terms of the applied voltage V and in terms of the net concentration according to

$$D = \sqrt{\frac{2 \cdot \epsilon \cdot V}{e \cdot c_{net}}}, \tag{1.23}$$

with ϵ given by the dielectric constant of the material and with the electric charge e. Therefore, the detection efficiency at a given bias voltage can be improved by minimizing the net concentration in the material. Because compensated materials need the same concentrations on donor and acceptor impurities, they are extremely difficult to produce. The amount of dopant atoms (p or n) needed in semiconductor detectors is usually very low with typical concentrations of $(10^{10} - 10^{13})$ atoms/cm^3 and are in principle very close to compensated crystals. Because the ideal detector contains a minimal concentration of impurities, the goal is always to come as close as possible to an intrinsic material and therefore to minimize the net concentration c_{net}. The first method to compensate semiconductor crystals was developed in 1960 using a lithium (donor) drifting technique applied to a precursor p-type crystal [52]. During the process, lithium diffuses from outside into the p-type bulk which changes the surface to a highly doped n-type layer (designated as n^+). Furthermore, the positive lithium ions are forced further into the bulk by applying a bias voltage. The diffusion reaches a natural equilibrium leaving a compensated volume within the crystal. To reduce the time of the compensation process, mobility of the lithium ions has been increased by heating up the crystal. However, even at room temperature, the lithium mobility is not negligible and therefore, in order to sustain the compensation and to prevent the lithium of diffusing out again, lithium drifted germanium detectors must be always kept at cryogenic temperatures.

Although lithium drifted germanium detectors are still in use, modern detectors are made of ultrapure germanium with impurity net concentrations reaching $\sim 10^9/\mathrm{cm}^3$. The technique was developed in the mid 1970's and is based on zone refinement performed through local melting of the crystal [53]. The melting allows the impurities to transfer from the solid to the melted zone. The final crystal impurity concentration is reached after repeating the procedure several times. In contrast to lithium-drifted detectors which are always made of p-type crystals, high purity germanium detectors (HPGe) can be produced from n-type or p-type materials. Contacting is performed by two highly doped n-type or p-type layers (n^+, p^+). While p^+ contacts are produced by boron implanting, n^+ contacts are usually produced by lithium surface diffusion. HPGe detectors are not compensated explicitly like lithium drifted crystals. Due to the minimal net concentration in HPGe materials, the types are designated as π-type and ν-type rather than n- and p- type. Both types are schematically illustrated in figure 1.9. The net impurity concentration in the bulk is not

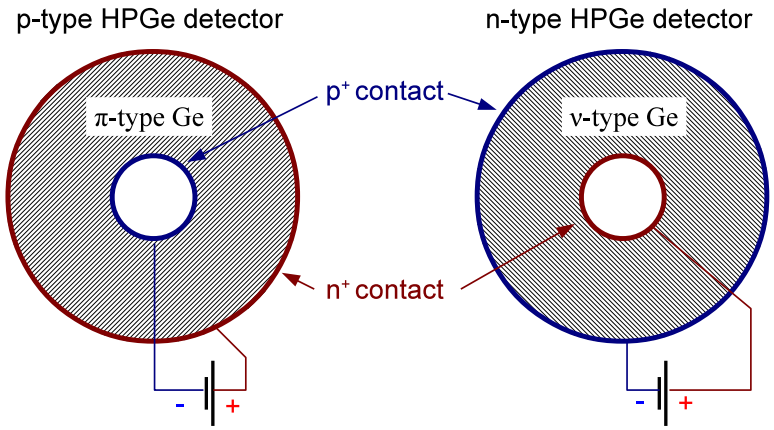

Figure 1.9: Electrode configurations of a HPGe n-type and p-type detector. The extremely low p-type and n-type concentrations in the bulk are designated as π and ν respectively, while the highly doped p-type and n-type contacts are designated as p^+ and n^+.

subject to environmental temperature conditions and hence HPGe detectors can be stored permanently at room temperature without any consequences to their performance in future.

Due to the crystal pulling procedure, germanium detectors are usually available in cylindrical configurations. Those entail planar detectors with the p^+ and n^+ contacts on the top and on the bottom side of the crystal but also coaxial detectors with an outer contact on the lateral surface and an inner bore hole contact along the z-axis. In true coaxial configurations, the inner bore hole is removed completely and the contact is placed over the whole inner cylindrical surface. True coaxial detectors have a fully radial electrical field distribution inside its volume, but the sensitive volume is not optimally used. Furthermore, the detectors are known for undesired leakage current effects over the front surface. In closed-ended coaxial detectors, only a part of the central core is removed and the outer electrode

is extended over the planar surface of the crystal. Closed-ended coaxial configurations are used in most cases, because they have a higher sensitive volume and lower leakage currents. In general, coaxial detectors are also more popular than planar detectors, due to their lower capacitance resulting in a better noise and resolution performance. It should also be noted that due to the very low band gap of 0.7 eV in germanium, electron-hole pairs are created already at room temperature in the region of depletion. In consequence, thermally induced leakage currents arise, followed by high noise and a bad resolution performance. Therefore, all germanium crystals are operated at cryogenic temperatures, cooled down usually with liquid nitrogen or argon to 77 K or 87 K respectively.

In order to understand the good performance of germanium detectors, it is crucial to understand the absorption mechanisms in Ge and the conditions required to induce ionization. In general, γ-ray interactions in a material can be characterized by three interaction processes:

• **The Photoelectric Effect:** This involves the absorption of an incoming γ-ray through excitation of a bound electron. Depending on the initial γ-ray energy $E_\gamma = h\nu$, the electron escapes the atom or excites into a higher energy level, followed by de-excitation and X-ray emission. The effect is dominant for gamma ray interactions below 100 keV. The cross section for the photoelectric absorption can be approximately expressed by

$$\sigma \propto \frac{Z^n}{E_\gamma^{3.5}}, \tag{1.24}$$

where Z is given by the atomic number and n is a constant ranging from 4 to 5.

• **Compton scattering:** The process describes elastic collisions between photons and electrons and is equivalent to an elastic, classical two-body collision. The energy transferred depends on the initial energy of the gamma and the scattering angle. The interaction probability scales with the target material density.

• **Pair production:** This process can take place if the gamma energy is at least twice higher than the mass of an electron. In this case, the gamma can induce the production of an electron-positron pair. The positron will annihilate after loosing its kinetic energy, resulting in the emission of two gamma particles with a total energy of $2m_e$. The cross sections for pair production can be expressed by

$$\sigma_{pair} \propto (Z^2 + Z)\ln(\frac{183}{3\sqrt{Z}}), \tag{1.25}$$

with a threshold value of $2m_e$.

The interaction probabilities of gamma rays in matter are highly dependent on the atomic number of the target nuclei as shown in equation (1.24) and in equation (1.25). Therefore,

germanium with a Z number of 32 and a relatively high density of $\rho_{Ge} = 5.32$ g/cm^3 is an ideal material for X- and γ- ray detection.

The intrinsic resolution of germanium detectors can be described in terms of the number of electron-hole pairs N_p, produced due to an incident gamma energy deposition. N_p can be expressed in terms of the energy gap δE_{ion} between the valence band and the conduction band, needed to produce an electron-hole pair. Given the incident gamma energy E_γ, N_p can be written as

$$N_p = \frac{E_\gamma}{\delta E_{ion}}. \tag{1.26}$$

Because N_p describes the number of ionization events, which in total sum up to the full energy measured, the statistical uncertainty on the measured energy σ_E can be expressed by

$$\sigma_E = \sqrt{N_p}. \tag{1.27}$$

Therefore, the relative statistical uncertainty defined by the number of ionisations

$$\sigma_R = \sqrt{N_p}/N_p \; = \; \sqrt{1/N_p} \; = \; \sqrt{\frac{\delta E_{ion}}{E_\gamma}} \tag{1.28}$$

can be directly translated into the intrinsic energy resolution of the detector, described by the ionisation energy of the sensitive material and the incident gamma energy. However, the statistical treatment described above, assumes Poisson statistics, which in many cases is not fully correct. Given the fact that often full energy deposition takes place, the statistical fluctuations are smaller than described above, resulting in a better resolution. The correction factor introduced to take the smaller fluctuations into account is called the Fano factor and is usually determined experimentally. The detector resolution considering the Fano factor is then written as

$$\sigma_R = \sqrt{\frac{F \cdot \delta E_{ion}}{E_\gamma}}. \tag{1.29}$$

With a typical Fano factor value of 0.12 for germanium detectors [54] and an ionisation energy δE_{ion} of 0.7 eV, the detectors reach resolutions below 1% ($\sim$0.2% at 1173 keV e.g.) and are usually limited by electronic or environmental noise.

Given the high gamma absorption in germanium, the excellent intrinsic resolution, and the extremely high radiopurity of the material, HPGe setups are widely used in low-background and rare-signal experiments like dark matter and neutrino experiments. Projects like GERDA or MAJORANA use enriched germanium detectors taking advantage of the high detection performance and the possibility of $0\nu\beta\beta$ decays of the ^{76}Ge isotope. As a consequence of the extreme requirements of the experiments, new detector configurations have been developed, differing from the classical closed-end coaxial geometries. Segmented detectors, for example, allow for a better event discrimination but require a higher cabling

effort. Although HPGe crystals are extremely pure, additional background can be introduced by cabling and first stage amplification modules, which must be considered in any low background experiment. Recently developed point contact detectors (BEGe) offer very good event discrimination characteristics, a better resolution performance and a minimal cabling effort. BEGe detectors will be operated, for example, in the second phase of GERDA. More about this type of detector can be found in chapter 8.

Chapter 2

The GERDA experiment

GERDA (GERmanium Detector Array) is a next-generation double beta decay experiment, which searches for the $0\nu\beta\beta$ decay of ^{76}Ge [55]. The experiment is located in the Gran Sasso Underground Laboratory (LNGS) in Italy. The excavation of the laboratory took place between 1982 and 1987 and is accessible through the Gran Sasso highway tunnel with a length of more than 10 km. With a depth of 1400 m and a water equivalent of 3200 m, the laboratory is one of the best-shielded facilities against cosmic radiation on Earth. For example, the μ flux in the laboratory is $\sim$5 orders of magnitude lower (with $\sim$1 μ/m^2h) than on the surface.

Figure 2.1 shows an overview of the area and a scheme of the underground facility with the three main halls provided for the operation of low background experiments. GERDA has been first proposed in 2004 [55], was assembled in the following years in Hall A and was commissioned in 2010. The experiment operates naked HPGe detectors enriched in ^{76}Ge to 86% which are immersed in cryogenic liquid argon. The detectors and 64 m^3 of 6.0 grade liquid argon are contained in a low background ($\sim$1 mBq/kg of ^{232}Th and ^{238}U) stainless steel cryostat with 4 m in diameter and a height of 6 m. The inner wall of the cryostat is furthermore lined with high purity copper for further background reduction. A second tank with a diameter of 10 m and a height of 9 m is filled with $\sim$600 m^3 purified water and mounted around the cryostat as shown in figure 2.2. Both the liquid argon as well as the water act as passive shielding against environmental radiation. In addition, 66 photomultiplier tubes are mounted in the water tank and comprise an active Cherenkov light muon veto.

A clean room located on top of GERDA allows to deploy or remove the Ge-detector strings, introduce calibration sources into the cryostat, or to perform maintenance work. On top of the cleanroom, 240 plastic scintillator modules are mounted as an additional active muon veto. With the passive and active background suppression, the background is expected to originate mainly from cosmogenic activation of the germanium diodes, impurities in the detector holders and cables, and from (α, n) reactions and spontaneous fission in the cryostat. Further contributions are bremsstrahlung from the ^{39}Ar β decay, ^{222}Rn gas em-

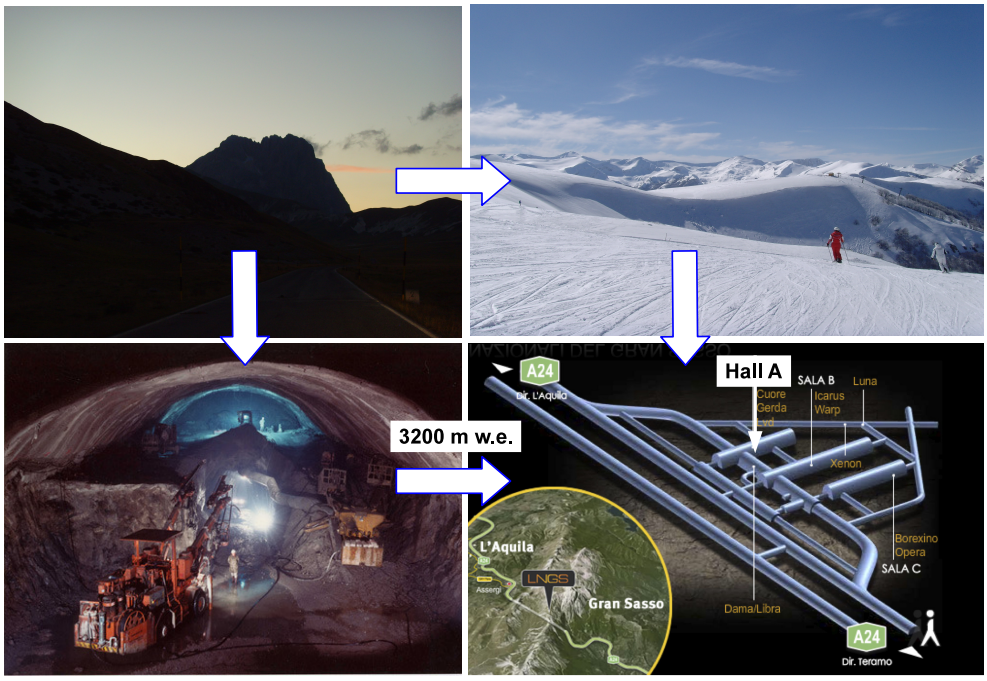

Figure 2.1: Top: the Gran Sasso mountain. Bottom left: excavation of the laboratory in the 1980's. Bottom right: scheme of the LNGS underground laboratory and the location of GERDA in Hall A.

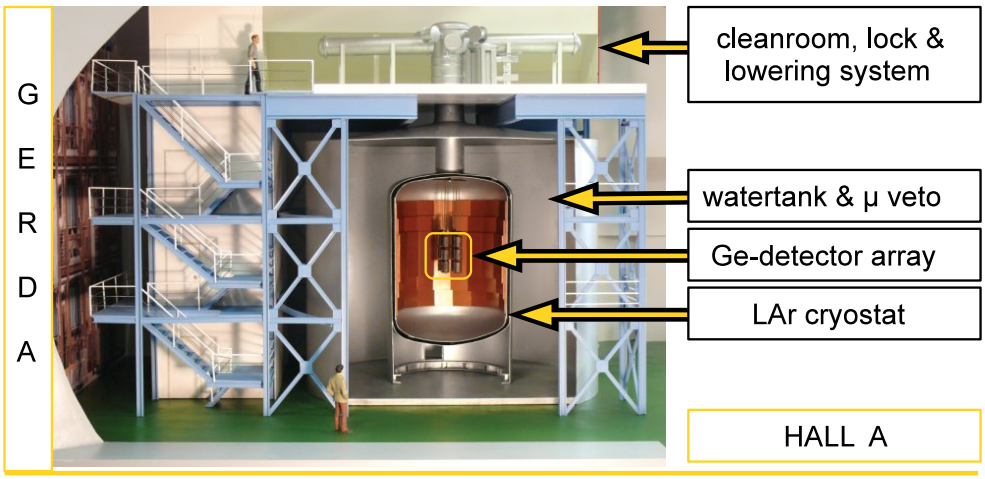

Figure 2.2: Scheme of the GERDA experiment located in Hall A in the LNGS laboratory. The detector array is introduced into the cryostat through a lock system mounted in the cleanroom on top of the water tank.

anation (from ^{238}U) and, not to forget, $2\nu\beta\beta$ decays from ^{76}Ge.

In the first phase of GERDA, 17.7 kg of enriched Ge detectors from the previous Heidelberg-Moscow and IGEX experiments are operated with a ^{76}Ge mass $m_{\beta\beta}^{Ge}$ of 15.2 kg. The detec-

tors are arranged in strings with a maximum of three detectors per string. Additionally, three reference detectors made of natural germanium are deployed to monitor the background in the $Q_{\beta\beta}$ region around 2 MeV. The first goal of the GERDA experiment is to reach a background level of 10^{-2} counts/(keV·kg·y) in the initial phase of operation. Such a background level in the region of interest ($Q_{\beta\beta} \pm 2$ keV) is one order of magnitude lower than the levels reached in previous $0\nu\beta\beta$ experiments. The envisioned background level will allow to verify or to reject the Heidelberg-Moscow claim of the $0\nu\beta\beta$-decay discovery [39] in only one year of operation. With an exposure of 15 kg·y, a half-life sensitivity of 3×10^{25} years for the ^{76}Ge $0\nu\beta\beta$ decay is within reach. Even if no $0\nu\beta\beta$ signal is found, rejection of the claim will allow to improve the current half-life limit.

Commissioning of GERDA took place in 2010 with three diodes made of natural germanium. In June 2011, the first enriched detectors were deployed. Up to now, GERDA is running with eight enriched Ge detectors and a total mass of 17.7 kg. Six natural germanium reference detectors from the Genius test facility [56] are available for testing and further background reduction. The first data taken showed a background rate of ∼0.17 counts/(keV·kg·y) which was ∼17 times higher than the background goal envisioned for the first phase. Although, the high background is still not fully understood, a part of it could be tracked down to the presence of ^{42}Ar with a higher concentration than expected. A prominent line at 1525 keV has been interpreted as resulting from the β decay of ^{42}Ar into ^{42}K with a Q-value of 599 keV and a half-life of 32.9 years. However, in a second step, the positive ^{42}K ions are subject to further β decay with a half-life of 12.4 hours. The decay involves the emission of a 1525 keV gamma line with a branching ratio of 18%.

In general, ion propagation induced by convection effects in the liquid argon or due to the attraction by an electrical field of the detectors would increase the number of charges on the naked crystals and hence increase the noise and background. Based on the ion hypothesis, a cylindrical, metallic mini shroud has been mounted around the detector strings. A power supply has been connected to the shroud in order to change the field configuration in the vicinity of the crystals and to prevent ions from drifting to the surface of the detectors. Furthermore, a second shroud has been mounted around the detector array, in order to reduce convection in the cryostat. Deploying the shrouds allowed to reduce the background to ∼0.07 ± 0.02 counts/(keV·kg·y) . Although the background could be reduced drastically using the shrouds, it is still higher than the envisioned goal of 0.01 counts/(keV·kg·y) . However, it is already lower than the background reached by the Heidelberg-Moscow experiment (0.11 ± 0.01) counts/(keV·kg·y) . Furthermore, discrimination methods based on pulse shape analysis have not been applied yet and hence a further background reduction will be reached in near future.

2.1 GERDA Calibration System

The cryostat of GERDA is only accessible through a CF360 flange ("cluster flange") mounted in the clean room on top of GERDA. The main flange used to deploy the detector strings is coupled to a glove box in order to prevent environmental impurities to be introduced into the cryostat. Calibration of the GERDA detectors involves introduction of the sources into the cryostat and their removal during physics runs. This procedure must be considered under the same impurity introduction aspects as in the case of the detectors. Furthermore, while detectors are usually deployed for operation once, calibrations are performed $\sim$ once a week. Therefore, a calibration system has been designed, which moves the sources into a shielded position on top of the cryostat without the need to physically remove the sources from the cryostat. After mounted, the calibration system is decoupled from the environment and is part of the volume of the cryostat. Details about the needed source strength, the position of the sources on the flange and the absorber configuration below the cluster flange can be found in [57]. Three DN40 flanges mounted on the cluster flange below the glovebox as shown in figure 2.3 were available to design an electro-mechanical, vacuum-tight calibration system allowing to operate the sources with a control unit or alternatively by a computer. The final source insertion system (SIS) has

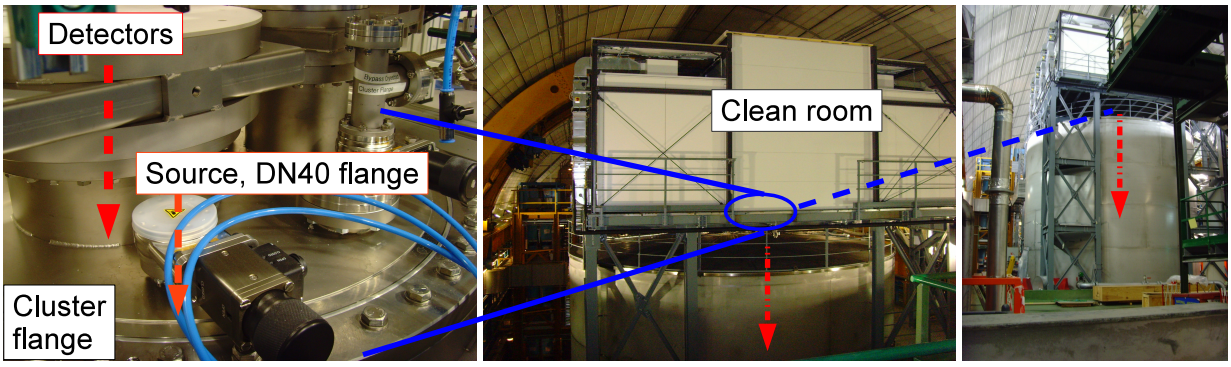

Figure 2.3: Left: part of the cluster flange with the detector deployment flange and one of the three DN40 flanges for the calibration source insertion. Middle: clean room on top of GERDA and the location of the cluster flange. Right: Full view of the GERDA experiment.

been designed and mounted by the group of the University of Zurich (UZH). Besides the mechanical parts, the system includes a microcontroller unit for status monitoring, motor operation, and for the control of two independent positioning systems. Furthermore, a graphical user interface was developed in LabView for the system control via a computer. More details about the mechanical setup, the electronic components, and the developed control software can be found in chapter 7. The γ background from the sources located on top of the cryostat, approximately 5 m above the detector array (parking position) has been determined with Monte Carlo simulations and is supposed to be well below the background goal for phase II of GERDA with $4.3 \pm 0.1(\text{stat}) \pm 0.1(\text{sys}) \times 10^{-5}$ counts/(keV·kg·y) , as described in detail in [57].

While γ rays are effectively shielded by a tantalum absorber mounted below the source and by the liquid argon, neutrons can propagate through matter over several meters without significant energy losses and increase the background in GERDA mainly through inelastic interactions in the Ge detectors. In chapter 3, the neutron flux from (α, n) reactions in the calibration sources has been calculated using hypothetical chemical composition assumptions about the interior of the source. Furthermore, a new concept has been developed to suppress the (α, n) channel, leading to a new technique to produce custom ^{228}Th sources with a reduced neutron flux. The calculated neutron spectra for a commercial and for a custom source were implemented in Monte Carlo simulations and the resulting background described in [57]. In total, three custom ^{228}Th sources with a reduced neutron flux have been produced. Two of them were mounted in the calibration system of GERDA, together with a third commercial source. Details about the neutron production aspects in a commercial (standard) source are described in chapter 3. Chapter 4 describes the concept of neutron suppression and the production of the custom sources.

2.2 GERDA Phase II

The background index envisioned for phase II of GERDA is $< 10^{-3}$ counts/(keV·kg·y) in the region of interest. This is approximately two orders of magnitude lower than background indexes reached in previous $\beta\beta$ experiments. To reach this goal, event discrimination methods like pulse shape analysis, anti-coincidence cuts between detectors and μ-veto cuts will be improved and optimized. Furthermore, liquid argon instrumentation with photomultipliers will be performed (see for example [58]) and the involvement of new materials and electronic components considered.
The sensitivity improvement of GERDA phase II will not only be a consequence of background reduction, but also of a higher detector mass. 20 kg of new enriched Ge detectors will be newly manufactured and added to the detector array in order to expand the sensitive and $\beta\beta$ -active mass. The detectors will be produced and transported with special regard to cosmogenic activation while on surface. This entails aspects of the time interval in which the diodes will be exposed to unshielded cosmic radiation during production, but also during transportation. Furthermore, the configuration of the diodes and their contacts will be changed. While phase I detectors are closed-ended HPGe coaxial detectors, the new detectors will be point contact detectors, called also Broad Energy Germanium detectors (BEGe). BEGe detectors are a combination of the planar and coaxial detector configurations. The crystal has no bore hole in the center and the inner contact is replaced by a point contact on the bottom planar surface. In contrast to planar detectors, the outer contact is not located on the upper planar surface, but covers the whole crystal and is only separated from the inner contact by a circular ditch. Besides the better noise, background and efficiency performance of BEGe detectors, pulse shape analysis methods allow for an efficient multi site event discrimination. More about the BEGe configuration will be presented in Chapter 8. An extensive description and characterization of the BEGe detectors

can be found for example in [59].
With a total mass of ∼40 kg and a planned exposure of 100 kg·years in phase II, the experiment will reach a $0\nu\beta\beta$ half-life sensitivity of $T_{1/2} > 2 \cdot 10^{26}$ years within 2-3 years.

It should be noted that plans for a third phase of GERDA exist with the goal to run an ultimate experiment with a mass of one ton. Because germanium crystals cannot be grown bigger than a few centimeters in diameter, the one ton experiment will involve a vast array of Ge detectors and will be challenging in terms of background, data analysis and design costs. Therefore, the project will be most probably realized in the frame of a world-wide collaboration of several $0\nu\beta\beta$ experiments.

Chapter 3

Neutron background in low background experiments

Experiments searching for rare events, such as the neutrinoless double beta decay, dark matter or neutrino interactions must perform an effective background suppression in order to reach sufficient detection efficiencies. The background can be classified into two contributions, consisting of a cosmic ray component and a natural radioactivity component, which are described below in more detail.

Cosmic rays: Primary cosmic rays consist mostly of high energy (up to 10^{20} eV) heavy particles like protons, α particles or hydrogen nuclei. Their interaction with atoms in the upper atmosphere induces a chain of reactions that result in a high energy particle shower. The shower consists of a soft γ component, a hadronic component (protons and neutrons mainly) and a charged, muonic component. Effective reduction of the background caused by cosmic rays can be achieved by locating the experiment in an underground facility. In underground laboratories, cosmic rays can be reduced up to 5 to 7 orders of magnitude with respect to the surface. However, muons still can be a notable source of background even at large depths. In fact, neutron production via muon spallation in the rock for example is an important background contribution in low energy experiments.

Natural radioactivity: Natural ^{238}U and ^{232}Th concentrations in the rock or in the components of the detector emit mainly γ radiation, but also α and β particles. The γ background can be efficiently suppressed by external high-Z shields like lead, and by using high purity materials in the detector setup. Due to their charge, α and β particles have very short interaction lengths in matter ranging from μm to a few millimeters. Therefore, the emission of these particles can mostly be neglected.

However, although usually α particles do not have to be considered under penetration aspects in low-background experiments, their emission can induce neutrons through (α, n) reactions with other light materials. A further source of neutrons correlated to the presence of radioactive traces in a material is the spontaneous fission of U and Th which in fact can

be found in almost any material with a non-zero concentration.

Given the electrical neutrality of neutrons, the particles can penetrate an experimental setup and induce a background by elastic and inelastic interactions in the sensitive volume. Elastic neutron interactions can for example mimic low energy dark matter signals, while inelastic scattering or neutron capture can emit high energy γ radiation imitating $0\nu\beta\beta$ signals. In addition, detector material activation can take place by neutron capture resulting in a higher intrinsic background. In the case of germanium detectors for example, unstable isotopes like ^{77}Ge/^{77m}Ge can be generated with half-lifes of 11.3 hours and 52.9 seconds respectively.

Although the water tank and the liquid argon of GERDA effectively suppresses external neutrons as well as α, β and γ radiation from natural radioactivity, a part of the neutrons still can propagate through the setup to the detectors and deposit energy through elastic and inelastic interactions in the detector array. In particular, inelastic neutron interactions can result in γ emission close to the $Q_{\beta\beta}$ energy of the neutrinoless $\beta\beta$ decay of ^{76}Ge.
While the external neutron flux contribution in Hall A of the LNGS laboratory has been measured [60] to be

$$\Phi_{tot} \sim 4 \cdot 10^{-6} \text{ neutrons/cm}^2 \cdot \text{ s}, \tag{3.1}$$

the internal neutron flux contribution from (α, n) reactions and spontaneous fission in the GERDA cryostat was calculated and simulated in [61]. The estimation yielded a neutron flux of

$$\Phi_{cryo}^{intern} \sim 1.3 \cdot 10^{-3} \text{ neutrons/s}. \tag{3.2}$$

This calculations did not take into account the contribution from the three ^{228}Th calibration sources which are permanently mounted on top of the cryostat about 5 m above the detector array during physics runs. The γ background from the sources and its suppression has been extensively described in [57]. Calculations of the neutron flux induced by a standard (commercial) source will be presented in the next section.

3.1 Neutron production in a commercial ^{228}Th γ source

As described in section 2.1, three ^{228}Th sources are mounted on top of the neck of the GERDA cryostat. Monte Carlo simulations have shown that the γ background originating from the sources can be sufficiently suppressed by the liquid argon and a tantalum absorber mounted below the source as described in [57]. With

$$B_{\gamma}^{source} = 4.3 \pm 0.1(stat) \pm 0.1(sys) \times 10^{-5} \text{ counts/(keV·kg·y)} \ , \tag{3.3}$$

the γ background induced by the calibration sources is well below the maximal background index B envisioned for phase II of GERDA (with $B < 10^{-3}$ counts/(keV·kg·y)).

However, neutrons from (α, n) reactions taking place in the encapsulation of a calibration source can propagate to the detector array and contribute to the background level in the region of interest around $Q_{\beta\beta}$. The (α, n) neutron production rate inside the source depends on the internal source structure and the target materials which are used within the encapsulation. In consequence, the neutron rate of a commercial ^{228}Th source depends on the manufacturer, the production chain and the chemical treatment. In the following, the neutron flux from a commercial ^{228}Th source will be estimated. Besides (α, n) reactions, the significance of spontaneous fission processes of ^{228}Th will be estimated.

3.1.1 Spontaneous fission

In general, neutron emission takes only place indirectly through highly excited nuclear states as they occur in (α, n) reactions or through spontaneous fission (SF) of heavy nuclei. The process of spontaneous fission can be described by the liquid drop model proposed by Carl Friedrich von Weizsäcker in 1935 and later refined by Bohr and Wheeler. It assumes a nucleus to be unstable if the Coulomb energy difference ΔE^C resulting from a nucleus deformation is higher than its change in surface tension ΔE^S. It can be shown that this condition is fulfilled for nuclei with

$$E_0^C \geq 2 \cdot E_0^S \text{ or } X_s = 1/2 \cdot E_0^C / E_0^S = \frac{a_c \cdot \frac{Z^2}{A^{1/3}}}{2 \cdot a_s \cdot A^{2/3}} \geq 1, \tag{3.4}$$

where E_0^C and E_0^S are the nucleus Coulomb and surface energies, respectively, without deformation. X_s is the fissionability parameter of the nucleus, Z is the atomic number, A is the atomic mass and $a_c = 0.714$ MeV/c^2 and $a_s = 18.33$ MeV/c^2 are empirical values for the correct description of the Coulomb and surface energy contributions. Using the above values for a_c and a_s, a nucleus can only undergo a spontaneous fission if

$$\frac{Z^2}{A} > 51. \tag{3.5}$$

For ^{228}Th with an atomic number of 90, $Z^2/A = 35.5$ and in principle the isotope can be regarded as stable against spontaneous fission.
However, similar to the α decay, spontaneous fission takes place via the quantum-mechanical tunnel effect and a remaining fission probability P, given by

$$P = e^{\frac{4\pi}{h} \cdot d\sqrt{2mE_f}} \tag{3.6}$$

can lead to a significant background contribution in low background experiments. In equation (3.6), d is the Coulomb barrier width, m is the reduced mass of the fission products and E_f is the fission activation energy. As a result of the tunneling effect, spontaneous fission still is possible at $Z^2/A > 20$ as shown in [62]. For ^{228}Th, no spontaneous fission has been observed so far [63]. Using the formalism described in [64] the spontaneous fission

half-lifes $T_{1/2}$ can be estimated by a phenomenological expression:

$$\begin{aligned}\log_{10}(T_{1/2}) &= 21.08 + \frac{1}{A}\cdot[C_1(Z-90-\nu) + C_2(Z-90-\nu)^2 \\ &\quad + C_3(Z-90-\nu)^3 + C_4(Z-90-\nu)(N-Z-52)^2, \end{aligned} \tag{3.7}$$

with $C_1 = -548.825021$, $C_2 = -5.359139$, $C_3 = 0.767379$, $C_4 = 4.282220$, $\nu = 0$ for even-even nuclei, and $\nu = 2$ for odd-odd nuclei. Equation (3.7) has been used to calculate the SF half-lifes of ^{228}Th. A comparison of the calculated values and literature values for SF half-lifes of four heavy nuclides is given in table 3.1. Based on the calculated SF half-life

Isotope	Z	N	$\log_{10}T_{1/2}^{Exp}$	$T_{1/2}^{Exp}$[a]	$\log_{10}T_{1/2}^{Cal}$	$T_{1/2}^{Cal}$[a]
^{228}Th	90	138	n.a.	n.a.	21.08	$1.2\cdot10^{21}$
^{238}U	92	146	15.91	$8.1\cdot10^{15}$	16.26	$1.8\cdot10^{16}$
^{240}Cm	96	144	6.28	$1.9\cdot10^{6}$	5.53	$3.4\cdot10^{5}$
^{252}Cf	98	154	1.93	85.1	1.68	47.9

Table 3.1: Comparison of experimental and calculated values for spontaneous fission half-lifes. The half-life of ^{228}Th is five orders of magnitude higher than from ^{238}U. Experimental data are taken from [65]. Measured data for ^{228}Th are not available.

of ^{228}Th, a fission rate has been estimated, assuming a ^{228}Th source activity A_0 of 1 kBq. The number of ^{228}Th nuclides N_0 has been calculated by

$$N_0 = \frac{A_0 \cdot T_{1/2}}{\ln 2} = 8.7\cdot10^{10}, \tag{3.8}$$

where $T_{1/2}$ is the ^{228}Th half-life given by 1.9 years. With a SF half-life of

$$T_{1/2}^{Cal}(SF) = 1.2\cdot10^{21}\ \text{years}, \tag{3.9}$$

for ^{228}Th which has been calculated according to equation (3.7), the spontaneous fission rate A_{SF} for a 1 kBq source can be determined by

$$A_{SF} = \frac{\ln 2 \cdot N_0}{T_{1/2}(SF)} = 5\cdot10^{-11}\frac{\text{decays}}{\text{year}\times\text{kBq}}. \tag{3.10}$$

The calculated rate in equation (3.10) is 7 orders of magnitude lower than the envisioned background goal B_3 for phase III of GERDA, with $B_3 < 1\cdot10^{-4}$ counts/(keV·kg·y) . Therefore it can be regarded as absolutely irrelevant for the GERDA experiment and will not be subject of further discussion.

3.1.2 (α, n) reactions

α particles emitted by a ^{228}Th γ source are not directly contributing to the background index of GERDA as they will be absorbed latest in the stainless steel encapsulation of the source. The α absorption process is dominated by Coulomb forces between electrons and the α particles resulting in excitation and ionization of the target material. X-ray or γ emission takes place which is uncritical due to its energy and the distance of the source to the detectors. However, besides the spontaneous fission described in section 3.1.1, nuclear fission processes triggered by high energetic α particles can be a further source of neutron emission. A prominent example which uses this mechanism for neutron production is the ^{241}AmBe source. If the process involves the emission of only one neutron after a nucleus has been hit by an α particle, the reaction is designated as (α, n). Because the emission of more than one neutron is also possible, the reactions are sometimes designated as (α, xn) reactions, giving a general description for a process with x neutrons emitted. (α, xn) reactions of the type

$$\alpha + X \rightarrow (\alpha X)^* \rightarrow Y_1 + Y_2 + x \cdot n \tag{3.11}$$

can be described in two steps. First a fusion of the incident α and the target nucleus X into an excited compound nucleus $(\alpha X)^*$ takes place. The binding energy of the compound is now distributed on further degrees of freedom allowing the compound nucleus to undergo a fission process into two nuclei Y_1 and Y_2 in the second step. The fission process involves the emission of x neutrons. (α, xn) reactions can only take place if the incident kinetic α energy is high enough to overcome the Coulomb barrier expressed by

$$U_c = \frac{Z_1 \cdot Z_2 \cdot e^2}{r_0 \cdot (A_1^{1/3} + A_2^{1/3})}, \tag{3.12}$$

where Z_1 and Z_2 are the atomic numbers of the α particle and the target nucleus, respectively, A_1 and A_2 are their atomic masses and r_0 is a constant given by $r_0 \simeq 1.2$ fm. The Niels Bohr compound model describes the process by kinematic considerations of the input and output channels. It can be shown [66] that the minimal incident kinetic energy for the reaction as described in (3.11) is given by

$$E_{kin}^{Thr} = Q \cdot (1 + \frac{m_\alpha}{m_X}), \tag{3.13}$$

where Q is the Q-value of the reaction and m_α, m_X are the masses of the α particle and the target nucleus. The energetically more favourable variant of equation (3.11) is the simple (α, n) reaction with only one neutron emitted

$$\alpha +^A X_Z \rightarrow {}^{A+4}(\alpha X)^*_{Z+2} \rightarrow {}^{A+3}Y_{Z+2} + n. \tag{3.14}$$

Because single neutron processes are dominating, the further estimation of neutron fluxes will focus merely on (α, n) reactions induced by α particles emitted by a ^{228}Th source. As shown in table 3.2, the ^{228}Th chain emits α particles with energies of up to 8.8 MeV. The energies are sufficiently high to overcome (α, n) threshold energies of the most low Z

	Half-life	α energy [MeV]	Atom density
^{228}Th $\downarrow$	1.91 a	5.42 (71.1 %) 5.34 (28.2 %) 5.22 (0.44 %)	ρ_{0Th}
^{224}Ra $\downarrow$	3.66 d	5.69 (94.9 %) 5.45 (5.1 %)	$\rho_{0Th}/1.9e^2$
^{220}Rn $\downarrow$	55.6 s	6.29 (99.9 %) 5.75 (0.11 %)	$\rho_{0Th}/1.1e^6$
^{216}Po $\downarrow$	0.15 s	6.78 (100 %)	$\rho_{0Th}/4.2e^8$
^{212}Bi $\downarrow$	60.6 min	6.09 (27.1 %) 6.05 (69.9 %)	$\rho_{0Th}/1.7e^4$
^{212}Po $\downarrow$	0.29 μs	8.79 (100 %)	$\rho_{0Th}/2.0e^{14}$
^{208}Pb	stable	-	-

Table 3.2: α energies of the ^{228}Th chain and calculated atom densities of the ^{228}Th daughters. The densities are expressed via an initial density ρ_{0Th} of ^{228}Th, assuming the chain to be in equilibrium. Energy and half-life data are taken from [67].

isotopes. Figure 3.1 shows (α, n) threshold energies for different atomic and mass numbers. There are only 17 isotopes with $Z < 50$ with (α, n) threshold energies higher than 8.8 MeV [68]. In order to calculate the probability P for an (α, n) reaction taking place in a target material, the α energy loss dE/dx, given by the Bethe Bloch formula (3.15) for heavy charged particles, must be taken into account,

$$-\frac{dE}{dx} = \frac{4\pi e^4 z^2}{m_0 v^2} \cdot NB, \tag{3.15}$$

where v is the velocity of the projectile, $z \cdot e$ is its charge number and m_0 is the rest-mass of an electron. N and Z relate to the target material and are given by the density and the atomic number respectively. B is an expression considering the impact parameter. It can be expressed in a relativistic correct manner as

$$B = Z[\ln\frac{2m_0v^2}{I} - \ln(1 - \frac{v^2}{c^2}) - \frac{v^2}{c^2}], \tag{3.16}$$

where I is an experimentally determined average excitation and ionization potential. With the (α, n) cross section $\sigma_{(\alpha,n)}$, the reaction probability for an α particle propagating through a material of thickness L with an initial energy E_α can be written as

$$P = \int_0^L N\sigma_{(\alpha,n)}(E(x))dx = \int_0^{E_\alpha} \frac{N\sigma_{(\alpha,n)}(E)}{(-dE/dx)}dE. \tag{3.17}$$

Based on equation (3.17) and on calculated cross section libraries, the software package SOURCES4A [69] can be used to determine the neutron fluxes from spontaneous fission,

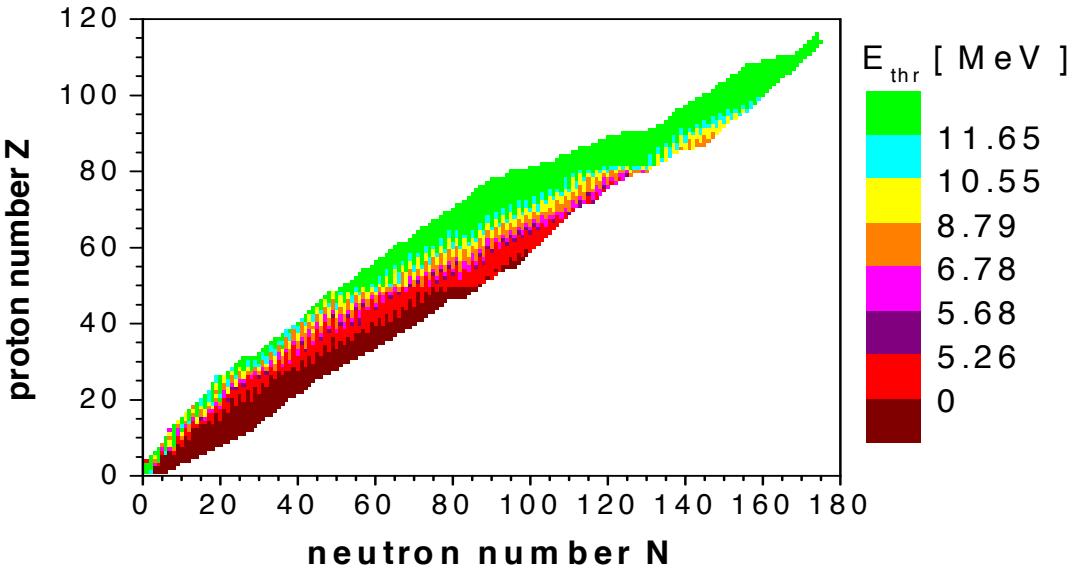

Figure 3.1: Color map of the threshold energies for (α, n) reactions in all target nuclei. Data taken from the AME2003 atomic mass evaluation [68].

(α, n) reactions and delayed neutrons for the most relevant target materials and α emitting radio isotopes. Because delayed neutrons and spontaneous fission of ^{228}Th are irrelevant as shown in section 3.1.1, the SOURCES4A package has been used to estimate neutrons merely from (α, n) reactions.

3.1.3 Internal setup of a ^{228}Th GERDA calibration source

In order to estimate the neutron background induced by a commercial ^{228}Th source, the internal arrangment of the encapsulation must be understood. Neutron fluxes cannot be calculated without considering the chemical components which are potential target materials for the α particles of ^{228}Th and its daughters.

The variety of available source encapsulations on the market covers plastic, ceramic, epoxy, platinum or stainless steel encapsulations in different designs and material combinations. The priority demands for the GERDA source are mechanical stability which allows for a safe operation in a cryogenic liquid and the possibility of an easy but safe mounting in the calibration system. In particular, leaking of the encapsulation in the cryogenic liquid must be avoided under any circumstances. This requirements are fulfilled, e.g., by the commercially available P02 or VZ3474 encapsulation types, offered by Eckert&Ziegler Nuclitec GmbH.

The encapsulation type shown in figure 3.2 consists of a stainless steel encapsulation with a thread allowing for an easy integration in the GERDA calibration assembly. The ac-

tive part consists of a porous ceramic, saturated with a chloride solution containing the radio isotopes of interest. An elastic stainless steel spacer foam is used to fix the active ceramic in the encapsulation after sealing, which is performed by welding a stainless steel window on top of the encapsulation. The source fulfills the ISO Norm C 66646 classi-

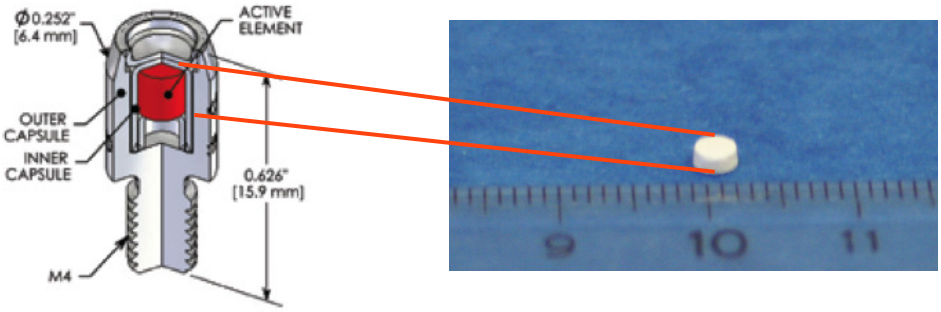

Figure 3.2: Left: Scheme of the P02 stainless steel encapsulation as provided by Eckert&Ziegler [70]. Right: porous ceramic used to be saturated with radionuclides before the encapsulation.

fication as certificated by Eckert&Ziegler. According to the ISO classification system, a C 66646 encapsulation sustains the most radical tests available. The minimal C 66646 source performance and the tests applied are shown in table 3.3. The ISO C 66646 tests

Test	minimal encapsulation performance
Temperature	-40°C - 800°C and thermal shock 800°C - 20°C
External Pressure	25 kPa absolute to 170 MPa absolute
Impact	20 kg from 1 m
Vibration	3x30 min 25-80 Hz at 1.5 mm amplitude peak to peak and 80-2000 Hz at 20 g peak amplitude
Puncture	1 kg from 1 m

Table 3.3: Minimal mechanical strength performance given by a C66646 certificated encapsulation. Most relevant for GERDA is the temperature test which is only performed down to -40°C.

do not include temperature tests below -40 °C. In order to ensure a safe operation in liquid argon at 87 K, additional leak and wipe tests of the sources have been performed in liquid nitrogen at 77 K after delivering.

Due to the low-Z components in ceramics like alumina, silicon, or beryllium and given the fact that the porous ceramics shown in figure 3.2, are saturated with radionuclides

during the source production, the ceramic is considered as the absolutely dominating material in the neutron production in any α -emitting source. Therefore, the following neutron calculations will focus mainly on the ceramic as target material for (α, n) reactions.

3.2 Neutron flux calculations for a commercial ^{228}Th source

While spontaneous fission of ^{228}Th and its daughters can be neglected as discussed in section 3.1.1, (α, n) reactions taking place in the inner volume of the calibration source are expected to play the dominant role in neutron production. The estimation of the neutron flux from a standard ^{228}Th source has been performed with the SOURCES4A code which will be introduced in more detail below.

SOURCES4A is a FORTRAN77 code from the Los Alamos National Lab which calculates rates and spectra of delayed neutrons, spontaneous fission and from (α, n) reactions with low-Z target materials. The code allows to investigate four different problem configurations: homogenous-, interface-, beam- and three region- problems. Spontaneous fission of ^{228}Th can be neglected in terms of neutron production with $\sim 10^{-11}$ decays/year/kBq. In consequence, second order processes like the emission of delayed neutrons which can occur after spontaneous fission processes are negligible, too. The only neutron producing process to be considered in the context of ^{228}Th are (α, n) reactions. SOURCES4A calculates (α, n) rates using the formalism described in section 3.1.2. The software package includes libraries of stopping powers dE/dx, (α, n) cross sections, α particle spectra of nuclide decays, and product nuclide level branching fractions. The latter in combination with mass, momentum and energy conservation are used for calculations of the spectral neutron distribution. Energy losses in composites can be calculated via the Bragg Klemann relation [71]

$$(\frac{dE}{dx})_c \cong \sum_{j=1}^{J} (\frac{dE}{dx})_j, \tag{3.18}$$

where $(\frac{dE}{dx})_c$ is the stopping power of the composite material and $(\frac{dE}{dx})_j$ is the stopping power of component j. Despite the fact that most of the cross sections and branching fractions have been evaluated, the agreement between SOURCES4A calculations and experimental data lies typically within 20 % [69].

As shown in figure 3.2, a typical commercial source consists of a cylindrical ceramic pellet which is saturated with the radionuclides of interest and which is enclosed in a stainless steel encapsulation. In this configuration, possible (α, n) reaction targets are the elements contained in the ceramic itself, but also in the stainless steel walls of the encapsulation. Due to the short range of α particles in matter ($< 50\mu$m in alumina e.g.), only those emitted on the surface of the ceramic pellet will be able to escape and to react with the

stainless steel targets. Neutrons induced by such α particles can be regarded as a second order contribution to the neutron production. For the neutron flux calculations within the ceramic a homogenous configuration was chosen in SOURCES4A, assuming the radionuclides to be homogeneously distributed within the ceramic material. The necessary input for the code contains:

- the configuration type
- the chemical composition of the target material
- the isotopic abundances of the target nuclides
- the α emitting radionuclides and their concentrations.

The radionuclide concentrations ρ_j for a decay chain in equilibrium A $\rightarrow$ B $\rightarrow$ C$\rightarrow$ ... can be calculated iteratively via

$$\rho_B = \rho_{A_0} \cdot \frac{T^B_{1/2}}{T^A_{1/2}} \Rightarrow \rho_j = \rho_{j-1} \cdot \frac{T^j_{1/2}}{T^{j-1}_{1/2}}, \tag{3.19}$$

where $T^j_{1/2}$ is the half-life of the chain member j and ρ_{A_0} is the initial concentration of the first chain member. In all SOURCES4A calculations presented, an initial concentration of

$$N_0(^{228}Th) = 8.704 \cdot 10^{10} \text{ nuclides/cm}^3 \tag{3.20}$$

has been chosen for the ^{228}Th isotope, which corresponds to an initial source activity of 1 kBq. Assuming the decay chain to be in equilibrium, the daughter concentrations has been calculated according to equation (3.19).

3.2.1 Neutron flux from (α, n) reactions in a ceramic

Depending on the manufacturer, the chemical composition of the ceramics used can be very different. Furthermore, the exact compositions are usually covered by industrial secret and are not provided by the producer. Therefore in a first approach, a $NaAlSiO_2$ ceramic considered as a representative material has been chosen in order to estimate the neutron flux from a commercial ^{228}Th source. In a second step, the neutron rates in an Al_2O_3 ceramic have been calculated for comparison. Furthermore, an estimation of the neutron rates produced by α particles which escaped the ceramic pellet and which undergo (α, n) reaction in the stainless steel walls of the encapsulation will be presented.

$NaAlSiO_2$ ceramic

To calculate the neutron rates in any material composition, the atomic fractions of each element must be taken into account under consideration of the isotopic abundances. Natural isotopic abundances can be found for example in [72]. Table 3.4 shows the isotopic abundances in $NaAlSiO_2$ as used in the SOURCES4A calculations. Furthermore, the (α, n) threshold energies calculated according to equation (3.13) are shown. With threshold energies higher than the maximal α energies emitted by the ^{228}Th chain, the ^{28}Si ($E_{Thr} = 9.25$

Isotope	^{23}Na	^{27}Al	^{28}Si	^{29}Si	^{30}Si	^{16}O	^{17}O	^{18}O
Atomic nat. abundance [%]	100	100	92	4.683	3.087	99.757	0.038	0.205
E_{Thr} (α, n) [MeV]	3.48	3.03	9.25	1.74	3.96	15.17	<0.1	0.85

Table 3.4: Natural isotopic abundances of Na, Al, Si and oxygen and their threshold energies for (α, n) reactions.

keV) and ^{16}O (E_{Thr} = 15.17 keV) isotopes can be excluded as (α, n) reaction partners. The (α, n) cross section libraries used by SOURCES4A include data of measurements as well as evaluated data from the EMPIRE or GNASH codes. Figure 3.3 shows the cross sections used for the ceramics isotopes as they appear in the SOURCES4A libraries. The vertical dashed lines indicate the calculated threshold energies taken from NNDC [73], which are explicitly shown in table 3.4. With an atomic number of 8, oxygen is the lightest

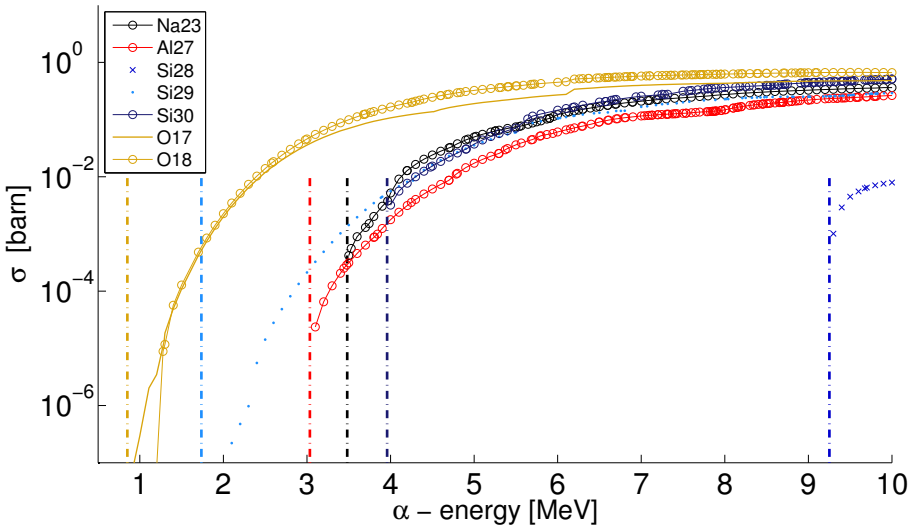

Figure 3.3: Cross sections for Na, Al, Si and oxygen as implemented in the SOURCES4A code. The vertical, dashed lines indicate calculated (α, n) threshold energies for each isotope.

element and has therefore the highest (α, n) cross section as shown in figure 3.3. The oxygen is chemically bound in $NaAlSiO_2$ with an atomic fraction of 40% and hence, oxygen is expected to dominate the neutron production. However, as a consequence of the double magic nature of ^{16}O, (with $Z = N = 8$), the isotope has a high binding energy which translates in a very high (α, n) threshold energy. With 15.17 MeV, the (α, n) threshold energy of ^{16}O is the highest one among the isotopes under consideration. Therefore, (α, n) reactions can not be triggered in ^{16}O by α particles emitted by the ^{228}Th source. Since additionally, the natural abundance of ^{16}O is 99.76 %, (α, n) reactions in natural oxygen are highly unlikely.

In order to determine the isotope with the highest probability for (α, n) reactions, the total isotopic fractions in the $NaAlSiO_2$ composite must be considered. The cross sections for (α, n) reactions after weighting them with the isotopic, natural abundances f_{iso} and the atomic fractions f_{el} of each element are shown in figure 3.4. The weighting factor for each isotope w_i has been defined as

$$w_i = f^i_{iso} \times f^j_{cmp} \tag{3.21}$$

for the i'th isotope of element j. Although quantitative results are given by the SOURCES4A

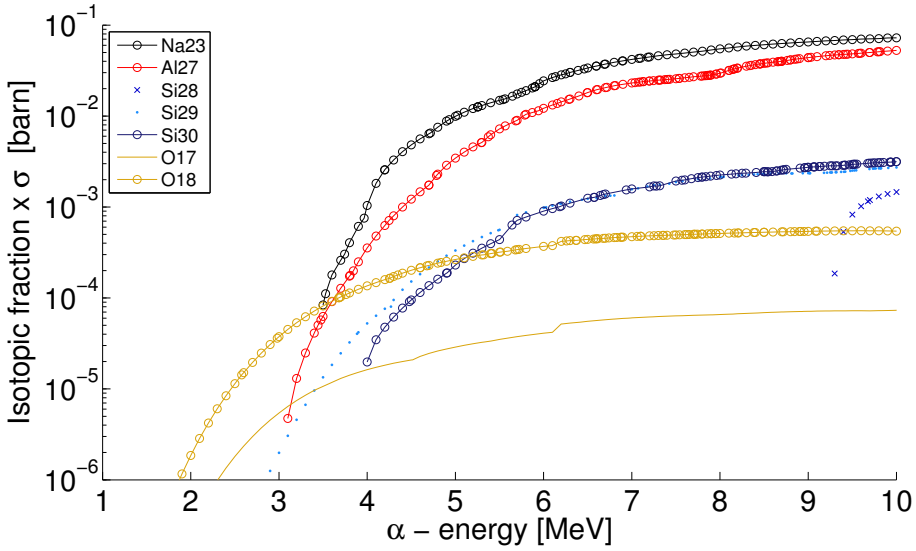

Figure 3.4: Weighted cross sections for (α, n) reactions in the Na, Al, Si and oxygen isotopes.

calculations, figure 3.4 allows to qualitatively estimate the relevance of each isotope for the neutron production, especially in terms of α energy dependency. Although the two oxygen isotopes ^{17}O and ^{18}O have the lowest reaction probabilities above ~5 MeV, their low threshold energy will make the isotopes dominant in neutron production at α energies below ~3 MeV. However, as shown in table 3.2, energies of α particles emitted in the ^{228}Th chain range from ~5 MeV to ~9 MeV and therefore sodium and alumina will be the elements with the highest contribution in neutron production in the ^{228}Th source. This conclusion is confirmed by the calculated neutron distributions for each element shown in figure 3.5. The isotopic neutron rate contributions from silicon and oxygen were summed up in the figure, while ^{23}Na and ^{27}Al are the only stable isotopes for this elements. As expected, highest neutron rates are given by Na and Al, followed by Si and oxygen.
With a mean neutron energy of 1.67 MeV, the total neutron rate calculated for a 1 kBq ^{228}Th source embedded in a $NaAlSiO_2$ ceramic results in about $2 \cdot 10^{-2}$ n/s/kBq. The spectral contributions of each chemical element to the total neutron rate are summarized in table 3.5. In order to estimate the background induced by the calculated neutron spectrum, emitted by three calibration sources in the parking position of GERDA, Monte Carlo simulations were performed and described in [57].

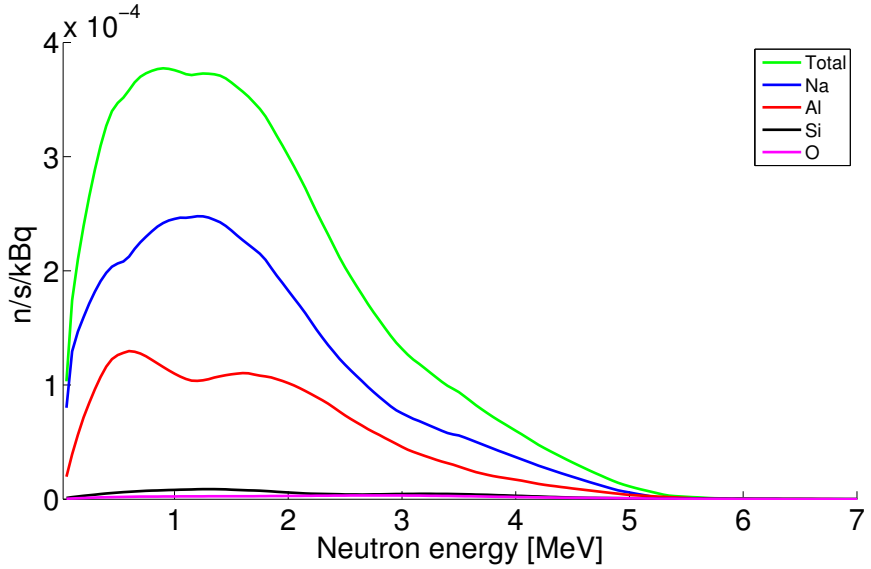

Figure 3.5: Total neutron spectrum given by SOURCES4A calculations for a $NaAlSiO_2$ ceramic. Also shown are the contributions from each constituent.

Target	Na	Al	Si	O	**$NaAlSiO_2$**
Target fraction	1/5	1/5	1/5	2/5	1
n-rate [n/s/kBq]	$1.24 \cdot 10^{-2}$	$6.43 \cdot 10^{-3}$	$4.86 \cdot 10^{-4}$	$2.40 \cdot 10^{-4}$	$1.99 \cdot 10^{-2}$
E_{mean} [MeV]	1.66	1.70	2.14	2.61	1.67

Table 3.5: Neutron rates and mean energies from the elemental constituents of the $NaAlSiO_2$ ceramic. The rates are calculated for a source strength of 1 kBq.

The total neutron spectrum shown in figure 3.5 has been implemented in the simulations which included the full Ge detector array with the sources located about 5 m above. The resulting neutron-induced background index B_n in the region of interest around $Q_{\beta\beta} \pm 0.5$ MeV has been found to be

$$B_n = (2.97 \pm 0.2) \cdot 10^{-5} \text{ counts/(keV·kg·y·kBq)} \tag{3.22}$$

after normalizing the source strength to 1 kBq. Assuming a total source strength of 100 kBq, the resulting neutron background would make approximately 30% of the background index envisioned for phase I of GERDA. A ^{228}Th activity of 100 kBq is a realistic assumption considering three sources in use with an activity of (20-40) kBq each. Considering that the background indexes envisioned are mainly composed of cosmogenics and external/internal radiation, the additional neutron background index resulting from the calibration sources would no longer be acceptable under the given conditions in phase II and phase III. This fact gave rise to the development a neutron-flux reduced ^{228}Th source,

Background	100 kBq ^{228}Th	goal: Phase I	goal: Phase II	goal: Phase III
Rate $[\frac{\text{counts}}{\text{kg·y·keV}}]$	$(2.97 \pm 0.2) \cdot 10^{-3}$	$1 \cdot 10^{-2}$	$1 \cdot 10^{-3}$	$< 1 \cdot 10^{-4}$

Table 3.6: Estimated neutron background in GERDA given by three ^{228}Th sources located in the parking position with a total activity of 100 kBq. The background reaches a level of the envisioned total background index of phase II.

which is described in detail in section 4.

Al_2O_3
As shown in table 3.5, 62% of the neutrons emitted in a $NaAlSiO_2$ ceramic result from (α, n) reactions in sodium. Because the exact chemical composition of the ceramics used by the manufacturer is not known, neutron rates from (α, n) reactions in a standard Al_2O_3 ceramic have been calculated additionally for comparison.

In the case of Al_2O_3, the elemental fraction of oxygen increases slightly from a fraction of 2/5 in $NaAlSiO_2$ to 3/5 in Al_2O_3. In addition, the two targets Na and Si are replaced almost fully by Al. Because the cross sections for (α, n) reactions in Na, Al and Si are of the same order of magnitude as shown in figure 3.3, no drastic change in the resulting total neutron rate is expected. Figure 3.6 shows the neutron spectra as it results from

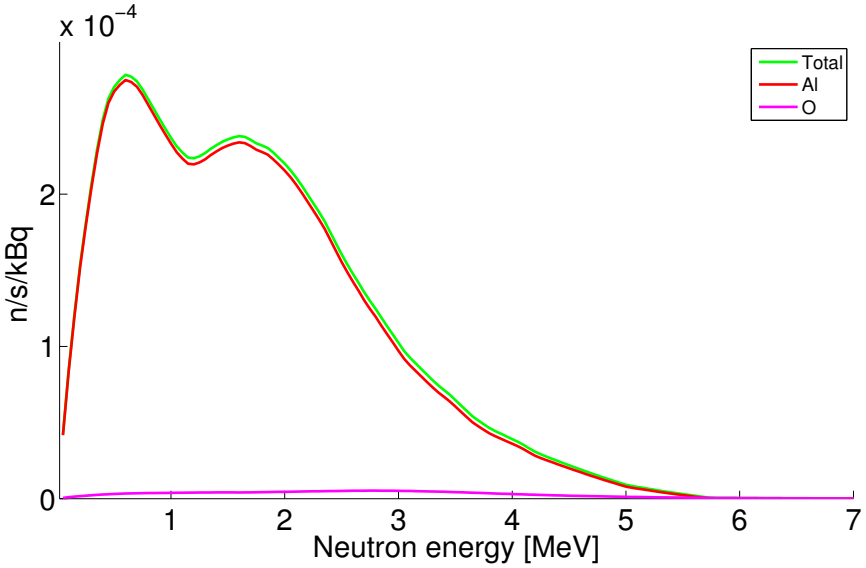

Figure 3.6: Total neutron spectrum resulting from (α, n) reactions in Al_2O_3 for ^{228}Th.

SOURCES4A calculations for Al_2O_3. The total rate is dominated merely by aluminum, as oxygen plays no significant role due to the 99.76% abundance of the ^{16}O isotope. As shown in table 3.7, the contribution of oxygen has slightly increased due to its higher elemental fraction in the Al_2O_3 composite. Given the fact that aluminum and silicon have

Target	Al	O	$\mathbf{Al_2O_3}$
Target fraction	2/5	3/5	1
n-rate [n/s/kBq]	$1.36 \cdot 10^{-2}$	$3.82 \cdot 10^{-4}$	$1.40 \cdot 10^{-2}$
E_{mean} [MeV]	1.68	2.61	1.70

Table 3.7: Resulting neutron rates and the mean neutron energies for Al, O, and the Al_2O_3 composite.

comparable but lower cross sections for (α, n) reactions with respect to sodium, the resulting total neutron rate is expected to be smaller than in $NaAlSiO_2$ but of the same order of magnitude. Furthermore, as shown in table 3.5, the neutron energy of the aluminum contribution is 1.7 MeV, while the mean neutron energy of the $NaAlSiO_2$ ceramic was 1.67 MeV. Therefore, a significant change in the mean neutron energy of the Al_2O_3 spectrum is not expected as it is dominated by aluminum. As summarized in table 3.7, a neutron rate of $1.4{\cdot}10^{-2}$ n/s/kBq with a mean neutron energy of 1.7 MeV has been determined for the Al_2O_3 composite in good agreement with the argumentation presented above.

3.2.2 Neutron flux from (α, n) reactions in stainless steel

In order to quantify the second order process of (α, n) reactions in the stainless steel walls of the encapsulation, SOURCES4A calculations have been performed using the configuration for a homogenous problem. In this configuration, the radionuclides are homogeneously distributed in the stainless steel. This situation does not reflect the real condition, where only surface α particles can escape the ceramic pellet and react with the stainless steel walls of the encapsulation. However, an estimation of the neutron rate can be done by taking into account only the fraction of α particles which can escape the ceramic. For this purpose, the α ranges in the ceramic must be known. Ranges of α particles in different elements or composites can be found for example in the NIST-ASTAR database [74]. If not available in the database, penetration depths in chemical compositions like $NaAlSiO_2$ can be calculated using the semi-empirical Bragg-Klemann formula [75]:

$$R_{comp}(E) = \frac{A_{comp}}{\sum \frac{a_i A_i}{R_i(E)}}, \tag{3.23}$$

where R_i is the α range in element i, a_i is the number of atoms of element i in the composite molecule, A_i is the atomic weight of element i and M_c is the molecular weight of the molecule.

Because α ranges in Na are not available in the ASTAR database, data for Al_2O_3 were taken instead to estimate the number of α particles escaping the ceramic. With a range of $1.56{\cdot}10^{-2}$ g/cm^2 for an 10 MeV α particle and an Al_2O_3 density of 3.94 g/cm^3, a range of

$$R_{cer}(10 \text{ MeV}) = 40\,\mu\text{m} \tag{3.24}$$

has been calculated. With typical ceramic pellet dimensions of 4 mm in diameter and 2 mm in height, the volume V_α allowing α particles to escape is about 25 times smaller than the full pellet volume V_0. Therefore, after performing the neutron rate calculations with 1 kBq of ^{228}Th in stainless steel, the rate will be scaled down by a factor of

$$f_{\delta V} = \frac{V_0}{V_0 - V_\alpha} \approx 25. \tag{3.25}$$

The stainless steel type X6CrNiMoTi17-12-2, used for the calculations of the neutron rates is the same as used for the GERDA cryostat [61] with the chemical composition given in table 3.8. With the natural isotopic abundances of the steel elements implemented in

Element	Cr	Mo	Ni	Ti	Fe
Mass fraction [%]	17.5	2.25	12	0.35	67.9

Table 3.8: Stainless steel composition of the GERDA cryostat. The same composition has been taken for the SOURCES4A calculations to estimate the neutron flux resulting from (α, n) reactions in the walls of the source encapsulation.

SOURCES4A, a rate of

$$R^n_{steel} = 2.5 \cdot 10^{-5} \text{ neutrons/s/kBq} \tag{3.26}$$

has been determined with a mean neutron energy of

$$E^{steel}_{mean} = 1.80 \text{ MeV}. \tag{3.27}$$

While this rate is already three orders of magnitude below the rates in the ceramics, the final value for the neutron rate R^n_{wall} resulting from (α, n) reactions in the walls of the encapsulation must be scaled down by the factor $f_{\delta V}$

$$R^n_{wall} = 1/f_{\delta V} \times R^n_{steel} = 1 \cdot 10^{-6} \text{ neutrons/s/kBq} \tag{3.28}$$

Although the calculated spectrum for stainless steel, shown in figure 3.7 is slightly harder than those determined for ceramics, the difference in the mean energies is only 100 keV. Therefore, an increased probability for inelastic interactions in the germanium array of GERDA can not be expected. Furthermore, given the fact that the final neutron rate for reactions in the encapsulation walls is four orders of magnitude lower than those induced in the ceramics, the stainless steel contribution will be no subject anymore to further discussion in this work.

3.2.3 Neutron flux calculations - uncertainty estimation

SOURCES4A calculations are afflicted with a systematic error of up to 20% [69]. The results base on fixed (α, n) cross section libraries implemented in the code. Because (α, n)

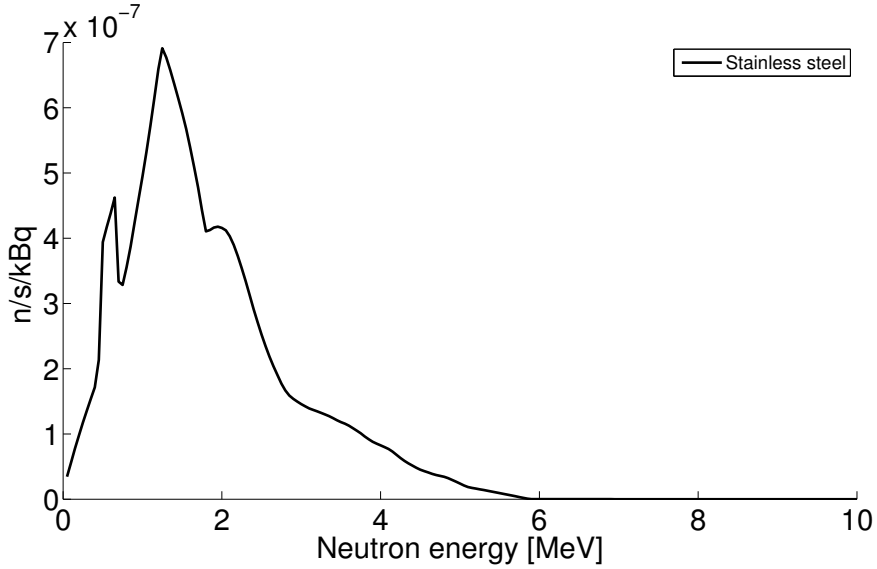

Figure 3.7: Neutron spectrum induced by (α, n) reactions in stainless steel.

cross sections are subject to large uncertainties, a study have been done with the goal to investigate the uncertainties resulting merely from the available cross section data.
To do so, all data from the SOURCES4A libraries have been taken into account as well as all available measurement data from the EXFOR [76] database. Furthermore, cross sections for the materials of interest were calculated explicitly using the EMPIRE code [77]. EMPIRE is a software which was developed to perform cross section calculations for incident particles using various nuclear models and nuclear reaction mechanisms. The EMPIRE libraries contain diverse parameters for optical models, nuclear masses, ground state deformations, decay schemes, level densities and fission barriers.

A comprehensive data set has been generated containing all calculated cross sections together with the data from SOURCES and EXFOR. A Matlab algorithm was developed to search for the maximal and minimal cross sections in order to define a band of maximal and minimal values for each chemical element. Experimental data at energies above 6 MeV are almost not available and the full energy range up to 10 MeV has been covered by linear interpolation of the available data points mostly given by EMPIRE calculations. Two examples of defining the cross section bands are shown in figure 3.8 and figure 3.9 for the ^{18}O isotope and ^{23}Na. The blue and green lines in the plots designate the maximal and minimal sets of cross sections used for the uncertainty estimation. Both lines merge at the (α, n) threshold energies in good agreement with the calculated values in table 3.4. Further cross section bands were determined for ^{17}O, ^{27}Al, ^{28}Si, ^{29}Si and ^{30}Si. The two data sets of upper and lower cross section bands for the considered isotopes were implemented separately in the SOURCES4A library in order to estimate upper and lower uncertainties in the rates. Table 3.9 summarizes the neutron rates and the mean energies as they result from SOURCES4A calculations with the maximal, minimal and original cross sections

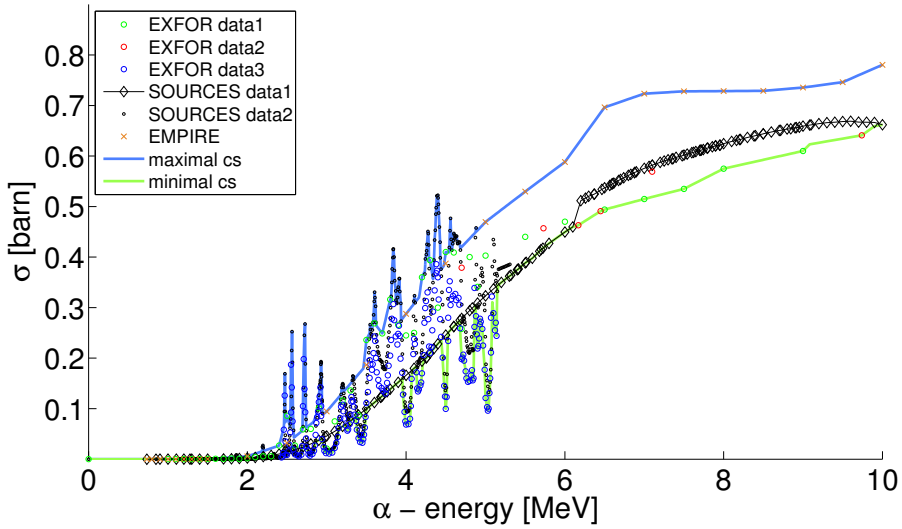

Figure 3.8: Determination of the band, which defines maximal and minimal cross sections for (α, n) reactions in ^{18}O.

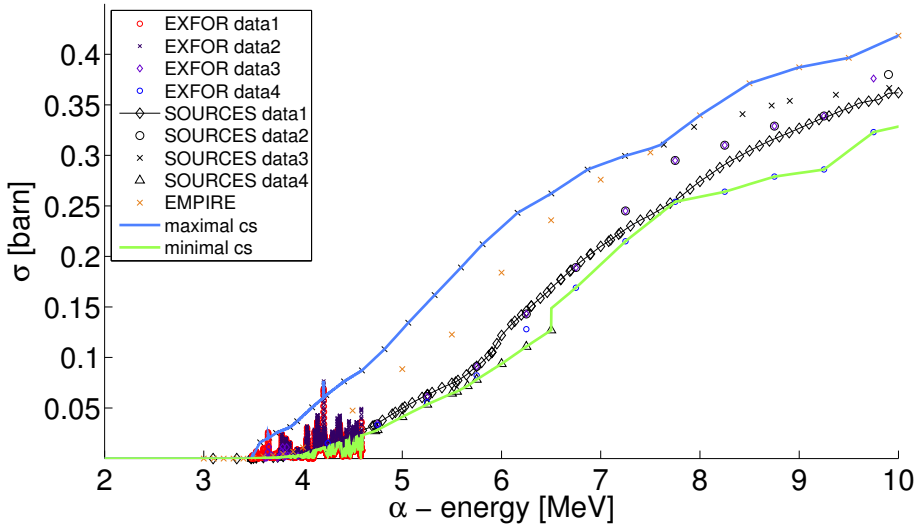

Figure 3.9: Uncertainty band of the (α, n) cross sections in ^{23}Na. The band merges at 3.5 MeV which is the threshold energy of ^{23}Na.

implemented for both ceramics, $NaAlSiO_2$ and Al_2O_3. As shown in table 3.9 the errors resulting from the available cross section data are asymmetric. Figure 3.10 and figure 3.11 illustrate furthermore the neutron spectra for both ceramics with the resulting spectral uncertainties. While the uncertainty of the mean neutron energies stays within an error of 10% with

$NaAlSiO_2$	(α, n) rate [n/s/kBq]	E_{mean} [MeV]
Maximal cross sections	$3.35 \cdot 10^{-2}$	1.51
Original cross sections	$1.99 \cdot 10^{-2}$	1.67
Minimal cross sections	$1.70 \cdot 10^{-2}$	1.70

Al_2O_3	(α, n) rate [n/s/kBq]	E_{mean} [MeV]
Maximal cross sections	$1.99 \cdot 10^{-2}$	1.60
Original cross sections	$1.40 \cdot 10^{-2}$	1.70
Minimal cross sections	$1.22 \cdot 10^{-2}$	1.75

Table 3.9: Results of the uncertainties in the rates and energies, based on the implementation of upper and lower cross section data in SOURCES4A.

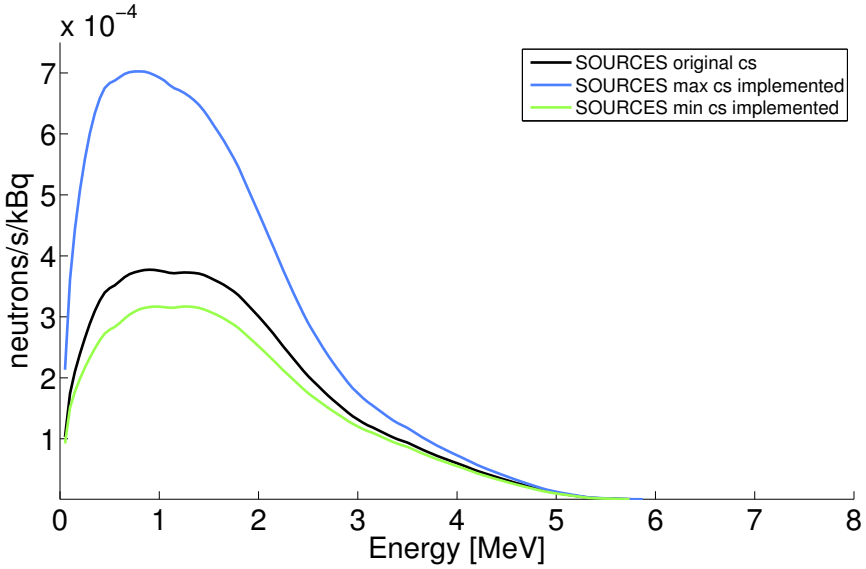

Figure 3.10: Three different neutron spectra calculated for the $NaAlSiO_2$ ceramic, resulting from calculations with the original cross sections and the upper/lower cross section bands.

$E_{mean}(NaAlSiO_2) = 1.67^{+1.80\%}_{-9.58\%}$ MeV

and

$E_{mean}(Al_2O_3) = 1.70^{+2.94\%}_{-5.88\%}$ MeV,

the upper rates differ from the rates originally calculated by up to ∼70% in the case of $NaAlSiO_2$ and up to ∼42 % for the Al_2O_3 ceramic. On the other side, the lower rates stay within an error of ∼15 % with:

$R(\mathrm{NaAlSiO_2}) = 1.99^{+68.3\%}_{-14.57\%} \cdot 10^{-2}$ neutrons/s/kBq

and

$R(\mathrm{Al_2O_3}) = 1.40^{+42.14\%}_{-12.86\%} \cdot 10^{-2}$ neutrons/s/kBq.

Using the uncertainty results obtained above, conservative neutron rate errors $\sigma^{+/-}$

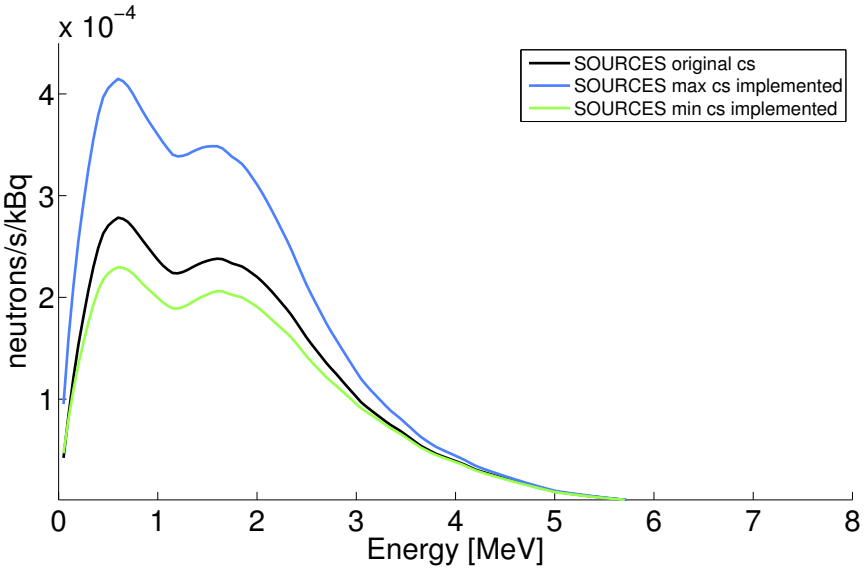

Figure 3.11: Comparison of the spectral uncertainties for the Al_2O_3 ceramic, calculated with SOURCS4A as described above.

can be calculated, considering additionally the standard uncertainty σ_0 of 20% given by SOURCES4A. With

$$\begin{aligned} \sigma^+ &= \sqrt{\sigma_0^2 + (\sigma_{cs}^+)^2}\,, \\ \sigma^- &= \sqrt{\sigma_0^2 + (\sigma_{cs}^-)^2} \end{aligned} \tag{3.29}$$

where σ_{cs}^+ and σ_{cs}^- are the upper and lower errors determined by the implementation of the maximal and minimal (α, n) cross sections in SOURCES4A, the rates in both ceramics can be given by:

$$R(\mathrm{NaAlSiO_2}) = 1.99^{+1.42}_{-0.49} \cdot 10^{-2} \text{ neutrons/s/kBq}, \tag{3.30}$$

and

$$R(\mathrm{Al_2O_3}) = 1.40^{+0.65}_{-0.33} \cdot 10^{-2} \text{ neutrons/s/kBq}. \tag{3.31}$$

3.3 Summary

In order to estimate the neutron background induced by the presence of the ^{228}Th calibration sources in the GERDA setup, the spontaneous fission half-life of ^{228}Th has been calculated in a first approach. With an estimated half-life of $\sim 1 \cdot 10^{21}$ years and a fission rate of

$$A_{SF} = 5 \cdot 10^{-11} \text{ decays/year/kBq} \tag{3.32}$$

per kBq source strength, the process has been considered as negligible for all phases of GERDA and will not be subject to further discussion in this work.

In a second step, (α, n) reactions in a commercial ^{228}Th source have been calculated with SOURCES4A. Reactions of α particles within the stainless steel walls of the encapsulation after escaping the ceramic, have been considered as a second order process. The rates determined for stainless steel were found to be negligible too, with an estimated neutron production rate of

$$R^{n}_{wall} = 1 \cdot 10^{-6} \text{ neutrons/s/kBq.} \tag{3.33}$$

In contrast, (α, n) reactions induced in ceramic pellets, saturated with α emitting radio nuclides were found to be dominant and yielded considerable neutron rates. Error estimation of the calculated rates was performed by generating maximal and minimal cross section data sets for each of the isotope and implementing them in SOURCES4A. The rates were determined for two different ceramics, $NaAlSiO_2$ and Al_2O_3 resulting in

$R(NaAlSiO_2) = 1.99^{+1.42}_{-0.49} \cdot 10^{-2}$ neutrons/s/kBq

and

$R(Al_2O_3) = 1.40^{+0.65}_{-0.33} \cdot 10^{-2}$ neutrons/s/kBq

with mean neutron energies of

$E_{mean}(NaAlSiO_2) = 1.67^{+0.03}_{-0.16}$ MeV

and

$E_{mean}(Al_2O_3) = 1.70^{+0.05}_{-0.1\%}$ MeV.

The impact of the determined neutron rates on the background index of GERDA has been estimated with Monte Carlo simulations in [57], and yielded a count rate of

$B_n = (2.97 \pm 0.2) \cdot 10^{-3}$ counts/(keV·kg·y)

in the $Q_{\beta\beta}$ region of interest, assuming a source strength of 100 kBq. Such a rate is

higher than the background index envisioned for phase II of GERDA.
Motivated by the considerably high neutron rates, induced by (α, n) reactions in the ^{228}Th sources, a technique has been developed to suppress the (α, n) channel, which will be presented in the next chapter 4.

Chapter 4

Low neutron emission γ source

As discussed in section 3.2, a commercial ^{228}Th source can be a relevant source of neutron background in GERDA and other low background experiments. Furthermore the uncertainty of the chemical composition of the ceramic used in the encapsulation can result in an unpredictable spread of the neutron flux estimations. In GERDA, the neutron background index from the source could reach $\sim 3 \cdot 10^{-5}$ counts/(keV·kg·y·kBq) in the region of interest around $Q_{\beta\beta}$. In consequence, a total source activity of 100 kBq would lead to a background index reaching the total foreseen background goal for phase II of GERDA. The neutron production results from the emission of α particles in the ^{228}Th chain with energies ranging from 5.34 MeV to 8.78 MeV and from the undergoing (α, n) reactions within the materials used for the source encapsulation. A reduction of this neutron emission can be achieved by suppressing the possible (α, xn) channels, which can be done by embedding the Th chain radionuclides in specific materials. The criteria of the first priority for such materials is an (α, n) threshold energy above the maximum α energy of 8.78 MeV emitted by the ^{212}Po daughter of ^{228}Th. Another requirement is the commercial availability, the possibility of an

Metal	melting point [K]	stable isotopes	lowest (α, n) threshold energy [MeV]
Ru	2607	7	$^{44}\mathrm{Ru}_{101}$, 4.372
Os	3400	5	$^{76}\mathrm{Os}_{189}$, 8.515
Rh	2239	1	$^{45}\mathrm{Rh}_{103}$, 6.993
Ir	2716	2	$^{77}\mathrm{Ir}_{193}$, 9.227
Pd	1825	6	$^{46}\mathrm{Pd}_{105}$, 4.99
Pt	2045	5	$^{78}\mathrm{Pt}_{198}$, 8.05
Ag	1234	2	$^{47}\mathrm{Ag}_{109}$, 6.607
Au	1334	1	$^{76}\mathrm{Au}_{197}$, 9.937

Table 4.1: Properties of the noble metals considered as matrix materials for ^{228}Th. Gold has been found to be the optimal material for the (α, n) suppression.

easy mechanical handling as well as thermic and chemical stability. The latter condition is

fulfilled by nobel metals, but not all of them fulfill the requirement of the (α, n) threshold energies or mechanical stability. Table 4.1 shows the properties of the noble metals which were considered as candidates. While all of them fulfill the criteria of chemical and thermal stability, only iridium and gold fulfill the threshold energy criteria of more than 8.8 MeV. Osmium with a threshold energy of 8.5 MeV can be also regarded as a good candidate with an at least drastically suppressed (α, n) channel. However, in contrast to gold, the two platinum group metals, iridium and osmium are brittle and very hard to machine. Foils are not available. Therefore, gold occurring in one single, stable isotope (^{97}Au) and with an (α, n) threshold energy of 9.94 MeV has been chosen as the only one material meeting all requirements. Figure 4.1 shows experimental data for the (α, n) cross sections of the ^{197}Au isotope confirming the threshold energy of around 10 MeV. In principle, suppression of the

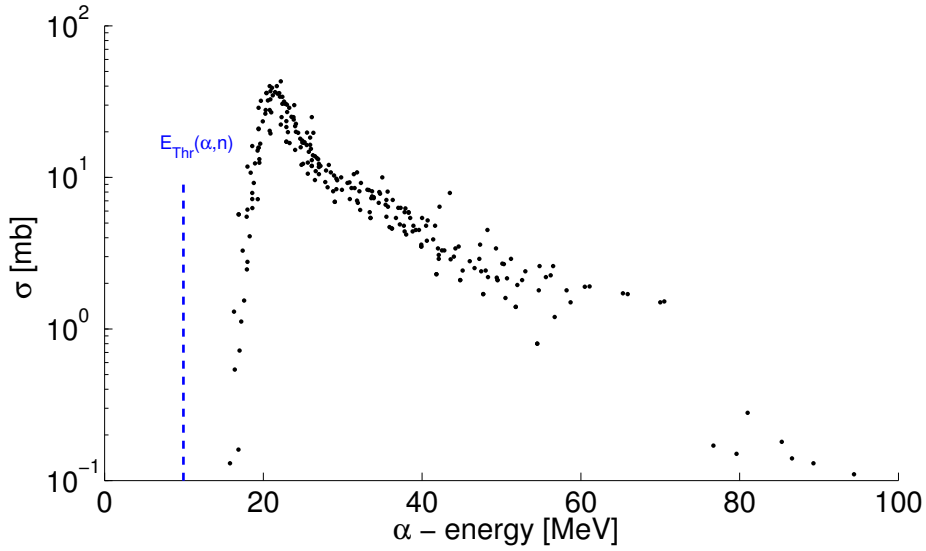

Figure 4.1: Measured (α, n) cross sections in gold. The dashed line indicates the calculated threshold energy of 9.94 MeV.

(α, n) channel can be achieved by replacing the ceramics used in commercial sources by ^{228}Th coated gold substrates for example. Because open ^{228}Th sources are only available in liquid solutions, a process of depositing ^{228}Th and its daughters on gold had to be developed, which was done in collaboration with R.Dressler, R.Eichler and D.Schumann from the Paul Scherrer Institute, Villigen in Switzerland. The method uses a liquid precursor of commercially available $ThCl_4$ in a 1M HCl solution. Chloride with a low atomic number of 17 has two stable isotopes, ^{35}Cl and ^{37}Cl. Both have a threshold energy of 6.53 MeV and 4.29 MeV respectively and would strongly contribute to the neutron background from (α, n) reactions. Hence, the chemical and thermal treatment of the solution includes a step of molecular unbinding and evaporation of the chloride atoms. The process leads finally to a layer of solid ThO_2, which is deposited on a gold foil. The treatment can be described in four steps.

• the $ThCl_4$ solution is pipetted into a heated conical teflon crucible. Nitric acid is added in order to unbind the chlorides, resulting in thorium-nitrate compounds

$$3ThCl_4 + 16HNO_3 \rightarrow 200^oC \rightarrow [3Th(NO_3)_4]_s + [(4NOCl + 8H_2O + 4Cl_2)]_g \quad (4.1)$$

While the products on the right side of the reaction (nitrosylchloride, water and chlorine) evaporate at 200^oC, $Th(NO_3)_4$ remains in the crucible in a solid state. The process is repeated in several steps until the initial $ThCl_4$ solution is used up with no liquid phase remained in the heated crucible.

• in a second step, HNO_3 is added again to the solid $Th(NO_3)_4$ in order to dissolve it. This step allows to transfer the $Th(NO_3)_4$ with a pipette from the teflon crucible into a gold foil crucible. The solution is heated again to evaporate the remnants and the HNO_3.

• in the third step, the nitrates are unbound from the $Th(NO_3)_4$ molecules by heating up the gold crucible up to $\sim 700^oC$, which forms ThO_2 in solid state on the surface of the gold substrate.

$$3Th(NO_3)_4 \rightarrow 750^oC \rightarrow [3ThO_2]_s + [12NO_2 + 3O_2]_g \quad (4.2)$$

In reaction (4.1) and (4.2), s and g stand for the solid state and the gas phase. The step is the last one in the chemical and thermal treatment chain.

• in the final step, the gold crucible with the deposited ThO_2 is folded several times and wrapped into an additionally gold foil for safety reasons. After that, the sealing of the such prepared activity sample can take place in a standard stainless steel encapsulation.

As shown in figure 4.2, the ranges of α particles emitted by the ^{228}Th chain in gold is below 20 μm for the highest energetic α particle. Considering a gold foil thickness of at least 25 μm and the fact that several gold layers cover the activity in 4π, the contribution of α particles escaping the gold trap is expected to be negligible. Although most of the relevant isotopes for (α, n) reactions has been removed by the chemical and thermal treatment, oxygen in the ThO_2 compound still can undergo (α, n) reactions. As discussed already in chapter 3.2.1, 99.757% of oxygen consists of the double magic ^{16}O isotope with an (α, n) threshold energy of 15.17 MeV. This is far above the maximal α energy of the Th chain. Only 0.2% of oxygen consists of ^{18}O and 0.038% of ^{17}O. Albeit the marginal isotopic abundance of ^{18}O and ^{17}O, their (α, n) threshold energies are below 1 MeV and were hence regarded as potentially dangerous in terms of neutron production. Neutron flux calculations for ThO_2 performed with SOURCES4A resulted in a rate of

$$R_{(\alpha,n)}(ThO_2) = 2.19^{+0.99}_{-0.51} \cdot 10^{-4} \text{ neutrons/s/kBq} \quad (4.3)$$

with a mean neutron energy of $2.58^{+0.01}_{-0.07}$ MeV. The errors were estimated in an analogue way as described in section 3.2.3 under consideration of the maximal and minimal cross section

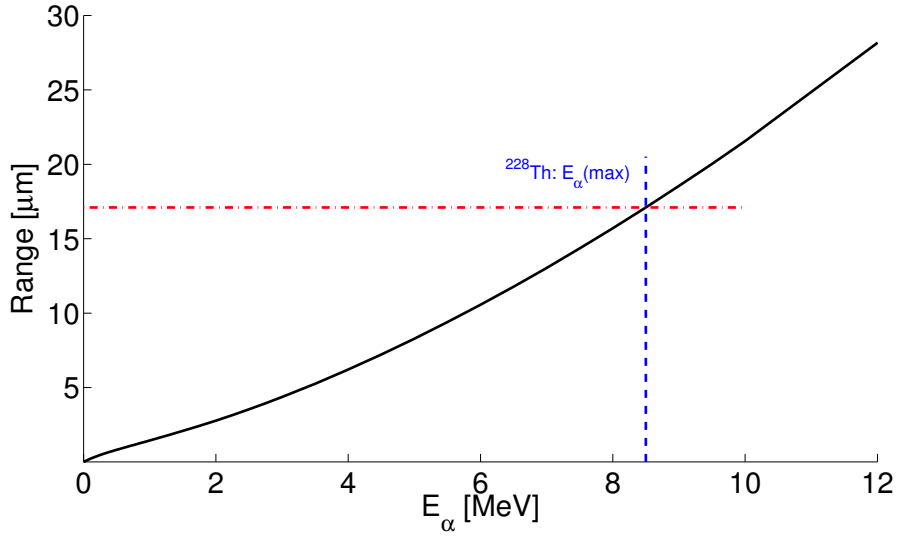

Figure 4.2: Ranges of α particles in gold, assuming a gold density of $\rho_{Au} = 19{,}28$ g/cm^3. Data taken from [74].

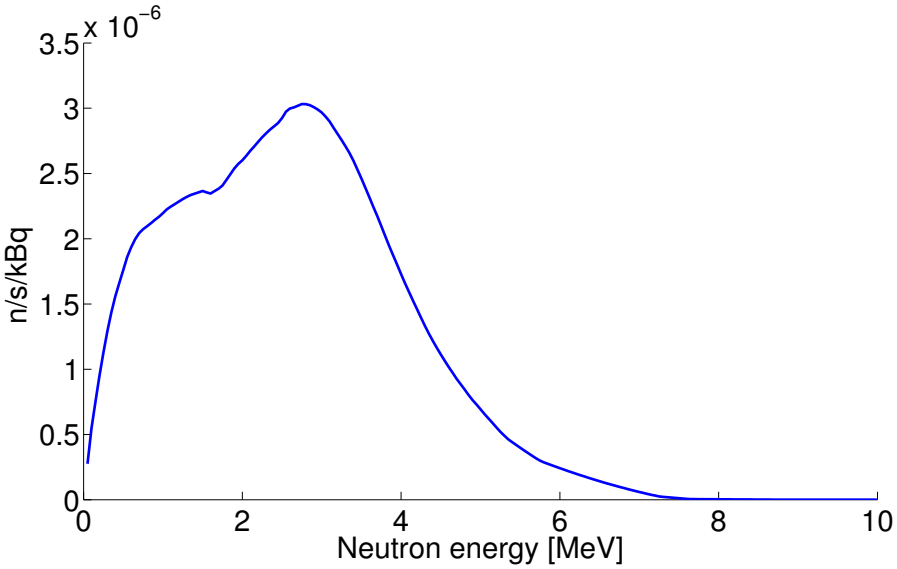

Figure 4.3: Neutron spectrum as calculated with SOURCES4A for ThO_2. The natural abundancies of the oxygen isotopes have been taken into account. The resulting total neutron flux is $2.2 \cdot 10^{-4}$ n/s per kBq with a mean neutron energy of 2.6 MeV.

bands for oxygen and a systematic error of 20% given by SOURCES4A. The resulting neutron spectrum is shown in figure 4.3. While, the mean neutron energy has increased by around 1 MeV with respect to the mean energies of the ceramics, the neutron flux has been reduced by almost two orders of magnitude. However, it must be considered that the ThO_2 compound represents the ideal case without any other impurities involved in the

initial solution or during the treatment. Given by data sheets of commercially available $ThCl_4$ solutions, it is known for example that Zr carrier are added. The zirconium is added during the production of the active solution to allow for an efficient separation of radioactive isotopes during sedimentation. Furthermore it inhibits activity losses on the vial walls during decanting. Although it is possible to remove the zirconium atoms from the liquid by anion exchange in a 9-12 M HCl solution as shown in [78], the process would increase the complexity of the source production with possible consequences for the final activity yield. Therefore, an estimation of a possible zirconium contribution in neutron production has been done first, in order to determine its relevance for the suppression of the (α, n) channel. Table 4.2 shows the natural abundance of zirconium and the isotopic threshold energies for (α, n) reactions. More than 50% of natural zirconium contain ^{90}Zr

Isotope	^{90}Zr	^{91}Zr	^{92}Zr	^{94}Zr	^{96}Zr
atomic nat. abundance [%]	51.45	11.32	17.19	17.28	2.76
$E_{Thr}(\alpha, n)$ [MeV]	7.95	5.35	6.67	5.60	5.34

Table 4.2: Natural abundancies of stable zirconium isotopes and their (α, n) threshold energies.

with a threshold energy of 7.95 MeV and hence this isotope is not regarded as critical. The remaining isotopes have relatively high threshold energies, but they allow for (α, n) reactions in contact with ^{228}Th. SOURCES4A does not contain zirconium in its libraries and therefore, the code could not be used in its original state to quantify the neutron flux resulting from the presence of zirconium. In order to include the Zr isotopes into SOURCES4A, the EMPIRE code has been used to calculate (α, n) cross sections for all stable Zr isotopes. The calculated cross sections are shown in figure 4.4. Threshold energies have been determined by the point of intersection with the abscissa in good agreement with the threshold energies in table 4.2. The five zirconium isotopes have been added to the SOURCES4A code by implementing the calculated values into the cross section libraries. Atomic level formation data for Zr were not available and hence only transitions to the ground level were considered. In consequence, the calculated SOURCES4A spectra are simplified and do not represent a detailed energetic distribution. Because of that, a mean neutron energy can not be determined. However, the total neutron flux estimation remains unaffected by the missing information and can be used in further considerations. Table

Isotope	^{90}Zr	^{91}Zr	^{92}Zr	^{94}Zr	^{96}Zr
Target fraction [%]	100	100	100	100	100
(α, n) rate [n/s/kBq]	$7.79{\cdot}10^{-6}$	$1.24{\cdot}10^{-5}$	$1.29{\cdot}10^{-5}$	$1.48{\cdot}10^{-5}$	$1.62{\cdot}10^{-5}$

Table 4.3: Neutron rates induced by (α, n) reactions in stable zirconium isotopes. The values were determined after calculating the cross sections with EMPIRE and after implementation in the SOURCES4A code.

4.3 shows the neutron rates calculated for each isotope, assuming all emitted α particles

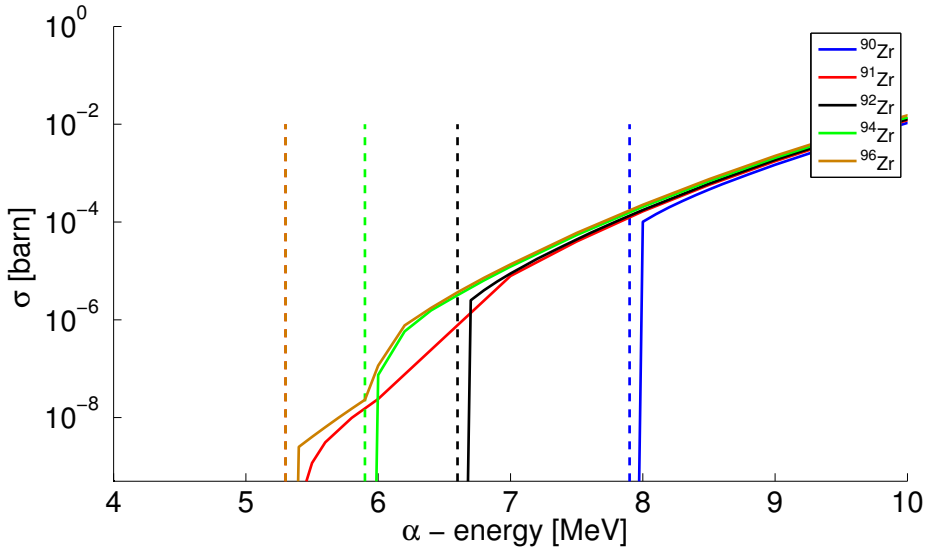

Figure 4.4: (α, n) cross sections calculated with EMPIRE for five zirconium isotopes. The dashed lines indicate calculated threshold energies.

to interact with each isotope at a probability of 100 %. This allows to scale the rates afterwards according to any abundance of interest. Considering the natural abundancies of Zr shown in table 4.2 and the rates in table 4.3 a neutron flux of

$$R_{(\alpha,n)}(Zr_{nat}) = 1.06 \cdot 10^{-5} \text{ neutrons/s/kBq} \tag{4.4}$$

has been estimated for natural zirconium. The rate given by equation (4.4) is one order of magnitude lower than the neutron rate for ThO_2 in equation (4.3). Furthermore the calculations, represent a scenario with zirconium as the only one target material for the α particles. This is not the case in the gold sample where most of α particles will be stopped by gold and hence the result given in equation (4.4) must be regarded as absolutely conservative. Consequently, the Zr carrier are not considered as potentially dangerous in terms of neutron production, and the solution treatment has not been extended by a further step to remove the Zr targets. It should be noted however that the presence of other unknown impurities or an contamination during the treatment can not be excluded.

4.1 Production of a neutron flux reduced ^{228}Th source at PSI

The first prototype source has been produced at the Paul Scherrer Institute (PSI), Villigen, Switzerland in March 2009. For the production, a 1M HCl $ThCl_4$ precursor solution from Eckert&Ziegler has been used with a nominal activity of 20 kBq. Classified as an open source, it has been delivered directly to PSI for further treatment. Details of the active solution are shown in table 4.4. The 0.5 mL vial shown in figure 4.5 contained five μg of

Activity	20 kBq ± 15%
Chemical form	$ThCl_4$ in 1M HCl
Carrier	10 μg/mL Zr
Volume	0.5 mL in V-vial glas
Radionuclidic Purity	>99%

Table 4.4: Data of the initial $ThCl_4$ solution processed at PSI into an active gold foil sample.

elemental zirconium carrier, which required further investigation in terms of its impact on the resulting neutron rate. As discussed above, with more than one order of magnitude less neutrons produced than in ThO_2, this contribution can be neglected in the first order. The custom source production took place in a sealed glovebox, connected to the air filter system of PSI. The filter system prevents ^{220}Rn which emanates during the thermal treatment to release into the atmosphere. Introducing and locking out of tools, equipment and

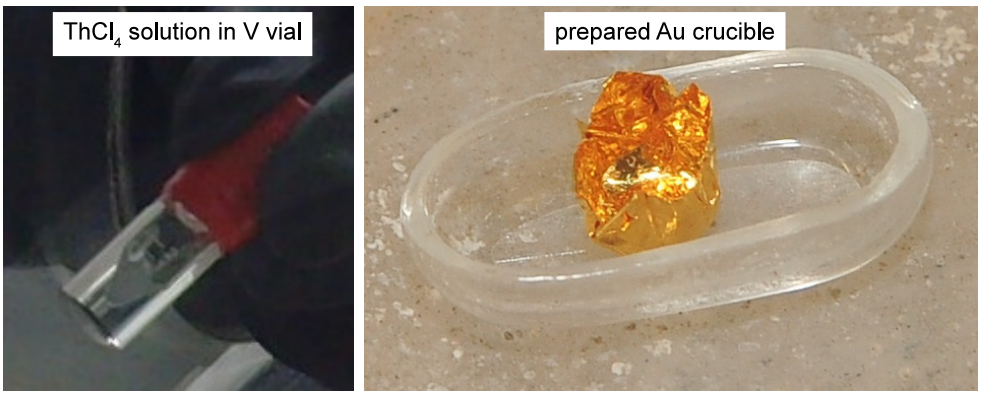

Figure 4.5: Left: $ThCl_4$ solution in V-vial before treatment. Right: Gold sample shaped into a crucible to be used as ^{228}Th substrate.

radioactive materials took place via a lubricator mounted on the side of the glovebox. In order to determine the activity losses which could occur during processing of the solution, γ spectroscopy measurements of the initial and the processed source have been performed with a coaxial Ge detector. Furthermore, a Geiger counter was used for monitoring the glovebox during the treatment. Tools, vials, equipment and the glovebox walls were the potential locations of possible activity losses. As substrate, a 25 μm thick gold foil has been prepared and folded into a crucible, shaped as shown in figure 4.5.

The size of the gold sample was around (5x5x5) mm. Following the treatment steps described in section 4, the following consecutive steps were performed:

Step 1: $3ThCl_4 + 16HNO_3 \rightarrow 200^oC \rightarrow [3Th(NO_3)_4]_s + [(4NOCl + 8H_2O + 4Cl_2)]_g$

As illustrated in figure 4.6, the $ThCl_4$ solution has been pipetted into an iconic teflon crucible and nitric acid (HNO_3) added. The teflon crucible has been heated up to about 200^{o}C in order to break the $ThCl_4$ binding and to form $Th(NO_3)_4$. The remanents nitrolsyl-

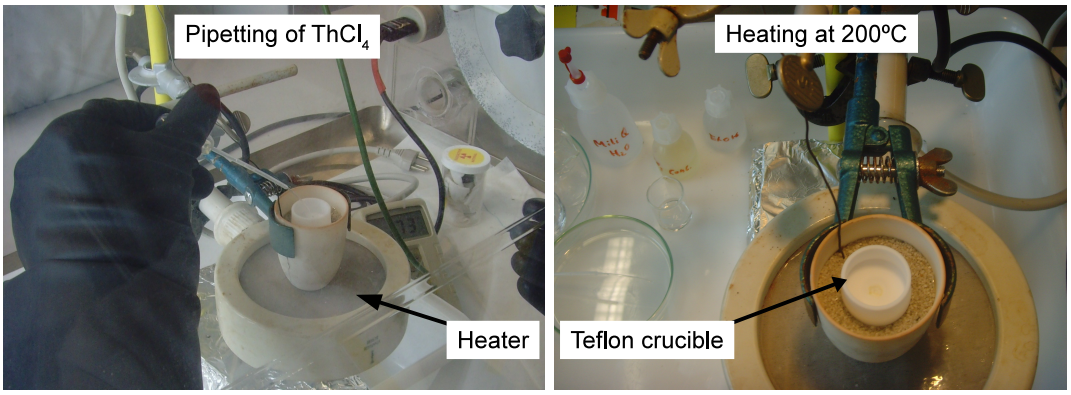

Figure 4.6: Left: Pipetting of the liquid $ThCl_4$ solution into a heated teflon crucible, before adding HNO_3. Right: $Th(NO_3)_4$ in solid state after the evaporation of all remanents.

chloride, water and chlorine evaporate at 200 ^{o}C. To ensure a complete molecular unbinding of the $ThCl_4$ compound, the step have been repeated $\sim$4 times.

Step 2: In order to transfer the solid $Th(NO_3)_4$ from the teflon crucible into the gold crucible, HNO_3 was added again as shown in figure 4.7. The liquid have been then pipetted into the gold crucible which was heated to $\sim$ 200 ^{o}C to evaporate the HNO_3. To reduce

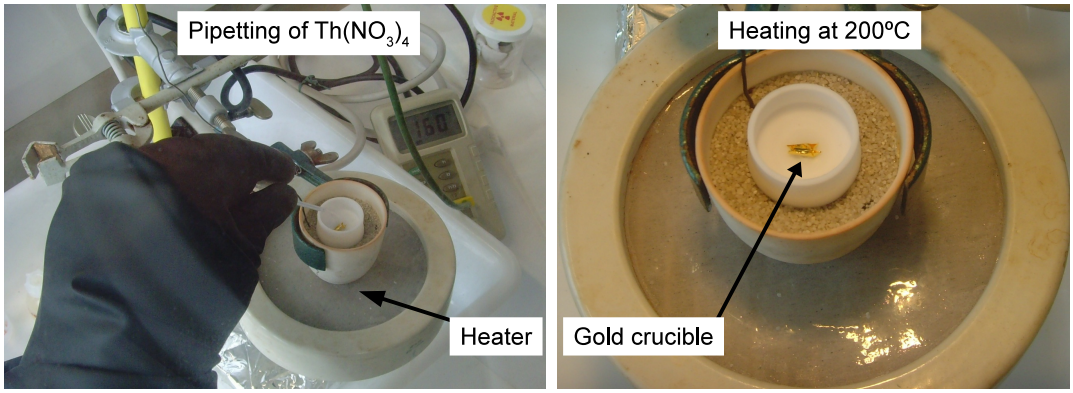

Figure 4.7: Left: Pipetting of the $Th(NO_3)_4$ solution into a heated gold crucible. Right: $Th(NO_3)_4$ in solid state, deposited on gold. The sample is ready for the last annealing step.

activity losses, the teflon crucible used in the first step has been washed out several times with HNO_3 and the content transferred into the gold crucible.

Step 3: $3Th(NO_3)_4 \rightarrow 750^oC \rightarrow [3ThO_2]_s + [12NO_2 + 3O_2]_g$

Breaking the thorium-nitrate bindings takes place during thermal annealing of the active gold sample at $\sim$ 750 ^{o}C. The process leads to the final ThO_2 formation on gold. For this purpose, an open ceramic furnace mounted in the glovebox was used which is shown in figure 4.8 A. The prepared gold sample with $3Th(NO_3)_4$ has been moved into a quartz glass crucible and heated up to 750 ^{o}C for about one hour.

Step 4: After cooling down, the sample has been folded several times. To reduce the risk of activity losses during handling and transportation, a second goldfoil has been wrapped around. Furthermore, the latter step increases the absorption probability for emitted α particles. The active sample is very plastic and can be shaped into any form. For the

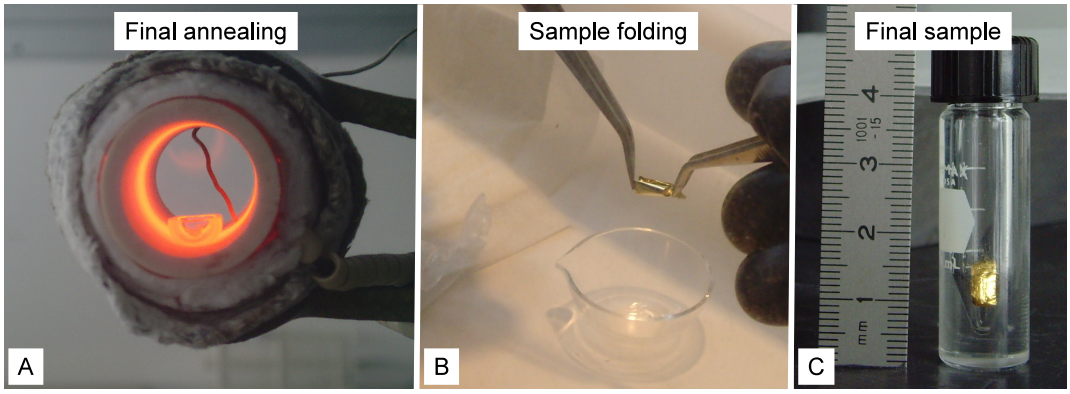

Figure 4.8: A: Forming of ThO_2 by annealing of the $3Th(NO_3)_4$ at 750^{o}C. B: Folding of the ThO_2 gold sample after annealing. C: Final ThO_2 gold sample, ready for sealing in a stainless steel encapsulation.

encapsulation, a flat shape of $\sim$ (5x3x2) mm has been prepared as shown in figure 4.8C.

The encapsulation of the first prototype sample has been done at Eckert&Ziegler Nuclitec GmbH in Prague. A P02 capsule has been used which has been introduced in section 3.1.3 and shown in figure 3.2. The capsule is provided with a M4 thread, allowing for an easy handling and mounting. After inserting the gold activity into the open capsule, it has been sealed by welding. Leakage and wipe tests were performed by Eckert&Ziegler before the sealed source has been shipped back to the University of Zurich.

4.2 ^{220}Rn emanation and production activity-yield

An inevitable consequence of the thermal treatment of the $ThCl_4$ solution described in section 4.1 is the emanation of ^{220}Rn daughters. As shown by the decay chain in (4.5), ^{220}Rn is the second daughter nuclide in the ^{228}Th chain. The emanation of ^{220}Rn gas breaks

the secular equilibrium of the chain, which affects amongst others also the emission of the 2.6 MeV line from the ^{212}Bi decay. The 2.6 MeV line and the correlated single escape line at 2.1 MeV are of special interest for the γ calibration of GERDA due to the energetic vicinity to the $Q_{0\nu\beta\beta}$ value of ^{76}Ge.

$$[^{228}\mathrm{Th} \rightarrow {}^{224}\mathrm{Ra}]_A \rightarrow [\mathbf{^{220}Rn} \rightarrow {}^{216}\mathrm{Po} \rightarrow {}^{212}\mathrm{Pb} \rightarrow {}^{212}\mathrm{Bi} \rightarrow ({}^{212}\mathrm{Po} + {}^{208}\mathrm{Tl}) \rightarrow {}^{208}\mathrm{Pb}]_B \tag{4.5}$$

While the first subchain in (4.5), $[^{228}\mathrm{Th} \rightarrow {}^{224}\mathrm{Ra}]_A$ remains in equilibrium, the repopulation process of subchain B is stopped during the treatment by ^{220}Rn emanation. To quantify the recovery of the chain, γ spectra of the initial $ThCl_4$ solution and of the gold sample after the treatment have been taken. Two peaks have been chosen for the analysis. The ^{224}Ra peak which is not affected by ^{220}Rn emanation and the ^{212}Pb peak, a daughter nuclide of the broken sub chain B. The two lines have energies of 241 keV and 238.6 keV respectively. Their proximity in energy makes energy dependent efficiency considerations redundant. Figure 4.9 shows the ^{212}Pb and ^{224}Ra peaks of the initial $ThCl_4$ solution

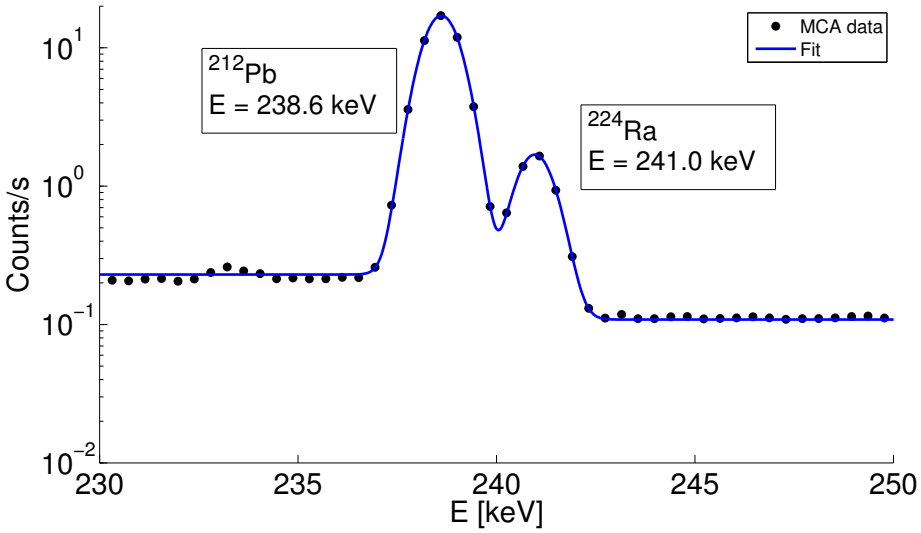

Figure 4.9: ^{212}Pb and ^{224}Ra lines of the initial $ThCl_4$ solution before ^{220}Rn emanation.

before the treatment. The counts ratio of the two peaks can be used as a measure of the equilibrium condition. Both peaks have been fitted as a superposition of two gaussian distributions and a smoothed stepfunction used to model the background. The count rates were determined by integration of the fits and subtracting the background component. The peak ratio determined for the $ThCl_4$ solution in equilibrium was found to be

$$R_{equi}(\mathrm{ThCl_4}) = 10.78 \pm 0.04. \tag{4.6}$$

After the thermal treatment of the solution, a decrease of the ^{212}Pb rate is expected in respect to the ^{224}Ra peak. Figure 4.10 shows the two ^{212}Pb and ^{224}Ra peaks of the gold

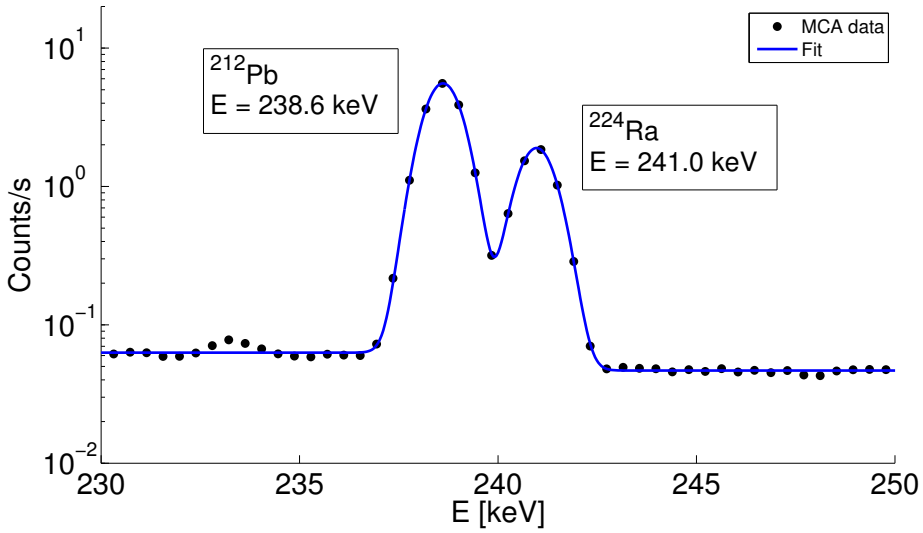

Figure 4.10: ^{212}Pb and ^{224}Ra lines after the secular equilibrium has been broken by ^{220}Rn emanation.

sample about one hour after the solution has been converted into ThO_2 on gold. The peak ratio which has been determined in the same way as described above for the initial solution in equilibrium, changed from 10.78± 0.04 to

$$R_{non-equi}(ThO_2) = 2.97 \pm 0.01. \tag{4.7}$$

The rate indicates a decrease of the ^{212}Pb population by about factor three after the ^{228}Th has been deposited on gold. However, due to the short half-lifes of the nuclides in chain B, a full recovery is expected within days after the source preparation. The time needed to establish the secular equilibrium between a mother- and its daughter- nuclide can be calculated by

$$A_2(t) = A_1 + \lambda_2 \cdot [N_2(t=0) - A_1/\lambda_2] \cdot e^{-\lambda_2 \cdot t} \tag{4.8}$$

where $A_2(t)$ is the activity of the daughter nuclide, $N_2(t=0)$ and λ_2 are the initial number of atoms and the decay constant respectively and A_1 is the initial activity of the mother nuclide. For ^{220}Rn and ^{216}Po the equilibrium is established almost instantly due to their short half-lifes of 55.6 s and 0.145 s.^{212}Pb has the longest half-life in chain B with 10.64 h and is hence the nuclide which determines the time of the equilibrium recovery. Using equation (4.8), it can be shown that after two days, the ^{212}Pb nuclides reach 95% of the activity given by an equilibrium condition. Figure 4.11 shows the recovery of the ^{212}Pb population one week after the source preparation. The ratio between the two peaks changed from $R_{non-equi}(ThO_2) = 2.97 \pm 0.01$ one hour after the preparation to

$$R_{equi}(ThO_2) = 10.71 \pm 0.04 \tag{4.9}$$

one week later. This is equivalent to a chain recovery of 99.3 % with respect to the initial equilibrium condition given in (4.6).

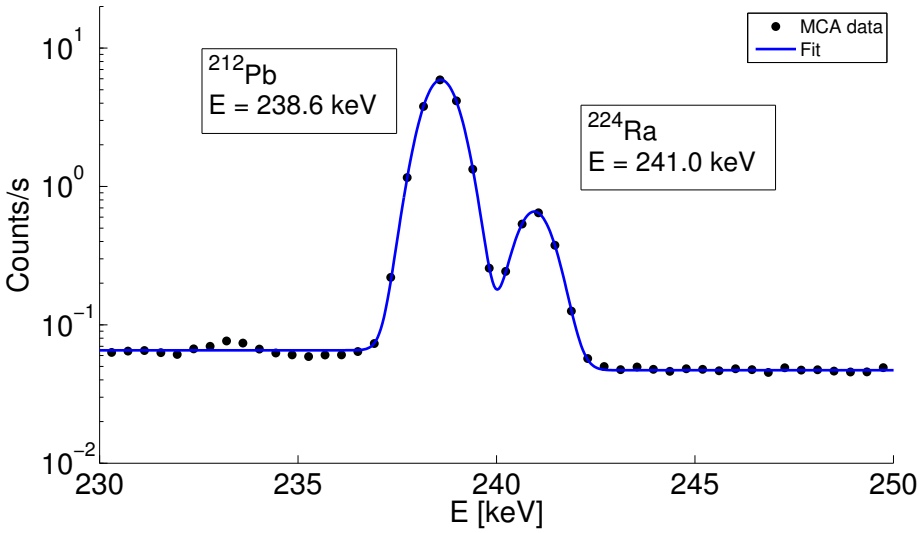

Figure 4.11: Recovery of the ^{212}Pb population one week after the source has been prepared at PSI.

Activity yield during production

Considering the fact that the ^{224}Ra peak stays unaffected by the ^{220}Rn emanation during treatment of the $ThCl_4$ solution, the question of activity losses could be investigated by comparing the count rates in the ^{224}Ra line before and after the source preparation. With the initial rate given by R_0^{Ra} and a rate after the treatment given by R_{Ra}^{Au}, the activity yield ϵ_A can be defined as

$$\epsilon_A = R_{Ra}^0 / R_{Ra}^{Au}. \tag{4.10}$$

For the prototype source, an activity yield of

$$\epsilon_A > 95\% \tag{4.11}$$

has been found. The estimation of ϵ_A was performed without considering the different geometries and materials of the two source configurations before and after the treatment. In fact the estimated yield was close to 100%. However, given the screening results of the tools and the glovebox after the source preparation, a systematic activity uncertainty of 5% has been introduced.

In January 2010, two further custom sources were produced at PSI for the GERDA experiment. The coating procedure was performed twice on two separate 20 kBq $ThCl_4$ solutions. During this campaign, activity losses of over 65% were observed during the production of both sources. Because, the samples were prepared following exactly the same steps as during the production of the prototype source, a high ϵ_A sensitivity to environmental conditions has been concluded. Table 4.5 shows the activity yields of all three ThO_2 samples

produced at PSI. While the first source was produced without activity losses, the activity yields of the following two sources were $\sim$ 30%. The lost ^{228}Th activity has been found mainly on the caps of the V-vials, on the glovebox walls, in the used crucibles and on the tools which were used during source preparation. The wide, spatial distribution of the

Source	P02 prototype	Sample1	Sample2
Solution nominal activity [kBq]	20 $\pm$ 15%	20 $\pm$ 15%	20 $\pm$ 15%
Production date at PSI	19.3'09	13.1'10	13.1'10
Production activity yield [%]	> 95	33.2 $\pm$0.2	31.1 $\pm$ 0.2

Table 4.5: Overview of the three sources produced at PSI and their activity yields.

activity indicates for an aerosol-like spreading of the radio nuclides. Such conditions can be created by overheating of the solution in combination with electro-static effects and low humidity levels in the glovebox.

In order to recover as much activity as possible, the used equipment has been washed out with HNO_3 in several steps and processed again into an active gold sample. The step allowed to recover another 17 % of the initial 40 kBq activity. In total, three samples have been produced out of the two 20 kBq $ThCl_4$ solutions:

- sample 1: $\sim$ 6 kBq
- sample 2: $\sim$ 7 kBq
- sample 3: $\sim$ 7 kBq

Sample 3 has been produced out of the HNO_3 solution used to recover the activity losses on instruments in the glovebox.

All three samples were finally combined into one with an activity of $\sim$ 20 kBq. The combined source has been designated as **SV303** after encapsulation.

The motivation to develop a neutron flux limited ^{228}Th source was the reduction of the neutron induced background in the GERDA setup. For the same reason, the technique of the ^{228}Th deposition on gold drew the attention of the BOREXINO collaboration. BOREXINO, is an experiment investigating solar neutrinos. Same as GERDA, it is located at the LNGS underground laboratory. In contrast to the GERDA setup, BOREXINO requires a ^{228}Th source with an activity of several MBq for a sufficient signal to noise ratio. In the first instance, neutrons are not problematic for BOREXINO, because they can be discriminated efficiently due to neutron capture reactions in the scintillator with typical energies of $\sim$ 2.6 MeV [79].

However, the collaboration had to face administrative limitations on neutron emitting sources at LNGS. The reason for this limitations are possible negative interferences with adjacent experiments in the laboratory. Nuclear recoils of neutrons can mimic dark matter signals for example. As shown in chapter 3.2.1, calculations of neutron fluxes from a commercial ^{228}Th source resulted in rates of $\sim 1 \cdot 10^{-2}$ n/s/kBq for two example ceramics. Under such conditions, the operation of a 1 MBq ^{228}Th source would result in a neutron flux of ∼10000 n/s. Because, neutron sources can not be operated under normal conditions in the LNGS laboratory, the BOREXINO collaboration has decided to produce a neutron reduced ^{228}Th source, using the neutron reduction process described in this chapter. The production of a ThO_2 source on gold for the BOREXINO experiment was performed by Werner Maneschg in collaboration with the Paul Scherrer Institute in Villigen, Switzerland and with the Institut für Kernchemie in Mainz, Germany. For the production, an analogue setup as at PSI has been established at the Institut für Kernchemie. Considering possible activity losses as they occurred at PSI in two out of three cases, modifications of the procedure had to be done in order to drastically reduce the risk of high activity losses in the glovebox. To prevent radiation health damage during the production, the $ThCl_4$ treatment was performed in a shielded radiation containment chamber. Before the production took place in Mainz, tests concerning activity losses were done at PSI with the objective to reduce the risk of contamination of the setup on a MBq scale. In conclusion, following modifications of the treatment were introduced during the production of the BOREXINO source:

• Reducing the temperatures during the treatment. Thorium-nitrates formation should take place at a temperature of $\sim 115^oC$. ThO_2 formation at $\sim 650\ ^oC$.

• Covering the heater used for thorium-nitrates formation with an alumina foil and grounding it to prevent electrostatic charges.

• Covering the teflon crucible during thorium-nitrates formation.

• Reducing charging effects in the air and on the walls of the glovebox by including a reservoir of distilled water. This step increases humidity in the air.

• Washing out the glass vial for several times with HNO_3 and involve the elution into the process.

Another safety precaution was the production of a test sample in the modified setup before processing the 5 MBq $ThCl_4$ solution for BOREXINO. The test sample had an activity of about 20 kBq and was later handed over to the University of Zurich with the designation **SV304**. For the BOREXINO source a final activity yield of more than 91% could be achieved with the modified setup in Mainz. The production procedure and the results have been discussed and published in [80].

Source encapsulation

The first prototype source produced at PSI was sent for encapsulation to E&Z in Prague. The P02 encapsulation type used is shown in figure 3.2. For administrative reasons, the two further sources SV303 and SV304 were encapsulated at E&Z in Braunschweig. In consequence, the encapsulation type has changed from the P02 type to the VZ 3474 type which is an analogue stainless steel encapsulation with a height increased by 1.7 mm. The technical drawing of the VZ 3474 encapsulation is shown in figure 4.12. The internal setup

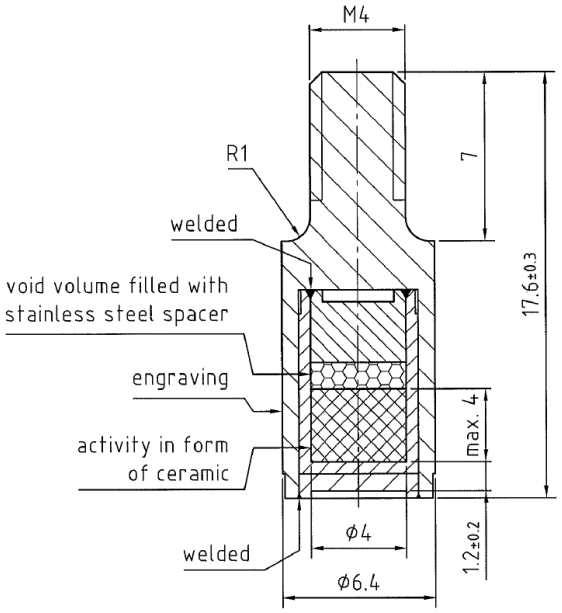

Figure 4.12: Schematic of the stainless steel VZ3474 encapsulation. Same as the P02 encapsulation it has a M4 thread and a stainless steel spacer to fix the activity in the inner volume. In total, the VZ3474 is 1.7 mm higher than the P02 capsule.

and mechanical strength of the VZ3474 capsule is fully equivalent to the P02 capsule. The type includes also a stainless steel spacer to fix the activity and is sealed by the same welding procedure.

4.3 Determination of the γ activity at UZH and IRMM

As described in section 4.2, the activity losses during the source preparation were ranging from $\sim$ 5% up to $\sim$ 70% in two cases. In the case of the sources produced at PSI, the activity yield has been determined on the ^{224}Ra peak, as it is not affected by the ^{220}Rn emanation. This procedure however, gives only relative activities. Absolute values could

be only determined using the nominal activities of the precursor $ThCl_4$ solutions with activity uncertainties of $\pm$ 15%. Furthermore, the geometries before and after the treatment have changed as well as the involved matrix materials. In order to estimate the absolute γ activities of the sources after preparation and after the encapsulation at E&Z, γ spectroscopy measurements were performed with two independent Ge detector setups:

1) **GeMini:** γ calibrations were performed in Zurich with the GeMini setup. Details of the detector and its operation will be described in the next chapter 5.

2) **IRMM:** γ calibrations were performed externally in collaboration with M.Hult et al. from the Institute for Reference Materials and Measurements (IRMM) in Geel, Belgium.

4.3.0.1 The GeMini Monte Carlo simulation and data comparison

The first calibration of the custom prototype ^{228}Th source has been performed in the laboratory of the University of Zurich using the GeMini detector, which operates a n-type HPGe crystal. The detector can be run in a standard vacuum-mode or immersed in a cryogenic liquid.

For the absolute γ activity determination, a full Monte Carlo simulation of the detector in vacuum mode was developed with the geometry as shown in figure 4.13. The simulation embraced detector-details like the crystal holder, the coldfinger, mechanical support structures and a dewar filled with nitrogen. The P02 encapsulation with an inner diameter of 2.5 mm has been composed of stainless steel with a density of 7.98 g/cm^3. The chemical composition of the steel implemented in the simulation is shown in table 4.6. The encapsulation contains the custom produced ^{228}Th gold sample which has been represented in the Monte Carlo geometry by a 100 μm thick gold sphere with an outer diameter of 2 mm. The ^{228}Th activity has been located at the center of the gold sphere as a point source. For the activity estimation, data with the custom ^{228}Th source have been taken at 55 mm

Element	Cr	Mo	Ni	Ti	Fe
Atomic fraction [%]	19.51	1.22	11.38	0.41	67.48

Table 4.6: Chemical composition of the stainless steel implemented in the Monte Carlo simulations for the P02 capsule.

above the endcap of the detector for 21 hours. The Monte Carlo simulation was performed in the same configuration with $240{\cdot}10^6$ ^{228}Th decays and an isotropic γ emission in 4π. The method of activity determination bases on the converging of the MC spectrum with the ^{228}Th data according to a minimal deviation given by the χ^2 value.

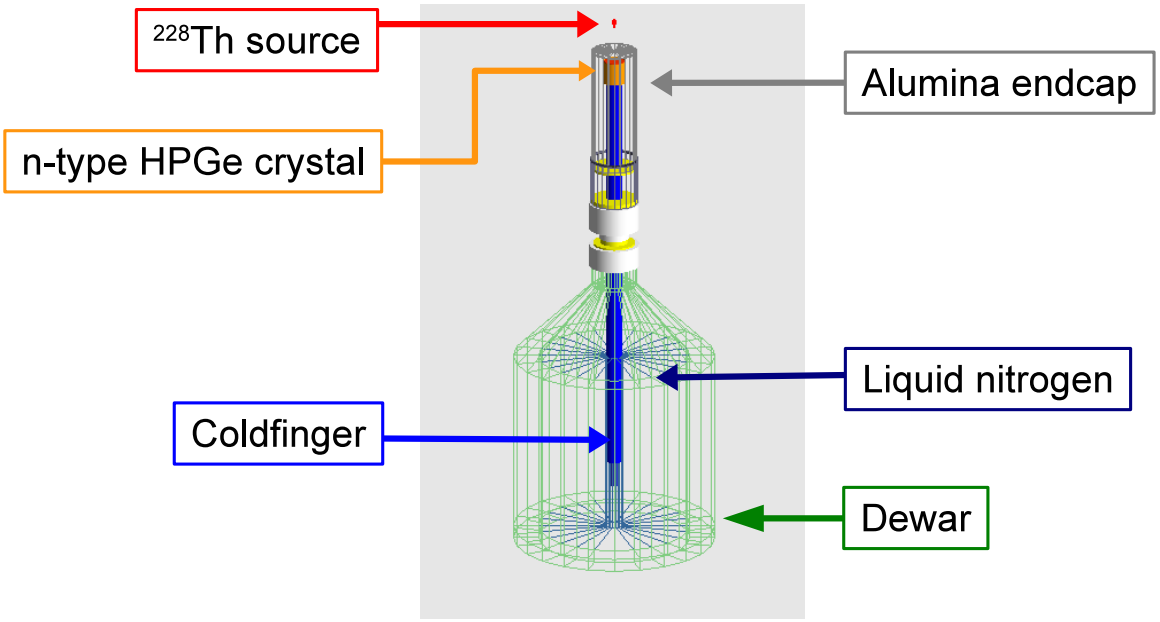

Figure 4.13: Geometry of the GeMini detector implemented in Geant4 to perform Monte Carlo simulations for the source activity determination.

Energy calibration of the MCA data has been performed using nine lines from the ^{228}Th decay. Furthermore, the measured peak resolutions σ_i were used to determine a function $\sigma(E)$ by linear interpolation. As shown in table 4.7, the single escape peak (SEP) of the ^{208}Tl decay at 2.1 MeV has the worst resolution of all lines considered with 3.7 keV. The exceptional low SEP resolution can be explained by the physical processes leading to the formation of the peak. Given the finite momentum of the e^-e^+ pair, induced by the 2.6 MeV γ interaction in germanium, the two annihilation γ's can differ in energy due to Doppler effects as described for example in [81]. In consequence a broadening of the energy measured is observable. This effect does not occur in the case of double escape peaks (DEP) or full energy deposition events.

In order to allow for a converging of both spectra, the determined energy resolution $\sigma(E)$ has been folded-in into the Monte Carlo data by randomizing the energy vector according to the normal distribution with the standard deviation $\sigma(E)$. Given the broadening of the single escape peak, the SEP line has not been considered in the $\sigma(E)$ interpolation, which results in an underestimation of the 2.1 MeV peak resolution in the Monte Carlo data. Because, the method of activity estimation compares the data spectrum and the spectrum generated by Monte Carlo simulations under the χ^2-test aspects, a lower resolution in one of the peaks will cause an increase of the absolute χ^2 value, but will not affect the position of the minimum in the χ^2 distribution.

To account for the background contribution, data have been acquired with the detector for 5.2 days without the ^{228}Th source. The calibrated and normalized background data

Peak/Isotope	γ energy [keV]	FWHM [keV]
^{212}Pb	238.63	1.47
^{212}Pb	300.09	1.73
^{208}Tl	510.77	2.23
^{208}Tl	583.19	1.93
^{212}Bi	727.33	1.74
^{208}Tl	860.56	1.88
DEP ^{208}Tl	1592.5	2.33
SEP ^{208}Tl	2103.5	3.69
^{208}Tl	2614.53	2.90

Table 4.7: ^{228}Th lines used for energy calibration of the data. The resolution of the SEP peak has not been considered due to its high value given by Doppler broadening during the SEP formation.

have been added to the Monte Carlo results, allowing for a comparison of data and Monte Carlo by the variation of an activity parameter.

Considering the MCA bin width bw of 0.36 keV/channel, the detector data Th_{Dat} have been normalized according to

$$Norm_{dat} = 1/T_{LT} \cdot bw \tag{4.12}$$

with the lifetime T_{LT}. The Monte Carlo data MC_{dat} were normalized under the assumption of a simulated source strength of $A_{MC} = 1$ kBq which can be translated into a simulated lifetime of

$$T_{MC} = N_{Sim}/A_{MC}, \tag{4.13}$$

with the number of simulated decays given by N_{Sim}. The norm factor $Norm_{MC}$ can be than expressed in an equivalent way by

$$Norm_{MC} = 1/T_{MC} \cdot bw. \tag{4.14}$$

The final Monte Carlo spectrum Dat_{MC} has been defined by a combination of the background data $Bckg_{dat}$, an activity parameter A and the MC data according to

$$Dat_{MC}(A) = (Bckg_{dat} \cdot Norm_{Bckg}) + (MC_{dat} \cdot Norm_{MC} \cdot A) \tag{4.15}$$

with the detector resolutions considered in MC_{dat}. The modeled spectrum Dat_{MC} has been compared with the normalized ^{228}Th data

$$Dat_{Th} = Th_{dat} \cdot Norm_{dat} \tag{4.16}$$

by variation of the activity parameter A and by determining the respective χ^2 values.

Figure 4.14 shows the Dat_{MC} spectrum brought into congruence with the Dat_{Th} spectrum. The activity parameter has been optimized according to the minimal χ^2 value defined as

$$\chi^2 = \Sigma_{i=1}^{N} \frac{(Dat_{Th} - Dat_{Estim})^2}{Dat_{Estim}} \tag{4.17}$$

where N is given by the number of energy entries in the considered energy interval. With the determined activity A_0 given by the minimal χ^2_{min} value, the error $\sigma_A^{\pm}$ on the activity estimation has been calculated according to

$$\chi^2(A^-) = \chi^2_{min}(A_0) + 1 \tag{4.18}$$

and

$$\chi^2(A^+) = \chi^2_{min}(A_0) + 1 \tag{4.19}$$

with $A^+ = A_0 + \sigma^+$ and $A^- = A_0 - \sigma^-$, which represents a confidence level of 68.3 %. Using the method described above an activity A_{P02} of

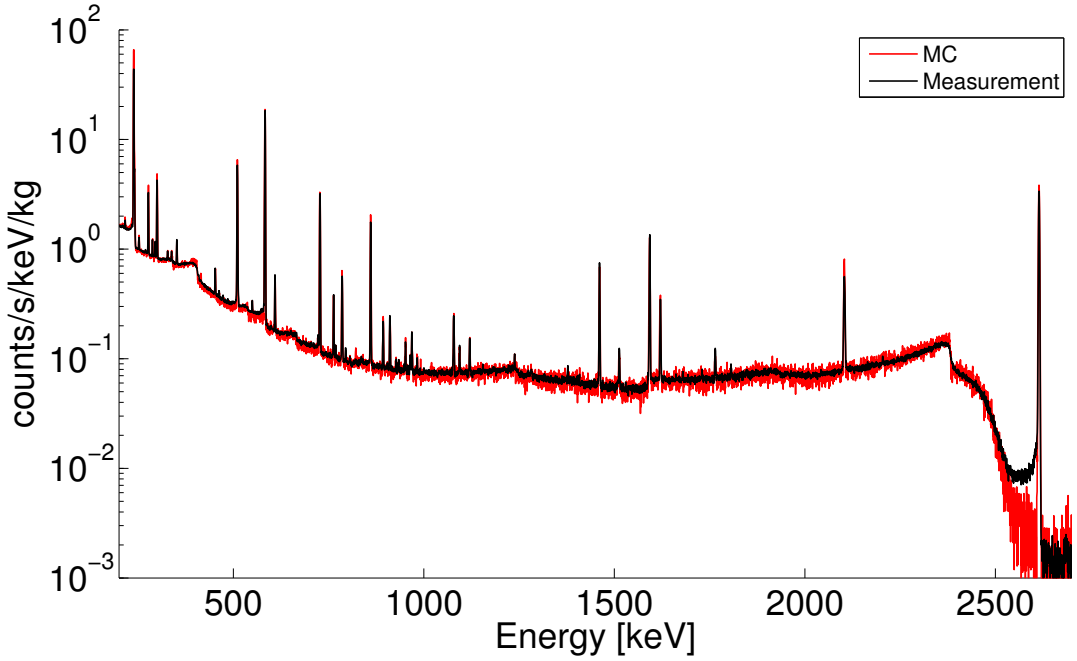

Figure 4.14: Activity estimation, based on the minimal χ^2 value between GeMini and Monte Carlo data, applied to the full spectrum.

$$A_{P02} = 18.53 \text{ kBq} \pm 2.7\% \text{ @ } 27.5.2009 \tag{4.20}$$

has been determined for the first prototype ^{228}Th source produced at PSI. The value is in good agreement with the nominal activity of the $ThCl_4$ solution of 20±15% kBq and an activity yield of $> 95\%$ during source production.

4.3.0.2 Results from γ calibrations at UZH and IRMM

The calibration method described above was used as a first approach to perform γ calibrations of the custom sources at the University of Zurich.
Further calibrations of the first prototype ^{228}Th source, but also of the two SV303 and SV304 sources produced afterwards at PSI and at the Institut für Kernchemie in Mainz were performed at IRMM in Geel, Belgium by M. Hult et al. Furthermore, a reference source was used to cross check the calibration method. The sources were calibrated using two germanium detectors and by taking data at three different source distances to the endcap. The detectors were located in a laboratory on the surface, but in contrast to the GeMini detector they were shielded in 4π with lead walls in order to reduce environmental background. Because the exact geometry of the gold samples and the stainless steel spacer used to fix the activity in the encapsulation are not known exactly, three different sample configurations with an iron content of 0%, 40% and 50% were simulated.

The source activities were determined using the model which resulted in the lowest activity spreads for each sample. In total eleven γ lines shown in table 4.8 were used to estimate the activity. Efficiency discrepancies between the detector setup and the Monte Carlo model of about 1.5% have been taken into account by an efficiency correction factor. Furthermore a coincidence summing correction, a branching factor correction and a chain

Peak/Isotope	γ energy [keV]
^{212}Pb	238.63
	300.09
^{224}Ra	240.99
^{208}Tl	277.37
	583.19
	763.2
	860.53
	1592.5
^{212}Bi	727.33
	785.37
	1620.74

Table 4.8: Lines used for the source activity estimation at IRMM.

equilibrium correction have been implemented in the data analysis. The final activity is given as the weighted mean of the activities determined for each peak. Table 4.9 shows the results for all three custom sources and the commercial reference source. The activity of the SK393 reference source determined at IRMM is consistent with the nominal activity provided by Eckert&Ziegler. The P02 activity determined with the GeMini detector in Zurich was overestimated by ca. 1 kBq. The overestimation may be a consequence of the correction factors introduced in the IRMM data analysis which were not applied to the

GeMini detector. Furthermore the calibration method used by IRMM based on an activity estimation applied to each of the eleven lines. In contrast, the GeMini calibration has been performed on the full spectra.

While the P02 source activity could be determined with an uncertainty of 3%, the activity spreads given by the calibration lines for the SV303 and SV304 sources were found to reach levels of about 7%. This concerns in particular, the SV303 source which has been produced out of three gold samples as described in section 4.2. The higher total gold mass introduced in the SV303 source implies a stronger γ attenuation which affects mainly low energy γ's. Furthermore, considering the limited space inside the capsule, the shape of the samples and the size of the spacer were not well defined in this case.

Therefore, a conservative uncertainty of 15%, consisting of a statistical and a systematic error has been introduced for the SV303 and the SV304 sources.

Reference date	1.1. 2011	1.1. 2011	1.1. 2011	1.1. 2011
Source	P02	SV303	SV304	SK392
Produced at	PSI	PSI	Inst. fuer Kernchemie	Eckert&Ziegler
Activity E&Z [kBq]	10.59 ± 15%	-	-	18.30±5%
Activity UZH [kBq]	10.37 ± 2.7%	-	-	-
Activity IRMM [kBq]	9.38±3.1%	18.09±15%	12.81±15%	19.02±3.1%

Table 4.9: Overview of the custom sources and their activities. The SK392 is a commercial reference source.

4.3.0.3 Leak and wipe tests

In general, all sources provided by Eckert&Ziegler, are extensively tested before leaving the manufactory site. The tests are mandatory and provide a consistent methodology for detecting source leakage and surface contaminations according to the ISO 9978 classification. The three custom sources produced for GERDA were encapsulated by Eckert&Ziegler and hence, they were subject to the standard testing procedures consisting of:

• **Immersion test:** The test allows to detect a leakage of the encapsulation and implies an immersion of the source in a suitable liquid at a temperature of 50 ^{o}C. The immersion takes place for at least four hours. Spectroscopic γ measurements of the liquid are performed before and after the immersion to detect the lost in activity.

• **Wipe test:** the test allows to detect surface contaminations. The wipes consist of a swab, moistened with ethanol or water and are screened with a γ spectrometer before

and after the testing to determine the net activity on the wipes.

The ISO classification (International Organization for Standardization) is a system applied to sealed radioactive sources which obligates the manufacturer to fulfill particular safety requirements. This includes the wipe and immersion tests described above. Sources pass the tests if the net activity levels fulfill the ISO 9978 criteria given by:

- Immersion test: activity limit $\leq$ 200 Bq
- Wipetest: activity limit $\leq$ 200 Bq

Besides the activity tests, the two encapsulation types P02 and VZ3474 have been tested in terms of mechanical and thermal stability. Both fulfill the C66646 ISO norm [70], ensuring a safe operation under the conditions given in table 4.10. However, the stan-

Test	minimal encapsulation performance
Temperature	-40°C - 800°C and thermal shock 800°C - 20°C
External Pressure	25 kPa absolute to 170 MPa absolute
Impact	20 kg from 1 m
Vibration	3x30 min 25-80 Hz at 1.5 mm amplitude peak to peak and 80-2000 Hz at 20 g peak amplitude
Puncture	1 kg from 1 m

Table 4.10: Tests which are performed on encapsulation-types classified as C66646.

dard tests performed by Eckert&Ziegler do not embrace conditions as they occur in the GERDA experiment with operational temperatures down to -185^{o}C given by the liquid argon. Therefore, the P02 encapsulation (equivalent to the VZ3474 type) has been tested at the University of Zurich in liquid nitrogen at -196^{o}C. The source has been enfolded in a filter paper sheet which was immersed in liquid nitrogen for about 10 minutes. Before the immersion test, surface wipes were taken using the same type of filter paper moistened with ethanol. In addition, wipe tests of an empty P02 encapsulation have been taken to provide a further reference measurement.

The test wipes and two unused reference wipes were shipped to the LNGS laboratory for screening with the GATOR detector. The high purity germanium detector is located underground with $\sim$ 3200 m w.e. overburden and has been explicitly designed for the screening of low radioactivity components. The setup includes a lead shield of 20 cm wall thickness, a nitrogen flushed glovebox and a lubricator to introduce the samples. Background rates of the detector range from 1.3 counts/day for the ^{214}Bi line at 1.12 MeV down to 0.13 counts/day for the ^{212}Pb line at 239 keV [82].

A net activity of the screened samples could not be detected with the GATOR setup, resulting in an upper limit of the ^{228}Th activity of

$$A_{wipe} < 1 \text{ mBq} \tag{4.21}$$

per wipe at a confidence level of 95 %. The measured value is five orders of magnitudes below the limit of 200 Bq required by the international ISO standard for neutral samples. Because no traces of surface contamination or source leaking caused by the immersion in liquid nitrogen could be found, the encapsulation type can be regarded as safe in terms of the operation under cryogenic conditions.
Further wipe tests of the two custom sources SV303 and SV304 as well as of the SK393 commercial source were performed and resulted in the same activity limit as given in (4.21).

Although no surface contamination has been detected on the ^{228}Th sources, an additional ^{137}Cs line as shown in figure 4.15 was found in the spectra of the SV303 and the SV304 sources with an activity of about 2 kBq. Even though, the ^{137}Cs line is not dangerous for

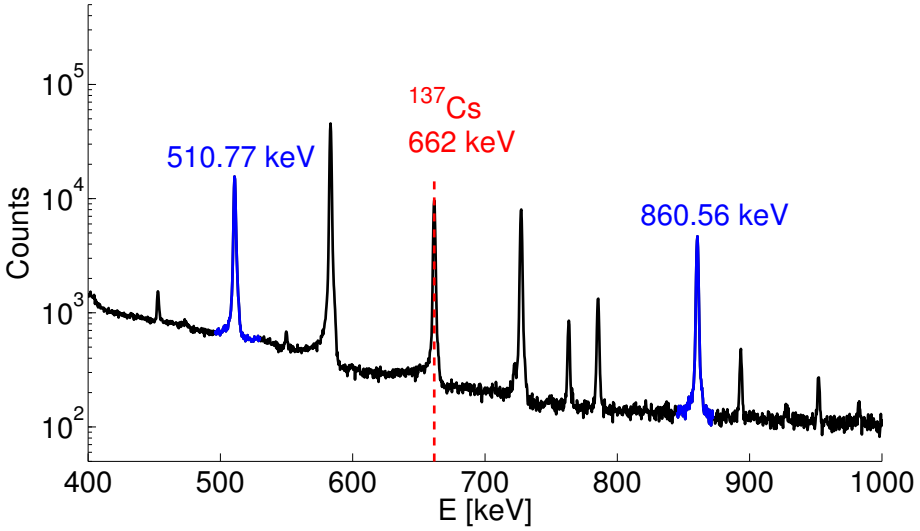

Figure 4.15: ^{137}Cs line at 662 keV, found in the two custom ^{228}Th sources - SV303 and SV304.

the double-beta decay search at energies of about 2 MeV, the origin of the ^{137}Cs contamination had to be understood to prevent a possible uncontrolled introduction of radioactive nuclides to the GERDA setup. In order to track down the origin of the ^{137}Cs isotope, ^{228}Th spectra have been compared, which were acquired at different stages of the source history. Of particular interest were spectra of the initial $ThCl_4$ solution, after the preparation of the gold sample and after the source encapsulation at Eckert&Ziegler. Because the ^{137}Cs peak has been found in two sources which were produced at two different laboratories, namely at PSI (SV303) and at the Institut für Kernchemie in Mainz (SV304), a cross contamination during the encapsulation process at Eckert&Ziegler has been suspected. The scenario is

confirmed by the data shown in figure 4.16, which shows the SV303 spectra at different locations and times. An equivalent picture is given by the SV304 data. The ^{137}Cs peak

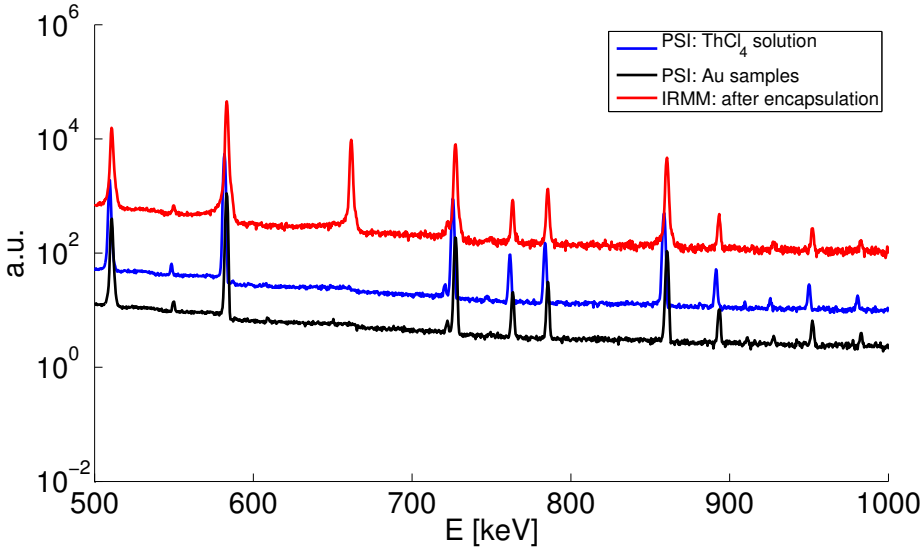

Figure 4.16: Tracking back of the ^{137}Cs contamination. While the initial $ThCl_4$ solution and the prepared gold samples do not show any ^{137}Cs tracks, the line appears directly after the gold sample encapsulation at E&Z.

appears only in the spectra acquired after the source encapsulation has been performed. Therefore it can be concluded, that the internal contamination has been introduced during the encapsulation process by Eckert&Ziegler. Surface wipe tests performed directly after the encapsulation and later at the GATOR facility exclude the possibility of a posterior surface contamination. Furthermore, the possibility of cross contaminations with other radionuclides during the encapsulation process has been confirmed by Eckert&Ziegler.

Given the low energy of the ^{137}Cs peak and its presence inside the encapsulation rather than on the surface of the encapsulation, the ^{137}Cs contamination can be regarded as irrelevant for the GERDA physics runs.

4.4 Summary

Motivated by SOURCES4A calculations which were performed to estimate the neutron flux from commercially available ^{228}Th sources, a technique has been developed in order to suppress the (α, n) channel. The technique bases on the deposition of ^{228}Th and its daughters on gold which has higher threshold energy for (α, n) reactions than the maximal α energy emitted by the ^{228}Th chain. The product of the deposition is ThO_2 embedded in a gold foil. Calculations of the oxygen contribution in (α, n) reactions resulted in a neutron

flux of

$$R_{(\alpha,n)}(\mathrm{ThO_2}) = 2.19^{+0.99}_{-0.51} \cdot 10^{-4} \text{ neutrons/s/kBq} \tag{4.22}$$

which is two orders of magnitude lower than expected for commercial sources. The contribution from zirconium carriers which are added to the $ThCl_4$ precursor solution has been estimated by calculating the (α, n) cross sections for all stable Zr isotopes using the EMPIRE code and by implementing the cross sections into the SOURCES4A libraries. With a neutron flux of

$$R_{(\alpha,n)}(\mathrm{Zr}_{nat}) < 1.1 \cdot 10^{-5} \text{ neutrons/s/kBq}, \tag{4.23}$$

the contribution is one order of magnitude lower than for ThO_2 and hence, further steps to remove the zirconium from the solution have not been implemented in the production process. The custom ThO_2 sources were produced at PSI, Villigen in Switzerland and at the Institut für Kernchemie in Mainz, Germany. Encapsulation of the active gold samples was performed by Eckert&Ziegler. First activity calibrations of the sources were performed with the GeMini detector at the University of Zurich and were continued by IRMM in Geel in Belgium. In total, three custom sources were produced with an initial activity of $\sim$20 kBq each.

Chapter 5

The GeMini detector

The GeMini (Gerda Mini setup) detector has been setup at the University of Zurich and was used for the calibration of the first custom ^{228}Th source as discussed in section 4.3. The experimental setup will be described in more detail in this chapter. The detector consists of a high purity, n-type Ge crystal in a coaxial, closed-end configuration as shown in figure 5.1 and has been produced by Canberra Lingolsheim in France. The dimension of the crystal is 40 mm in diameter and 40 mm in height with a mean dead layer of 0.5 mm as was given by Canberra, [83]. The full-depletion bias voltage can be estimated by

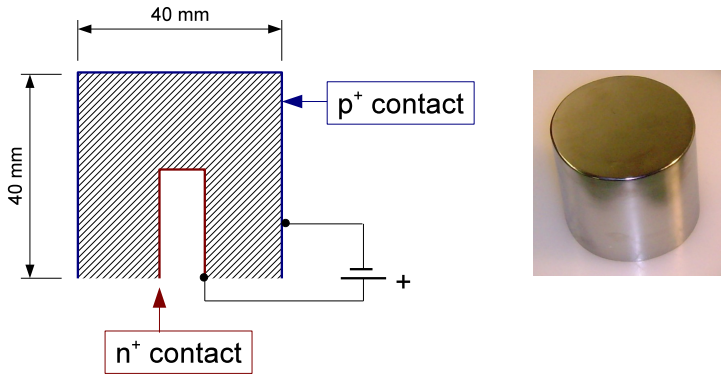

Figure 5.1: Left: scheme of a coaxial Ge n-type crystal. Right: naked coaxial Ge crystal of the same type as used in the GeMini setup.

$$V_{bias} = \frac{R_{det}^2 \cdot e \cdot N_D}{2 \cdot \epsilon} \tag{5.1}$$

where R_{det} is the crystal radius, e is the electrical charge, N_D is the donator net-concentration in the crystal and ϵ is the dielectric constant in germanium. With a typical donator concentration of $\sim 10^{10}$ atoms/cm^3 and a depletion thickness of 20 mm given by the radius of the crystal, equation (5.1) leads to a full-depletion voltage of

$$V_{bias} = 2.3 \text{ kV} \tag{5.2}$$

which is in good agreement with the operational bias voltage of ∼3 kV recommended by Canberra. The detector has been originally designed to be operated in a standard vacuum configuration with the cooling performed by a cold finger dipped in liquid nitrogen. For the operation at the University of Zurich, the detector has been modified by Canberra such that it can be disassembled into a configuration which allows to operate the Ge crystal directly immersed in a cryogenic liquid. In this mode the crystal is naked and unprotected but it allows to mimic the conditions similar to those given by the GERDA experiment on a minimalistic scale. The germanium crystal is mounted in an alumina holder which acts also as an infrared shield. It is thermally coupled to the cold finger by a dismountable copper belt. In the standard vacuum operation mode, the cold finger is dipped in liquid nitrogen and the detector mounted on a dewar. The crystal itself is enclosed and sealed in an evacuated alumina cylinder (endcap) with a wall thickness of 1 mm. The operational pressure inside the endcap is $\sim 4 \cdot 10^{-6}$ mbar. Figure 5.2 shows the detector in a standard operation configuration without being mounted on a dewar. The vacuum pump connector

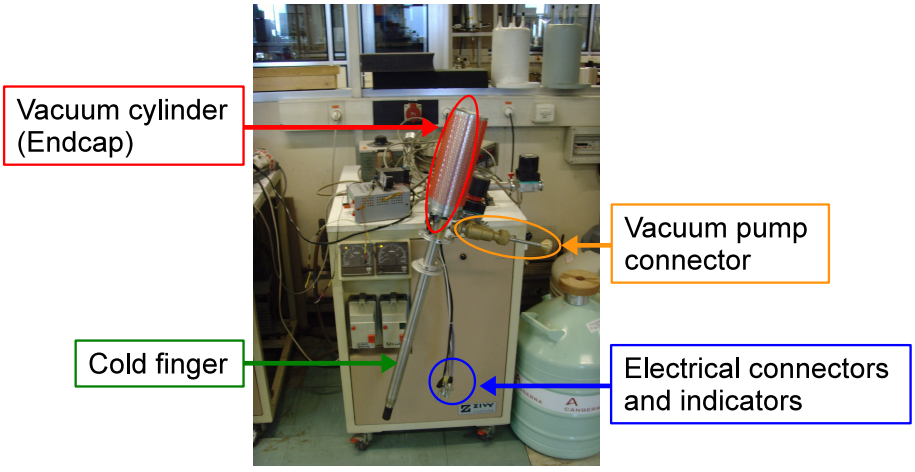

Figure 5.2: GeMini detector in a standard vacuum configuration. The inner volume of the endcap is connected to a turbo pump for evacuation. Cooling takes place via the coldfinger dipped in a cryogenic liquid.

is a dismountable piston which allows to operate the vacuum valve below the endcap and to connect the inner volume to a turbo pump. The electric connectors include the cabling for the power supply, pre-amplifier, high voltage contacts, testsignal input, two signal outputs, crystal temperature readout and two control LED's. The LED's indicate a critical status of the FET and of the crystal temperature.

The first stage signal amplification is performed by a PSC823 charge amplifier from Canberra. The preamplifier board is mounted directly under the endcap and is operated at room temperature. However, to improve the noise- and resolution- performance, the FET and the feedback resistor of the PSC823 amplifier are mounted on the cold finger in the direct vicinity of the crystal. Furthermore, the vacuum volume contains a heat resistor, to be used during the warm-up procedure of the detector and a PT100 element to control the

temperature of the crystal.

Figure 5.3 shows the internal setup of the detector after breaking the vacuum and after the endcap has been dismounted. The original position of the endcap is indicated by the dashed lines. The picture shows the top surface of the Ge crystal which is mounted in an alumina holder. Bore holes in the holder prevent air trapping during runs in immersion mode. In the standard vacuum mode, the boreholes are closed by a conductive tape in order to sustain the additional infrared shield functionality. A copper belt below the holder, which is fixed with two clamps acts as thermal coupling between the coldfinger and the crystal. To operate the detector in immersion mode, the thermal coupling has to be

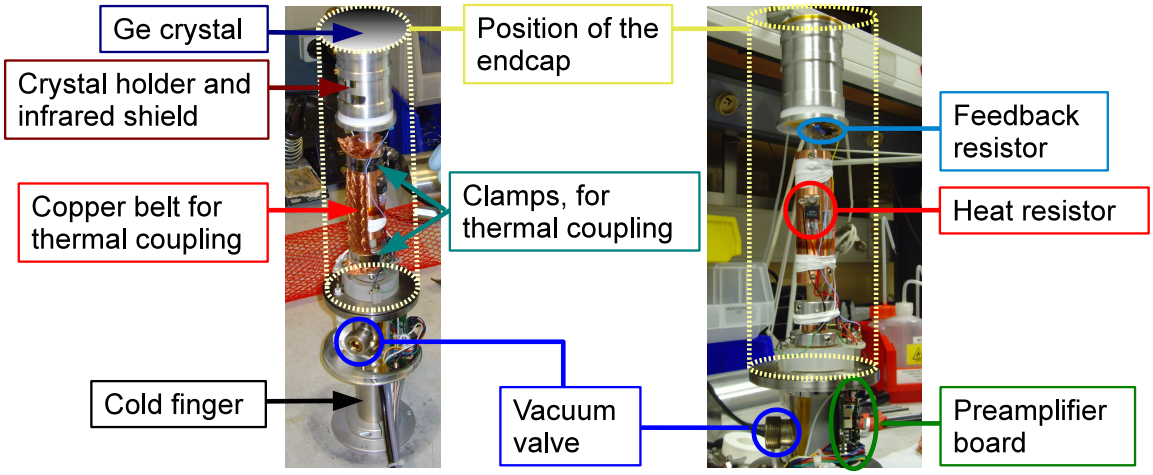

Figure 5.3: Left: internal setup of the GeMini detector with the thermal coupling mounted. Right: dismounted thermal coupling for the operation of a naked crystal. The white teflon tapes must be removed before immersion.

removed by dismounting two clamps. The uncoupling prevents losses of the cryogenic liquid through heattransfer to the cold finger which has no cooling function in the immersion mode. To prevent damage of the electrical connections, the cables are fixed with teflon bands which are wrapped around the coldfinger stem. All internal cables are connected to a base, which passes the cables to the preamplifier board through a vacuum sealed feedthrough. The connector base and its layout is shown in figure 5.4 with the following pin designation:

(1) High voltage connection. The negative operational voltage of the detector is -3 kV.

(2) Pt100 temperature control element of the crystal. The status of the Pt100 is monitored by the preamplifier mainboard.

(3) The source channel of the cold FET which is mounted in the vicinity of the crystal.

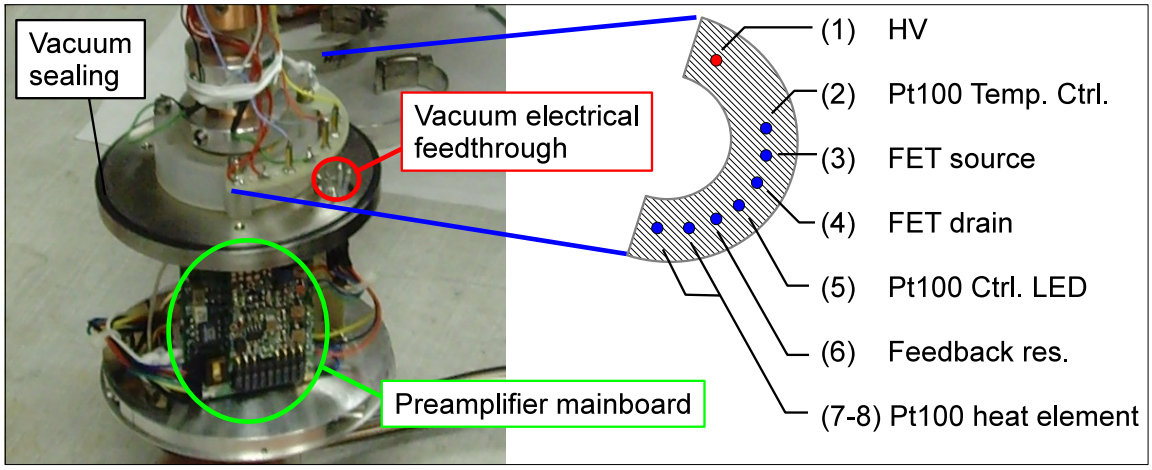

Figure 5.4: Pin designation of the base and the electric feedthrough of the GeMini detector. In the standard vacuum mode, the base is covered by the evacuated endcap.

(4) The drain channel of the cold FET.

(5) Connection to the control LED indicating a critical temperature at the crystal.

(6) Connection to the feedback resistor of the PSC823 preamplifier. The resistor is mounted below the crystal.

(7,8) Connectors to the Pt100 heat element used for the warm-up procedure of the crystal.

In the following the operation in the standard vacuum mode will be discussed.

The vacuum operation mode

For the standard running mode of the GeMini detector in vacuum, the thermal coupling must be mounted and the cables within the vacuum volume must be fixed with a teflon tape. After the endcap has been mounted and fixed on the base using two clamps, the endcap must be evacuated. For the pump-out procedure, a VOP10 vacuum operator from Canberra has to be connected to a valve located below the endcap. The VOP10 operator is a mechanical part consisting of a moveable piston to operate the vacuum valve on the detector. It includes a KF25 flange for the pump connection and a ring attachment which allows to mount the VOP10 on the detector.

After evacuation of the pump line, the VOP10 operator is used to open the valve and to evacuate the endcap until an operational pressure of

$$P_{op} \leq 10^{-6} \text{ mbar}. \tag{5.3}$$

Once the operational pressure has been reached and the valve closed, the VOP10 can be deattached and the vacuum line dismounted. At this stage the detector is ready for cooling. The frontend electronics board located below the endcap can be additionally protected by a dismountable alumina cylinder. The cylinder prevents ice formation on the electronics during cooling and protects against mechanical impacts from outside. Cooling of the GeMini setup is performed by a 100 l dewar filled with liquid nitrogen. An intermediary teflon part shown in figure 5.5, located between the base of the detector and the dewar has been designed, allowing a nitrogen refilling without the need of dismounting the detector. Furthermore, a Pt100 holder has been implemented in the design for monitoring of the liquid nitrogen level in the dewar. The teflon interface is mounted on the neck of the

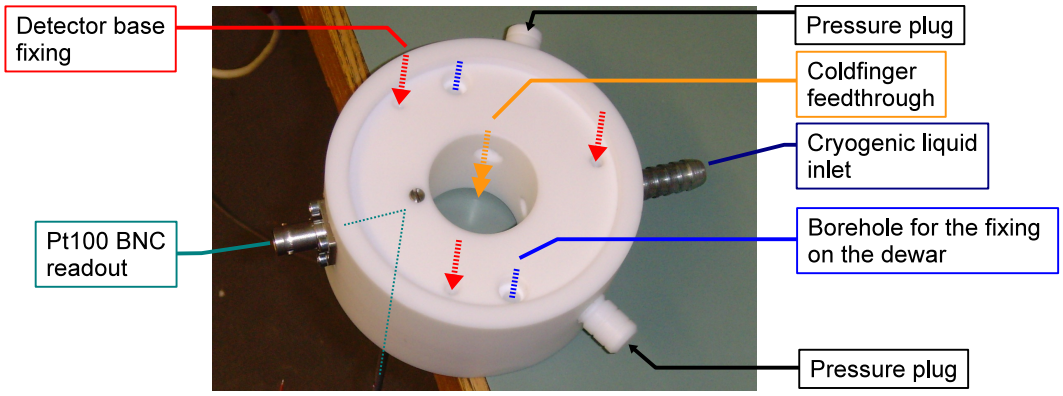

Figure 5.5: Top view of the teflon interface used for the refilling of the dewar and for the readout of the nitrogen level. The component is mounted on top of the dewar and has a socket on top for the base of the detector.

dewar and fixed with two screws. The detector fits into a socket on top of the interface and can be fixed with three screws from the top. The inlet for the nitrogen is connected to a tube which redirects the liquid downwards. To prevent overpressure, two plugs are available which can be removed during refilling. A third plug allows to close the inlet once the detector is cooled down and the dewar refilled. For the monitoring of the temperature and of the nitrogen level in the dewar, three Pt100 elements connected in series are used. A vertical tube mounted on the bottom side of the interface acts as the Pt100 holder and as a cable feedthrough to the BNC readout connector.

A second teflon piece shown in figure 5.6 has been designed for further thermal isolation of the coldfinger part between the base of the detector and the bottom side of the endcap. The part consists of two halfmoon shaped pieces which can be mounted around the open coldfinger section. In addition, the part acts as a holder for a BNC connector which is used for the monitoring of the leakage current of the germanium crystal. Further details about the readout of the liquid level and of the leakage current will be given in section 5.2.

The immersion operation mode

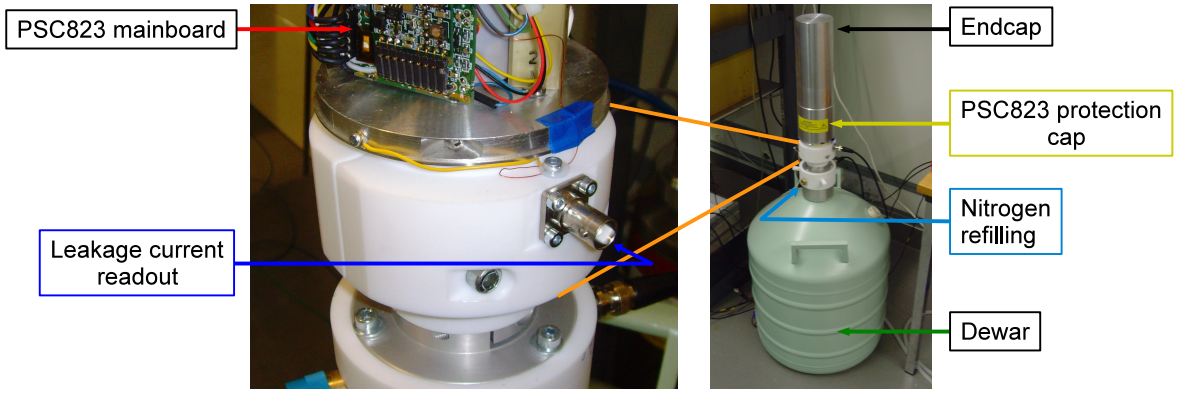

Figure 5.6: Left: Teflon part for additional thermal isolation with an integrated BNC connector for the leakage current measurement. Right: Fully mounted GeMini detector, ready for use in vacuum mode.

The design of the GeMini detector allows to operate the Ge crystal unprotected, directly immersed in a cryogenic liquid. To change the detector configuration into the immersion mode, the detector must be at room temperature or higher in order to avoid ice formation on the crystal. Furthermore, the detector must be removed from the dewar. Before dismounting the endcap, the vacuum must be broken which is performed with the VOP10 operator described above. Nitrogen flushing through the KF25 of the VOP10 can be performed during this procedure as a protective sanction. To allow for a safe handling of the

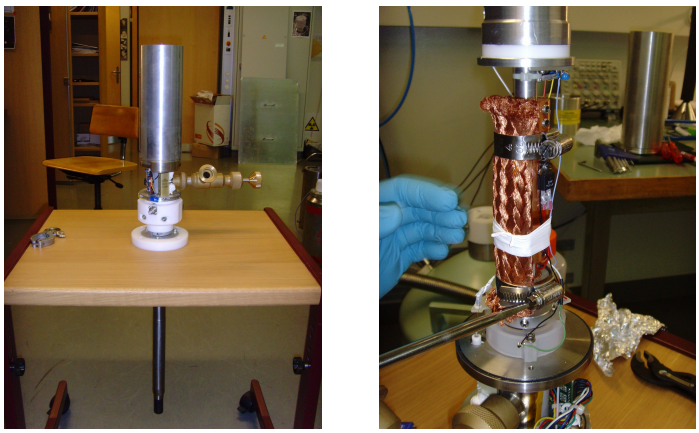

Figure 5.7: Left: GeMini detector mounted on a mobile bench used to assemble and disassemble the detector. Right: Removing of the thermal coupling by untightening of two clamps. The coupling must be removed if the detector is run in immersion mode.

setup during reconfiguration, a mobile bench as shown in figure 5.7 has been designed, allowing to fix the detector in a teflon socket with a feedthrough for the coldfinger in a vertical bearing. After removing of the endcap, the thermal coupling copper belt must be deattached by opening the two clamps shown on the right side of figure 5.7. The teflon

tapes which are used to fix the cables must be removed too. For the operation in the immersion mode, a 5 ltr. dewar has been designed and provided by Canberra with special regard to the warm-up procedure in order to prevent ice formation on the crystal. The dewar, shown in figure 5.8 includes plug-ins for nitrogen gas flushing which must be permanently performed while warming-up. A heating resistor mounted on an alumina socket at the bottom of the dewar is used to minimize the heating time. Furthermore, a Pt100 temperature sensor located on the bottom of the dewar is used to monitor the temperature. Cables from the heater and the Pt100 resistors are fed through a tube to a connector

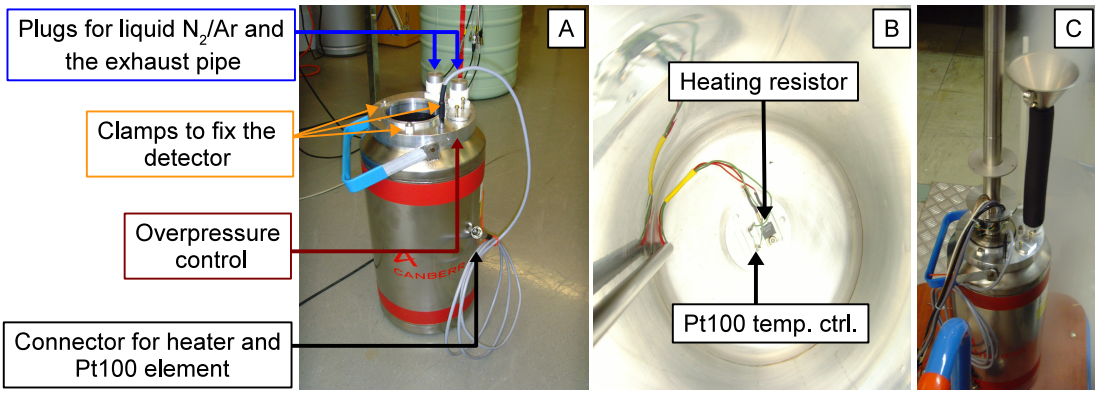

Figure 5.8: A: Five liter dewar used to operate the GeMini detector in immersion mode. B: Inside view of the dewar showing the alumina base with the heat resistor and the Pt100 element. C: Immersed detector and cooling down procedure.

located outside the dewar. To run the detector in immersion mode, the dewar must be filled with liquid nitrogen or argon up to a level of ∼15 cm below the upper flange. After thermal equilibrium has been reached, the dismounted detector can be immersed upside down into the cryogenic liquid and fixed with three clamps on top of the dewar. To reduce sputtering of the cryogenic liquid during immersion, a funnel can be introduced in one of the gas flushing plugs. The funnel can be additionally used to refill the dewar. To prevent ice formation on the unprotected frontend electronics, a heat gun should be used during the crystal cooling. The dewar allows to operate the detector for about 30 minutes. If needed, refilling can be performed using the funnel described above, otherwise the warm-up procedure must be initialized.

Warm-up procedure

For the warm-up procedure of the immersed crystal, a drainage pipe must be mounted on one of the two N_2/Ar plugs on the dewar and a constant nitrogen gas flow through the second N_2/Ar plug established. Given the overpressure in the dewar, the liquid nitrogen drains through the pipe into a second retention dewar. While draining, a constant gas flow of

$$\phi_{drain} \sim 4 \text{ ltr./min.} \tag{5.4}$$

should be assured. Once the dewar is empty, the gas flow can be reduced to

$$\phi_{flush} \sim 2 \text{ ltr./min.} \tag{5.5}$$

and sustained until the crystal reaches room temperature. Heating during the nitrogen flush is performed by two resistors located on the crystal holder and on the bottom of the dewar. Both are connected to a temperature control- and monitoring- unit. The bottom of the dewar is heated at a temperature of

$$T_{bottom} \sim 25^o\text{C} \tag{5.6}$$

while the heat resistor on the crystal holder is kept at

$$T_{det} \sim 35^o\text{C} \ (\sim 0.4 \text{ A at } 12 \text{ V}). \tag{5.7}$$

The temperature of both resistors should never reach more than 75 ^{o}C. Once the temperature of the detector reaches ∼35 ^{o}C, another heating period of ca. 30 min should follow while the dewar is still flushed with gas nitrogen. After warming-up, the gas flow can be stopped, and the detector mounted on the mobile workbench to be reassembled into the standard vacuum configuration. The cables within the endcap must be fixed again with a teflon tape, the copper thermal coupling has to be mounted and finally the detector must be covered with the endcap. Reassembling of the detector and evacuation should take place

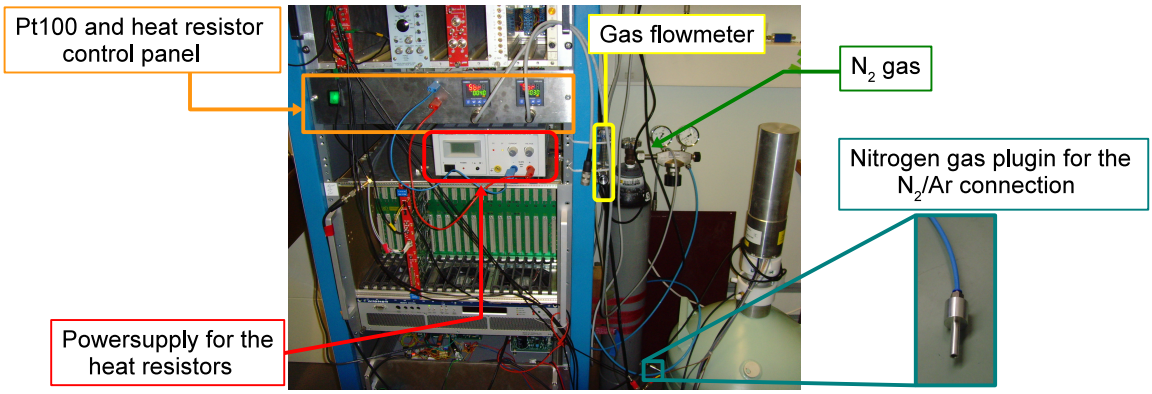

Figure 5.9: Setup used for warming-up of the detector after the operation in immersion mode. A control panel allows to monitor the PT100 temperatures on the crystal and in the dewar. The power supply is used together with two heat resistors. A constant gas nitrogen flow is assured by the nitrogen bottle and a flowmeter.

as fast as possible in order to avoid oxidation and impurities on the crystal. Any contact between the crystal and the dewars walls or the endcap must be avoided.

For the warm-up procedure a control setup has been assembled and integrated in the DAQ rack as shown in figure 5.9. The warming-up system consists off a:

• Voltcraft, PS 1302D regulated DC power supply for the heating.

• Panel with two EMKO ESM4450 process-controller for temperature regulation and temperature monitoring.

• Flowmeter from Kobold with a range of 0-10 ltr/min

• Nitrogen gas bottle

The process-controller is responsible for a constant temperature of both heat resistors (see fig. 5.10) which are powered by the external power supply. The nitrogen gas line leads through the gas flow meter and ends at an alumina plugin which has been designed to fit the N2/Ar plugs on the dewar. A schematic view of the warm-up system is shown in figure 5.10.

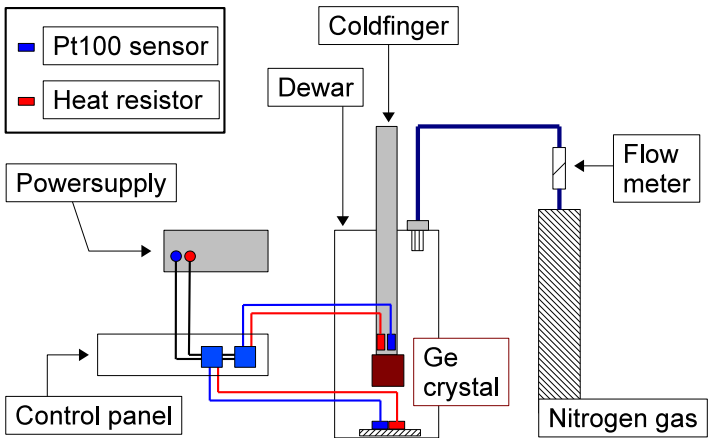

Figure 5.10: Schematic view of the setup designed to warm-up the GeMini detector after operation in immersion mode.

5.1 The GeMini DAQ (Data Acquisition)

DAQ part I:

The DAQ of the GeMini detector has been designed to perform spectral measurements and to allow additionally for pulse shape acquisition. In the following, an overview of the full cabling set of the detector will be given. The connectors include also the readout of the crystal temperature sensor which is implemented in the slow control described in section 5.2:

• **1x NRK200 connector:** used for the Pt100 temperature sensor and for the internal heat resistor

- **1x BNC in:** test signal input for the preamplifier
- **2x BNC out:** two identical detector signal outputs
- **1x SHV:** high voltage connector
- **1x 9 pin sub-D:** power supply connector for the preamplifier
- **2x LED:** used for the FET and temperature control

The cabling as well as the pin assignment of the NRK200 connector and the preamplifier power supply are shown in figure 5.11.

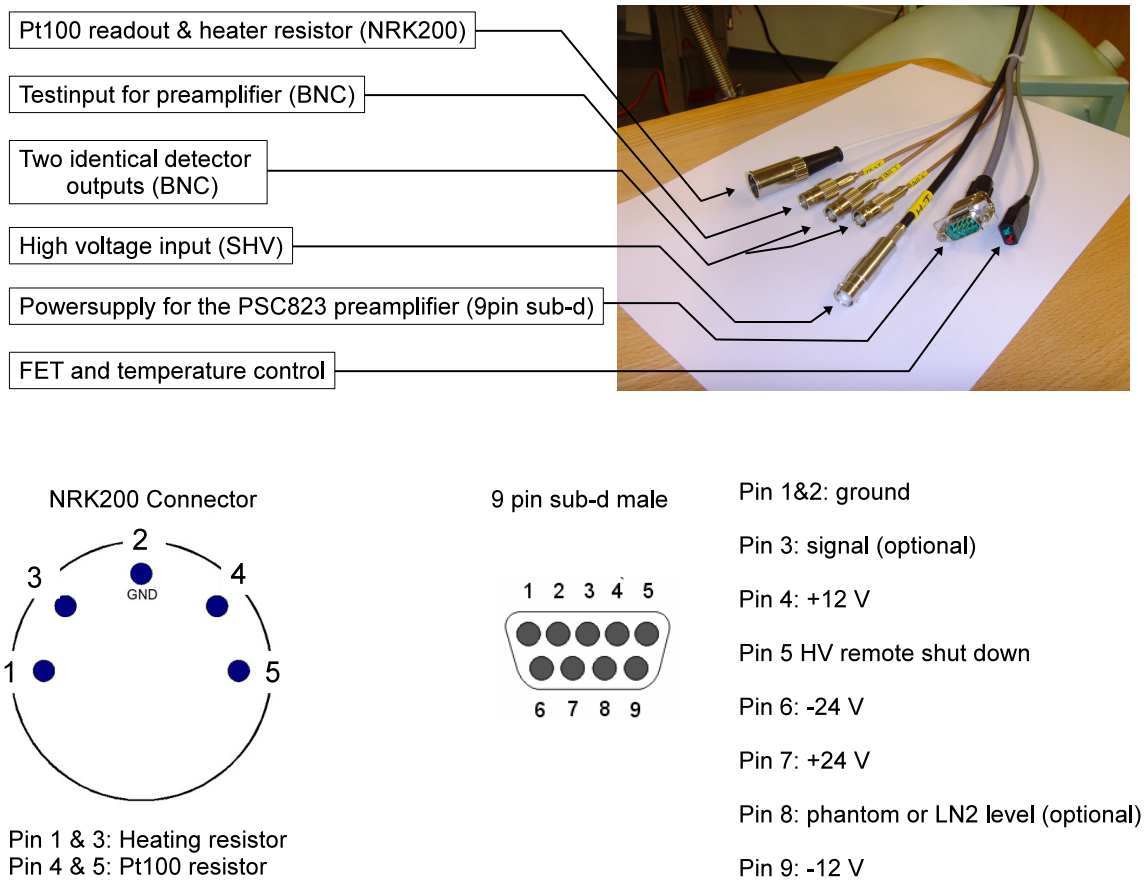

Figure 5.11: Top: Cable and connector designation of the GeMini detector. Left bottom: NRK200 pin assignment for the Pt100 connection and the heat resistor. Right bottom: Pin assignment for the sub-D power supply connector of the PSC823 preamplifier.

For the spectroscopic measurements, the detector signal outputs are connected to a shap-

ing amplifier, followed by a 8k MCA. The full spectroscopic chain consists of the following modules:

• PSC823 charge preamplifier with a cold FET from Canberra. The preamplifier is permanently fixed on the detector.

• Dual high voltage power supply from Canberra, model 3125 with a range of up to 5 kV negative or positive voltage.

• N968 shaping amplifier from CAEN with a gain range of up to 3000 and an output dynamic of 0 to 10 V.

• N957, MCA from CAEN with a 0 - 10 V input dynamic, 8k channels resolution and an USB interface.

All modules besides the PSC823 preamplifier are single width NIM modules. On the back panel of the N968 shaping amplifier, a nine pin sub-d output is available which has the same pin assignment as shown in figure 5.11. It is used therefore as the power supply for the preamplifier. Two positive signal outputs of the PSC823 preamplifier, designated as *outE* and *outT* are available. Both are equal and can be used for the monitoring of the signals and for taking data simultaneously. The spectroscopic chain is schematically illustrated in figure 5.12. One of the detector signal outputs is connected to the shaping

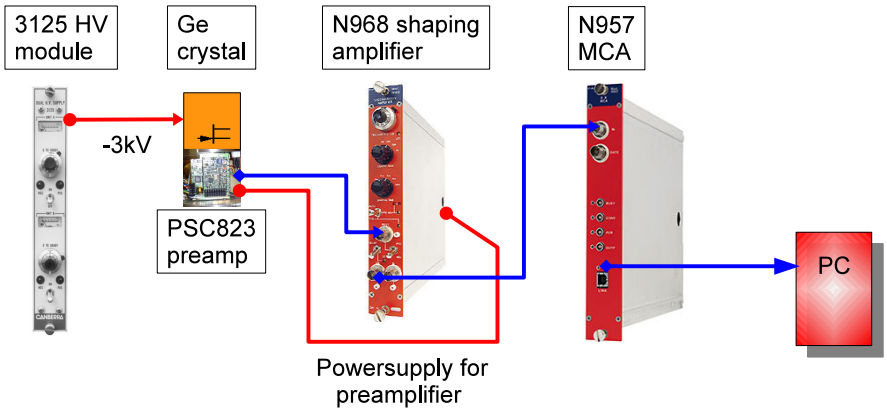

Figure 5.12: Scheme of the DAQ chain to perform spectroscopic measurements with the GeMini detector.

amplifier with a shaping time of $\sim 1\mu$s and a coarse gain of 50. The resulting quasi-gaussian pulse from the shaping amplifier is transferred to the MCA, which is connected via USB to an acquisition PC.

Figure 5.13 shows an example of the spectra taken with a ^{60}Co source during a run in immersion mode. The channel calibration has been performed on the two ^{60}Co lines at

1173.2 keV and 1332.5 keV and on the potassium line at 1460.8 keV. Table 5.1 shows the

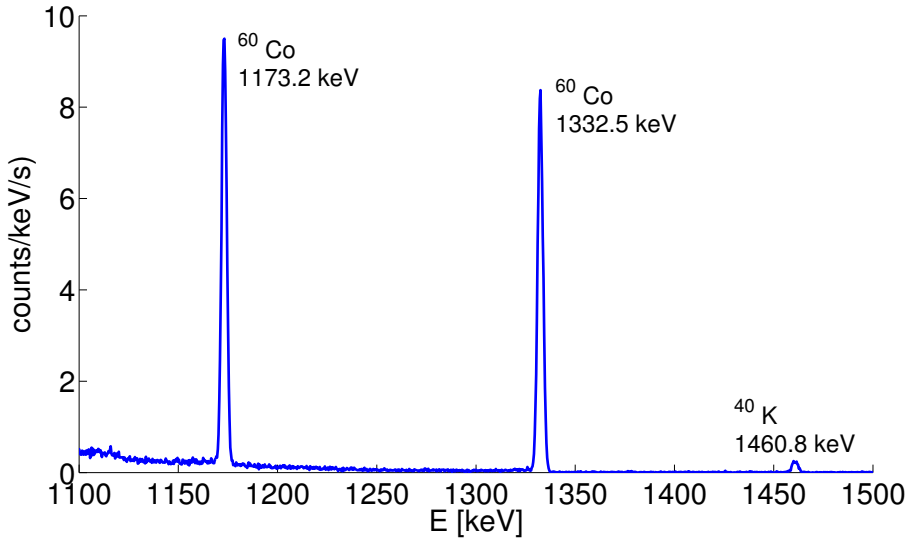

Figure 5.13: ^{60}Co spectra taken with the GeMini detector in immersion mode.

resolutions in FWHM as determined with the GeMini setup at UZH in comparison with a value for the 1173 keV line as reported by Canberra. The resolution of the 1173 keV line taken with the CAEN setup at UZH is worse by a factor of two with respect to the value reported by Canberra. The N957 MCA has a resolution of 13 bit given by 8192 channels, while the MCA used by Canberra had a twice better resolution of 14 bit with 16384 channels. However, the twice worse resolution can not be fully explained by a higher

^{60}Co line	FWHM [ch]	FWHM [keV]	MCA
1173 keV [UZH]	11.31	4.2	N957, 8k, CAEN
1332 keV[UZH]	11.88	4.42	N957, 8k, CAEN
1173 keV[Canberra]	-	2.1	Multiport II, 16k, Canberra

Table 5.1: Comparison between the GeMini resolutions provided by Canberra and the measured values at the University of Zurich.

MCA channel number. Acquiring the data in constant time intervals with the 8k MCA revealed an unstable behavior of the N957 MCA as shown in figure 5.14 for the 1332 keV line of ^{60}Co. The spectra were acquired in one minute intervals and show a drifting in time of the peak positions, which leads to a broadening of the lines in the summed up spectra. An energy dependence of the peak drifts could not be found and in principle an off-line correction for each time interval can be performed to remove the drift. The procedure requires to determine the peak positions for each time interval and to apply a shift in channel relative to a reference time frame. Figure 5.15 shows the same data set for the

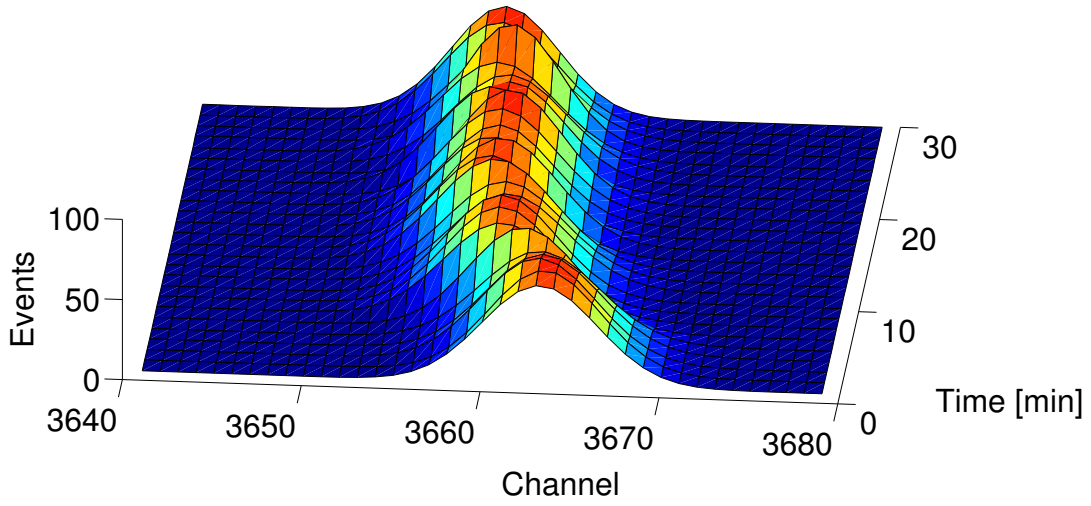

Figure 5.14: The 1332 keV line of ^{60}Co acquired in one minute intervals. The observable peak drift causes a resolution degradation of the detector.

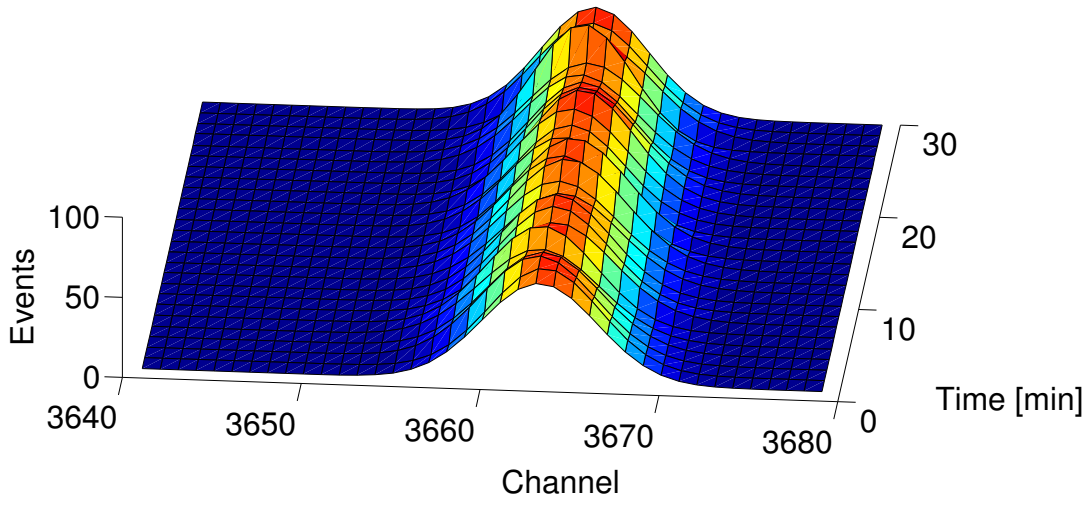

Figure 5.15: The 1332 keV line vs time after an off line correction on the peak drift has been performed.

1332 keV line, after the correction has been performed. The resolutions determined after correction were

$$\mathrm{FWHM}_{1173} = 10.02 \text{ ch} \tag{5.8}$$

for the 1173 keV line and

$$\mathrm{FWHM}_{1332} = 10.4 \text{ ch} \tag{5.9}$$

for the 1332 keV line. In total a resolution improvement of 13.1% and 14.7% for the two lines could be gained. Further improvement can be probably achieved by decreasing the time intervals but it involves also lower statistics in the peaks which introduces higher statistical uncertainties. Because the resolution degradation is expected to origin from the MCA noise characteristics and its instability, no further effort has been done to investigate the resolution performance.

DAQ part II:

The DAQ chain designed to acquire pulse shapes involves the operation of a trigger unit and an ADC which digitizes the data given by the PSC823 preamplifier without further shaping. Following modules have been used in the chain:

• CAEN V1720, VME flash ADC with a 12 bit resolution, a sampling rate of 250 Ms/s and an input dynamic of 2 Vpp.

• CAEN A2818 PCI optical link. The link allows for the communication between the V1720 module and a PC. Data transfer takes place via two optical fibers.

• CAEN N625 linear fan in/out NIM module with a built-in discriminator and an adjustable trigger threshold.

• SIN DT102 trigger unit.

The two latter modules are combined into a trigger circuit for the V1720 ADC. Figure 5.16 shows the schematic setup of the DAQ chain for the waveform acquisition. In contrast to the spectroscopy chain, both detector outputs, OUT E and OUT T are used in this circuit. While the detector output OUT T is connected directly to the ADC input,

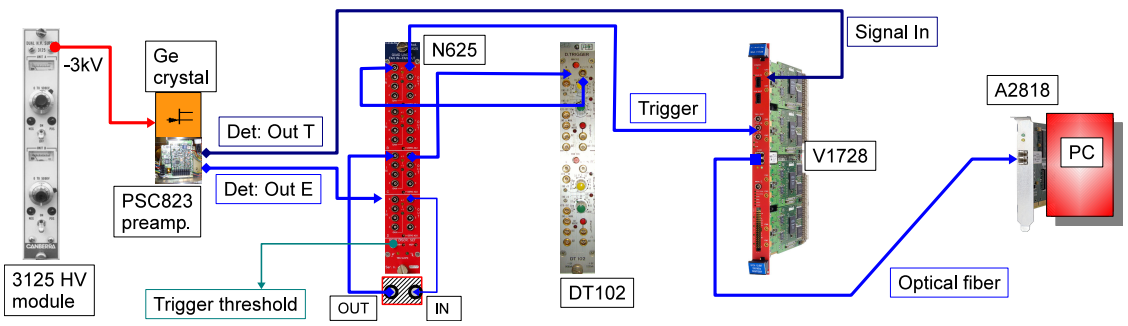

Figure 5.16: DAQ chain for pulse shape acquisition with the GeMini detector. Triggering of the ADC is performed by the N625 and the DT102 modules.

the parallel output signal OUT E is used for triggering the flash ADC. For this purpose, the single channel discriminator of the N625 fan in/out module is used. The DC coupled input and the output of the discriminator are located at the backpanel of the module. The threshold level is adjustable via a screwdriver trimmer at the frontpanel. A test point to monitor the threshold level is available and monitored with the slowcontrol described in section 5.2. The NIM standard logic output of the discriminator is connected to the DT102 trigger module in order to generate trigger pulses.

In order to use the full 2 Vpp input dynamics of the V1728 ADC, the amplification of the PSC823 preamplifier has been increased by a factor of ∼5. The PSC823 uses an inverting operational amplifier at the last stage, with an input resistivity of

$$R_{In} = 1.15\ \mathrm{k}\Omega \tag{5.10}$$

and a feedback resistivity of

$$R_{FB} = 5.1\,\mathrm{k}\Omega. \tag{5.11}$$

The output voltage V_{out} of an inverting operational amplifier is given by

$$V_{out} = -R_{FB}/R_{In} \cdot V_{in} \tag{5.12}$$

where V_{in} is the input signal. Therefore, increasing the amplification gain can be achieved by either increasing the feedback resistivity or by decreasing the input resistivity. The latter does not require any removing of the original circuit components, because a lower input resistivity can be achieved by connecting a second resistor in parallel. Figure 5.17

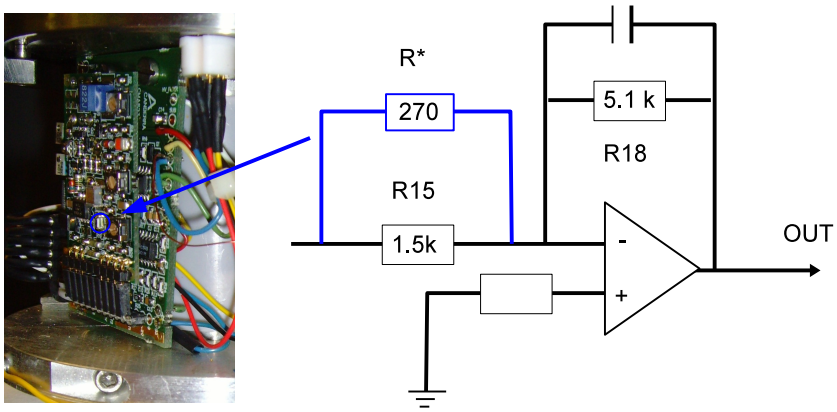

Figure 5.17: Modification of the PSC823 preamplifier. The input resistivity has been changed in order to increase the amplification gain by a factor of ∼5.

shows a part of the PSC823 amplification stage and the modification performed on the input resistor. A SMD 270 Ω resistor R^* has been soldered in parallel to the original input resistor on the PSC823 mainboard. The amplification gain α performed by this modification can be expressed by

$$\alpha = R_{In} \cdot (1/R_{In} + 1/R^*) \tag{5.13}$$

which results in an additional amplification gain of

$$\alpha = 5.26. \tag{5.14}$$

The acquisition time window of the flash ADC must be sufficiently wide to include part of the signal baseline and the rise-time component which allows to determine the pulse height.

The leading edge flank of a pulse contains information about the charge collection on the signal electrode and is hence important for pulse shape analysis studies. This includes in particular the development of discrimination methods concerning different types of interactions. The signal fall time contains merely information about the preamplifier discharging specification given by a decay time constant τ. According to the specification of the PSC823 preamplifier, the pulse decay time is

$$\tau_{Decay} = 50\ \mu\text{s}. \tag{5.15}$$

Typical values for signal rise-times in germanium detectors range from several hundred ns up to $\sim$1 μs. Because the sampling rate of the V1720 ADC is given by 250 MS/s, which translates into 4 ns per channel, the ADC buffer memory has been chosen to be 2000 samples wide to cover a window of 8 μs in total. The posttrigger, which allows to read

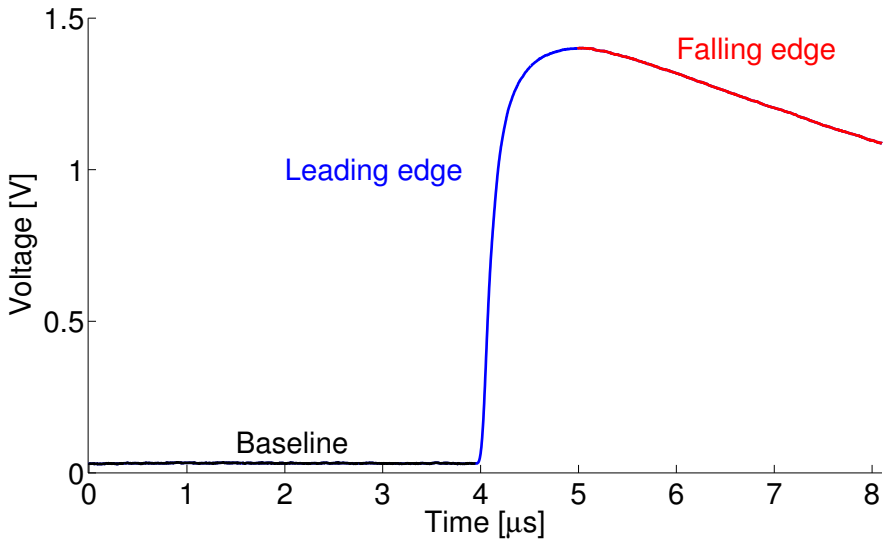

Figure 5.18: Example of a GeMini pulse acquired with the DAQ chain described above. The buffer memory of the ADC has been adjusted to cover 8μs with the posttrigger time set to 4μs.

historical buffer data has been set to 1000 samples. Figure 5.18 shows an example of a pulse acquired with the GeMini detector with a rise-time of $\sim$500 ns.

5.2 The GeMini Slow Control

In order to assure a safe operation of the GeMini detector, a control system has been developed allowing to monitor the following four parameters of the setup during operation:

• **Temperature of the crystal:** Leakage currents and noise behavior of germanium detectors do strongly depend on the operational temperature. This is a consequence of the small bandgap in germanium of 0.7 eV which allows for thermally induced charges. Furthermore, the FET of the first stage amplification of the GeMini detector is designed to be operated at low temperatures and should never be operated at room temperature. The measurement performed is independent from the temperature in the dewar.

• **Leakage current of the crystal:** Leakage currents occurring in parallel to signal currents can be a remarkable source of noise. The bulk leakage current is a consequence of impurities in the bulk and thermally generated electron-hole pairs within the depletion region of the crystal. Furthermore surface contaminations lead to an additional increase of the leakage current over the surface of the crystal. Monitoring of the parameter allows for conclusions about the crystals condition, its quality and long term stability.

• **Trigger threshold:** The trigger threshold used in the DAQ chain for pulse shape acquisition allows to reduce the size of data by discriminating low energy events consisting mostly of noise. Furthermore, the DAQ dead time can be decreased significantly without loosing relevant information.

• **Temperature in the cryostat:** The temperature in the cryostat is monitored to indicate a critical cryogenic liquid level. This allows to react before the temperature of the crystal starts to increase.

The four parameters described above are read out by a slow control consisting of the following three main components:

- **Periphery/Sensors:** This part includes the cables, connectors and feedthroughs for the leakage current measurement, the trigger threshold and the four Pt100 temperature sensors. Three of the Pt100 elements are mounted in a vertical configuration for the temperature control inside the dewar. The fourth Pt100 element measures the temperature of the crystal.

- **K8061 USB interface board:** The digitizer board includes eight analog inputs with a signal input range of up to +5 V. Optionally, a jumper allows to increase the range up to +10 V. The data are digitized by an internal ADC with a resolution of 10 bit. The communication between the board and a PC takes place via an USB interface. Dynamic link libraries allow to implement and control the board in a LabView environment for example.

- **Signal processing unit (SPU):** The unit has been designed to meet the analog input requirements of the K8061 interface board. It allows to amplify the monitored signals, to invert their polarity if necessary and to convert resistivities into voltage signals.

A LabView GUI has been furthermore developed to monitor all measured parameters given by the K8061 digitizer and to display them on a computer. More details about the SPU components will be given in the following.

The leakage current measurement
The measurement has been established with a minimal intervention on the original PSC823 amplification circuit. Figure 5.19 shows part of the first stage amplification of the PSC823. The crystal, the JFET, $R2$ and the capacitor C are located inside the endcap and cooled during operation. Both elements, $R2$ and C are part of the amplification feedback loop and are connected to the PSC823 mainboard through a vacuum feedthrough. The voltage

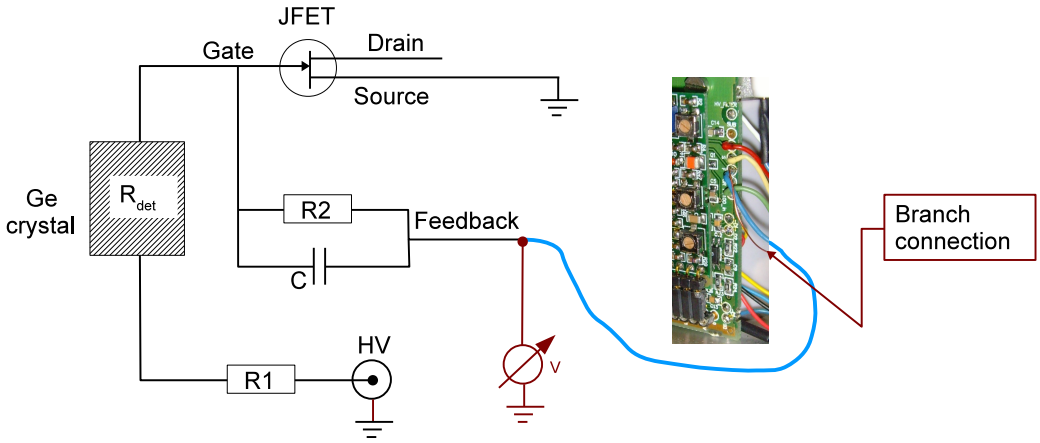

Figure 5.19: Leakage current measurement of the GeMini detector. The voltage drop measured on the feedback side of the PSC823 preamplifier represents the leakage current of the crystal.

drop at the feedback point is the product of the overall current and the sum of the resistors $R1$, R_{det} and $R2$. According to the specifications given by Canberra, the total resistivity of the loop shown in figure 5.19 is approximately

$$R_{Tot} = R1 + R_{det} + R2 \approx 200\ \mathrm{M\Omega} \tag{5.16}$$

The total current I through the crystal can be calculated by Ohm's law with $I = U/R_{tot}$, where U is the high voltage applied to the detector. Particle interactions in the crystal with energies higher than 0.7 eV induce electron hole pairs causing an additional net current which is equivalent to a drop of R_{det}. On the other side, the drop of R_{det} translates into a lower voltage drop on the feedback measurement side. Interactions with γ particles occur permanently in the detector, and hence the current measured through the crystal shows spikes which represent particle interactions with their energies given by the current pulse

height. In principle, although with poor resolution, spectroscopic measurements could be performed merely by the leakage current measurement. All pulses have a common baseline which represents a state of the detector without interactions taking place. Determination of absolute leakage current values is only possible by considering the bias given by this baseline. In order to perform the measurement, a branch connection on the feedback side of the PSC823 has been established as shown in figure 5.19. The connection is given by an isolated copper wire soldered to the feedback point on the motherboard. The wire is routed to a grounded BNC connector which is mounted on the thermal isolation teflon part shown in figure 5.6.

The negative leakage current signal is fed into the signal processing unit (SPU), which amplifies the signal and changes its polarity to fit the input range of the K8061 unit. The main module of the SPU is a TL064 four channel operational amplifier which can be operated in an inverting or non-inverting mode. Figure 5.20 shows the inverting circuit used

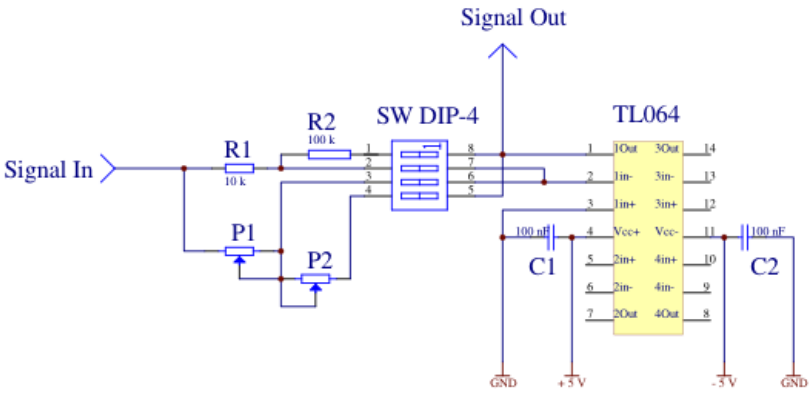

Figure 5.20: SPU circuit used to acquire the leakage current signal. The circuit inverts and amplifies the signal.

for the leakage current signal measurement. The voltage signal from the feedback loop of the PSC823 preamplifier is connected via a BNC cable to the signal input which is wired over an input resistor $R1$ to the inverting input of the TL064 amplifier. The feedback loop is established over the resistor $R2$. The amplifier gain G is adjustable via $R1$ and $R2$ and can be calculated according to:

$$G = -\frac{R2}{R1} \tag{5.17}$$

By default, a gain of $G = 10$ has been set with $R1 = 10$ kΩ and $R2 = 100$ kΩ. However, to give the circuit more flexibility, a four channel DIP switch can be used to replace $R1$

and $R2$ by two potentiometers $P1$ and $P2$ with a maximal resistivity of 500 kΩ and 1 MΩ respectively.

Liquid nitrogen control

The measurement of the three PT100 elements used for the liquid nitrogen level control takes place on the second amplifier channel of the TL064, which is run in the non-inverting mode. In order to translate the total resistivity of the Pt100 elements into a voltage drop, the constant current source LM334Z is used with a maximal adjustable current of up to 10 mA. The range of operation of the current source lies between 1 V up to 40 V and meets the operational voltage of the signal processing unit given by ±5 V. The current

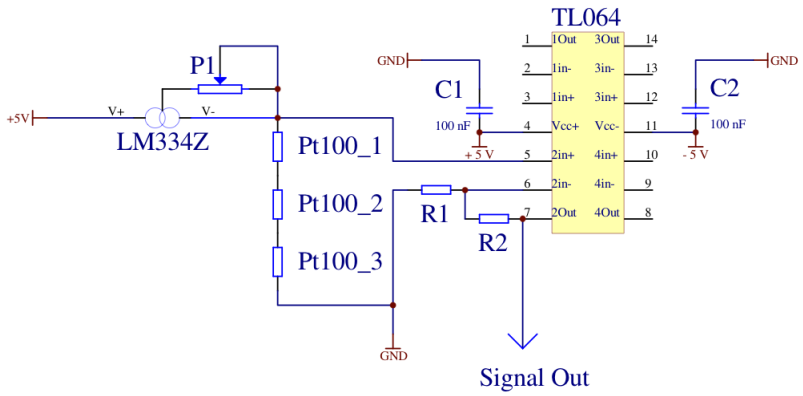

Figure 5.21: SPU circuit to measure the resistivity of the three Pt100 elements used for the liquid nitrogen control.

I_{SET} provided by the LM334Z can be adjusted by a setting resistor R_{SET} according to

$$I_{SET} = \frac{227\mu\text{V} \cdot T[\text{K}]}{R_{SET}} \tag{5.18}$$

where T is the operational temperature. Figure 5.21 shows the circuit used for the liquid nitrogen control. Because heating of the Pt100 resistors can be helpfull in determining the liquid nitrogen level, the current setting resistor is replaced by a potentiometer $P1$ allowing to maximize power losses on the Pt100 elements. In order to sustain the adjusted current, a voltage builds up at the V^- terminal of the LM334Z source, which is proportional to the total Pt100 chain resistivity. The voltage signal is directly connected to the non-inverting input of the TL064 amplifier. In the non-inverting mode, the input resistor $R1$ has to be

grounded and the feedback loop must be closed via the resistor $R2$. The signal gain in the non-inverting mode is given by

$$G = 1 + \frac{R2}{R1}. \tag{5.19}$$

By default, the current is set to a maximum of 10 mA resulting in signals up to 3 V. Hence, further signal amplification is not necessary. Because the input resistor $R1$ is given by 10 kΩ, $R2$ has been set to zero (alternatively a resistor of 300 kΩ is available).

Trigger threshold control

Channel three of the TL064 operational amplifier has been used for the trigger threshold measurement which is set on the N625 module for pulse shape acquisition. The signal is positive and does not require an inversion. However, the channel has been used to test the integration of a switch logic allowing to acquire both positive or negative signals. To switch between the inverting and non-inverting mode it is sufficient to ground the signal input connection, while redirecting the signal to the non-inverting input of the amplifier and vice versa. The switch logic has been realized by two ILQ74 optocoupler with four channels

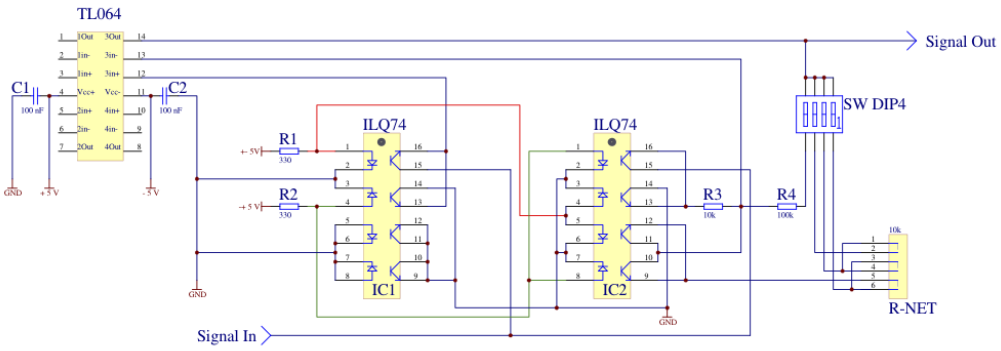

Figure 5.22: SPU measurement of the ADC trigger threshold. The circuit has been used to test a signal inversion, based on two optocoupler modules.

per module. Figure 5.22 shows the tested scheme. A switch can be used to set the $R1$ terminal on +5V, while changing the $R2$ terminal to -5V or vice versa. The non-inverting mode is activated by applying a positive voltage at $R2$. This opens channel 16/15 at $IC1$, transferring the signal directly to the non-inverting input of the TL064. Simultaneously, channel 13/14 and 11/12 of $IC2$ open which establishes a feedback circuit with the input resistivity $R3$ and the feedback resistivity $R4$. Furthermore a resistor-network $R - NET$ is available which consists of three 10 kΩ resistors. Those can be setup in parallel to the feedback resistivity by a DIP4 switch allowing to change the amplification gain.

Switching to the inverting mode, is performed in an analogue way by applying a positive voltage to $R2$ and a negative voltage to $R1$. In this configuration, channel 15/16 of $IC1$ closes, while channel 15/16 at $IC2$ opens. The signal is transferred over the input

resistor $R3$ to the inverting input of the TL064. The non-inverting input is grounded now over channel 13/14 of $IC1$, while the feedback loop including the resistivity network circuit keeps its functionality. Depending on the running mode, the gains can be calculated via equation (5.19) for non-inverted signals and via equation (5.17) for inverted signals.

Crystal temperature control

In a first attempt, the temperature control of the crystal has been established in full analogy to the liquid nitrogen control in the non-inverted mode as shown in figure 5.23. However, in contrast to the liquid nitrogen level control, high currents through the Pt100 on the germanium crystal are not desired. Hence, the current setting resistor has been fixed at 100 Ω, resulting in a current

$$I_{set} = 0.66 \text{ mA} \tag{5.20}$$

as can be calculated by equation (5.18). This translates into a voltage signal of 60 mV at room temperature. The input resistor and the feedback resistor has been set to 10 kΩ and 600 kΩ respectively providing a gain of G = 61, given by equation (5.19). The resulting signal of maximal ∼ 3.7 V at room temperature fully fits the input dynamic of the K8061 ADC. The temperature can be determined by calculating the actual Pt100

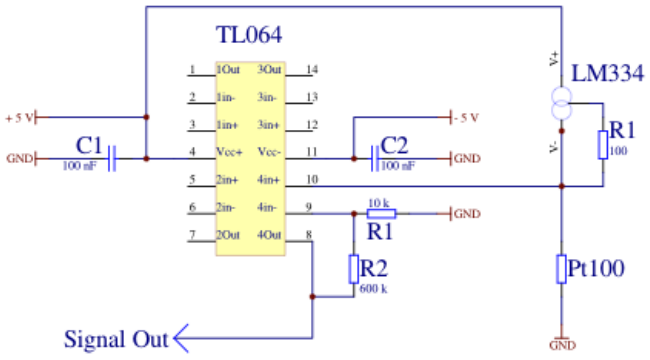

Figure 5.23: First version of the crystal temperature measurement circuit. The resistivity of the Pt100 element is performed in a two-wire configuration.

resistivity based on the measured voltage signal. A calibration table provided by Canberra allows to determine the absolute temperature of the crystal at a given Pt100 resistivity. The Pt100 resistivity measurement described above takes place in a two wire configuration. Signal losses due to the cable resistivity can occur as well as undesired ground loop effects. Both influencing the measured signal in a negative way. Because the temperature of

the crystal is a critical parameter in terms of detector resolution and leakage currents, an alternative measurement circuit has been set up in order to minimize negative effects on the signal propagation. The alternative circuit shown in figure 5.24 uses an INA114 instrumentation amplifier which in contrast to the TL064 module performs a differential signal amplification. This allows to perform measurements which are independent from a global reference voltage. The signal output of the INA114 is proportional to the voltage difference occurring between the ${}^{+}V_{in}$ and the ${}^{-}V_{in}$ terminals. Furthermore, to improve the performance of the measurement, the circuit has been set up in a four wire configuration, which minimizes signal losses given by wiring resistivities. The 100 Ω resistor $R1$ used in

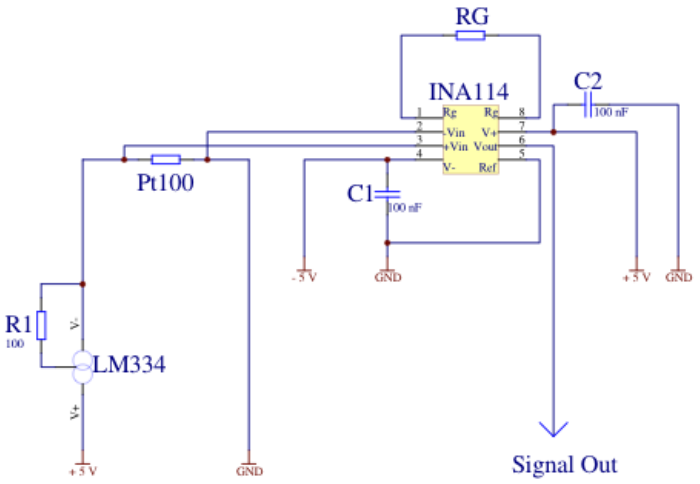

Figure 5.24: Improved circuit for the crystal temperature measurement. Signal amplification is performed differentially and the resistivity is measured in a four-wire configuration.

combination with the LM334 module sets the current through the Pt100 element to 0.66 mA. Adjusting the gain of the amplifier can be performed with the resistor R_G, located between pin 1 and pin 8 of the INA114 module. The gain is given by

$$G = 1 + \frac{50\ \text{k}\Omega}{R_G}. \tag{5.21}$$

In the test circuit, a potentimeter of 20 kΩ has been used for R_G, allowing to use the full input range of the K8061 ADC module. By default, R_G has been set to 5.5 kΩ resulting in a gain of 10.

Power Supply

Powering of the K8061 interface board and the SPU board is performed by a Convel 32215A open frame power supply. The bipolar module delivers ± 12 V. While, the K8061 board

requires positive 12 V, the SPU requires a bipolar ±5 V for its full functionality. The bipolar voltage has been down-regulated from ±12 V to ± 5 V by two DC voltage regulators as shown in figure 5.25. A three terminal connector on the SPU is used to establish the

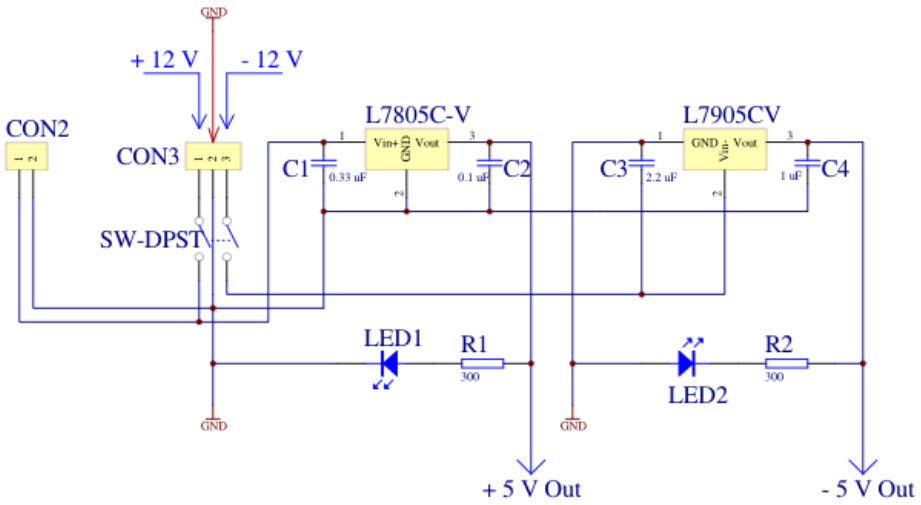

Figure 5.25: Circuit providing the bipolar ±5 V voltage required for the operation of the SPU.

±12 V connection and the grounding. The L7805C-V module regulates the positive 12 V down to + 5 V. The analogue module L7905CV regulates the negative -12 V down to -5 V. Two LED's are used to control the functionality of both regulators. A two pin terminal connector is used for the 12 V powering of the K8061.

All three modules, the bipolar power supply, the K8061 interface board and a test version of the SPU have been mounted in an alumina chassis from Schroff as shown in figure 5.26. The chassis has been mounted in the DAQ rack which includes also a NIM crate and a VME crate with the data acquisition modules. The original SPU test board has been extended by a second board used for the crystal temperature control. The additional board contains the differential INA114 instrumentation amplifier used to measure the resistivity in a four wire configuration. The 12 V bipolar power supply is down-regulated to ± 5 V on the SPU board. The board contains furthermore a junction for the +12 V power supply of the K8061 digitizer. Details about the layout of the SPU are shown in figure 5.27. The three BNC input connectors are used for the leakage current, the liquid nitrogen control and for the trigger threshold measurement. The circuit of the leakage current channel is extended by a DIP4 switch and two potentiometers allowing for a gain variation. Position 3 and 4 of the DIP switch establishes a circuit with fixed input- and feedback resistors. Deactivating both and activating position 1 and 2 instead, establishes a circuit which replaces both resistors with two potentiometers. The trigger threshold chan-

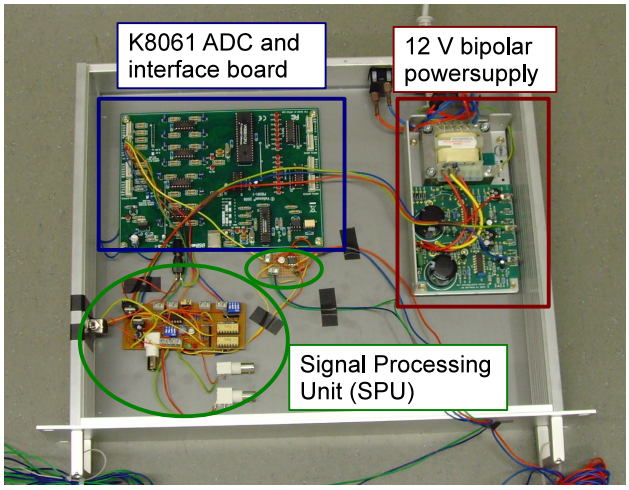

Figure 5.26: Overview of the slowcontrol components, mounted in an alumina chassis which has been integrated in the DAQ rack.

nel circuit includes a switch logic based on two optocouplers, allowing to change between an inverted or non-inverted running mode of the TL064 amplifier. The inversion of the signal is performed by a switch mounted on the side of the chassis. Two LED's indicate the current running mode with green = non-inverting and red = inverting. Furthermore, another DIP4 switch can be used to manipulate the gain by including 10 kΩ, 20 kΩ or 30 kΩ in parallel to the 100 kΩ feedback resistor. A fourth resistivity measurement channel,

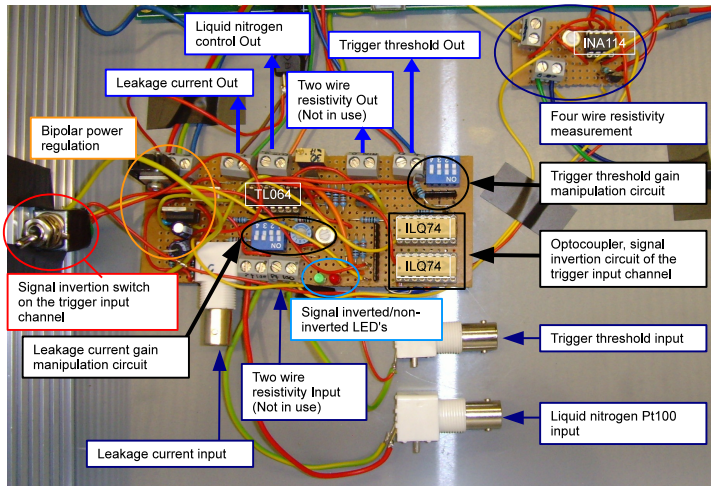

Figure 5.27: Overview of the SPU test board with the description and location of the most relevant components.

setup in a two wire configuration is available. It was designed originally for the crystal temperature control and is not in use anymore.

Based on the experience gained during the setup of the SPU test board, an extended

circuit has been designed with a wide spectrum of functionality. The circuit includes:

• four analog signal input terminals, each with the option of signal inversion.

• four resistivity measurement channels in a four-wire configuration.

• broad and continuous signal gain variety

The circuit shown in figure 5.28 can be divided into five main sections:

A) Power regulation: delivers ± 5 V for the SPU and +12 V for the K8061 board. Two LED's are indicating the status of the two L7805 and L7905 power regulators.

B) Non-inverting signal amplification: all four channels of the TL064 ($IC2$) amplifier are implemented in a non-inverting configuration. Per channel, two resistivity networks, consisting of four 10 kΩ resistors are used to change the feedback resistivity. A ten terminal DIP switch allows to change the feedback resistor in an interval of

$$R_{FB} = 0 - 90 \text{ k}\Omega. \tag{5.22}$$

in 10 kΩ steps. The input resistor R_{in} is set to 10 kΩ, which in combination with the feedback resistor allows for a gain range of

$$G_{noninv} = 2 \ldots 10 \tag{5.23}$$

according to

$$G_{noninv} = 1 + \frac{R_{FB}}{R_{In}}. \tag{5.24}$$

Furthermore a 50 kΩ potentiometer in series with a 5 kΩ resistor can be connected additionally in parallel with a jumper, allowing for a continuous gain variation up to

$$G_{noninv}^{max} = 28. \tag{5.25}$$

C) Inverting signal amplification: Four channels of a second TL064 module ($IC1$) have been setup in an inverting configuration. Two resistor networks per channel and a DIP switch allow to change the feedback resistivity in a range of

$$R_{FB} = 10 \ldots 100 \text{ k}\Omega. \tag{5.26}$$

The input resistor R_{in} is set to 10 kΩ. It is possible to connect a further 5 kΩ resistor and a 50 kΩ potentiometer in parallel. The gain in the inverting configuration is given by

$$G_{inv} = \frac{R_{FB}}{R_{In}} \tag{5.27}$$

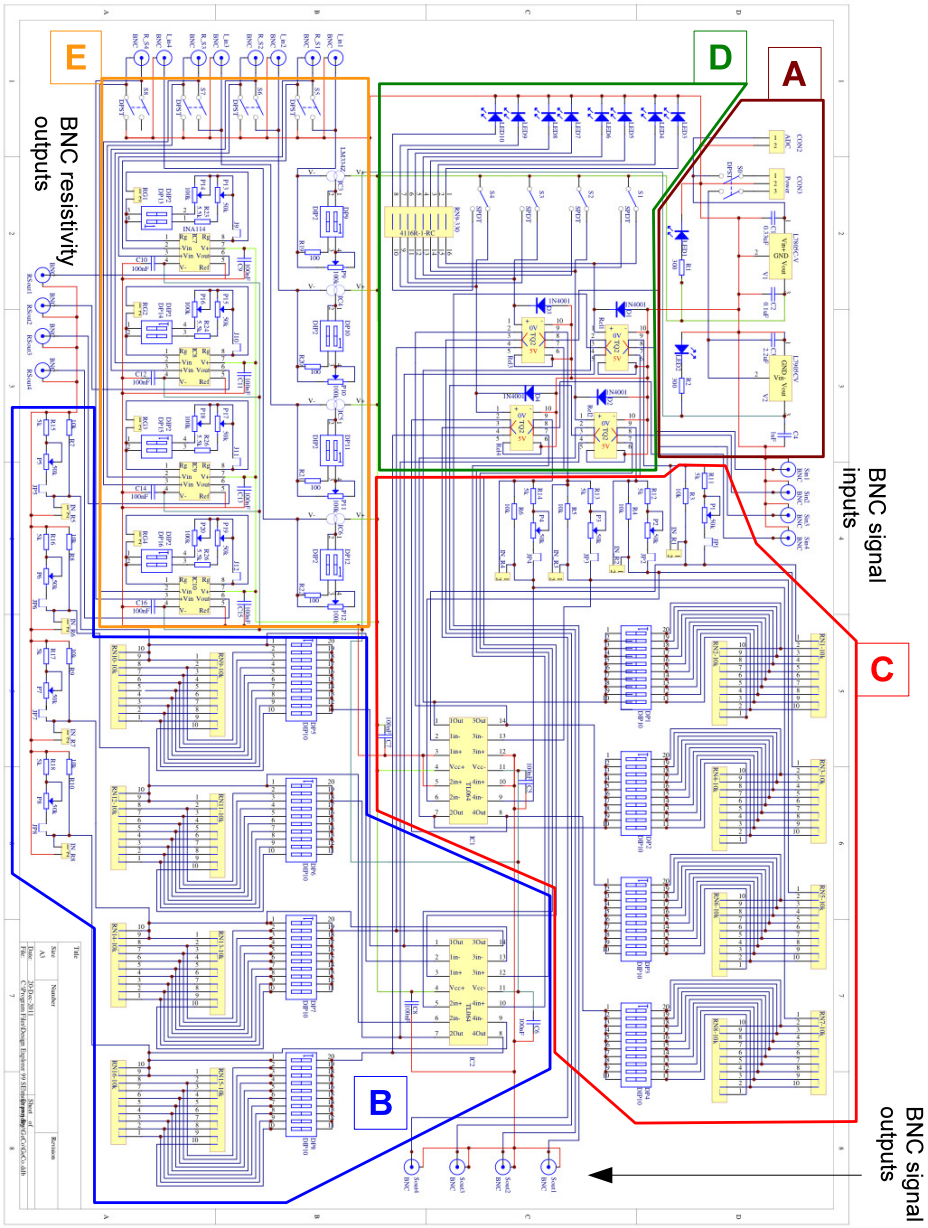

Figure 5.28: Full design of the extended SPU unit. The design bases on the experience gained with the test SPU board.

and can be set in a range of

$$G_{inv} = 1 \ldots 10 \tag{5.28}$$

if only the 10 kΩ input resistor is in use. Switching-in the potentiometer increases the range up to a maximal gain of

$$G_{inv}^{max} = 30. \tag{5.29}$$

Especially while working with the feedback potentiometer, it is crucial to measure the total feedback resistivity in order to determine the gain of the circuit. For this reason, test points were included in the design allowing to measure the total input resistivities.

D) Switch logic for the inverting and non-inverting mode: the two TL064 modules are running permanently. $IC1$ is setup in the inverting- and $IC2$ in the non-inverting configuration. The switch logic makes sure that the non-inverting signal output of $IC2$ is provided to the BNC output if no signal inversion is required. In full analogy, it provides the inverting signal output of $IC1$ to the BNC output if the signal has to be inverted. In contrast to the SPU test board, switching takes place not anymore via optocouplers but via single-side stable relays of the TQ2-5V type. Using relays prevents signal losses which were observed during the operation of phototransistor couplings. Four protective diodes are preventing inductive circuit damage caused by activating or deactivating the relays. The four single pole switches are used to activate or deactivate the inverting or non-inverting modes. Eight LED's are indicating the running mode of each channel.

E) Four-wire resistivity measurement: The resistivity measurement is performed by the LM334Z constant current source and the INA114 instrumentation amplifier. Four channels are available, which are setup in four identical circuits. A two terminal DIP switch per channel allows to set the current to

$$I_{SET} = 0.66 \text{ mA} \tag{5.30}$$

if only the fixed 100 Ω current setting resistor is used. Alternatively the DIP switch allows to switch between the fixed resistor and a 1 MΩ potentiometer, allowing to set the current in a range of

$$I_{SET} = 0.07 \text{ mA} \ldots I_{max}. \tag{5.31}$$

With $I_{max} = 10$ mA, which is given by the maximal current of the LM334 module. The current is provided via a BNC connector (I_S) to the resistivity to be measured. Another BNC connector (R_S) is used to measure the voltage drop on the resistor in a four-wire configuration. One double pole switch per channel allows to switch between a four-wire and a two-wire configuration. In the two-wire configuration, the R_S BNC connector stays open without establishing a connection to the resistor. This is the simplest method to determine resistivities, but the measured signal is increased by the cabling resistivity which can play a role at distances >1 m. The signal is transferred to the INA114 module and differentially amplified. The gain is adjusted via a resistor R_G and can be calculated

by

$$G_{INA114} = 1 + \frac{50\ \text{k}\Omega}{R_{G.}} \tag{5.32}$$

A two terminal DIP switch allows to use a 100 kΩ potentiometer to set a gain of

$$G_{INA114} = 1.5 \ldots G_{max,} \tag{5.33}$$

where G_{max} is the maximal possible gain of 10^3, which is theoretically reachable by the INA114 module. Furthermore the DIP switch can be used to connect a 5.5 kΩ resistor in series with a 50 kΩ potentiometer, allowing for a fine gain adjustment in a range of

$$G_{INA114} = 2 \ldots 10, \tag{5.34}$$

if the 100 kΩ resistor has been disconnected. A combination of the three gain resistors in parallel is also possible. A test point allows to read the total gain set resistivity in order to precisely determine the amplification factor.

5.3 Summary

In this chapter, the HPGe GeMini detector, assembled at the University of Zurich has been introduced under technical and operational aspects. In the standard mode, the detector can be operated with the crystal covered by an evacuated endcap. Cooling takes place via a coldfinger dipped in liquid nitrogen. The detector was used in the standard operational mode to perform γ calibrations of the first, custom ^{228}Th source produced at PSI.

The configuration of the detector can be changed in a way, which allows for the direct immersion of the crystal into cryogenic liquids. In the immersion mode the endcap is disassembled, the thermal coupling dismounted and the detector immersed upside down into a special 5 ltr. dewar. A warming-up setup has been integrated in the DAQ rack to assure a safe heating of the crystal in a nitrogen atmosphere. The setup has to be used before reassembling the detector into the standard mode to prevent damage of the naked crystal.

Data acquisition is performed by two DAQ chains, which allow for spectroscopic measurements and for pulse shape acquisition. The gain of the PSC823 preamplifier has been increased by factor 5 in order to fit the ADC input dynamic of 2 Vpp. A connection on the feedback loop of the PSC823 has been established in order to measure leakage currents. To monitor detector parameters like the leakage current or the crystal temperature, a slow control has been developed which consists of a signal processing unit and a digitizer. An USB interface allows to monitor the data on the computer using a LabView GUI. Based on the test SPU board, an extended SPU unit has been designed with four inverting and four non-inverting channels. Another four channels can be used for resistivity measurements in a two-wire or optionally in a four-wire configuration.

Chapter 6

Neutron measurements - custom vs commercial ^{228}Th source

SOURCES4A calculations presented in chapter 3 and in chapter 4 have shown that the neutron flux from a custom produced ^{228}Th source could be up to two orders of magnitude lower than the neutron flux from a commercial source. The reduction is a consequence of different (α, n) threshold energies and cross sections for the target materials involved in the internal setup of the source.

However, given the unknown exact chemical composition of the ceramics used in a commercial source, the calculated fluxes must be regarded under hypothetical aspects. The liquid $ThCl_4$ precursor used for the production of the custom source contains besides Zr, unknown impurities which accumulate in the ^{228}Th layer on gold. During the production at PSI in particular, a yellow tint of the liquid has been observed which can be an indication for an iron content in the precursor liquid. The impurities in the precursor can only be taken into account by performing a chemical composition analysis with ICP-MS for example. Although, chemical analysis and neutron flux calculations can be performed to understand the origin of the neutron emission which is important for the process optimization, in the first instance, neutron measurements have been performed in order to determine the achieved impact in neutron reduction through the deposition of ^{228}Th on a gold foil. The measurements were done with a ^{3}He counter and with a second europium doped lithium-iodide (LiI(Eu)) detector. Both detectors were located at LNGS in order to minimize the environmental neutron background. Furthermore, in order to improve the performance of the commercial LiI(Eu) detector, a second, high purity LiI(Eu) setup has been designed and operated at LNGS.

6.1 ^{3}He neutron detector

In contrast to charged particles, neutrons can penetrate a nucleus without undergoing Coulomb interactions, which often results in a high probability to trigger nuclear reac-

tions. The cross sections for nuclear reactions depend on target properties like mass and nuclear energy levels, but also on the incoming neutron energy E_n. For this reason, depending on their kinetic energy, neutrons are classified in the following energy groups:

- Thermal neutrons: $E_n < 0.025$ eV
- Epithermal neutrons: 0.025 eV $< E_n < 0.5$ eV
- Intermediate neutrons: 0.5 eV $< E_n < 0.5$ MeV
- Fast neutrons: 0.5 MeV $< E_n < 20$ MeV
- High energy neutrons: $E_n > 20$ MeV

The cross sections for nuclear reactions triggered by neutrons are inversely proportional to the neutron velocity v and are hence inversely proportional to the square root of their energy:

$$\sigma_n \sim 1/v \sim 1/\sqrt{E_n} \tag{6.1}$$

However, the $1/v$ dependence can not be applied to all energies. Resonances can occur if the compound nucleus excites to one of its discrete energy levels. Figure 6.1 shows an example of the total cross sections for neutrons in ^{3}He. Due to the energy dependence

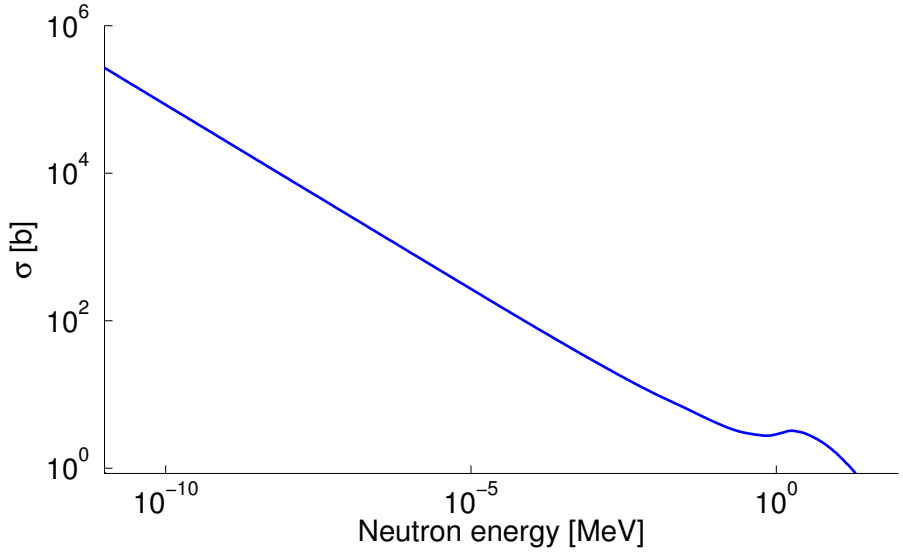

Figure 6.1: Total neutron cross sections in ^{3}He, data taken from [84].

of the neutron cross sections as expressed in (6.1), the detection efficiency of a detector can be drastically improved by the moderation of neutrons down to thermal energies. On the other side, the improvement of detection efficiency by moderation causes the loss of

spectral information. In general, the detection of neutrons is based on the detection of secondary reaction products. Reactions like (n,γ), (n,p) or (n,α) are characterized by discrete energies given by the Q-value, but the spectra are usually accompanied by an additional environmental γ background contribution. In order to identify neutrons, pulse shape analysis techniques are often applied in scintillator detectors. Alternatively, distinct nuclear reactions with a high Q-value can be used to distinguish between neutron and γ interactions. The latter method requires the presence of target isotopes with high cross

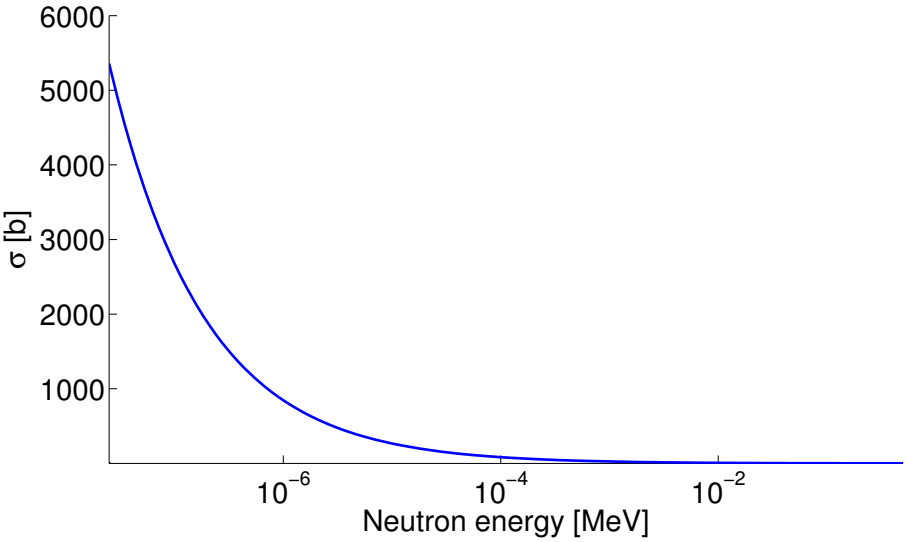

Figure 6.2: Neutron capture cross sections for the ^{3}He(n,p) reaction with a Q-value of 0.764 MeV, data from [84].

sections for the reaction and a Q-value which is sufficiently high to allow for an effective γ background rejection. An example for such an reaction is the neutron capture reaction in ^{3}He given by

$$ {}^3_2He + {}^1_0 n \rightarrow {}^3_1H + {}^1_1p \tag{6.2} $$

with a Q-value of

$$ Q = 0.764 \text{ MeV}. \tag{6.3} $$

The kinetic energies of the outcoming reaction products can be calculated by the energy and momentum conservation with:

$$ E_{H^3_1} + E_p = Q \tag{6.4} $$

and

$$ m_{H^3_1} \cdot v_{H^3_1} = m_p \cdot v_p. \tag{6.5} $$

Equation (6.4) and (6.5), allow to express the energies of the outcoming particles according to

$$ E_{H^3_1} = \frac{m_p}{m_p + m_{H^3_1}} \cdot Q = 0.191 \text{ MeV} \tag{6.6} $$

and

$$E_p = \frac{m_{H_1^3}}{m_p + m_{H_1^3}} \cdot Q = 0.573 \text{ MeV}. \tag{6.7}$$

The cross sections for the ^{3}He(n,p) reaction described above are shown in figure 6.2 for an energy range between 25 meV and 500 keV. At energies below 25 meV, the neutrons are thermalized and reach cross sections of at least $\sim$ 5.3 kb. Cold neutrons at energies below $1 \cdot 10^{-4}$ eV reach values up to 85 kb.

A scheme of a typical ^{3}He ionization chamber is illustrated in figure 6.3. An incoming neutron triggers the reaction described in equation (6.2). The two reaction products tritium and proton induce ionization tracks inside the tube which induces a signal on the high voltage inner electrode. The signal is proportional to the energy deposited which is equal to the reaction Q-value and therefore the signal amplitude does not depend on the initial neutron energy. Although, the detector is sensitive also to γ particles, environmental gam-

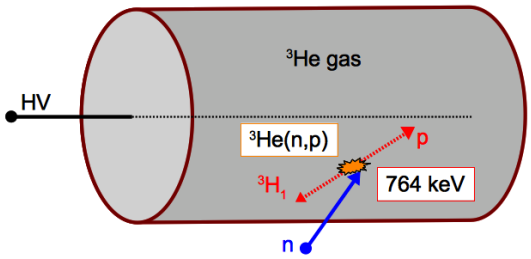

Figure 6.3: Schematic view of a ^{3}He counter. The products of the nuclear reaction triggered by the incoming neutron give rise to ionization tracks. The charges induce a signal on the high voltage electrode.

mas interact mostly in the walls of the tube and give rise to electrons which deposit about 2 keV/cm in the sensitive gas volume. Therefore, the energy deposited by γ interactions is mostly limited to several hundreds keV in contrast to the energy deposition given by the heavy reaction products of the neutron capture reaction. Thus, discrimination between neutrons and gammas in ^{3}He detectors can be performed very efficiently by a pulse height analysis.

As described above, the detection efficiency can be improved by moderating fast neutrons down to thermal energies. Moderation in matter takes place through interactions with target nuclei until thermal equilibrium with the environment has been reached. Neutron interactions in matter can be divided into three categories:

• **Elastic scattering:** Describes a scattering within the potential of a nucleus or through the formation of an excited nucleus. The process of elastic scattering can be described classically, considering the energy- and momentum conservation. The mean energy loss of

a neutron with energy E_n in matter can be expressed by

$$\Delta\overline{E} = 2 \cdot E_n \frac{m_n \cdot m_t}{(m_n + m_t)^2} \tag{6.8}$$

where, m_n is the mass of the neutron, m_t is the mass of the target nucleus and $\Delta\overline{E}$ has been averaged over a solid angle of 4π. Equation (6.8) shows that maximal energy losses are reached through elastic scattering on target nuclei with the same mass as the neutron mass. During one elastic collision with a proton for example, the neutron looses half of its energy. Fast neutrons with energies of $\sim$ 1 MeV are thermalized after $\sim$ 25 collisions with hydrogen nuclei. Therefore, effective moderators contain a significant amount of hydrogen atoms. Water can be used in reactors for example, but in many applications a solid state moderator is desired. For this reason, hydrocarbons like polyethylene (C_2H_4) or paraffin (C_nH_{2n+2}) can be found in many setups requiring neutron moderation.

• **Inelastic scattering:** The interaction takes place if the kinetic neutron energy exceeds one of the discrete excitement energy of a nucleus. The excited nucleus de-excites to its ground state by the emission of γ particles. Inelastic neutron scattering takes place preferably on heavy target nuclei with first level excitation energies of $\sim$100 keV. Unless the neutrons are high-energetic, light target nuclei like hydrogen with excitation energies of $\sim$1 MeV must not be considered as a medium were inelastic neutron scattering takes place.

• **Neutron capture:** The reaction does not belong to the elastic or inelastic interaction category. The neutron penetrates a target nucleus and forms either a new compound nucleus or triggers a nuclear reaction like (n, p), (n, γ) or (n, xn). In analogy to the (α, n) reactions, which were already discussed in detail in chapter 3, the threshold energy for (n, y) reactions can be expressed by the masses of the neutron and the target nuclei, and by the Q-value according to

$$E_{Thr} = -Q \cdot \frac{m_n + m_t}{m_t} \tag{6.9}$$

with typical energies of $E_{Thr} > 1$ MeV.

For the neutron measurements of the custom ^{228}Th sources, a ^{3}He detector has been used with a gas tube of 5 cm in diameter and 25 cm in length. The tube contains a gas mixture of CO_2, Ar and ^{3}He in a partial pressure ratio of

$$CO_2 : Ar : {}^3He = 91 : 1520 : 2950 \tag{6.10}$$

The first custom ^{228}Th neutron measurement, has been performed by Serena Fattori in a configuration described in [85]. The setup has been originally used for neutron background measurements in the LNGS laboratory. Shielding against environmental neutrons has not been performed. The ^{3}He tube was embedded in a polyethylene moderator of 30 cm in diameter and 75 cm in height. The ^{228}Th source has been located on top of the setup resulting in an effective moderator thickness of 12.5 cm.

Further measurements were performed with a modified ^{3}He configuration which was optimized for the custom ^{228}Th source measurements. In particular a neutron shield has been added, which consisted of two components, a ^{113}Cd foil and a shield constructed of paraffin blocks. As shown in figure 6.4, the ^{113}Cd isotope has very high absorption cross sections for neutrons. In particular, the cross sections increase rapidly for neutrons below the cutoff energy at ∼0.5 eV. A cadmium foil with a thickness of 0.5 mm has been wrapped around

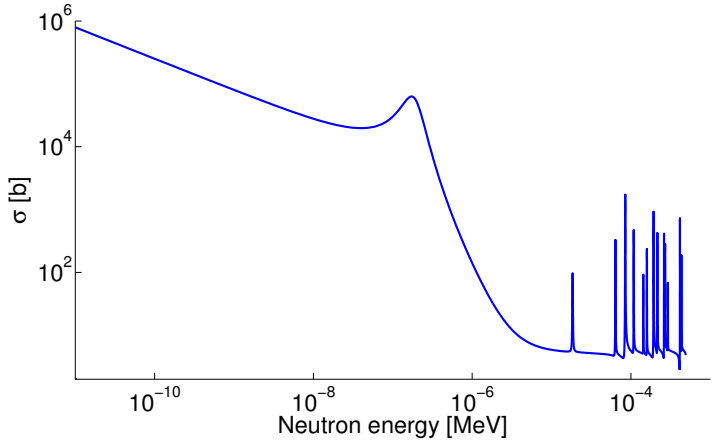

Figure 6.4: Total neutron cross sections in ^{113}Cd. Neutrons below ∼0.5 eV are absorbed very efficiently. Data are taken from [84].

the polyethylene moderator to absorb low energy neutrons from the environment. Higher energetic environmental neutrons have been shielded by 10 cm thick paraffin blocks, doped with boron and mounted around the Cd foil. As shown in figure 6.5 and figure 6.1, the

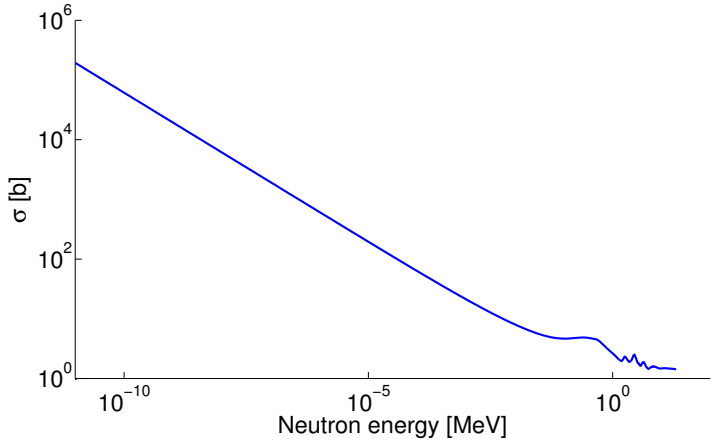

Figure 6.5: Total neutron cross sections in ^{10}B, data from [84].

^{10}B isotope has comparable neutron capture cross sections to the cross sections given in

^{3}He. Therefore, boron is also used in neutron detectors such as BF_3 gas counters but furthermore it can be combined into neutron shield materials such as borated paraffin or borated polyethylene.

The ^{3}He tube has been placed in a cylindrical polyethylene moderator with a wall thickness of 6.5 cm. For the neutron measurements of the ^{228}Th sources, a borehole has been drilled on the side of the moderator located in the middle of the ^{3}He tube as illustrated in figure 6.6. The borehole can be closed from the top with a polyethylene plug after the source has been inserted. In this configuration the minimal moderation path is 1.1 cm which is the minimum distance between the gas tube wall and the bottom part of the drilling. However, the source is surrounded by the moderator in 4π giving rise to a moderated neutron cloud which covers the active detection volume. The detector has been operated with positive 2 kV applied to the inner electrode. The HV connector is used simultaneously as the signal output. Figure 6.6 shows a schematic view of the internal setup as well as

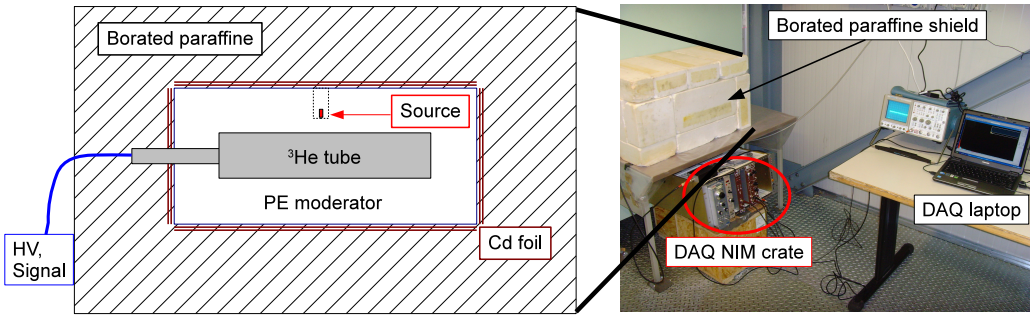

Figure 6.6: Left: Scheme of the ^{3}He setup used for the neutron flux measurements of the ^{228}Th sources. The ^{3}He tube is mounted within a polyethylene moderator. The source is located inside the moderator. Environmental neutrons are shielded with a Cd foil surrounded by borated paraffin. Right: Detector and DAQ after the source has been inserted and the neutron shield reassembled.

the fully assembled detector. The detector signal is connected to a preamplifier, followed by a shaping amplifier. Digitization of the semi-gaussian signal amplitudes takes place with a 13 bit multichannel analyzer which is connected via USB to an acquisition PC. The schematic of the DAQ chain used is shown in figure 6.7. Typical spectra acquired with

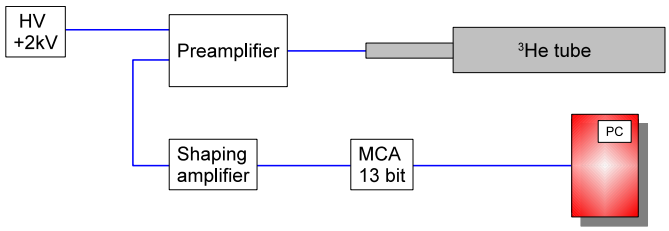

Figure 6.7: DAQ chain used for the ^{3}He detector.

a ^{3}He setup are characterized by a continuum and a neutron peak at the Q-value of 764

keV given by the nuclear reaction described in (6.2). The continuum arises from electronic noise and γ interactions. However, most of the γ interactions are expected at energies up to several hundreds keV. A higher energetic component of the continuum forms through the Wall-Effect which arises through neutron interactions taking place close to the walls of the detector. The reaction products of such events can hit the housing of the detector and loose their energy in the walls rather than in the sensitive gas volume. Full energy deposition is not possible anymore and a continuum below the neutron peak appears, which overlaps with the low energetic γ continuum. The Wall-Effect is significant, if the range of the reaction products in the gas is comparable to the diameter dimensions of the gas tube. Typical ranges of tritium in ^{3}He tubes are about 1 cm. The radius of the gas chamber of

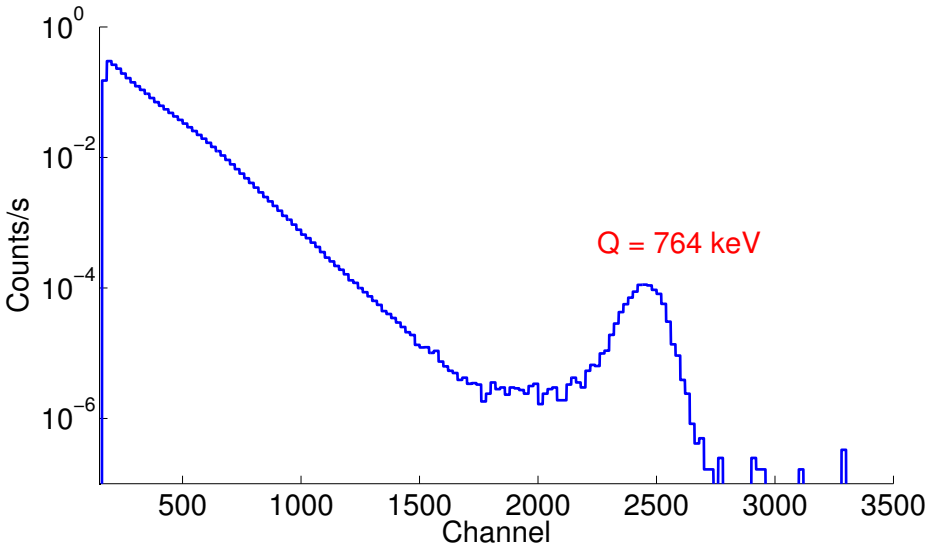

Figure 6.8: Full ^{228}Th spectra acquired with the ^{3}He detector. The neutron peak appears at channel ∼2500.

the ^{3}He setup described above is 2.5 cm and therefore, a significant wall effect is expected to be observed. An example of a spectrum taken with a ^{228}Th source is shown in figure 6.8. The figure shows a neutron peak at channel ∼2500 which is preceded by a continuum resulting from γ particles and neutron capture interactions with their energy deposition suppressed by the Wall-Effect.

6.2 LiI(Eu) neutron detector

The extremely low natural abundance of ^{3}He of 0.000137 % and the necessary isotopic enrichment process makes ^{3}He gas counters very expensive. In order to test an alternative setup, an europium activated lithium iodide detector has been assembled additionally to measure the neutron fluxes from the custom ^{228}Th sources. ^{6}LiI(Eu) crystals are solid state scintillators with a density of ∼4 g/cm^3 and are very cost effective with respect to ^{3}He

counters. Therefore, LiI(Eu) detectors are often regarded as a good alternative technology to ^{3}He detectors. In analogy to ^{3}He, the neutron detection principle in LiI(Eu) bases on a specific nuclear reaction triggered by the neutron. The main role in the detection process plays the ^{6}Li isotope which is involved in the following reaction:

$$^6_3\mathrm{Li} + \mathrm{n} \rightarrow {}^7_3\mathrm{Li}^{(*)} \rightarrow {}^3_1\mathrm{H} + {}^4_2\mathrm{He} + Q \tag{6.11}$$

with a reaction Q-value of

$$Q = 4.78 \text{ MeV}. \tag{6.12}$$

The Q-value energy is shared between the two reaction products triton and α and can be expressed in terms of their masses according to

$$E_{H^3} = \frac{m_\alpha}{m_{H^3} + m_\alpha} \cdot Q = 2.73\, MeV \tag{6.13}$$

and

$$E_\alpha = \frac{m_{H^3}}{m_{H^3} + m_\alpha} \cdot Q = 2.05\, MeV. \tag{6.14}$$

Even though, the reaction products have a total energy of 4.78 MeV, the measured gamma equivalent energy (GEE) of the reaction is about (3 - 3.5) MeV due to quenching effects in the scintillator. However, environmental γ background is dominated by ^{238}U and ^{232}Th decays with maximal γ energies of about 2.7 MeV, which is ∼800 keV below the measured neutron peak energy. For this reason, LiI(Eu) detectors are very effective in neutron detection under high gamma background conditions like they occur in the presence of a ^{228}Th source for example. The discrimination between gamma and neutron events can be performed by a pulse height separation without the need of pulse shape analysis or further γ background suppression.

As shown in figure 6.9, cross sections for thermal neutron capture in ^{6}Li start at ∼1000 barn and increase with $1/\sqrt{E_n}$ with decreasing neutron energies E_n. Given the cross sections in figure 6.9, the detection efficiency can be further improved by neutron thermalization. The absorption of neutrons in LiI(Eu) follows an exponential trend and can be expressed by

$$N_{Abs} = N_0 \cdot (1 - e^{-\mu \cdot L}) \tag{6.15}$$

where N_{Abs} is the number of absorbed neutrons, N_0 is the number of neutrons hitting the lithium target, μ is the linear absorption coefficient and L is the target thickness. For the LiI(Eu) crystal, the absorption coefficient for thermal neutrons is given by

$$\mu = 16.7 \text{ cm}^{-1}, \tag{6.16}$$

which in consequence means that a target thickness of 3 mm is sufficient to absorb 99.3 % of thermal neutrons trespassing the crystal. The commercial LiI(Eu) detector used for the neutron measurements of the ^{228}Th sources contains a LiI(Eu) crystal with a diameter of 25.4 mm and a height of 3 mm. Due to its hygroscopic properties, the crystal shown in fig-

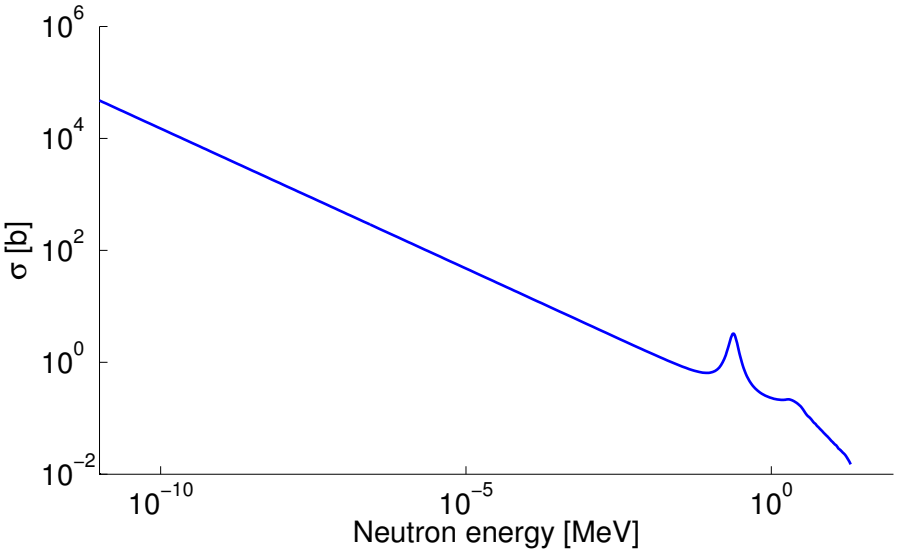

Figure 6.9: Neutron capture cross sections in ^{6}Li. Cross sections for thermalized neutrons start at ∼1000 barn. Besides the resonance at ∼0.5 MeV, high detection efficiencies can be reached only through neutron thermalization. Data taken from [84].

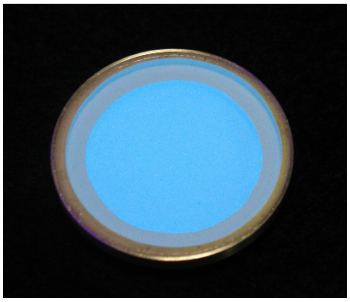

Figure 6.10: LiI crystal mounted in an alumina housing. The housing is sealed to prevent contact of the hygroscopic crystal with water. The scintillation light quartz window is optically coupled to a PMT.

ure 6.10 is hermetically encapsulated in an alumina housing in order to protect the crystal from water and moisture. Hydration of the crystal significantly reduces the homogeneity and intensity of the light output and causes efficiency and resolution losses. In order to allow scintillation light to be detected, the capsule is equipped with a quartz window on one side. The window is optically coupled to a cylindrical photo multiplier (PMT) with a diameter of 38 mm, which is mounted in an alumina housing. Furthermore, the PMT is shielded against external magnetic fields with a solid μ metal shield. The 25.4 B3 / 1.5M-E1-Li detector from SCIONIX and its schematic illustration of the inner setup are shown in figure 6.11.

The DAQ chain, shown in figure 6.12 has been designed in a compact way using only portable, stand-alone components. The high voltage supply as well as the signal amplification are performed by the AMP1000-HV-E3-X4 module from SCIONIX which is powered by a 12 V DC supply. The amplification module has been designed explicitly for the oper-

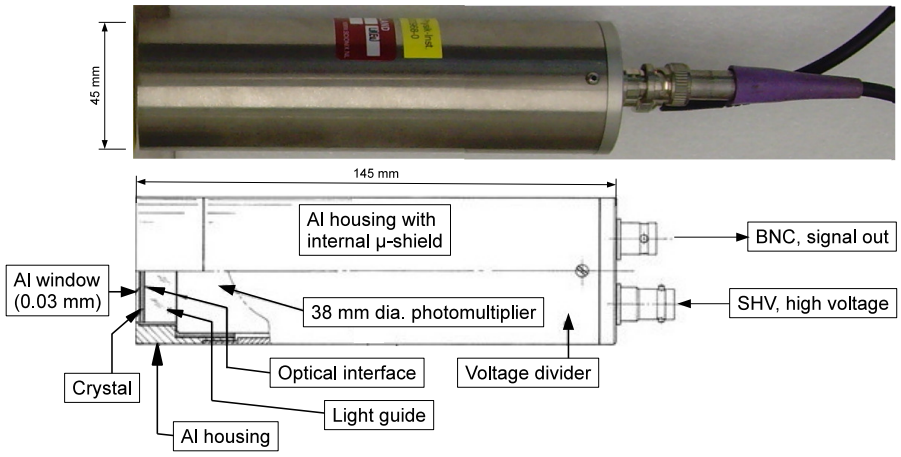

Figure 6.11: Model 25.4 B3 / 1.5M-E1-Li detector from SCIONIX. The alumina housing contains the LiI(Eu) crystal which is optically coupled to a PMT. The PMT is shielded with a μ metal. High voltage is supplied via SHV to the voltage divider of the PMT.

ation of LiI(Eu) detectors and contains a semi-gaussian shaping amplifier with a shaping time of 0.56 μs and a maximal output voltage of +10 V. An analog signal output is avail-

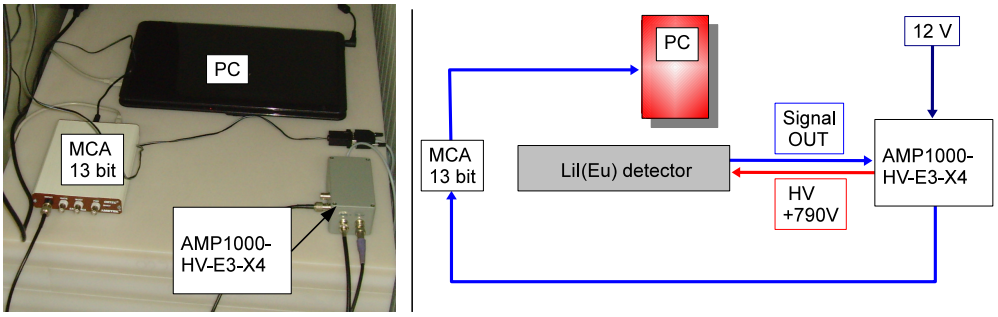

Figure 6.12: DAQ chain used for the LiI(Eu) setup. The AMP1000-HV-E3-X4 module is powered with 12 V DC and provides the high voltage for the PMT inside the detector.

able for spectral acquisition. A second digital TTL output allows to use the module as a counter in combination with an discriminator integrated in the device. Furthermore, the module contains a high voltage converter with a range of up to +1250 V. The high voltage is adjustable via a trimmer and can be monitored by a testpoint contact with a conversion of 250 V output voltage per 1 V measured voltage at the testpoint. For the neutron measurements of the ^{228}Th sources, the analog output has been used in order to acquire full spectra. Data digitization was performed by a stand-alone MCA from ORTEC. The EASY-MCA-2k/8k model with a resolution of 13 bit has been connected via USB to the acquisition PC.

To assure a stable mechanical detector configuration, a detector base made of polyvinyl chloride (PVC) has been build. The base shown in figure 6.13 is used to fix the detector and the moderator discs on the center line. It includes furthermore a source holder, mounted on a lateral guide which allows to change the distance between source and detector. The holder is equipped with a M4 thread allowing to fix any encapsulation of the P02- or VZ3474- type. The thickness of the moderator cylinder can be changed by adding or removing polyethylene discs of 1 cm thickness.

The optimal detection efficiency depends on the moderator thickness and on the solid angle covered by the LiI(Eu) crystal which is given by the source distance. Decreasing of

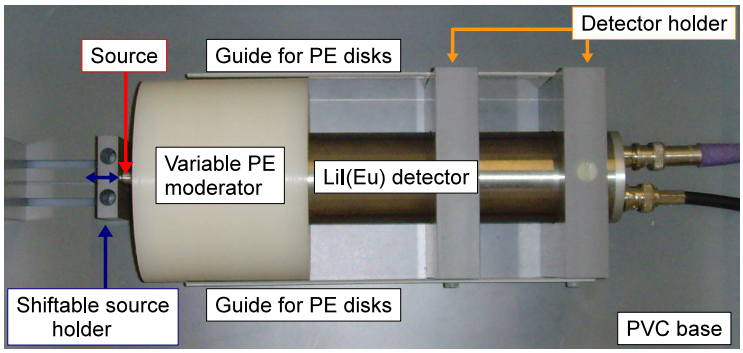

Figure 6.13: LiI(Eu) detector base. The detector tube is fixed by two holders. The moderator block consists of 1 cm thick polyethylene discs, which are centered by two lateral side-guides. The source can be mounted on a source holder which is moveable along the z-axis of the detector.

the source distance increases the neutron flux through the crystal, but it implies also a lower moderator thickness and less thermalized neutrons on the crystal side. This correlates to a lower detection efficiency as discussed above. To find the optimal combination of the source distance and the polyethylene thickness, the moderator can be assembled into one cylindrical block consisting of up to fifteen single polyethylene discs. The discs are 10 cm in diameter and 1 cm thick. The distance between source and detector can be adjusted by the shiftable source holder in order to maximize the solid angle covered by the LiI(Eu) crystal. The detector base is shielded against environmental neutrons in 4π by a boron doped polyethylene shield which has been assembled in a box-configuration. The shield has a density of 1.05 g/cm^3 and consists mainly of polyethylene with a boron mass fraction of 5%. Incoming neutrons are thermalized by the polyethylene and than captured by ^{10}B, which prevents the neutrons to propagate into the inner volume. The shield has been constructed out of 5 cm thick plates assembled in eleven layers. If fully mounted, it forms a box of (80 x 60 x 55) cm with an inner volume of (40 x 20 x 15) cm which contains the detector. The shield assures a minimal shielding distance of 20 cm in 4π. Figure 6.14 shows the LiI(Eu) setup fully mounted in the borated polyethylene shield.

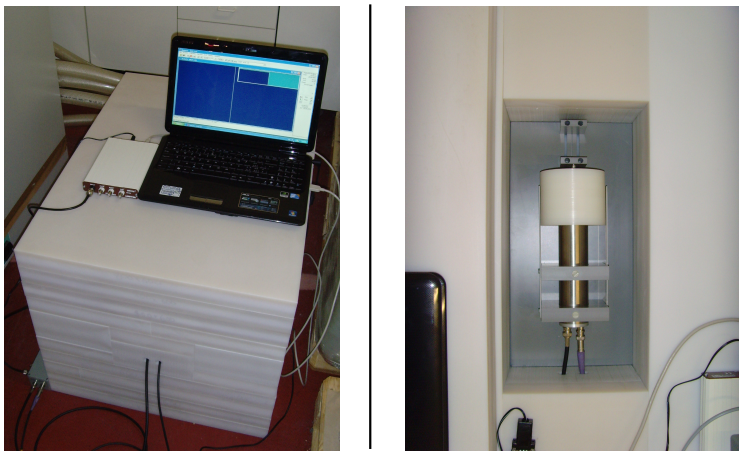

Figure 6.14: Left: LiI(Eu) detector fully mounted in a shield box consisting of borated polyethylene with 20 cm wall thickness. Right: top view of the detector after uncovering the upper shielding.

Before ^{228}Th measurements with the LiI(Eu) setup were performed at LNGS, detector characterization and optimization of the detector configuration took place in an external laboratory located on the surface of the LNGS facility. Besides γ calibrations, the optimal moderator thickness has been determined using a neutron source. Figure 6.15 shows an example of a spectrum acquired with a 37 MBq ^{241}AmBe source and a moderator thickness of two cm. The spectrum in figure 6.15, shows a falling gamma continuum which ends in

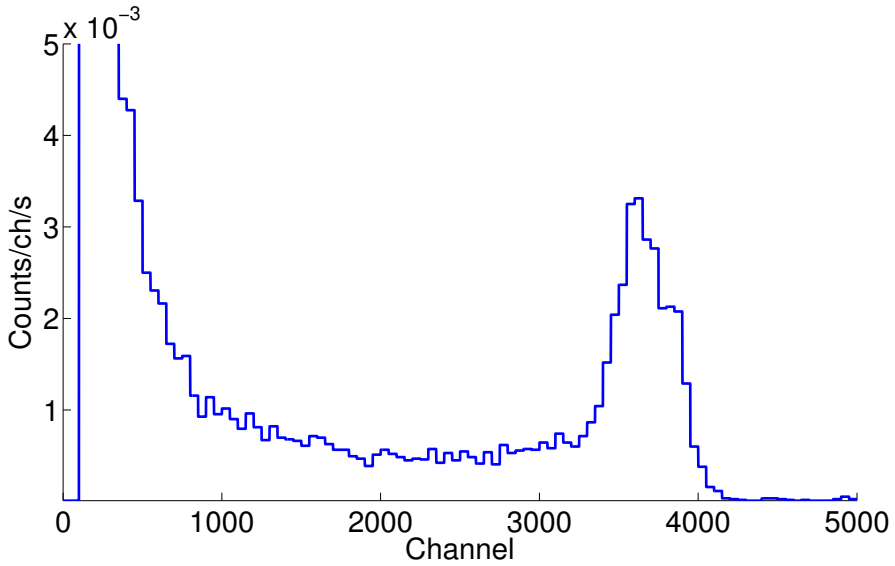

Figure 6.15: LiI(Eu) spectrum taken with a ^{241}AmBe source. The neutron peak at channel $\sim$3650 is followed by a γ continuum at low energies.

the neutron peak at channel $\sim$3600. A further contribution to the spectrum below the

neutron peak is expected from high energetic α particles and from incomplete energy deposition events of the neutron capture reaction. The latter is equivalent to the Wall Effect which was discussed above for ^{3}He detectors.

γ source	^{241}Am	^{133}Ba	^{137}Cs
Energy [keV]	59.54	356.01	661.66
BR [%]	35.92	62.05	84.99

Table 6.1: Gamma sources used for the energy calibration of the LiI(Eu) detector. All three sources emit lines below 1 MeV with branching ratios (BR) between 36 % and 85 %.

Given the crystal thickness of 3 mm, full γ-energy deposition in the detector practically does not occur at energies above ~1 MeV. High energy ^{228}Th lines for example can not be resolved anymore with the detector. For this reason, energy calibration has been performed with three γ sources, which emitted lines below 700 keV. Table 6.1 shows the three sources and their lines used for the energy calibration of the LiI(Eu) setup. The spectra of

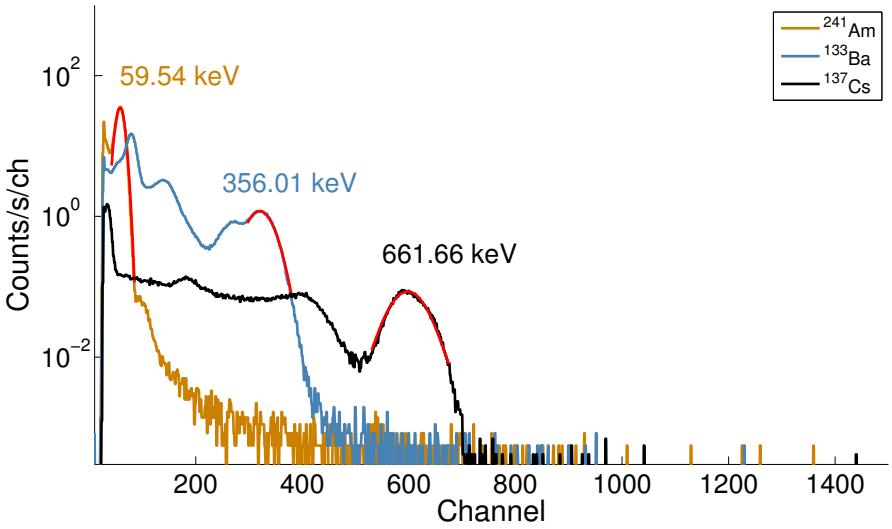

Figure 6.16: LiI(Eu) spectra taken with ^{241}Am, ^{133}Ba and ^{137}Cs. For the energy calibration three prominent lines have been used.

the three sources are shown in figure 6.16. For the calibration, three prominent lines have been used and their positions determined by gaussian fitting. Based on a linear channel calibration fit, the neutron peak position at channel ~ 3650 in figure 6.15 corresponds to an energy E_n of

$$E_n = 3.28 \text{ MeV} \tag{6.17}$$

on the GEE scale.

The relative resolutions σ_R given in table 6.2 range from 45 % for the 59.54 keV line down to 13 % for the 661.66 keV line and follow a distribution which is roughly inversely proportional to the square root of the energy, according to

$$\sigma_R \propto 1/\sqrt{E}\,. \tag{6.18}$$

By definition, σ_R is the ratio between the energy resolution and the event energy which

γ source	^{241}Am	^{133}Ba	^{137}Cs
Energy [keV]	59.54	356.01	661.66
Position [ch]	57.71	319.74	597.8
R FWHM [%]	45.24	19.19	12.88

Table 6.2: Gamma calibration results for the LiI(Eu) detector performed with three sources. The relative resolution improves inversely proportional to the square root of the gamma energy.

is given by the pulse height H,

$$\sigma_R = FWHM/H. \tag{6.19}$$

Because the energy resolution is a consequence of the variations in the number of photo-electrons N_{Ph} emitted by the photocathode of the PMT, equation (6.19) can be written as

$$\sigma_R \sim \sqrt{N_{Ph}}/H. \tag{6.20}$$

Furthermore, the number of emitted photons N_{Ph} is proportional to the energy deposited by a particle interaction in the scintillator and hence the variance in N_{Ph} translates directly into a variance of energy. Thus, equation (6.19) can be written as

$$\sqrt{N_{Ph}}/H = \sqrt{E}/E = 1/\sqrt{E} \tag{6.21}$$

which explains the observed correlation between energy and resolution.

The first measurements to determine the optimal moderator thickness for the LiI(Eu) setup were performed at the University of Zurich with a ^{241}AmBe neutron source. However, the setup was not equipped with the neutron shield yet and therefore the measurements were repeated at LNGS with a fully mounted and shielded detector configuration as shown in figure 6.14. Neutron data were taken at different moderator thicknesses dPE in a range between 0 cm and 12 cm. To maximize the solid angle, the source distance dS has been always kept minimal according to

$$dPE_i = dS_i \tag{6.22}$$

where i is the i'th moderator thickness. The moderator discs were arranged into one single cylinder as illustrated in figure 6.17, allowing to take data at different moderator thicknesses with little effort. Data were taken only after the neutron shield has been fully

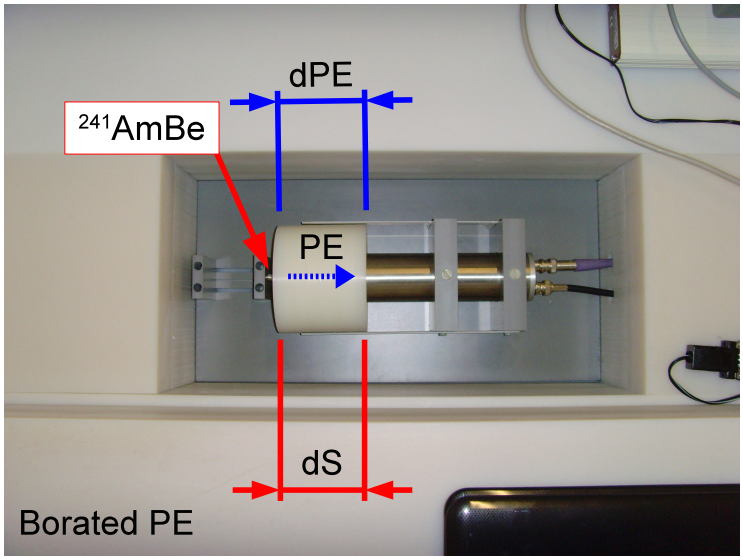

Figure 6.17: Moderator thickness optimization. ^{241}AmBe data were taken at different moderator thicknesses dPE. The source distance dS has been changed according to $dS = dPE$.

mounted and closed.

In order to determine the neutron counts at each moderator thickness, the peaks have been fitted with a gaussian, superimposed with a function B given by

$$B = \alpha + \frac{\beta}{e^{(ch-\mu)/\sigma} + 1} \tag{6.23}$$

where α describes a fixed shift on the y-axis, β is a stepheight, μ is given by the peak position and σ is the peak resolution. The function B describes a smoothed step function which has been used to describe the different background levels around the peak. After the modeled background has been subtracted from the data, the integration interval has been defined by a cumulative plot of the net-peak data. Lower and upper integration limits were defined by 2% respectively 98% of the height of the cumulative distribution.

An example of the neutron peak acquired with an ^{241}AmBe source is shown in figure 6.18. The figure illustrates also the determination of the integration interval. Because the neutron peak is asymmetric, the number of counts has been calculated by the integration of the background subtracted data rather than by integration of the gauss fits.

Furthermore, the integration interval changes for each measurement as a consequence of statistical variations and environmental conditions. For this reason, a final integration interval $[ch_{min}\ ch_{max}]$ has been determined by calculating the mean values of the integration limits for each measurement, resulting in

$$ch_{min} = 3145 \text{ and } ch_{max} = 4126. \tag{6.24}$$

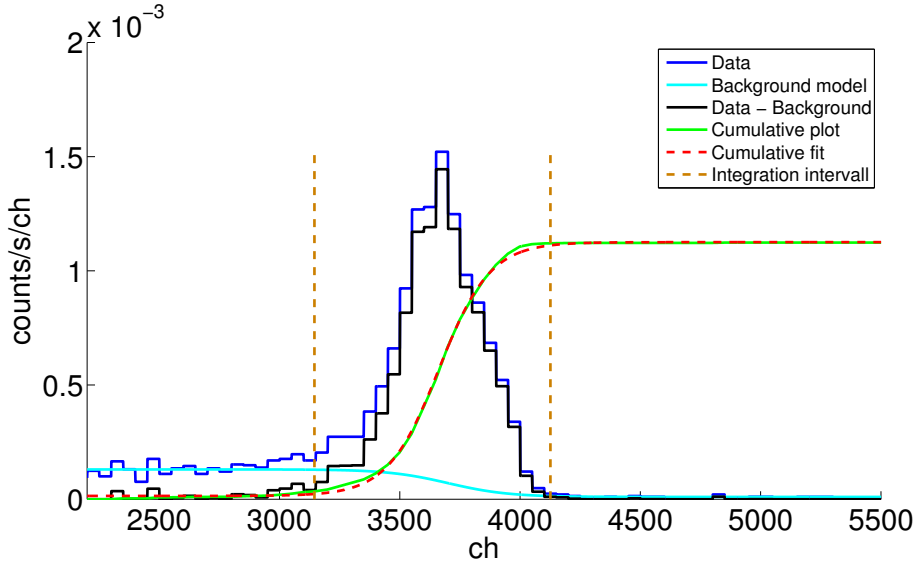

Figure 6.18: Determination of the neutron peak integration interval. The background is modeled and subtracted from the data. The cumulative distribution of the background-subtracted data is fitted and the interval defined by two points at 2% and 98% height of the cumulative fit.

Figure 6.19 shows the count rates as a function of moderator thickness ranging from 2 cm to 12 cm. The results shown were taken at LNGS with a 3.7 MBq ^{241}AmBe source in a P02 type encapsulation which could be mounted on the source holder of the detector base. Further data were taken with a 37 MBq ^{241}AmBe source encapsulated in a lead cylinder of 68 mm in height and 30 mm in diameter. Because the source holder could not be used for such an encapsulation, the source has been fixed on a PVC support instead.

Maximal count rates were obtained at a polyethylene thickness and a source distance of 4 cm with both ^{241}AmBe sources. Measurements performed at a constant source distance and a variable PE thickness resulted in an optimal thermalization at 5 cm, while data taken at the UZH laboratory in the same configuration but without a neutron shield indicated an optimal moderator thickness of 6 cm.

In addition, independent measurements were performed at the University of Zurich with an equivalent LiI(Eu) setup, which has been designed to monitor the environmental neutron background for the XENON experiment. An optimal moderator thickness of 7 cm at a constant source distance has been determined for this detector as described in [86]. However, the analysis method of the data acquired with the latter setup did not include a background modeling for example.

Table 6.3 shows a summary of the optimal moderator thickness as they were determined in different locations and detector configurations with three different ^{241}AmBe sources. While

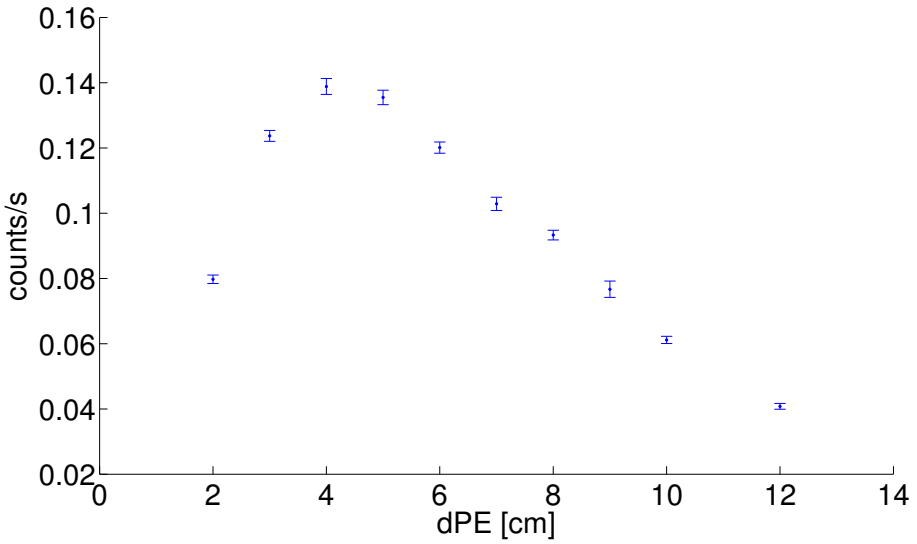

Figure 6.19: Count rates determined with the LiI(Eu) setup at different polyethylene moderator thicknesses. The data were taken at LNGS and the source distance has been changed according to the moderator thickness.

Location	LNGS	LNGS	UZH	UZH
Configuration	$dPE = dS$ LiI(Eu)	$dS = const.$ LiI(Eu)	$dS = const.$ LiI(Eu)	$dS = const.$ LiI(Eu) for XENON
optimal dPE [cm]	4	5	6	7

Table 6.3: Optimal moderator thickness determined with the LiI(Eu) detector at LNGS and at the UZH laboratory with ^{241}AmBe sources.

all measurements performed at LNGS resulted in an optimal moderator thickness of 4 cm, a discrepancy of up to 3 cm occurs with respect to the data acquired at the University of Zurich. It should be also noted that the latter were not optimized in terms of the solid angle.

As shown by the distribution in figure 6.19, an overestimating of the moderator thickness by 1 cm does not lead to drastic losses in the count rates in contrast to an underestimating of the moderator thickness. Count rates taken at 5 cm are reduced by about 3% with respect to count rates measured at 4 cm. Given the discrepancies occurring between the LNGS and the UZH data and the moderate count rate losses towards higher dPE values, a polyethylene thickness of 5 cm has been finally chosen for the measurements of the ^{228}Th sources.

In contrast to the data taken with an ^{241}AmBe source, a remarkable γ continuum from the ^{228}Th source is expected with energies up to 2.6 MeV. Depending on the γ activity of the source, coincident gamma ray emission in the ^{228}Th chain could in principle contribute to

a γ background in the region of interest of the neutron peak. Further pile-up effects could occur in combination with the environmental γ background. In order to reduce the risk

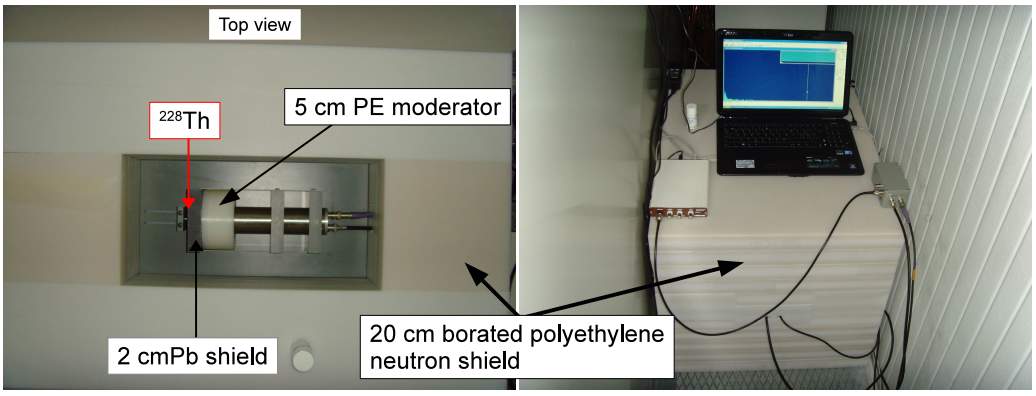

Figure 6.20: Left: internal LiI(Eu) setup used for the ^{228}Th and background measurements at LNGS. Two cm of lead has been used in order to shield against gamma background. Five cm of moderator thickness has been chosen for the measurements. Right: Fully assembled detector at LNGS at a depth of 3400 m.w.e.

of a γ contribution in the neutron peak, a lead block of two cm thickness has been placed in-between the source and the moderator as shown in figure 6.20.

After the determination of the optimal moderator thickness, the LiI(Eu) setup was re-assembled at LNGS in the direct vicinity to the GATOR detector in Hall A. Data were taken with the two commercial sources, TF656 (47.9 kBq) and TF657 (46 kBq) and with the two custom sources SV303 (17.1 kBq) and SV304 (12.28 kBq). Background data has been taken for about 3 months in total. Figure 6.21 shows background data and SV304 ^{228}Th data together with the previously determined integration interval and the expected neutron peak position at channel 3650. Both spectra have been normalized to counts/s/ch. As expected, given the high γ activity of the ^{228}Th source with respect to the environmental γ background, the ^{228}Th spectrum shows a much stronger gamma flank formation than observed in the background data. Although a peak appears in both data sets in the region of interest, both are shifted towards lower energies with respect to the expected position by approximately 330 channels. The shift is equivalent to $\sim$296 keV on the GEE scale. Furthermore, with count rates in the region of interest given by

$$R_{SV304} = (7.92 \pm 0.83) \cdot 10^{-5} \text{ counts/s/ch} \tag{6.25}$$

for the custom SV304 ^{228}Th source, and

$$R_{Bckg} = (7.80 \pm 0.31) \cdot 10^{-5} \text{ counts/s/ch} \tag{6.26}$$

for the background data, both rates are consistent with each other within 1σ.

Although the peak shift could be in principle explained for example by a gain or high

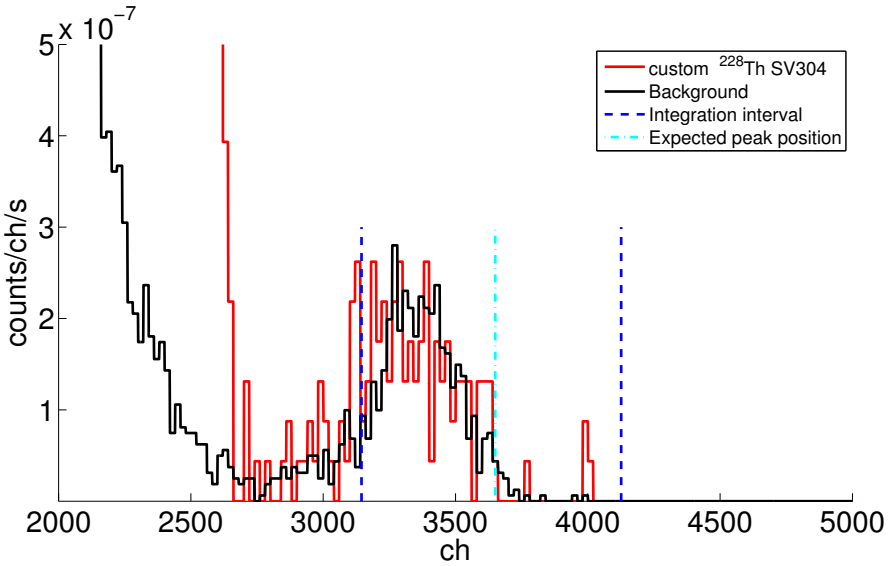

Figure 6.21: Comparison of the LiI(Eu) background and data taken with the custom ^{228}Th source SV304. A peak can be found at channel 3320 instead of channel 3650 as was determined previously for the neutron peak with an ^{241}AmBe source.

voltage de-adjustment during transportation of the detector, a surprisingly different picture appears given by the data taken with a commercial source. Figure 6.22 shows the background spectra and a spectra of the TF656 commercial ^{228}Th source, normalized to counts/s/ch. The higher statistics in the neutron peak of the TF656 data is a consequence

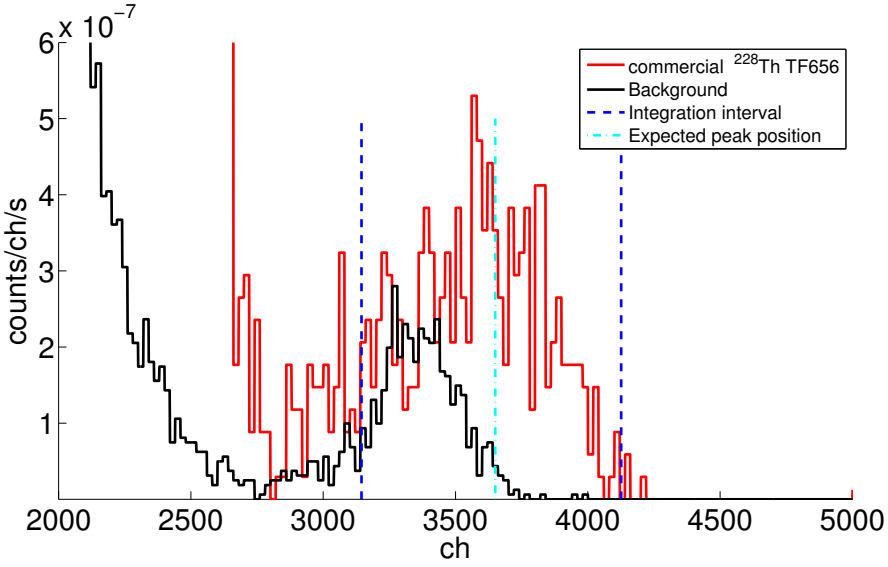

Figure 6.22: Comparison of the LiI(Eu) background with the commercial ^{228}Th TF656 source. The data of the TF656 show a neutron peak at channel $\sim$ 3650.

of a higher activity with respect to the custom SV304 source. Furthermore, commercial sources are expected to have a higher neutron flux than custom sources.

However, the neutron peak of the commercial source appears at the expected position of ∼3650 channels. Hence, the peak shift observed with the custom source is not an artifact of different DAQ conditions. It can be concluded, that the neutron peak is accompanied by a second unidentified peak at around

$$E_{Bckg} = 3 \text{ MeV GEE} \tag{6.27}$$

and that the observed TF656 neutron peak is in fact superimposed with a second background peak of unknown origin.

Single site events of the neutron capture reaction in Li can in principle occur, but with energies given by

$$E_{H^3} = 4/7 \cdot Q \text{ and } E_\alpha = 3/7 \cdot Q, \tag{6.28}$$

they can not explain the observed background peak. With 3.3 MeV GEE measured for the neutron capture reaction, the escaping of one of the reaction products without energy deposition in the scintillator would result in a peak at 1.4 MeV or at 1.87 MeV. Both energies would correspond to a channel number equivalent to 1560 and 2080 respectively.

The second possible neutron reaction channel in ^{6}Li

$$^6\text{Li} + \text{n} \rightarrow {}^7\text{Li} + \gamma + Q \tag{6.29}$$

with a Q-value of 7.2 MeV does not come into consideration, as the reaction is accompanied by a 7.2 MeV γ, which would be represented by a high energetic continuum rather than by a peak. An alternative reaction with the ^{7}Li isotope

$$^7\text{Li} + \text{n} \rightarrow {}^8\text{Li} + \gamma + Q \tag{6.30}$$

can be excluded as well due to the low Q-value of 2 MeV. Secondary reactions with ^{3}H and $^4_2$He like

$$^6\text{Li} + {}^4_2\text{He} \rightarrow {}^{10}\text{B} + \gamma + 4.46 \text{ MeV} \tag{6.31}$$

$$^6\text{Li} + {}^3\text{H} \rightarrow {}^9\text{Be} + \gamma + 17.69 \text{ MeV} \tag{6.32}$$

$$^6\text{Li} + {}^3\text{H} \rightarrow {}^5\text{He} + {}^4_2\text{He} + 15.22 \text{ MeV} \tag{6.33}$$

$$^6\text{Li} + {}^3\text{H} \rightarrow {}^8\text{Li} + \text{p} + 0.8 \text{ MeV} \tag{6.34}$$

can be excluded under the same Q-value considerations as described above.

Given the fact, that the detector is shielded against environmental radiation with 20 cm of borated polyethylene and that in addition it is located underground at 3400 m.w.e., it can be concluded that the formation of the background peak is correlated to the presence

of ^{238}U and ^{232}Th impurities in the components of the detector.

High energetic γ's give rise to a continuous spectral distribution in the LiI(Eu) scintillator and can be excluded. α and β particles are expected to be mostly absorbed in the housing of the detector, given their short ranges in matter. In addition, α particle energies emitted by the ^{238}U and ^{232}Th chains range from 4 MeV to 8.8 MeV with branching ratios up to 100%. The gamma equivalent energy of 3 MeV of the background peak corresponds to an α energy of ∼4.3 MeV if taking into account the quenching factor of 1.44 for the heavy neutron capture reaction products. ^{238}U emits for example 4.2 MeV α particles, but a sensitivity to such α's implies also a sensitivity to higher energetic α particles. In consequence, the spectra would show several α peaks up to ∼8.8 MeV.

In full analogy to the neutron capture reaction, a unique peak at a distinct energy which is independent from the initial α energy can only arise in an α capture reaction. However, the only possible channel is the (α, γ) reaction as described in equation (6.31). Because the Q-value energy of 4.46 MeV is carried away only by the γ, a peak formation like the observed background peak can not be explained by the (α, γ) reaction.

In summary, none of the options considered above can explain the background peak observed in the LiI(Eu) detector in a plausible way. However, although the scintillator consists also of iodine with an atomic fraction of 50%, only lithium targets have been discussed so far. ^{127}I is the only one stable isotope occurring with an natural abundance of 100 %. α reactions with ^{127}I like

$$^{127}\mathrm{I} + {}^{4}_{2}\mathrm{He} \rightarrow {}^{131}\mathrm{Cs} + \gamma + Q \tag{6.35}$$

can take place, but they can also be excluded due to the Q-value of 1.5 MeV. In contrast, a possible explanation for the background peak is given by the following neutron reaction

$$^{127}\mathrm{I} + \mathrm{n} \rightarrow {}^{124}\mathrm{Sb} + \alpha + Q \tag{6.36}$$

with a Q-value of

$$Q = 4.28 \text{ MeV} \tag{6.37}$$

and no γ particles involved. Similar to the neutron capture reaction in ^{6}Li, the total Q energy of this reaction will be shared between heavy particles with short ranges in the crystal. 97 % of the energy will be carried by the α particle and 3% by the ^{124}Sb atom. Assuming the same quenching factor of 1.44 as for the ^{6}Li neutron capture reaction, the energy of 4.28 MeV is equivalent to 2.97 MeV on the GEE scale, which corresponds to a channel number of 3308, a consistent value for the background peak observed at channel ∼3320.

As shown in figure 6.23, the (α, n) cross sections in ^{127}I increase with increasing neutron energies and reach their maximum at ca. 20 MeV. The cross sections range from $\sim 10^{-7}$ b at 3 MeV to 10^{-4} b at 10 MeV. Therefore, thermalized neutrons are not expected to undergo (n,α) reactions in ^{127}I. However, the contribution of ^{127}I in neutron production

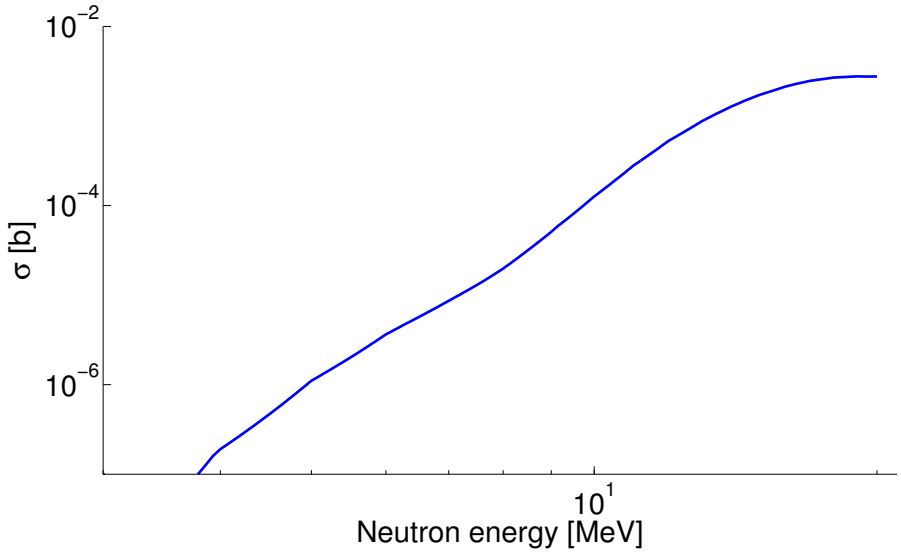

Figure 6.23: Cross sections for the (α, n) reaction in ^{127}I. In contrast to the neutron capture cross sections in ^{3}He, the (α, n) cross sections in ^{127}I increase with increasing energies. Data from [84].

increases with increasing energies, while the contribution of ^{6}Li decreases with increasing energies as shown in figure 6.9. While neutrons from the custom and commercial sources are thermalized by the polyethylene moderator, most of the background neutrons will not pass the moderator and hit the crystal unmoderated with their initial energy.

Background neutrons in the detector setup arise from spontaneous fission of ^{238}U and ^{232}Th which are present as impurities in the mechanical components of the setup, but also from (α, n) reactions within the detector. The materials located in the vicinity of the scintillator crystal are stainless steel, quartz glas, alumina and polyethylene. Neutron rates and spectra from spontaneous fission in ^{238}U and ^{232}Th have been calculated with SOURCES4A with the results shown in table 6.4. The calculations were performed assum-

Spontaneous fission		
Chain	^{238}U	^{232}Th
Neutron rate [n/s/kBq]	$1.09 \cdot 10^{-3}$	$3.02 \cdot 10^{-8}$
Mean energy [MeV]	1.69	1.6

Table 6.4: Neutron rates and mean energies resulting from spontaneous fission of ^{238}U and ^{232}Th.

ing an activity of 1 kBq for each of the two chains. The mean energies of the two calculated spontaneous fission spectra are similar with 1.7 MeV for the ^{238}U chain and 1.6 MeV for the ^{228}Th chain. In contrast, the neutron rate is dominated by ^{238}U with a neutron flux

five orders of magnitudes higher than from spontaneous fission of the ^{228}Th isotope.

While the total neutron rates from spontaneous fission do only depend on the radioactive impurity concentration, neutrons from (α, n) reactions depend also on the matrix material containing the impurities. Table 6.5 shows the results from (α, n) calculations in four materials which are considered as detector material components located in direct vicinity of the crystal. Alumina is used for the endcap and the crystal holder, the housing is composed of stainless steel, polyethylene acts as moderator and is located in front of the crystal and quartz glas (SiO_2) is used for the LiI(Eu) optical interface window. All (α, n)

(α, n) **reactions**		
Chain	^{238}U	^{232}Th
Al: neutron rate [n/s/kBq]	$1.34 \cdot 10^{-2}$	$2.79 \cdot 10^{-2}$
Mean energy [MeV]	1.55	1.68
Steel: neutron rate [n/s/kBq]	$1.49 \cdot 10^{-3}$	$2.25 \cdot 10^{-3}$
Mean energy [MeV]	1.58	1.56
Quartz: neutron rate [n/s/kBq]	$2.13 \cdot 10^{-3}$	$2.09 \cdot 10^{-2}$
Mean energy [MeV]	1.83	2.03
PE: neutron rate [n/s/kBq]	$2.73 \cdot 10^{-3}$	$2.62 \cdot 10^{-3}$
Mean energy [MeV]	3.09	3.78

Table 6.5: Neutron rates and mean energies resulting from (α, n) reactions in the presence of ^{238}U and ^{232}Th in four different materials. The materials are considered as detector component materials located in the vicinity of the crystal.

rate calculations with SOURCES4A were performed assuming an activity of 1 kBq/cm^3 for the ^{238}U and ^{232}Th chains. Although the genuine ^{238}U and ^{232}Th concentrations in the detector components are not known, the calculated spectra show mean neutron energies ranging from 1.5 MeV to 3.8 MeV.

As shown in table 6.5, a higher energetic neutron component could be given for example by (α, n) reactions in polyethylene. The neutron capture cross sections in ^{6}Li for such neutrons would be still five orders of magnitude higher than in ^{127}I and therefore the background data should be characterized by a second line arising at the expected neutron peak position at channel ∼3650. This is not the case as shown in figure 6.21. Assuming the calculated neutron capture cross sections in ^{127}I to be correct, the background peak can not be fully explained by the (α, n) reactions in ^{127}I, unless an unconsidered, high energetic neutron component in the background exists.

6.3 Development of a high purity LiI(Eu) detector

Although the background peak described in the previous section is not fully understood, its origin is suspected to be correlated to the presence of ^{238}U and ^{232}Th impurities in the mechanical components of the LiI(Eu) detector. While moderated neutrons could contribute mainly to the peak at ∼3.3 MeV GEE via the neutron capture reaction in ^{6}Li, high energetic background neutrons could possibly contribute to the neutron capture reaction in ^{127}I with ∼3 MeV GEE. Whatever the solution is, both peaks do overlap which results in poorer discrimination efficiency between the neutrons from the source and the background.

Despite the hypothetical considerations about the origin of the background peak, neutrons from spontaneous fission and (α, n) reactions of ^{238}U and ^{232}Th impurities in the detector do contribute to the background without doubt. Therefore, to reduce the internal neutron background of the LiI(Eu) detector, a new LiI(Eu) setup has been designed consisting mainly of ultraclean copper components. For the new setup, a commercial LiI(Eu) crystal with a diameter of 25.4 mm and a height of 3 mm was used. The same type is implemented in the detector described in subsection 6.2 and shown in figure 6.11.

Given the hygroscopic properties of the LiI(Eu) scintillator, the crystal encapsulation has not been customized and is the only one commercial component in the new setup. Therefore, if α particles are the main contributor to the background peak formation, the rate should not change in the new setup assuming the encapsulation to be the dominant source of α's which can penetrate the scintillator crystal. Although the quartz window is also in direct contact with the scintillator, it is extremely radio pure in contrast to alumina. Table 6.6 shows examples of measured radio impurities in different materials. The highest

Material	^{238}U [ppb]	^{232}Th[ppb]
Alumina	400	16.2
Steel	<160	<150
Si (quartz)	<5	<4
Glas	950	2980
Polyethylene	60	270
Copper	<3	<3

Table 6.6: Examples of ^{238}U and ^{232}Th screening results performed on different materials. The data were taken from the ILIAS radiopurity database [87].

impurities can be found in glass, alumina and stainless steel. Copper is the cleanest material in terms of ^{238}U and ^{232}Th concentrations. Besides the alumina housing of the crystal which has not been replaced by a high purity encapsulation, the other detector components like the housing, the endcap and the base structure were replaced by high purity copper. All parts of the new LiI(Eu) detector were designed with regard to a minimal mass and

minimal material impurities. Figure 6.24 shows the mechanical and electrical components involved in the detector. Furthermore, the commercial PMT has been replaced by a high purity PMT from Hamamatsu, equipped with a quartz window. The radio impurities of commercially available PMT windows provided for example by SCIONIX, [88] range from

$$100 \text{ ppb to } <10 \text{ ppb for } ^{238}\text{U} \tag{6.38}$$

and

$$250 \text{ ppb to } <10 \text{ ppb for } ^{228}\text{Th}. \tag{6.39}$$

The PMT used in the new detector is an ultraclean, cubic module of the R8520 type with a lateral length of 25.7 mm and a total mass of 25.14 g. The module has a borosilicate

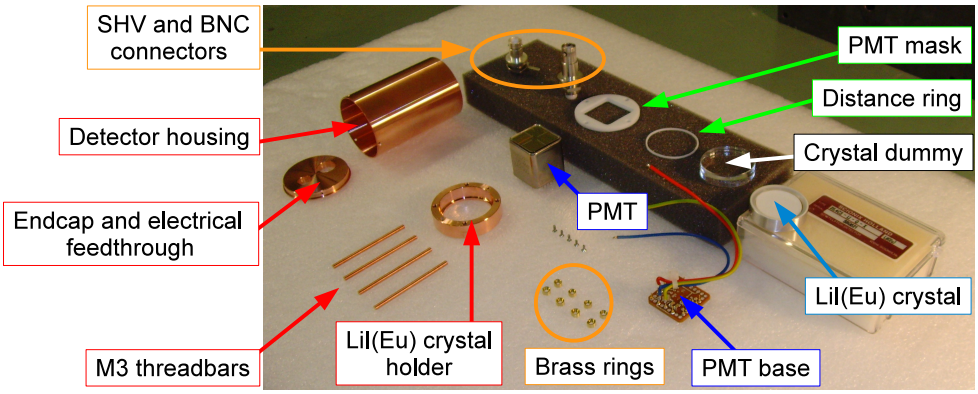

Figure 6.24: Complete set of components used in the design of the high purity LiI(Eu) detector.

glass window with a quartz fraction of 70%. The same PMT type is in use for the XENON experiment. The PMT's have been screened in the GATOR facility at LNGS in the past [89] with the screening results shown in table 6.7. The PMT has been optically coupled

PMT R8520	^{238}U	^{232}Th	^{40}K	^{60}Co
Impurity [mBq/PMT]	1.4	0.85	4.6	0.6

Table 6.7: Radioimpurities in the Hamamtsu R8520 PMT. The PMT type is used in the XENON experiment and was adopted in the high purity LiI(Eu) design. Data are taken from [89].

to the LiI(Eu) scintillator using a commercial silica high vacuum grease from WACKER as illustrated in figure 6.25. For the coupling, the silicon grease has been applied on the window of the PMT and the LiI(Eu) crystal. The crystal has been pressed against the PMT window from the top. In order to prevent air bubbles to be enclosed in the grease and to minimize the thickness of the interface layer, the crystal has been rotated several times under pressure. Furthermore, the procedure has been trained with a dummy crystal consisting of a transparent PVC disc. The latter allowed for an optical verification of

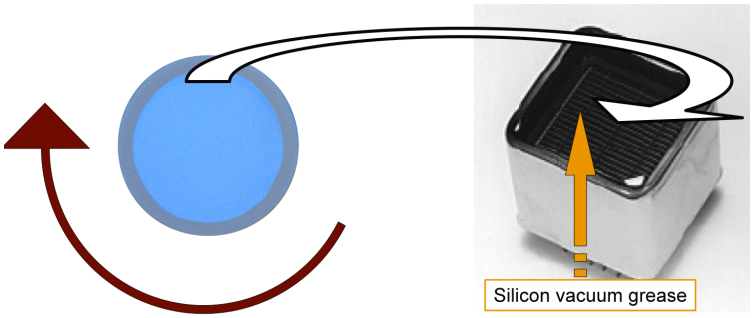

Figure 6.25: Optical coupling between the Hamamatsu PMT and the LiI(Eu) crystal. In the first step, a silicon vacuum grease is applied to the crystal window. The crystal is than pressed on the PMT and rotated several times in order to avoid air bubbles enclosed in the coupling layer.

the grease layer obtained. The alignment of the crystal and the PMT on the z-axis has been performed by the support structure made of copper and a teflon mask mounted on the signal readout side of the PMT. Teflon has been chosen instead of copper in order to prevent the risk of pin bypassing or electrical discharge between the PMT connectors and the mask. The mask is fixed on the holder by four M3 copper thread bars which are fixed by eight rings made of brass. Because the housing of the PMT is at high voltage, a 1 mm thick teflon ring between the copper crystal holder and the window of the PMT has been mounted to prevent any contact between the PMT and the copper housing. The housing is a closed-end cylinder with a wall thickness of 1 mm and a height of 80 mm. The diameter has been chosen to be 45 mm. The dimensions of the cylindrical housing allow to mount the detector in the already existing base and neutron shield designed for the commercial LiI(Eu) detector, as described in section 6.2.

The endcap of the housing includes two feedthroughs for the electrical connection of the high voltage and the BNC signal readout. After mounted, the cap can be fixed by screws from the side. To assure full light tightness, a teflon tape is used between the cap and the housing wall. An isolation tape can be wrapped around the interface edge between the cap and the housing additionally. Table 6.8 shows the detector components and their masses. In total, 214.2 g of copper, 1.4 g of brass and 5 g of teflon have been used. Because the alumina used for the LiI(Eu) encapsulation could not be removed and given its direct vicinity to the crystal, the highest background contribution is expected from the alumina, followed by quartz glass and copper which has been chosen to be ultraclean with a chemical impurity of >99.99 %. Additionally, in order to remove surface contaminations of the copper, the components have been etched in a sulfuric acid bath with a concentration of 2% before mounting. The etching took place for about six hours at room temperature.

Figure 6.26 and figure 6.27 show the different stages of the detector mounting. First, the copper threadbars are mounted on the copper crystal holder and fixed with the brass

Component	Material	Total mass [g]
Housing	Copper	98.5
Crystal holder	Copper	49.2
Endcap	Copper	57.1
Threadbars	Copper	9.4
Fixation rings	Brass	1.4
Distance ring	Teflon	0.2
PMT mask	Teflon	4.8

Table 6.8: Materials and their masses used in the high purity LiI(Eu) setup. The highest mass contribution with a total mass of 214.2 g is given by the copper parts.

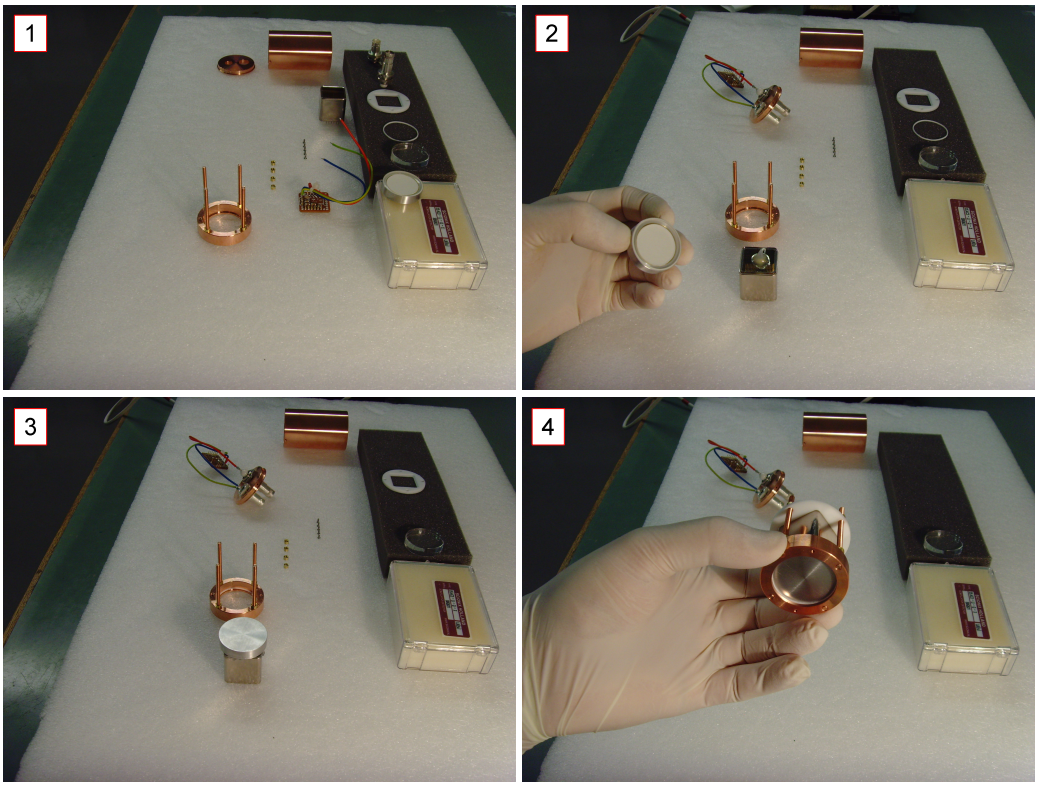

Figure 6.26: First detector mounting steps: 1) mounting of the four copper threadbars on the holder. 2) Assembling of the electrical connectors on the endcap and coupling of the PMT to the LiI(Eu) crystal. 3) Crystal and PMT are coupled and ready to be fixed and aligned in the holder. 4) Mounted crystal and PMT. The structure is ready to be enclosed in the housing.

rings. The electric connectors are mounted on the endcap and connected to the PMT base. The teflon distance ring is placed in the copper holder and the crystal optically coupled to the PMT. Both elements are placed in the holder and aligned by the teflon PMT mask.

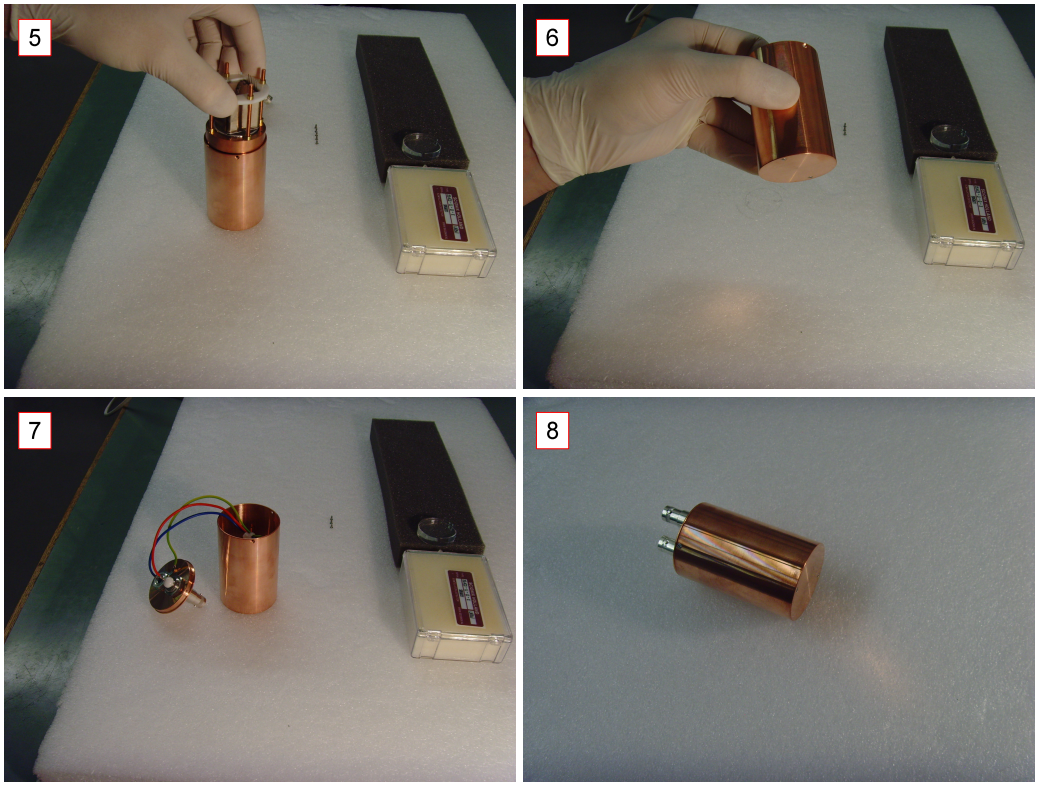

Figure 6.27: Final detector mounting: 5) inserting the PMT structure with the coupled crystal into the housing. 6) Fixing of the crystal holder from the bottom of the housing, using two M2 screws. 7) PMT base is mounted and the detector ready to be closed. 8) Fully assembled detector.

Fixation of the mask takes place via four brass rings mounted from the top. The structure is inserted in the copper housing and fixed with two M2 screws from the bottom side of the housing. After mounting of the base structure with the PMT and the crystal, the detector can be closed and light tightened.

The different type and geometry of the PMT used in the high purity LiI(Eu) setup, as well as the different optical couplings can influence the scintillation light gain, and hence both, commercial and high purity detector configurations are expected to have different signal gains, resulting in spectra which are shifted with respect to each other. However the total detector efficiency is given merely by the LiI(Eu) crystal and its scintillation light induced by particle interactions. Both configurations use the same LiI(Eu) crystal and therefore it can be assumed that both detectors have the same detection efficiency.

The setup has been transported to LNGS and mounted in the superstructure of the commercial detector in November 2011. At this time, the custom ^{228}Th sources were not available anymore for neutron measurements, as they were already mounted in the GERDA calibration system. Direct neutron flux comparisons of the commercial and custom sources

were not possible and therefore a campaign has been started with the goal of determining merely the background reduction gained with the new LiI(Eu) setup with regard to future neutron flux measurements.

Due to the negative high voltage required by the R8520 PMT used in the high purity detector, the original DAQ chain had to be modified. A portable DSA1000 spectrum analyzer from Canberra has been used, which is equipped with all components required for the detector operation. The module includes a negative and a positive high voltage supply, a 14 bit MCA and a shaping amplifier. The operation voltage has been adjusted to -750 V. As described above, assuming that both LiI(Eu) crystals used are identical, the efficiency for both detectors is expected to be the same. This applies to neutrons and high energetic γ's in particular. Detection efficiencies for α-, β- and low energy γ- particles can be different in both detectors given by the different housing materials involved in both setups.

Although, a quantitative confirmation of the equal efficiencies can be performed by ^{241}AmBe measurements with both detectors, such measurements would require the operation on the surface of LNGS and were skipped at first for practical reasons. Conclusions on the background reduction achieved with the high purity detector can be done independently of the detection efficiency by comparing the background to signal ratios. To do so, the high purity

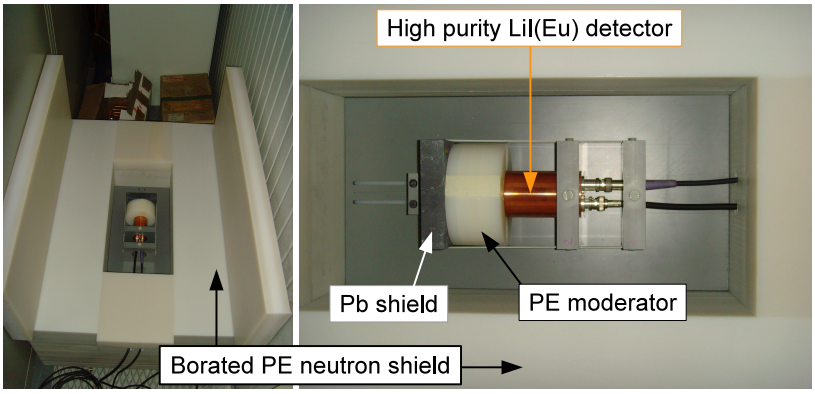

Figure 6.28: High purity LiI(Eu) detector set up at LNGS. The configuration is the same as used with the commercial detector. It includes five cm of a polyethylene moderator, a lead shield of two cm thickness and the borated polyethylene neutron shield.

detector has been set up in the same configuration as the commercial one, including five cm of a polyethylene moderator and a gamma lead shield of two cm thickness as shown in figure 6.28.

High purity detector data of the commercial TF656 ^{228}Th source have been taken for 22 days, while background has been acquired for 79.2 days. The two data sets acquired with the high purity detector have been compared with the equivalent data acquired with the commercial LiI(Eu) setup. Table 6.9 shows an overview of the data collected for the determination of the background reduction. Because TF656 data were acquired with both

Commercial LiI(Eu)	TF6556 ^{228}Th	Background
Lifetime [d]	19.65	93
Activity [kBq]	47.9	-
High purity LiI(Eu)	TF6556 ^{228}Th	Background
Lifetime [d]	22.05	79.22
Activity [kBq]	40.9	-

Table 6.9: Overview of the runs with the commercial and the high purity detectors. The data were used to determine the background reduction of the high purity LiI(Eu) detector.

detectors within a time period of about five months, the different γ activities of the TF656 source had to be taken into account in the spectral normalization. Figure 6.29 shows a comparison of the commercial ^{228}Th source (TF656), acquired with both detectors. The spectra were normalized to counts/s/ch/kBq. Because, two different DAQ chains were

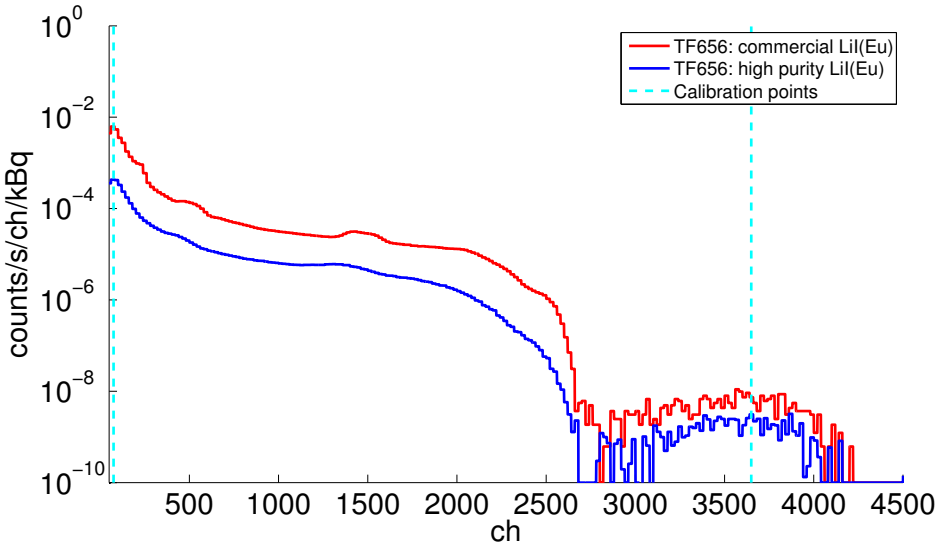

Figure 6.29: Spectra of the commercial TF656 ^{228}Th source acquired with the commercial and the high purity LiI(Eu) detectors.

used for both detectors, the channel scale of the high purity setup has been calibrated on the scale of the commercial detector in order to allow for a direct data comparisons. The calibration has been performed on the neutron peak and a low energy gamma peak as indicated in the figure. Assuming the same detection efficiencies for both detectors, the reduction in the rates which is also observable in the full γ continuum, can be interpreted as a drastic reduction of the ^{238}U and ^{232}Th activities which translates into a lower neutron rate induced by (α, n) reaction with adjacent materials. The rates in the spectrum of the high purity detector are lower by about a factor of 10 with respect to the commercial

detector.

The background spectra shown in figure 6.30 indicate a change in the ^{238}U and ^{232}Th fractions given for example by different slopes of the spectra below channel ∼1500. Furthermore, a peak appearing at channel ∼1400 in the background data of the commercial detector, does not appear anymore in the background of the high purity detector. The dis-

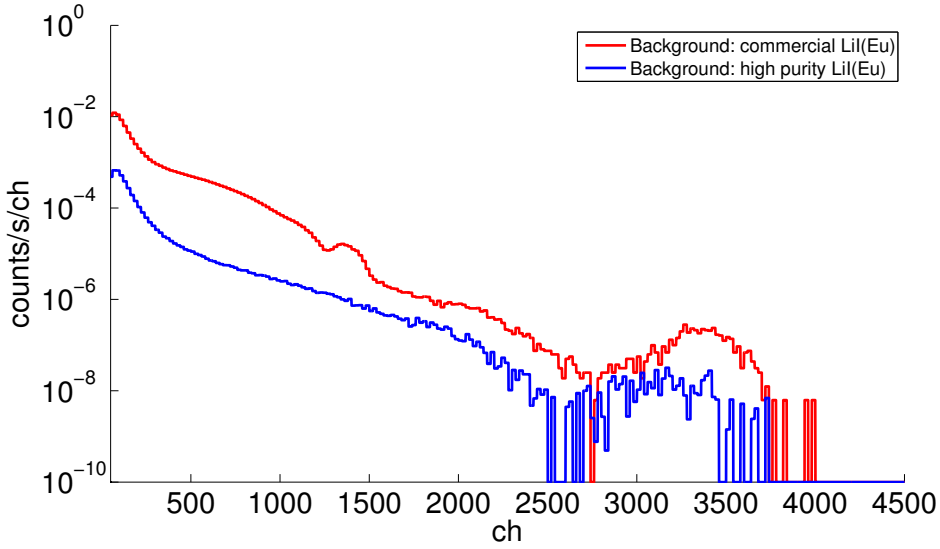

Figure 6.30: Full background spectra acquired with the commercial and the high purity LiI(Eu) detectors. The different spectral shapes indicate different U and Th impurity contributions in both setups.

tributions above channel 3100 in the region of the expected neutron peak are also different in shape and count rates.

In order to quantify the effect of background reduction and to exclude efficiency effects, the background to signal ratios have been analyzed in both detectors. Figure 6.31 shows the spectra for both detectors taken with the TF656 ^{228}Th source and the acquired background data. The integration interval as it has been previously determined with an ^{241}AmBe source is marked, as well as the position of the background peak (pos1) and the position of the expected neutron peak (pos2). The bin size was chosen to be 200 channels wide and the data were not normalized on the activity yet.

The TF656 high purity data show a neutron peak at the expected position but also a reduction in the count rate which can not be explained by the lower source activity and which furthermore is not consistent with the data of the commercial detector within statistical errors. The same applies to the background peak which has been drastically reduced with respect to the commercial background data.

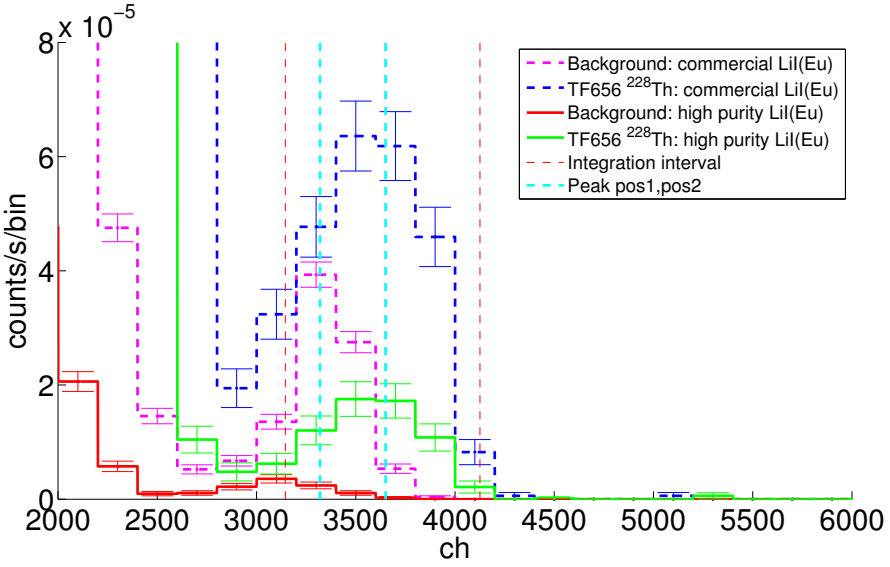

Figure 6.31: Comparison of the background and commercial ^{228}Th data taken with the commercial and the high purity LiI(Eu) detectors. The binsize chosen in the plot is 200 channels. Although not normalized on the source activity, the plot indicates a drastic background reduction, assuming equal efficiencies of both detectors.

The mean background reduction has been calculated by determining the net rate in the integration interval of the data taken with a source, normalizing on the source activity and dividing by the background rate integrated in the same interval according to

$$\frac{S}{B} = \frac{\int\limits_{ROI} (\text{Counts(Source)}/T_S \text{ - Counts(Background)}/T_B)/A_S}{\int\limits_{ROI} \text{Counts(Background)}/T_B} \tag{6.40}$$

where T_S and T_B are the lifetimes of source and background data respectively, A_S is the source activity at the time of data taking and ROI is the region of interest defined by channel 3145 and channel 4126.

Applying equation (6.40) to the available data, a signal to background ratio per 1 kBq source activity of

$$\frac{S}{B}\,|_{cmr} = 4.25 \cdot 10^{-2} \pm 3.68 \cdot 10^{-3} \tag{6.41}$$

for the commercial detector and

$$\frac{S}{B}\,|_{hp} = 2.62 \cdot 10^{-1} \pm 5.16 \cdot 10^{-2} \tag{6.42}$$

for the high purity detector has been determined. Both results do not depend on the detector efficiency and can be translated into a background reduction G_{Bckg} represented

by the ratio between both S/B values with

$$G_{Bckg} = \frac{\frac{S}{B}\,|_{hp}}{\frac{S}{B}\,|_{cmr}} = 6.17 \pm 1.33. \tag{6.43}$$

Equation (6.43) represents the mean background reduction in the neutron peak. A more specific, energy dependent view of the reduction is shown in figure 6.32. The plot shows the background to signal ratios for both detectors in each bin together with the two peak positions in the region of interest. The ^{228}Th data have been normalized to an activity of 1 kBq. While the B/S ratios below channel 3200 are consistent with each other for

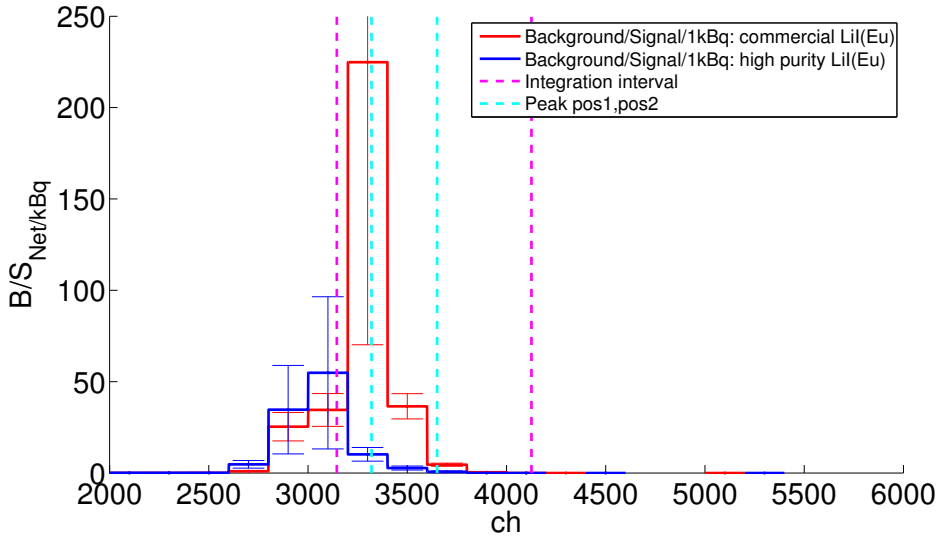

Figure 6.32: Background to signal ratios in the commercial and in the high purity LiI(Eu) detectors. The signals were defined as the net rates normalized to 1 kBq source activity.

both detectors, a significant difference in the ratios can be observed in the region of the background peak at channel 3320 and above. Figure 6.33 shows the relation between the B/S ratios for both detectors for each bin in analogy to equation (6.43). A default value of one for B_{cmr}/B_{hp} has been chosen for bins containing zero events. Those should not be considered. Considering the bins within the integration interval, a mean background reduction of

$$G_{Bckg}\,|_{BIN(ROI)} = 8.8 \pm 3.8 \tag{6.44}$$

was determined, which is consistent with the mean value calculated with equation (6.43). Based on equation (6.43) and (6.44) a mean background reduction of

$$G_{Bckg} = 7.5 \pm 2.0 \tag{6.45}$$

can be calculated in the region of interest around the neutron peak for the high purity LiI(Eu) detector.

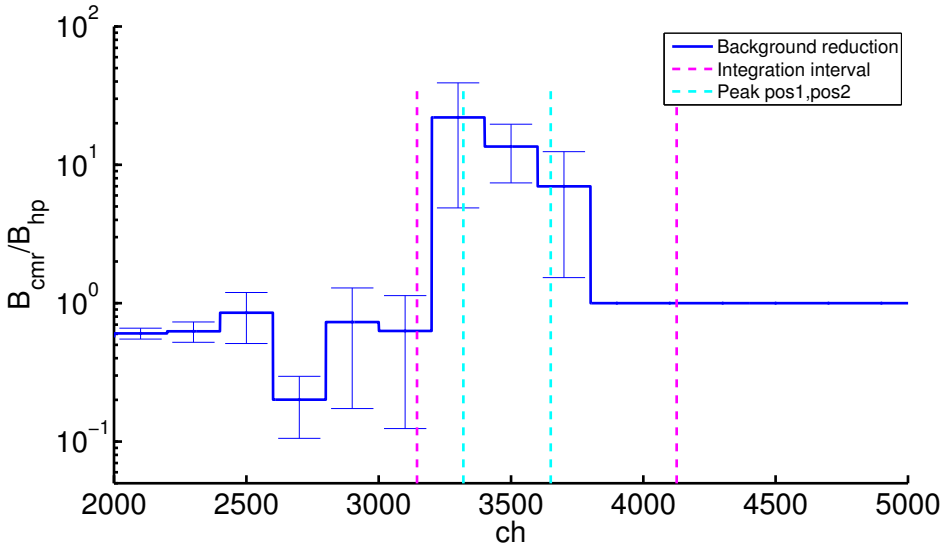

Figure 6.33: Background gain G_{Bckg} of the high purity detector with respect to the commercial detector as a function of energy.

6.4 Neutron flux reduction - Results

First neutron flux measurements campaign

After the production of the prototype ^{228}Th source, a first neutron flux measurement campaign was performed in 2009 at LNGS with the ^{3}He setup in collaboration with Serena Fattori, Roberto Santorelli, Carla Cattadori and Enrico Bellotti. Because, the conditions of the measurements and the analysis procedures are not known exactly, the results are listed below but will not be subject to a detailed, further discussion.

The very first neutron measurement was performed by S.Fattori with a ^{3}He setup which was used for neutron background measurements at LNGS. The detector was equipped with a cylindrical polyethylene moderator but had no shield against environmental neutrons. Monte Carlo simulations for the setup were available allowing for a total neutron flux determination of

$$A_{Abs} = 9.6 \cdot 10^{-4} \pm 1.7 \cdot 10^{-4} \text{ neutrons/s/kBq} \tag{6.46}$$

for the P02 custom source.
The neutron rate calculated with SOURCES4A for a ThO_2 source is

$$A_{Abs} = 2.2^{+0.99}_{-0.51} \cdot 10^{-4} \text{ neutrons/s/kBq} \tag{6.47}$$

However, the result obtained with SOURCES4A describes the ideal case with oxygen as the only target material for the α particles emitted by the source. Impurities of the precursor solution are expected and can increase the neutron rate of the custom source to some

extent. A relative measurement comparing the neutron rates from a commercial and from a custom source has not been performed with the detector configuration described above.

The second modified version of the ^{3}He detector has been equipped with a neutron shield consisting of a cadmium foil and borated paraffin blocks of 10 cm thickness. The detector shown in figure 6.6 had a polyethylene moderator thickness of 6.5 cm. The setup has been used to compare the neutron fluxes of the first custom source and a commercial source. The count rates in table 6.10 were obtained after the background has been subtracted. For

Source	neutron count rate [counts/s]
^{228}Th commercial	$(9.63 \pm 0.2)\cdot 10^{-3}$
^{228}Th custom	$(1.89 \pm 0.1)\cdot 10^{-3}$

Table 6.10: Net count rates in the ^{3}He detector obtained for a commercial and for the first custom ^{228}Th source. Background has been subtracted in the data.

the commercial ^{228}Th source, a gamma activity of

$$A_{cmr} = 43 \pm 4 \text{ kBq} \tag{6.48}$$

has been reported, while for the custom source an activity of

$$A_{cstm} = 14.6 \pm 1 \text{ kBq} \tag{6.49}$$

was determined at the time of data taking. Furthermore, based on Monte Carlo simulations a detection efficiency of

$$\epsilon_{He} = (7 \pm 1)\% \tag{6.50}$$

was calculated for the detector configuration.
Based on the γ activities reported, and the detection efficiency ϵ_{He}, the absolute neutron fluxes shown in table 6.11 have been measured for the commercial and for the custom source. The effective neutron flux reduction G_{nRed} gained by a custom produced ^{228}Th

Source	neutron count rate [counts/s/kBq]	Total neutron rate [n/s/kBq]
^{228}Th commercial	$(2.24\pm0.2)\cdot 10^{-4}$	$(3.20\pm0.5)\cdot 10^{-3}$
^{228}Th custom	$(1.30\pm0.1)\cdot 10^{-4}$	$(1.86\pm0.3)\cdot 10^{-3}$

Table 6.11: Total neutron fluxes from a commercial and a custom ^{228}Th source under the activity assumptions from equation (6.48) and (6.51). A detection efficiency of 7% has been used.

source is expressed by the measured ratio of the total neutron flux rates from the commercial and the custom source and is given by

$$G_{nRed} = 1.7 \pm 0.4. \tag{6.51}$$

The two independent total neutron flux measurements of the custom source resulted in a rate of

$R^1_{cstm}(^3\text{He}) = (9.6\pm1.7)\cdot10^{-4}$ neutrons/s/kBq determined with the first setup and

$R^2_{cstm}(^3\text{He}) = (1.86\pm0.3)\cdot10^{-3}$ neutrons/s/kBq given by the second, modified ^{3}He setup.

Both values are consistent with each other within two sigma and are of the same order of magnitude as the value calculated for a ThO_2 source with SOURCES4A

$R_{cstm}(\text{SOURCES4A}) = 2.2^{+0.99}_{-0.51} \cdot 10^{-4}$ neutrons/s/kBq.

On the other hand, neutron flux calculations for a commercial ^{228}Th source resulted in

$R_{cmr}(\text{SOURCES4A}) = (1.4^{+0.65}_{-0.33}$ - $2^{+1.42}_{-0.49})\cdot10^{-2}$ neutrons/s/kBq

depending on the assumed chemical composition of the ceramic. The measured absolute neutron flux of the commercial source has been found to be

$R_{cmr}(^3\text{He}) = (3.20\pm0.5)\cdot10^{-3}$ neutrons/s/kBq,

which is one order of magnitude lower than the value calculated with SOURCES4A. The neutron flux reduction value of 1.7±0.4 determined with the modified ^{3}He setup indicates that the assumptions of the chemical composition within a commercial source were wrong in this case or that the gamma activity of the same was different from the reported value. Because, no data sheet of the commercial source was available including the information about the source activity and the internal design, the discussion of the results will not be continued.

Second neutron measurement campaign

The two custom ^{228}Th sources SV303 and SV304 and two commercial sources TF656 and TF657 from Eckert&Ziegler, were measured in a second campaign in year 2011. The goal of the campaign was to perform relative neutron flux measurements. Data were taken of all four sources with the shielded ^{3}He setup as shown in figure 6.6 and with the alternative LiI(Eu) detector shown in figure 6.14. The campaign did not embrace measurements with the high purity LiI(Eu) detector described in section 6.3, because the custom sources were mounted in the calibration system of GERDA at the time when the high purity detector was ready for operation.

Table 6.12 shows an overview of the data taken with the ^{3}He and the commercial LiI(Eu) detector. The measurements were performed in parallel with both detectors at LNGS, before the two custom sources have been mounted in the GERDA calibration system. Data

^{3}He detector		
Source	Lifetime [days]	Activity [kBq]
SV303 custom	11	17.29 ±15%
SV304 custom	19	12.1 ±15%
TF656 commercial	9.5	49.21 ±5%
TF657 commercial	7	50.31 ±5%
Background	52	-

LiI(Eu) commercial detector		
Source	Lifetime [days]	Activity [kBq]
SV303 custom	18.2	17.1 ±15%
SV304 custom	13.2	12.3 ±15%
TF656 commercial	19.7	47.9 ±5%
TF657 commercial	75.5	46.1 ±5%
Background	93	-

Table 6.12: Overview of the measurements performed during the second neutron campaign at LNGS. Two custom ^{228}Th sources and two commercial sources were measured with a ^{3}He detector and a LiI(Eu) detector.

acquisition took place for at least one week for each source with the ^{3}He detector which gave sufficient statistics in the neutron peak as a result of the high detection efficiency of ∼7%. Although the LiI(Eu) detection efficiency for thermal neutrons reaches almost 100%, the total detection efficiency determined with an AmBe source is two orders of magnitude lower than of the ^{3}He tube and is given by ∼0.07%. The relatively low LiI(Eu) efficiency is mainly a consequence of the small sensitive volume of the crystal with respect to the sensitive volume of the ^{3}He tube. Therefore data acquisition with the LiI(Eu) detector should be performed with significantly longer lifetimes. However as a result of the time constraints given by the schedule for phase I of GERDA, lifetimes of only eighteen and thirteen days could be reached for the SV303 and SV304 sources.

In the following the results of the ^{3}He measurements and of the LiI(Eu) measurements will be discussed in more detail.

6.4.1 ^{3}He results

Figure 6.34 shows a background spectrum acquired for 52 days and a spectrum of a commercial ^{228}Th source acquired for 7 days with the ^{3}He detector. The background shows a falling gamma continuum which develops into a flat distribution above channel 1500, without an indication for a neutron peak in the region of interest between channel 2000 and channel 3000. In contrast, the TF657 spectrum shows a parallel gamma distribution reaching a local minimum at about channel 2000, before it develops into a neutron peak

with a maximum at channel 2450 and an energy equivalent of 764 keV. Because of the flat

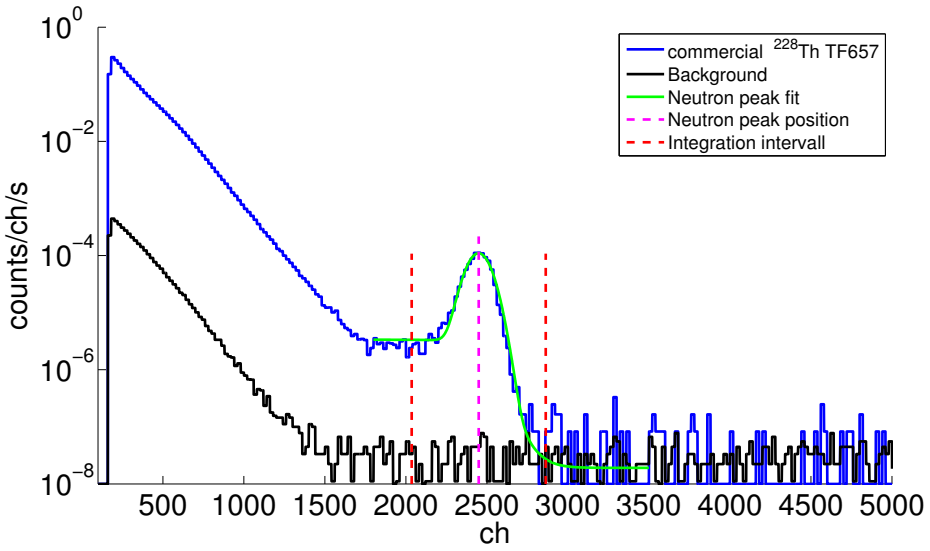

Figure 6.34: Background and ^{228}Th spectra taken with the ^{3}He detector. The flat background distribution in the region of interest around the neutron peak and the broad and flat saddle point around channel 2000 allow for an integration interval of $\pm 6\sigma$ for the determination of the neutron counts.

distribution of the saddle point around channel 2000 with a width of about 300 channels and a constant background above the neutron peak at channel >3000, a broad integration interval can be chosen in order to determine the neutron counts. The neutron peak in figure 6.34 can be fitted with a function P_{fit} which is the superposition of a gaussian and a smoothed step function expressed by

$$P_{fit} = A \cdot exp[-(\frac{ch-\mu}{\sqrt{2}\cdot\sigma})^2] + \alpha + \frac{\beta}{e^{(ch-\mu)/\sigma}+1} \tag{6.52}$$

where A is the amplitude, μ is the peak position, σ is the peak resolution and α and β are constants determining the stepheight and the level of the flat background above the peak. Due to the agreement between the fit and the spectral distribution in a wide range around the peak and the flat saddle point distribution around channel 2000, an integration interval of $\pm 6\sigma$ has been chosen for the neutron counts determination with

$$ch_{min} = 2036 \text{ and } ch_{max} = 2863. \tag{6.53}$$

Figure 6.35 shows the data off all four sources and of the background. Outstanding in the plot is the full data set of the commercial TF656 source with a lifetime of 9.5 days. The spectrum shows a background above the neutron peak which is higher up to two orders of magnitude with respect to the other four spectra. Furthermore the saddle point plateau is higher by about a factor of 10 with respect to the spectrum of the comparable TF657

source. The period of data taking with the TF656 source covers with a water damage caused by condensed water dropping from the top at the detectors location. The presence of water on the DAQ entailed finally a failure of the preamplifier and the shaping amplifier. It can be assumed, that over the period of water dropping, a consecutive loss of the DAQ noise- and stability performance took place, before finally the modules lost their full functionality. Data were saved automatically every 12 hours and a spectral improvement could be achieved by considering only data of the first 7 days of acquisition as shown in figure 6.35. Although the seven days data show a consistent background performance in comparison with the TF657 data, a deviation from a gaussian distribution can be still observed between channel 2600 and channel 2800. A further reduction of the data set does not eliminate the deviation, which indicates that an unstable signal amplification took place since the beginning of the TF656 data acquisition. However, besides the reduction of the lifetime by 2.5 days, the data are treated in the same manner as the other spectra in the further analysis. The procedure of the determination of the gain in neutron flux reduction is

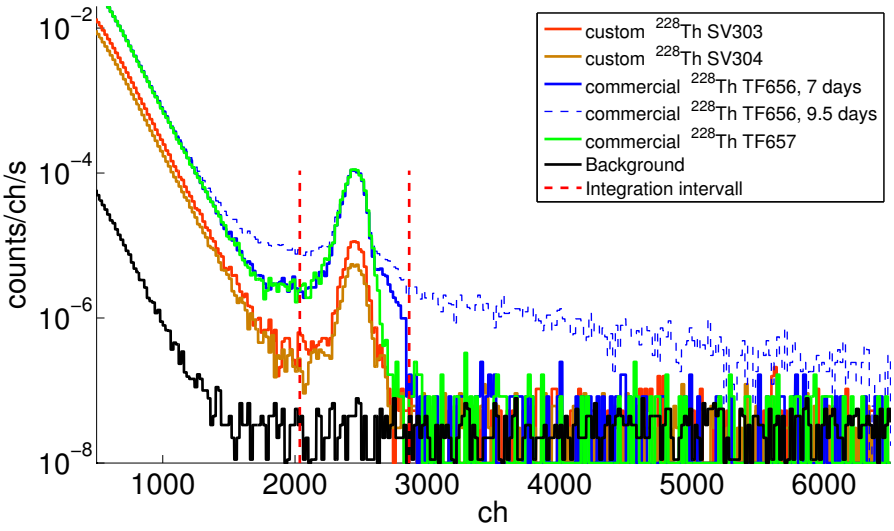

Figure 6.35: ^{3}He spectra of the background, two custom and two commercial ^{228}Th sources. The spectrum of the TF656 commercial source shows a perturbed spectrum as a consequence of a water damage on the DAQ. An improvement could be achieved by considering only the first seven days of acquisition. The sources data are not normalized on their activity in this plot.

illustrated in figure 6.36 and figure 6.37. The measured background is subtracted from the data and the net rates are normalized on the activities of the sources. In order to extract a gaussian distribution, the transition between the continuum below channel 2000 and the remaining background above channel 3000 is modeled with a function B_{fit} expressed by

$$B_{fit} = \alpha + \frac{\beta}{e^{(ch-\mu)/\sigma} + 1} \tag{6.54}$$

which is the step component on the right side of equation (6.52) used for the peak fitting. The fit is treated as a second background component and subtracted from the data. The

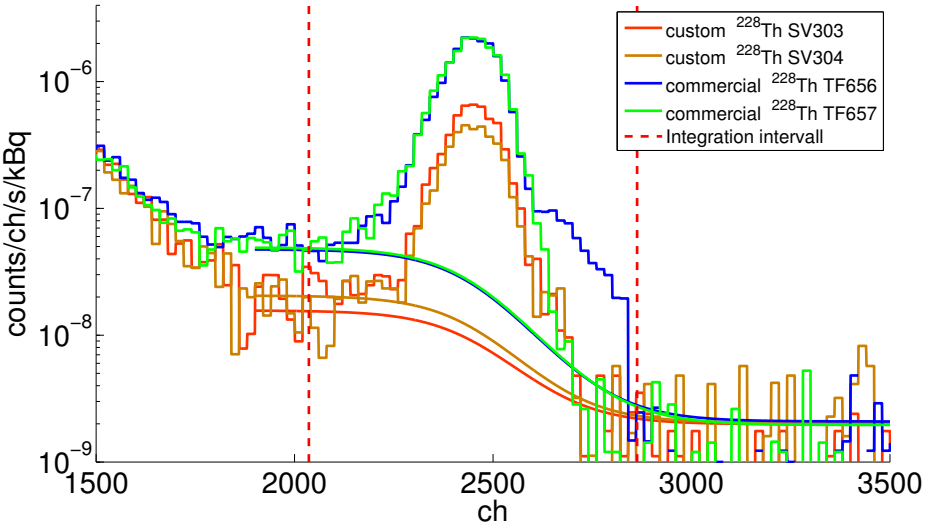

Figure 6.36: ^{3}He rates of the custom and commercial ^{228}Th sources after subtracting the measured background rate and after normalizing on the activities. A smoothed transition between the backgrounds below channel 2000 and above channel 3000 is modeled and subtracted from the data.

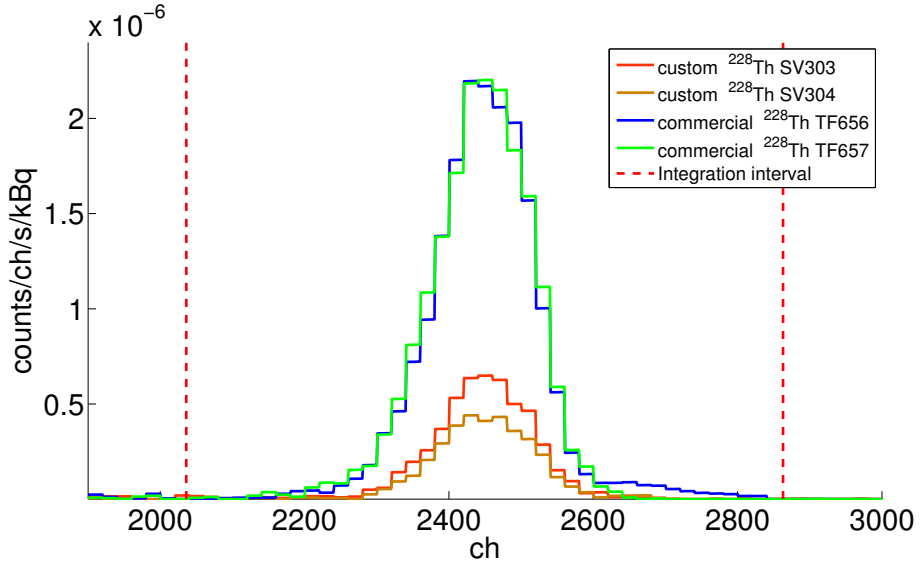

Figure 6.37: Sources data taken with the ^{3}He detector after subtracting the measured background and the remaining step transition expressed by B_{fit} in equation (6.54).

final net rate calculation can be expressed by

$$R_{Net} = \int_{ROI} [\frac{(\text{Counts(Source)}/T_S - \text{Counts(Background)}/T_B}{A_S} - B_{fit}] \tag{6.55}$$

where T_S and T_B are given by the lifetimes of the source data- and of the background data- acquisition respectively and A_S is given by the source activity. Figure 6.37 shows the rates after the measured background and B_{fit} have been subtracted. The distinctive tail of the TF656 data between channel 2600 and channel 2800 is a consequence of the DAQ signal amplification instability, which occurred during data taking. Therefore, the counts in the tail are assumed to origin from neutron events which took place at higher DAQ gains.

The rates in figure 6.37 represent normalized neutron fluxes which can be compared with each other. The two overlapping peaks of the commercial sources show maxima which are roughly 4 times higher than those of the two custom sources, which indicates for a neutron flux reduction, obtained by depositing ^{228}Th on gold. Table 6.13 shows the neutron net rates R_{Net} for all four sources, obtained after the integration of the normalized and background-subtracted data over the whole region of interest. The errors in the table are combined of statistical errors and the uncertainties in the source activities. With the

^{228}Th source	Neutron rate R_{Net} [counts/s/kBq]
TF656 commercial	$3.74 \cdot 10^{-4} \pm 1.9 \cdot 10^{-5}$
TF657 commercial	$3.75 \cdot 10^{-4} \pm 1.9 \cdot 10^{-5}$
SV303 custom	$1.05 \cdot 10^{-4} \pm 1.6 \cdot 10^{-5}$
SV304 custom	$7.40 \cdot 10^{-5} \pm 1.1 \cdot 10^{-5}$

Table 6.13: Neutron rates acquired with the ^{3}He detector after normalizing on the activity of the commercial and custom sources.

neutron flux reduction G_{nRed} defined as

$$G_{nRed} = \frac{R_{Net}(\text{commercial})}{R_{Net}(\text{custom})}, \tag{6.56}$$

neutron reduction values between 3.5 and 5 could be determined as shown in table 6.14 . As a representative neutron reduction value for all sources, the numbers in table 6.14 were used to calculate a weighted mean value according to

$$\overline{x} = \frac{\sum_{i=1}^{n}(x_i \cdot w_i)}{\sum_{i=1}^{n} w_i)} \tag{6.57}$$

with the weights w_i defined by the errors of each value, given by

$$w_i = 1/\sigma_i^2 \tag{6.58}$$

commercial/custom	G_{nRed}
TF656/SV303	$3.56 \pm 5.7 \cdot 10^{-1}$
TF656/SV304	$5.06 \pm 8.1 \cdot 10^{-1}$
TF657/SV303	$3.57 \pm 5.7 \cdot 10^{-1}$
TF657/SV304	$5.06 \pm 8.1 \cdot 10^{-1}$

Table 6.14: Neutron reduction of the custom sources in all four combinations with the commercial sources. The data were taken with the ^{3}He detector.

and a mean error given by

$$\sigma_{\overline{x}} = \sqrt{\frac{1}{\sum_{i=1}^{n} 1/\sigma_i^2}} \tag{6.59}$$

With $n = 4$ as the number of measurements and x_i given by the four G_{nRed} values in table 6.14, a mean neutron reduction of

$$\overline{G}_{nRed} = 4.06 \pm 0.33 \tag{6.60}$$

can be calculated, indicating a neutron reduction of about a factor of 4 gained by the custom produced ^{228}Th sources.

6.4.2 LiI(Eu) results

Figure 6.38 shows the full spectra taken with the LiI(Eu) detector with all four sources and the background with a lifetime of nearly three months. The gamma continuum below channel ∼2500 develops into a broad neutron peak with a maximum at channel 3650. In addition, the figure shows the integration interval as it was determined in chapter 6.2 with an ^{241}AmBe source. The limits were set by considering the 98% and 2% levels of a cumulative fit performed on the data. As indicated by the background data in figure 6.38, the peak between channel 3000 and channel 4000 is a superposition of the neutron peak at channel 3650 and an unidentified background peak at channel 3320.
The background peak could be for example a consequence of unmoderated neutron capture reactions in ^{127}I with a Q-value of 4.28 MeV. Remarkable in the picture is also the contrast between the data of commercial sources and custom sources. While the spectra of the commercial sources in the region of interest are clearly distinguishable from the background distribution, spectra of the custom sources are mostly consistent with background data in the neutron region of interest. This is also a strong indication for a neutron flux reduction in the custom sources. An unknown part of the background peak consists most probably also of neutrons emitted by the sources, however due to the speculative nature of the peak, it will be treated as a background component in the further analysis and hence, a broadening of the previously determined integration interval will not take place. Furthermore, due to

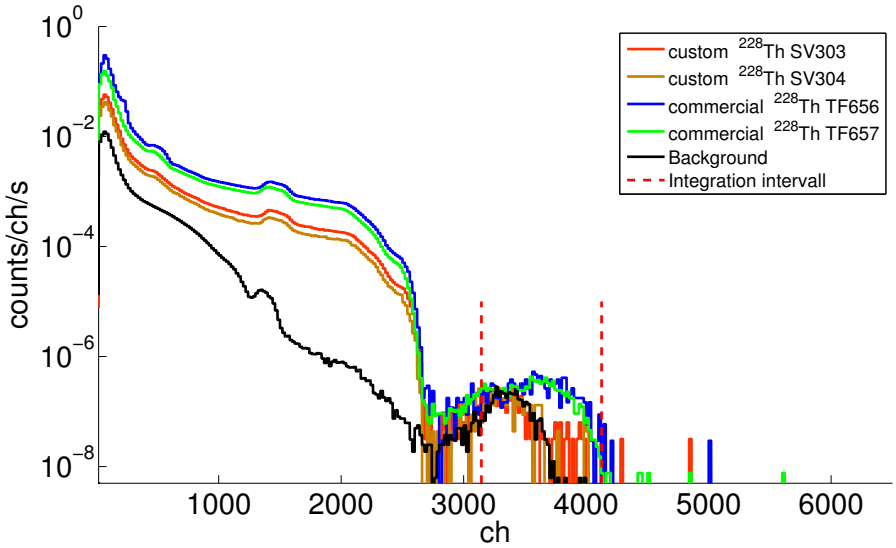

Figure 6.38: LiI(Eu) spectra for the background, two commercial and two custom ^{228}Th sources. The peak in the region of interest shows a broad distribution due to an overlapping of a background peak and the neutron peak.

the low statistics of the custom sources data, background subtraction is not performed to prevent negative values in the spectra. Instead, the integration interval is shifted up to a 90% rejection level of the background signal. The determination of the lower limit has

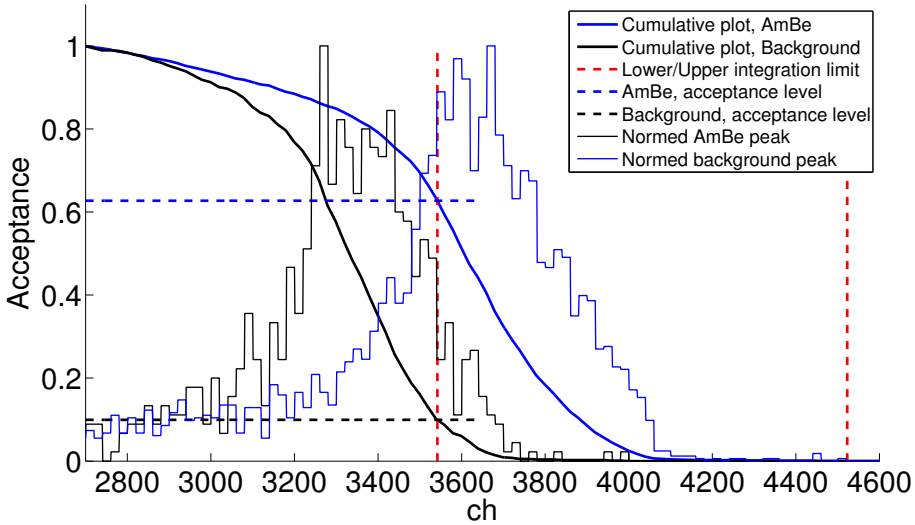

Figure 6.39: Determining of the lower integration limit. The cumulative plots of the background and of an ^{241}AmBe source are used to set a background rejection limit of 90%. The limit implies a signal acceptance level of 63%.

been done by considering the background data and ^{241}AmBe data. Figure 6.39 shows the background peak and an ^{241}AmBe peak scaled in arbitrary units with a maximal height of one. Due to the ^{241}AmBe activity of 37 MBq, the background component in the neutron peak can be neglected. The lower integration limit at channel 3542 is defined at a level which rejects 90% of the normalized background signal. The acceptance level for the signal is the value of the ^{241}AmBe cumulative distribution at the point of the lower integration limit and has been determined to be 63%. The upper integration limit has been calculated by keeping the integration interval width of 981 channels as it was determined for the ^{241}AmBe data in chapter 6.2. Thus the old integration interval

$$I_{AmBe} = [3145, 4126] \tag{6.61}$$

has been shifted by 397 channels to

$$I_{Th} = [3542, 4523] \tag{6.62}$$

in order to perform a 90% rejection level on the background peak. The net rates in the

^{228}Th source	Neutron rate R_{Net} [counts/s/kBq]
TF656 commercial	$2.73 \cdot 10^{-6} \pm 2.3 \cdot 10^{-7}$
TF657 commercial	$2.43 \cdot 10^{-6} \pm 1.5 \cdot 10^{-7}$
SV303 custom	$5.31 \cdot 10^{-7} \pm 1.6 \cdot 10^{-7}$
SV304 custom	$7.18 \cdot 10^{-7} \pm 2.5 \cdot 10^{-7}$

Table 6.15: Neutron rates of the commercial and custom sources as they result from the LiI(Eu) measurements. The rates are normalized on their activity.

integration interval for all four sources and after normalizing on the activities are shown in table 6.15. The data confirm a total detection efficiency of the LiI(Eu) setup which is roughly two orders of magnitude lower than the detection efficiency of the ^{3}He detector if compared with the values in table 6.13. Because the lifetime of data taking with the LiI(Eu) detector could not be significantly increased, the relative errors reach values of up to 32%. However, as shown in table 6.16, the neutron reduction values G_{nRed} determined

commercial/custom	G_{nRed}
TF656/SV303	5.1± 1.6
TF656/SV304	3.8± 1.4
TF657/SV303	4.6± 1.4
TF657/SV304	3.4±1.2

Table 6.16: Neutron reduction of the custom sources in all four combinations with the commercial sources. The data were taken with the LiI(Eu) detector.

with the LiI(Eu) detector according to equation (6.56) are consistent with the ^{3}He data shown in table 6.14 within 1σ for all four sources. The weighted mean value for the neutron reduction measured with the LiI(Eu) detector has been calculated according to equation (6.57) and equation (6.59) and results in

$$\overline{G}_{nRed} = 4.09 \pm 0.69. \tag{6.63}$$

This value is in full agreement with $\overline{G}_{nRed} = 4.06 \pm 0.33$ obtained with the ^{3}He detector.

6.5 Summary

In chapter 4, the production of a custom ^{228}Th source has been discussed which was produced to reduce the neutron flux by the suppression of the (α, n) channel in the source. In order to determine the neutron flux reduction achieved by the custom ^{228}Th sources with respect to commercial sources, neutron measurements of both types were performed with a ^{3}He detector and a commercial LiI(Eu) detector. Data taking took place at LNGS in order to reduce the environmental background.

In the first campaign, absolute neutron flux measurements of the first P02 prototype source were performed in two different ^{3}He configurations resulting in consistent neutron fluxes within 2 σ. The absolute neutron flux of a commercial source was determined only with the second ^{3}He configuration. Based on this results, a neutron flux reduction of

$G_{nRed} = 1.7 \pm 0.4$

has been determined.

During the second campaign, the ^{3}He detector was used together with a LiI(Eu) detector. Only relative measurements were performed with two commercial and two custom sources. The values of the mean neutron reduction obtained with both detectors are consistent with each other within 1σ with

$\overline{G}_{nRed}(^3\text{He}) = 4.06 \pm 0.33$

and

$\overline{G}_{nRed}(\text{LiI(Eu)} = 4.09 \pm 0.69.$

Both results are not consistent with the value obtained in the first campaign which has been performed under not fully transparent conditions.

However, although a neutron reduction of about factor 4 was observed in the second

campaign, the numbers allow to conclude that neutron fluxes given by SOURCES4A calculations were overestimated for the commercial source and underestimated for the custom source.

After the sources have been mounted in the GERDA calibration system, a second high purity LiI(Eu) detector was designed for a better detection efficiency. The detector could not be used so far to compare custom and commercial sources, but a promising improvement in the signal to background ratio of

$G_{Bckg}(S/B) = 7.5 \pm 2.0$

could be achieved in the region of interest. The detector will be used in future neutron flux measurements at LNGS.

Chapter 7

Source Insertion System - SIS

The two custom produced sources, SV303 and SV304 and one commercial SK393 ^{228}Th source have been mounted in the Source Insertion System (SIS) of GERDA in June 2011. As described in chapter 2, the SIS is an electro-mechanical device which is mounted on the top of the GERDA cryostat. The system can be accessed from within the clean room which is located above the neck of the cryostat. Three identical, vacuum sealed units are used to drive the calibration sources into position during calibration runs and removing them into a parking position 5 m above the detector array for physics runs. Each of the three sources is mounted on top of a tantalum absorber, which is fixed on a perforated stainless steel band. The band is enrolled on a pulley which can be operated by a DC

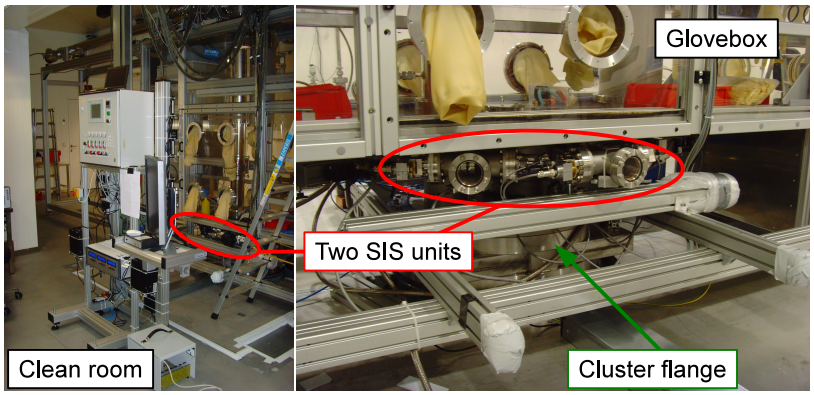

Figure 7.1: The GERDA clean room, mounted on top of the GERDA cryostat. The room contains a glovebox for detector deployment through the cluster flange. Three gate valves mounted on the cluster flange below the glovebox are used to connect the SIS units for the operation of the calibration sources.

motor. Tantalum rings mounted below the main cluster flange, assure a sufficient gamma background reduction if the sources are in their parking position. Details about the design and choice of the material used for the absorber can be found in [57].

All three source strings can be controlled individually by a control unit and moved in

a range of up to 6.5 m. The SIS system was designed and constructed at the University of Zurich as a successor of a previously mounted calibration system with a lower positioning accuracy. The new system was developed with special regard to positioning accuracy, system redundancy and safety. Figure 7.1 shows the clean room with the glovebox mounted on top of the cluster flange. The cryostat and the detector array are located below the clean room. The glovebox allows to access the cryostat through the cluster flange and serves as a lubricator for the detector deployment. Figure 7.1 shows also two of the three SIS units fully mounted below the glovebox on the cluster flange. A third SIS unit is located on the other side of the glovebox and is not visible in the picture. The mechanical connection between the cluster flange and the SIS units is performed by three DN40 gate valves mounted in between. The valves can be closed to decouple the cryostat from the environment in order to mount or dismount the SIS units. The status of the gate valves is monitored permanently in order to prevent a string operation if the valves are closed.

7.1 SIS hardware

The SIS hardware can be divided into four main components which will be described in the following:

GERDA cryostat and cluster flange: The cryostat is the volume where the sources are immersed during calibration runs and which contains the detector array. The cluster flange is mounted on top of the cryostat and is accessible from the clean room. It is connected to a glovebox and allows to insert the detectors from the top into the cryostat. Furthermore, it contains three DN40 flanges mounted below the glovebox for the SIS units.

Gate valves: The three gate valve shutters are mounted on the DN40 flanges of the cluster flange. They allow to mount the SIS units under sealed conditions and can be opened to allow the sources to be lowered into the cryostat. Two switches inside the

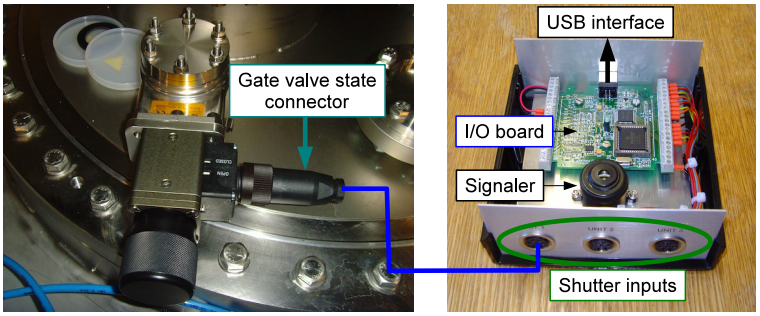

Figure 7.2: Left: Electrical connector for the two switches indicating the valve gate states. Right: I/O box used for the monitoring of the valve gates. Critical states are indicated acoustically by a buzzer. The device has been implemented in the LabView GUI of the SIS system.

valve allow to monitor the status of the shutter. Three modi are possible: closed, open or undefined. Undefined means that the shutter is either fully closed nor fully opened. To monitor the states of the shutters, a digital RedLab 1024LS I/O module has been used. The module has 24 programmable I/O channels and an USB interface. As shown in figure 7.2, the device has been dismounted and assembled in a box providing all connectors for an easy handling. The shutter control box includes 5V pull-up resistors to monitor the gate states and a buzzer which is used as an alarm for critical gate states. The front panel includes three plug-in connectors fitting the formate of the shutter connectors. Although implemented in the SIS LabView graphical user interface (GUI), monitoring of the gates is not explicitly implemented in the hardware of the SIS control unit. Therefore, the gate valves are treated as separate components.

SIS units/arms: The units contain the calibration sources, two positioning readout systems, the band mechanics and vacuum sealed electronic feedthroughs. Each SIS arm is operated by a DC motor which is mounted outside of the unit and coupled via a vacuum sealed rotary feedthrough to the internal mechanical components. The internal setup of a SIS unit with its mechanical and electrical components is illustrated in figure 7.3. The absorber with the calibration source is fixed on a stainless steel band. The band is connected through a band guide to a crank which can be rotated by the motor. The motor is coupled to the crank axis via a vacuum sealed rotary feedthrough. Furthermore, for

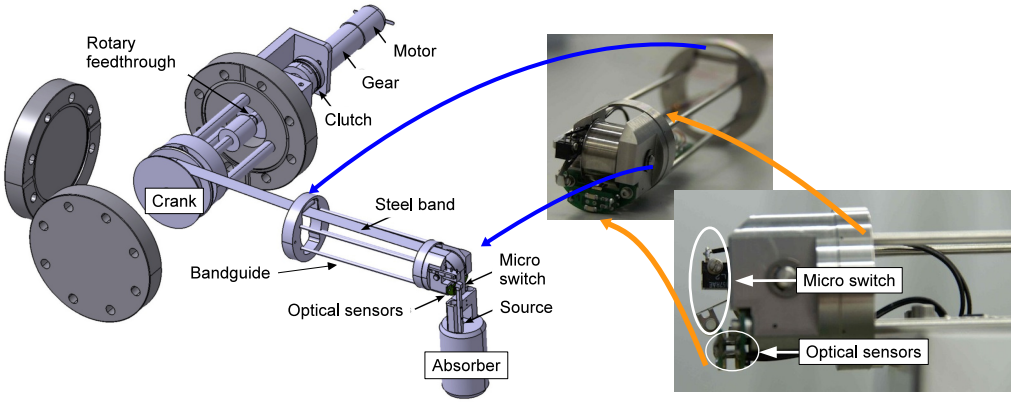

Figure 7.3: Internal setup of the SIS arm. Cabling of the micro-switch and the optical sensors are fed through a vacuum sealed electrical connector which is not shown in the picture. Also not shown is the second positioning encoder which is mounted outside of the SIS housing. Technical drawing from [57].

safety reasons, an adjustable clutch is used to limit the maximal torsional momentum of the motor which can be applied to the axis. The band has laser-cut holes of 2 mm diameter at a constant pitch of 4 mm. The holes are part of one of the two positioning systems. An optical incremental encoder consisting of two LED's mounted at the end of the band guide in a distance of 5 mm counts the holes passed by. The motion direction of the band is determined by the phase difference between the two optical sensors, while the absolute

position is given by the number off holes counted relatively to a reference point. The reference point is given by a micro-switch (end-switch) which is activated by the absorber during the initialization procedure. Cables for the end-switch and the optical sensors are fed through an electrical vacuum sealed connecter mounted on the side of the SIS housing. The second, redundant positioning system is an absolute encoder device located outside of the SIS arm in the direct vicinity of the motor. The absolute encoder is coupled to the main rotary axis via a gear wheel as shown in figure 7.4. The AVM36M-03SBEA0BN-1212

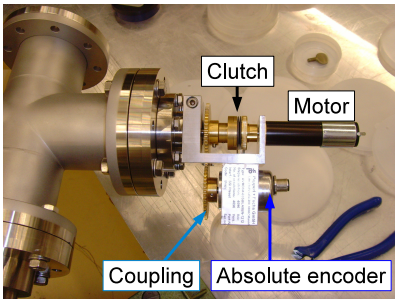

Figure 7.4: Mounted absolute encoder. The device is coupled to the main axis via a gear wheel mounted behind the clutch. After resetting, the encoder measures the absolute angle passed during rotation.

encoder from Pepperl+Fuchs is a magnetic sampling device which registers motion also if it is not powered. Therefore, a forced movement of a SIS string without the involvement of the motor will be registered and the information about the absolute position will be still available. Data from the absolute encoder are transferred via a serial interface to the control unit. The raw position data consist of a singleturn value which corresponds to a position within one full turn with a resolution of 12 bit. A second parameter, the multiturn value represents the total number of full turns in a range of 12 bit.

The housing of the SIS unit contains also a glass window allowing for visual cross checking of the band and the main crank. A gas connection located on the side allows for the

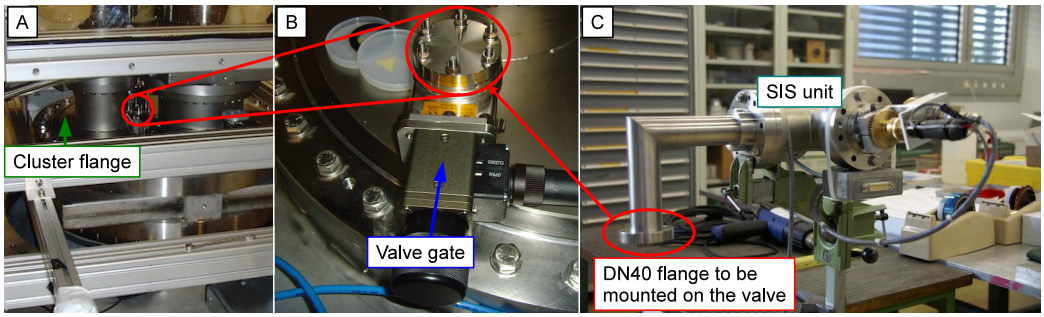

Figure 7.5: A: Cluster flange mounted below the glovebox. Marked in red is one of the valve gates mounted on top of the cluster flange. B: Zoom-in on the valve gate. The valve is operated manually and has a DN40 flange on the top which is used to mount a SIS unit. C: fully assembled SIS unit, ready to be mounted on the valve gate.

evacuation after mounting on the shutter. The mechanical components described above are assembled in a way as illustrated in figure 7.5. After fully mounted, the cryostat, the

valve gates and the SIS arms comprise one vacuum sealed volume.

Control unit: All three SIS units are controlled and monitored by a microcontroller device, developed and designed at the University of Zurich. Data from the incremental encoder, the micro-switch and the absolute encoder for example are processed and interpreted by the control unit with a build-in 18LF8722 PIC processor. Although the controller is a stand alone device allowing to operate the SIS units, it contains also an RS422 and an RS232 interface for the communication with a PC and for system controlling via a LabView GUI. In contrast to the control unit, the GUI allows to program source-motion sequences with precise timing and positioning. It provides also a permanent visualization of the system status, displays system parameters like error flags or activated buttons on the control device and shows specific onboard settings activated on the controller main board.

The front panel of the module consists of three displays with the following four buttons for each source string:

- Remote On/Off: Enables or disables the optional control over a PC.

- Park/Init: Before operation, the system must be initialized first. During the initialization procedure, the string is moving up until the activation of an micro-switch takes place. The activation point is used as a reference level for the incremental encoder which is calibrated during each initialization. If the system is already initialized, the button will move the source into the parking position which is 2 cm below the reference point.

- Up: If the system is initialized and the source is located below the parking position, the string will move upwards with a speed of 10 mm/s. Otherwise the button will not trigger any activity.

- Down: If the system is initialized, the source will move down until the maximum of 6.5 m (given by the EEPROM configuration settings) with a speed of 10 mm/s.

The backpanel of the control unit includes the power switch, and two RS232- , RS422-connectors for the serial interfaces. The serial interface to be used can be chosen via jumper located on the mainboard inside the control box. Furthermore, three periphery connectors for the position encoders, the micro-switches and the powering of the motors are available on the back panel. The front- and the back- panel of the control unit are shown in figure 7.6. The operation in standard mode, does not require any intervention from outside on the mainboard. However, in the case maintenance work is required, the control unit can be opened allowing for further functions which can be disabled or enabled by jumpers or by the activating of DIL switches. Figure 7.7 shows a scheme of the mainboard with the functions accessible directly on the board. The settings available are divided into three groups with the following functions:

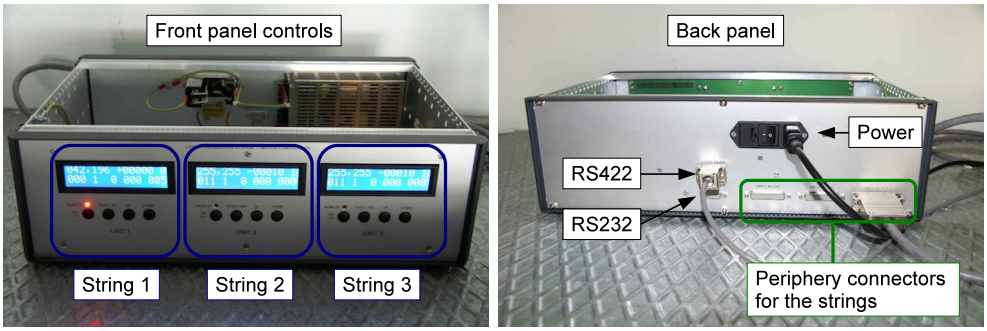

Figure 7.6: Left: Front panel of the SIS control unit. Three displays for each string show the status of the units. Basic controls can be performed by four buttons for each string. Right: Back panel of the SIS control unit. The two RS422 and RS232 interfaces are used for the system control over a PC. Three additional connectors are used for the communication between the SIS units and the controller.

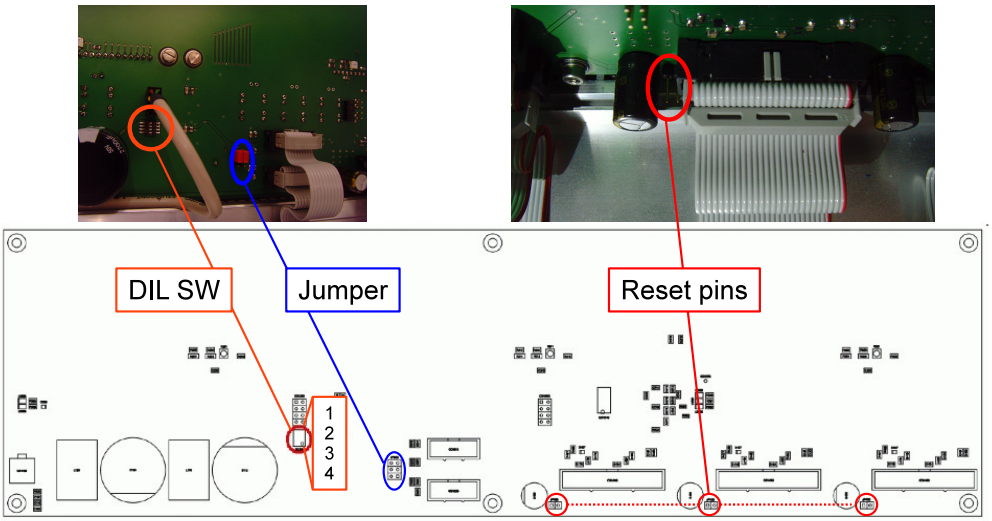

Figure 7.7: Layout of the control unit mainboard with the locations of the DIL switch used to enter special modes of the unit. The jumper are used to chose the interface and the pins are for the resetting of the absolute encoder.

I) DIL SW: A four pole switch, which allows to select the following modi starting from the top switch position:

- SW1, LCD debug mode: This mode allows to display further system information like electrical current flow through the motor, to monitor the string speed or to show the raw data of the positioning encoders.

- SW2, Absolute encoder bypass: This mode allows to ignore an error on the ab-

solute encoder. In this case, the system relies on the information given merely by the incremental encoder. In the standard mode, an error automatically stops the system.

- SW3, Incremental encoder bypass: This mode prevents the system from intervention if an error on the incremental encoder occurs. The system can be run considering only the data from the absolute encoder. In the standard mode, an error automatically stops the system.

- SW4, controller configuration data write access: This mode allows to write certain configuration parameters to the EEPROM of the microcontroller. Those are for example the thermal expansion coefficient, the crank diameter, band length, position correction tables or the liquid argon level. All this values are critical in terms of correct position determination of the incremental encoder. Both, reading and writing of the parameters can be performed with two separate LabView GUIs. While the SW2 and SW3 modi should be always treated with cautiousness, the SW4 mode is absolutely critical for the correct functionality of the system and should be activated only if absolutely necessary. Therefore, an activated SW4 switch is indicated by a blinking of the red LED's on the front panel.

II) Jumper: The two jumper indicated in figure 7.7 allow to change between the RS422 interface and the RS232 interface. Bridging the two upper pins on the left and on the right sets the board to the RS422 mode, while RS232 is accessed by bridging the two lower pins on left and right. However, the RS232 interface is a design artifact which can be used for data transfer below a distance of 15 m. The RS422 interface allows for data transfer at much longer distances and is furthermore more robust against signal corruption caused by environmental interferences. Therefore, the jumper is to the RS422 interface by default.

III) Reset pins: Similar to the SW4 mode, the reset pins are critical in terms of the correct functionality of the system. Three pin pairs, one for each string are available. Bridging of two pins resets the absolute encoder to zero. Resetting the encoder sets automatically the maximal reachable source depth to the current position. Resetting for example at the parking position would not allow to move the source at all and a time consuming system recalibration would need to be done.

7.2 SIS software/LabView GUI

The firmware of the control unit defines the functionality of the SIS system and is responsible for error and status feedback of the internal components like the motor driver, I^2C bus, ADC or the power supply. It interprets also the periphery signals from the positioning systems and of the end-switches. Additionally it includes a command set for the serial interface communication between the control unit and a PC. The communication takes place through the interpretation of a RX-packet received by the controller from the PC and an answering TX-packet transmitted from the controller to the PC. Each command contains

a 7 bytes RX-packet and a TX-packet of up to 250 bytes including at least a command byte and a checksum byte for the signal transmission control. Further byte designation is defined individually depending on the function described by the command. The following commands are available for the communication between the control unit and a PC:

• **INIT:** Initializes the system by driving a string up to the reference point defined by the micro-switch mounted within the SIS arm. The process resets the incremental position to -20 mm at the micro-switch position and moves down the source to the 0 mm position automatically. Furthermore, the reference point is used for the recalibration of the absolute encoder position.

• **GET POSITION:** Calls the position information of the absolute encoder and the incremental encoder. If the system is not initialized, the incremental encoder returns a value of -9999, indicating an unknown position.

• **GOTO POSITION:** Moves the string to the specified position which is given by the incremental encoder. The position of the absolute encoder is used for position crosschecking or redundantly if the incremental encoder fails.

• **GET STATUS:** Returns status information of the system. This includes the internal electronic components of the controller, the buttons activated, the onboard settings, the micro-switch state and errors on the absolute or incremental encoder.

• **GET PARAMETER:** Allows to return one of the following configuration parameters: main crank diameter, tape thickness, tape length, tape hole pitch.

• **STOP:** Stops any activity of the strings.

• **SET CONFIGURATION DATA:** Allows to write configuration data into the EEPROM memory of the controller at the specified address offset. The data are crucial for the correct position determination.

• **GET CONFIGURATION DATA:** Allows to read configuration data from the EEPROM memory of the controller at the specified adress offset.

• **GET CONFIGURATION MEMORY:** Returns the complete configuration data from the EEPROM memory of the controller.

Active commands like INIT, STOP or GOTO POSITION triggered by the LabView GUI are rejected by the control unit until the remote control has been activated on the front panel. An active remote control mode is indicated by a red LED on the panel.

To allow a control over LabView, the commands described above were used to create

a set of LabView driver to be implemented in the control GUI shown in figure 7.8. The layout of the LabView program developed, consists of a main control panel, a settings section and a servicing and error section. The three sections will be described in the following:

LabView GUI - Main control panel

The main control panel allows for the positioning of the sources with an accuracy of 1 mm, but also to save custom positions and to program motion sequences. Furthermore it visualizes dynamically the status of the whole SIS system. Since string oscillation can

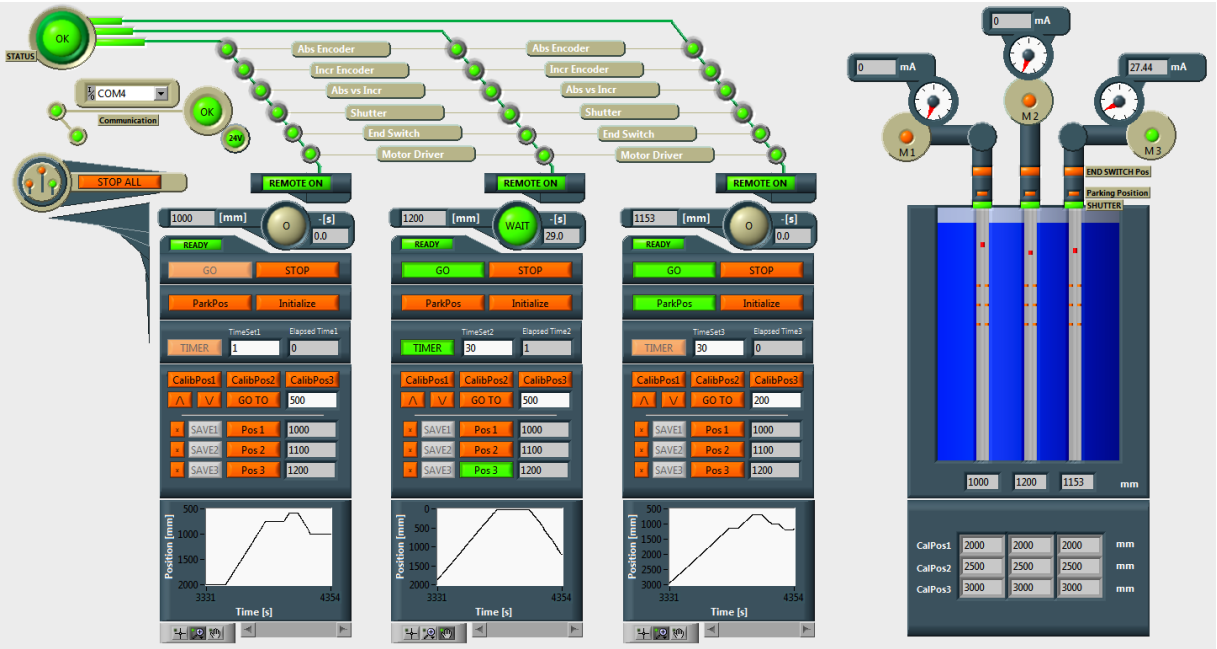

Figure 7.8: Main LabView SIS control panel. Three status strings for each SIS unit indicate errors and error-bypass modes. Three control panels are enabled or disabled by a global status flag. Graphical displays show the motion history of the sources. Furthermore a scheme of the system on the right shows motor activity, shutter and end-switch states and indicates the adjusted cryogenic liquid level as well as the source positions.

occur during the absorber immersion from the top into the cryogenic liquid, a function has been implemented to automatically stop the string movement at the level of the liquid and to wait for a given time before continuing to move the source downwards. Another critical point in terms of oscillations is the process of moving the source into the parking position. String oscillation could result in a blocking of the absorber on the bottom side of the SIS arm before entering the parking tube. Furthermore, absorber oscillations in the ϕ plane during initialization could cause the micro-switch not to be activated. In the two latter cases, the system would stop automatically but it would cause material stress with unknown consequences for the system on a long time scale. Therefore, a second function stops the string automatically before the absorber enters the SIS arm. After a given time

has elapsed, the function allows to continue with the execution of the last active command. Both functions do not take effect if a command is triggered on the front panel of the control unit.

To prevent cross talks between the GUI and the control unit, all programmed tasks of the GUI are resetting automatically once a button has been activated on the control unit. Furthermore, all GUI controls with an active functionality are disabled for the time of activity on the front panel of the control unit, which makes cross talking with the LabView side impossible. The GUI in figure 7.8 shows a global status indicator on the top left side which is combined of six status flags arranged in three strings for each SIS unit. Error bypassing is possible for the absolute encoder, the incremental encoder and the shutter. Once an error occurs, the system will be blocked and an error flag will be activated on the status string. Bypassed errors are indicated on the status strings by a green ring around the affected status flag. Additionally the global status flag shows an outer red ring with a green core which indicates an operational system with bypassed errors. An error which can not be bypassed blocks the whole system. Section 7.4 describes how to handle errors and how to proceed if error bypassing is not possible.

Three control panels for each SIS string allow for the operation of the sources. The panels were programmed as interactive state machines, reacting on the given conditions and status flags. Functions are blocked or enabled automatically under given conditions allowing the user to be intuitively guided during operation. If the remote control is disabled for example, all active block functions will be disabled while a red REMOTE OFF indicator will be displayed. For further control, three graphical displays on the bottom show the motion history of the sources. A schematic of the SIS system and the dewar is displayed on the right side of the GUI. The scheme shows the motor activity of each string including an electrical current measurement which should not exceed 50 mA under normal conditions. Three further indicators per string show the status of the end-switch and the shutter. A source located in the parking position, 2 cm below the end-switch is also indicated explicitly by a green flag. Furthermore, the scheme shows the currently adjusted cryogenic liquid level at which the sources stop automatically to reduce oscillations, the source positions, and three calibration positions per string. The latter are set in the settings section of the GUI described below.

LabView GUI - Settings panel

The settings panel shown in figure 7.9 is located in the LabView GUI on top of the main control panel and can be accessed by scrolling up. The section allows to set the times and positions of the string motion pausing, which has been implemented in order to reduce oscillations before continuing to execute a command. Furthermore it allows to set three calibration positions for each string j, designated as $CalibPos_i\_S_j$ ($CalibPos1$, $CalibPos2$, $CalibPos3$ in the main control panel) and three additional custom positions designated as $SetPos_i\_S_j$ ($Pos1$, $Pos2$ and $Pos3$ in the main control panel) with $i = 1, 2, 3$. The parameters which have been set are only valid if the SIS system is controlled by the LabView

Figure 7.9: The SIS setting section located in the GUI above the main control section. The panel allows to set basic functionality parameters like pausing times and positions, calibration positions and three custom positions per string.

GUI. All panel settings are explicitly described in the following:

• **Time@Neck (String1-3):** Defines the time to wait in seconds before entering the SIS arm tube from below.

• **Time@LArLevel (String1-3):** Defines the time to wait in seconds before continuing with the absorber immersion into the cryogenic liquid.

• **Pos@Neck (String1-3):** Defines the level at which the string is stopped before it enters the SIS arm from below.

• **Pos@LAr (String1-3):** Defines the level of the cryogenic liquid at which the source is paused before the full immersion of the source takes place.

• **CalPos i_S j:** Defines the i'th calibration position for the j'th source string, with i = 1, 2, 3 and j = 1, 2, 3. New calibration position settings update automatically and do not require an explicit confirmation.

• **SetPos i_S j:** Defines the i'th custom position of the j'th source string, with i = 1, 2, 3 and j = 1, 2, 3. In contrast to the calibration positions, the three custom positions can be saved at any time in the main control panel ($Pos1$, $Pos2$ and $Pos3$). To do so, the source must be located at a given position, which is saved by activating the SAVE button in the main control panel. Alternatively, the desired positions can be entered in the settings panel and confirmed by the SET button.

LabView GUI - Servicing and error panel

The third GUI section shown in figure 7.10 is a panel containing the full set of error indicators, the error codes, hardware status flags and checksum flags which are read at specific locations in the LabView code. The section is located below the main control panel and can be accessed by scrolling down. Thirteen status bytes are displayed on the top left side

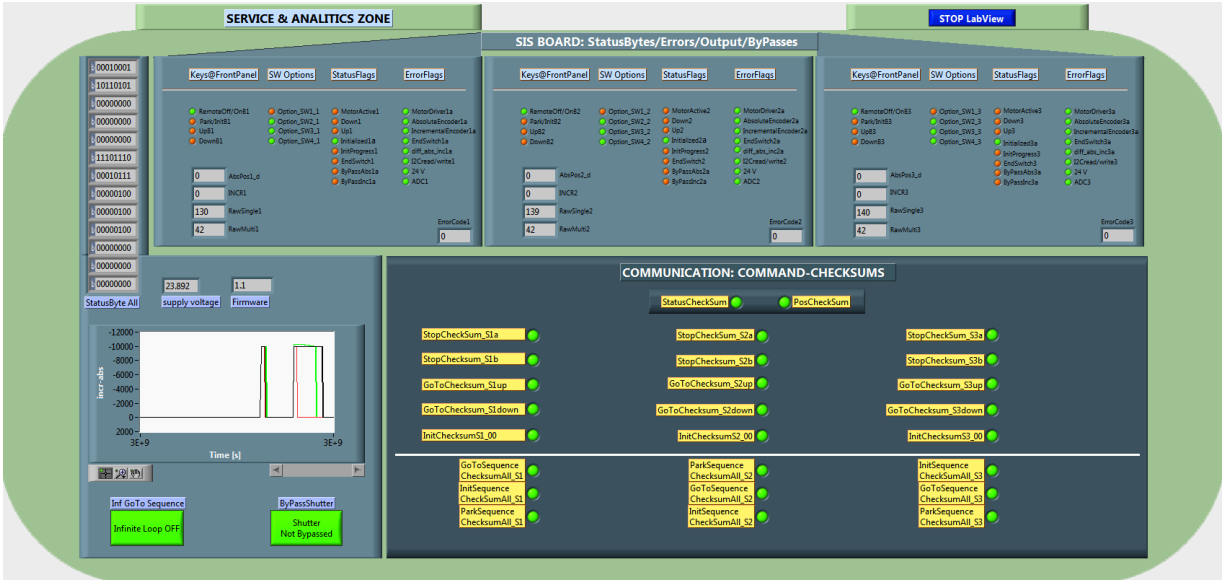

Figure 7.10: The SIS servicing and errors section located in the GUI below the main control section. The section gives the full status information of the system, monitors the discrepancies between the absolute and incremental encoder, and displays the communication flags at different code execution stages.

of the panel. The bytes represent the return values of the GET STATUS command and include the full set of available hardware status information. The first status byte represent the firmware version while the last byte contains error information of the third string for example. However, the status byte column serves only as a debugging tool for the LabView code and the full interpretation of the binaries is additionally displayed graphically in the three blocks to the right. All three blocks contain the same status information as included by the bytes block. Starting from the left, each of the three blocks gives the full status information for each string. This includes:

• **Keys@FrontPanel:** Indicates currently activated buttons on the front panel of the control unit.

• **SW Options:** Indicates the DIL SW settings on the mainboard as shown in figure 7.7 and described in section 7.1. Because, the available options should not be activated in the standard mode, the activation of one of the four options is indicated by a red indicator informing the user about an exceptional setting mode. The SW options are system wide and allow for error bypassing and for changing of the microcontroller parameters.

• **StatusFlags:** The status flags indicate a current motor activity, the direction of the source motion, current initialization status, status of the end-switch and bypassed errors.

• **ErrorFlags:** Shows errors of the hardware components of the system. This includes the periphery with the two positioning systems, the end-switch and electronic components on the mainboard.

Each of the blocks contains the information of the current position given in mm by the absolute and the incremental encoder and two numbers designated as *RawSingle* and *RawMulti* which represent the raw data of the absolute encoder. Based on the two raw data values, the position of the absolute encoder in mm is calculated by the microcontroller. The *RawMulti* value represents the number of full turns relatively to the absolute encoder reference position at 6.5 m. The *RawSingle* value represents the position within one turn with a resolution of 8 bits. If an error occurs, it will be indicated visually by the error flags, but also represented by an *ErrorCode* which is a binary combination of all errors that have occurred. The displayed error code value is a decimal interpretation of the binary error code number.

Another panel on the bottom left side shows the voltage of the power supply of the control unit and the current firmware version. The voltage of the power supply should be around 24 V. A graph indicates the history of the discrepancy between the incremental and the absolute encoder. In the case the system is not initialized, the position of the incremental encoder is given by -9999 mm which results in discrepancy peaks of $\sim$ -10000 mm. In the standard, initialized mode the discrepancies should stay within a range of $\pm$ 3 mm. A reconfiguration of the system should be considered if the discrepancies exceed this range. The procedure of system configuration is described in section 7.3. It should be noted, that a systematic long term drift of the discrepancies can indicate for a deformation of the band and should never be ignored. Two additional buttons $InfGoToSequence$ and *ByPassShutter* are located below the discrepancy graph. The two buttons are the only ones having an active function in the servicing and error panel. The $InfGoToSequence$ function can be used for long term stability tests of the system. After activating, the function will automatically move the source between the parking position and a position set on the control panel in an infinite loop till explicit deactivation takes place. The *ByPassShutter* function disables any coded system intervention resulting from a forbidden shutter state. The function has been implemented, because the shutter control and the readout electronics is decoupled from the SIS control unit. A failure of the shutter readout system or maintenance work performed on the shutter would block the functionality of the LabView GUI which is not always desired.

Finally, the *Communication* panel monitors the data transfer activated by commands within the LabView GUI. Because the position and the status of the SIS strings is monitored permanently, the two checksums on top of the block are by far the most frequently

called functions. Therefore, communication errors will most probably be represented by the *StatusCheckSum* or by the *PosCheckSum* flags. However, further communication flags are monitored in different code fragments and at different code execution stages. The flags include the communication integrity for the *Stop*, *GoTo* and *Initialize* commands and must be identified within the code itself in the case of errors.

7.3 SIS configuration

If the system has been mounted for the first time or if the absolute encoder has been decoupled and dismounted, the absolute encoder must be reset to zero at the lowest possible position at about 6500 mm. For safety reasons, the reference point for the absolute encoder has been set to be equivalent to the depth at which the band is fully unrolled. This limits the maximal reachable depth which prevents damaging of the band by an over-coiling in the wrong direction. For the first configuration it must be ensured that the current position of the absolute encoder is high enough to stay in its operational range above zero once the band has been unrolled. The system should be fully mounted and connected to the control unit. It is also advantageous to establish a connection to the control PC and monitor the system on the LabView GUI. In the first step, the actual multiturn value of the absolute encoder must be determined. Reading raw data of the absolute encoder can be achieved by entering the debug mode of the control unit. This can be performed by activating the SW1 DIL switch on the main board and by pressing the Park/Init button on the front panel during the start up procedure. Alternatively, the raw data can be read in the *Servicing and error section* of the LabView GUI. The full band length of $\sim$ 6700 mm requires a minimal multiturn value of

$$RM_{min} = 43 \tag{7.1}$$

with the source located in the parking position. Therefore, once the system has been initialized and the source moved to its parking position, the multiturn value of the absolute encoder must be checked. If the value is below RM_{min}, the absolute encoder should be decoupled from the main axis gear as illustrated in figure 7.11. A screw on the holder must be released and the encoder decoupled by shifting it in one of the two possible directions. The multiturn value of the encoder can be now changed manually by rotating the encoder axis without changing the position of the source. For the GERDA system an initial multiturn value of

$$RM_{init} \sim 50 \tag{7.2}$$

is recommended for the first configuration. After, the position of the encoder has been changed to a multiturn value of $\sim$50, it should be coupled back to the motor gear and fixed. After reinitializing of the system with the new settings, the source can be driven down to $L_{max} = 6500$ mm. L_{max} is set as a parameter in the EEPROM memory and defines the maximal depth which can be reached by the control unit. For safety reasons L_{max} is smaller than the real band length. From this point, the source can be moved down manually

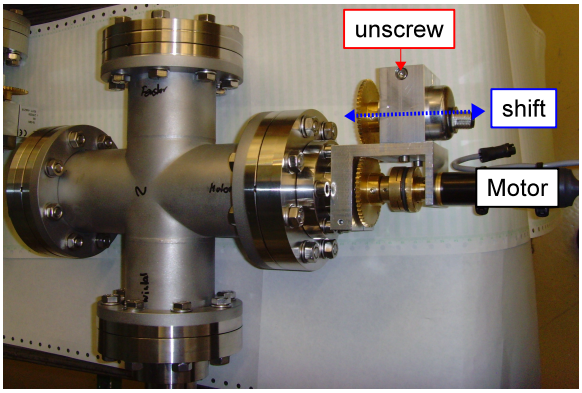

Figure 7.11: Decoupling of the absolute encoder. After the screw on the encoder holder has been released, the device can be shifted until no coupling between the encoder- and axis gear takes place. This allows to change the position values of the absolute encoder without changing the position of the source.

until the end of the band is visible through the front window of the SIS arm. To move the source manually, the gear wheel of the absolute encoder must be rotated by overforcing the clutch between the motor and the gear. Once the position has been reached, the absolute encoder can be reset to zero by overbridging the reset pins of a given string as shown in figure 7.7. The resetting procedure requires the control unit to be opened. Opening of the SIS unit can be avoided by decoupling of the absolute encoder a second time and rotating the encoder manually, till the two parameters $RawMulti$ and $RawSingle$ reach a value of zero.

An alternative to the overforcing of the clutch is to reset the absolute encoder at 6500 mm. Although, this will set the reference point at a value which is not equivalent to the band length, it will not have any further consequences for the general SIS operation. The configuration of the three absolute encoders must be performed only once and do not need to be repeated unless the system has been dismounted or the absolute encoder decoupled.

Further system configuration does not require mechanical intervention anymore and concerns only the calculation of the position based on the EEPROM configuration data. Following parameters are considered for the position determination:

• **PhiWheel:** The parameter represents the diameter in mm of the main crank.

• **TapeThickn:** Band thickness in mm used in the SIS system.

• **TapeLength:** Maximal reachable depth in mm (L_{max}). It defines the operation range of the SIS system and must not be necessarily exactly equivalent to the tape length.

• **TapeHolePitch:** Distance in mm between the holes in the band. The value is used by the incremental encoder.

• **LArLevel:** Represents the cryogenic liquid level in mm. The value is used for thermal expansion and contraction corrections.

• **ThermalCoeffTape:** Thermal expansion coefficient of the band material.

• **PosCorr:** Table of 64 correction values given in mm, used to eliminate discrepancies between the absolute encoder and the incremental encoder. A correction table is used, because the discrepancies depend on the current source position and are not given by a constant value.

In order to read the current microcontroller settings, a LabView GUI (READ.VI) shown in figure 7.12 has been written, which also allows for the saving of the current settings in a text file. The position correction tables include 64 values, representing the discrepancies at

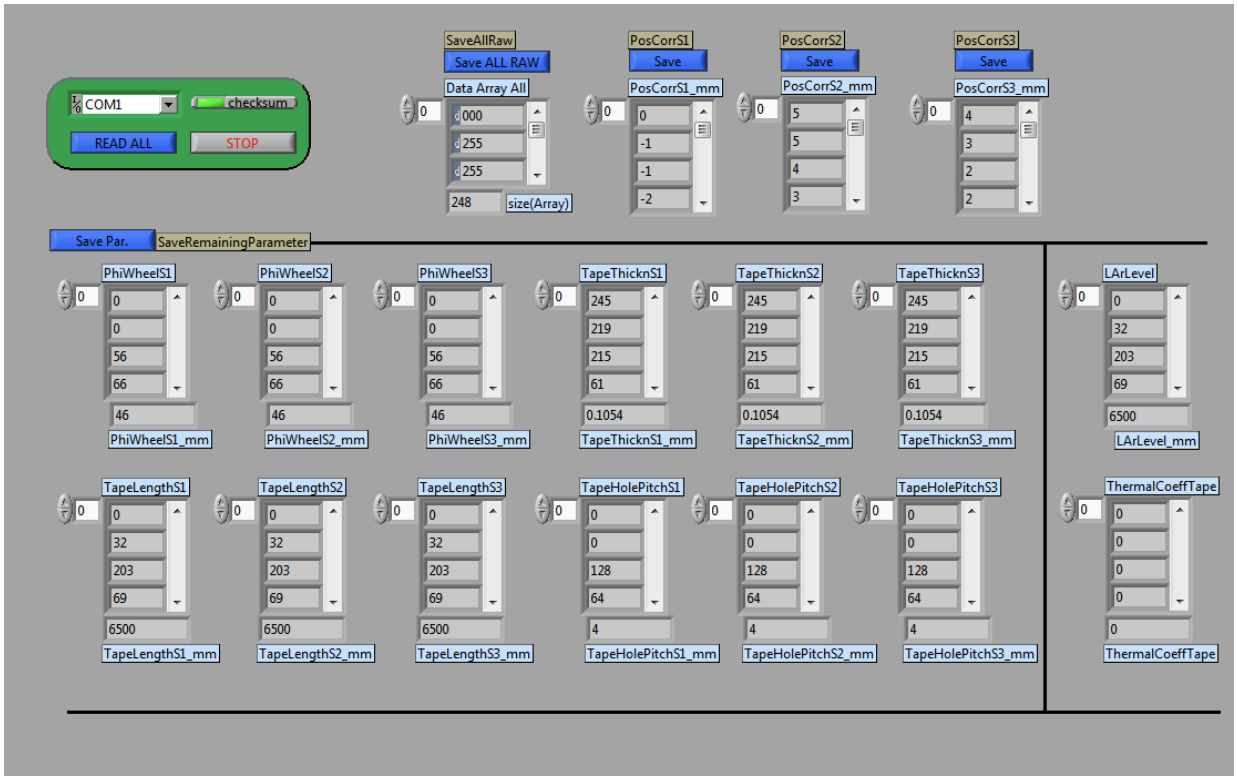

Figure 7.12: The READ.VI LabView GUI used for reading of the EEPROM configuration data. The parameters are used for the position calculation and for position corrections.

each full multiturn value of the absolute encoder with a maximum of 64 multiturns. The reference point for the absolute encoder is defined by the lowest possible source position given by a multiturn = 0 value. The highest multiturn value is given at the parking position with a value between 42 and 43. The correction table goes up to 64 multiturn values in order to assure a flexibility in adapting to new hardware conditions, which possibly can

take place in future. The numbers in the position correction tables must be given in mm for each string. The remaining parameters are read and written according to the IEEE754 floating point representation consisting of four bytes per parameter. In order to make the READ.VI user friendly, the GUI returns also the decimal values making an explicit interpretation of the bytes superfluously. The READ.VI should be only used if the SIS control GUI is off. Additionally, it should be noted that updated parameters will be returned by the GUI only after the control unit has been switched off and on again.

Changing of existing configuration data is critical, because it has a direct impact on the position output of the system. Furthermore, the set of parameters, including the position corrections must always be complete. An incomplete correction table for example will cause inconsistent parameter interpretation with consequences for the system functionality. To write the configuration data, a separate LabView GUI (WRITE.VI) shown in figure 7.13 has been developed, which serves only for the overwriting of existing parameters in the EEPROM memory. However, the GUI should only be used if necessary and treated with cautiousness. Before using the WRITE.VI, the current settings should be always saved

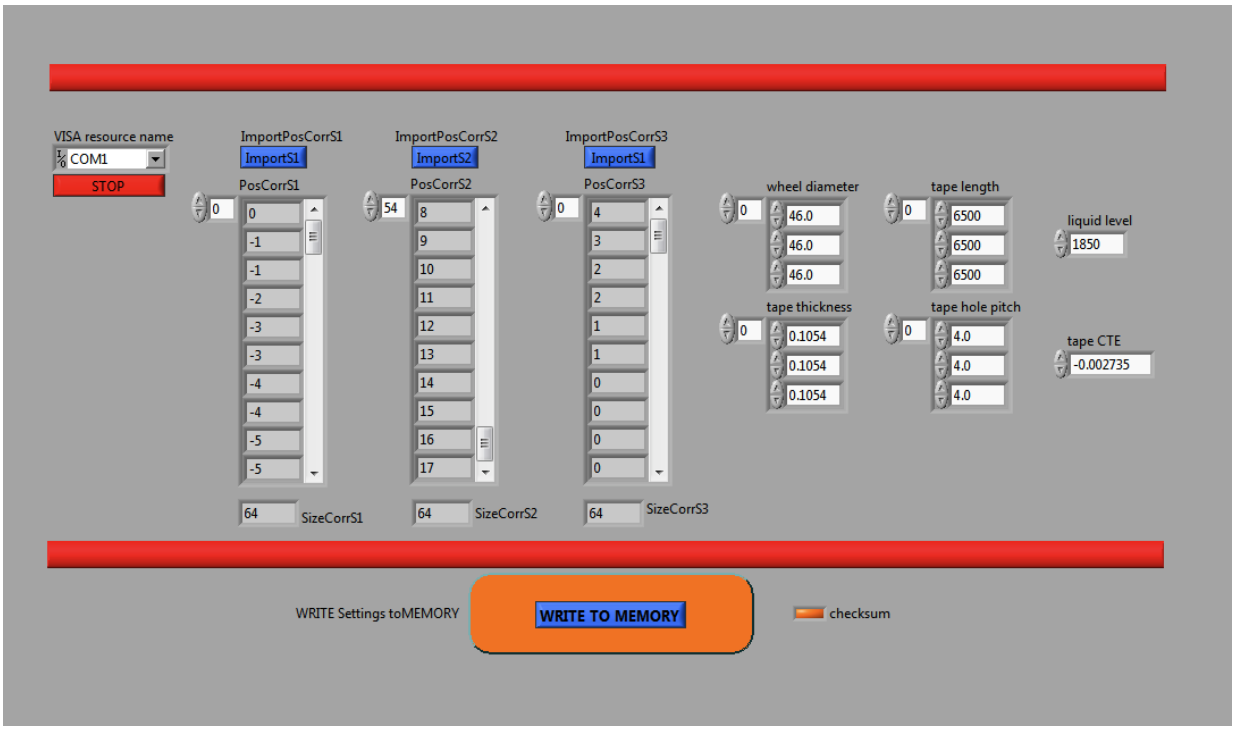

Figure 7.13: The WRITE.VI LabView GUI can be used to overwrite existing configuration data in the EEPROM memory of the SIS control unit.

first using the READ.VI. To write new parameters, the SIS control GUI must be switched off and the SW4 DIL switch must be activated on the mainboard of the SIS control unit.

To perform a position correction on a string, a table with 64 zero values must be im-

ported first and the string must be run in the full range between 0 mm and 6500 mm. Once a movement takes place, the SIS control GUI saves all relevant data like the positions of the incremental and absolute encoder into a text file. This data set has to be used to determine the discrepancies (incremental minus absolute encoder positions) at the positions given by the absolute encoder. Because data given by the incremental encoder are not affected by parameters like crank diameter, band thickness or band length, the correction is performed merely on the absolute encoder. The correction table can be generated by a fit of the discrepancy plot and must contain exactly 64 values for each multiturn. To implement a correction table, a text file containing the corrections must be located in a hard coded path on the SIS PC and imported into the WRITE.VI. The remaining parameters can be entered directly in the GUI. After all parameters have been set and all three correction tables imported, the data can be written into the memory by activating the WRITE TO MEMORY button. The data are finally adapted after switching off and on of the SIS control unit.

It should be also noted that the configuration of the absolute encoder as described at the beginning of this section can also be performed using the WRITE.VI. This requires to change the tape length in the configuration data to ∼7000 mm, which allows to drive the source down to a level at which the band is fully unrolled. However, although comfortable, this method requires full attention of the operator in order to prevent an over-coiling and damaging of the band. Furthermore, after resetting the absolute encoder, it is important to change back the band length setting to 6500 mm.

7.4 SIS error handling

The variety of errors, their combinations and causes makes it impossible to give a general rule on how to handle problems on the SIS system. An error which occurs during a source operation stops the system resulting in a stuck string in the cryostat. Such a situation makes physics runs and maintenance work impossible. Errors of the system can be bypassed in some cases making the system still operational. This section focuses on the procedures which can be undertaken in order to move the source back into the parking position once a system failure occurs. It allows to decouple the broken system and to undertake further servicing steps.

To allow errors to be ignored, the SIS control unit must be switched off and opened to gain access to the DIL switches on the mainboard shown in figure 7.7. An error on the absolute encoder for example can be bypassed by activating the SW2 switch. After the DIL switch has been set according to the error to be ignored, the control unit must be switched on again and the Park/Init button of the respective string pressed while a bulk propagates through the display, as shown in figure 7.14. Successfully activated error bypassing will automatically force the debug mode of the respective LCD. In this mode, the display shows additional system information according to the pattern shown on the right side of figure

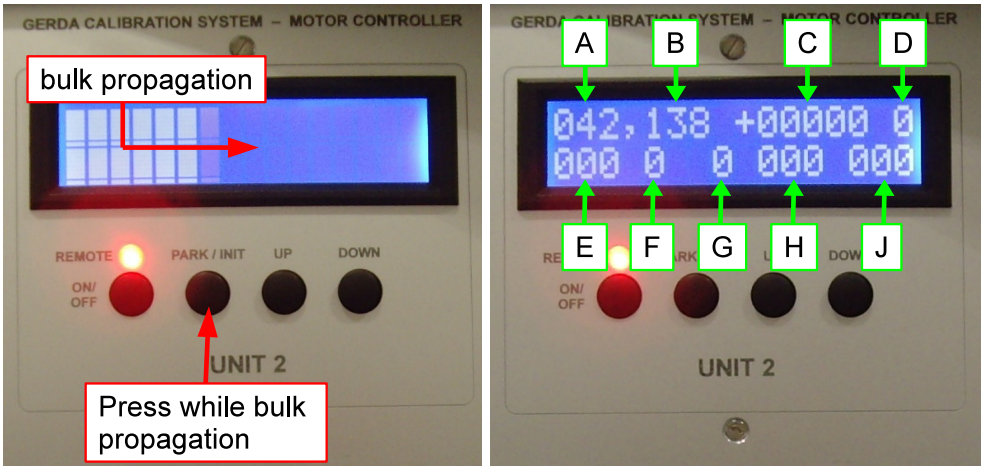

Figure 7.14: Left: entering the debug mode. After activating SW1 on the mainboard, the control unit must be switched on and the Park/Init button activated during the bulk propagation. Right: after entering the debug mode, the display shows additional information about the system. The designation of the fields is explained in table 7.1.

7.14. The meaning of the values displayed in the debug mode is described in table 7.1. Because, bypassing requires to switch off the control unit, the system loses its *initialized* status and the only operation which can be performed after powering-up, is to call of the *initialize* function. Initializing can be triggered either by using the control unit or via the

Position	Meaning
A	multiturn raw data of the absolute encoder (number of full turns)
B	singleturn raw data of the absolute encoder (position within one turn with 256 bit resolution)
C	position in mm given by the incremental encoder
D	status of the end-switch, 0 = open, 1 = closed (standard position)
E	error code
F	status of initialization, 0 = not initialized, 1 = initialized
G	motor activity, 0 = stopped, 1 = moving up, 2 = moving down
H	motor current, 8 bit resolution with 1.96 mA per LSB (*)
J	1/2 × string speed given by the incremental encoder

Table 7.1: Values displayed in the debug mode on the front panel of the control unit. The locations on the LCD are indicated in figure 7.14.
(*)LSB=least significant bit.

LabView GUI. The initializing process moves the source automatically into the parking position, allowing for further system debugging. After bypassing of one of the encoders and after initializing, the system remains operational. In this case the source positioning

relies on one of the still functioning positioning systems. However, operation with one positioning system is highly not recommended and should be performed only in exceptional cases. Positions given by only one encoder are indicated by a red blinking of the position indicators in the main control panel of the LabView GUI. Simultaneous bypassing of both encoders is possible but a failure on both positioning devices will fully block the system even if the two are bypassed.

Table 7.2 shows an overview of the system components which are monitored and the three errors which can be bypassed. Two of this errors are concerning the functionality of the absolute and incremental encoders. The third one (Diff_Abs_Incr) concerns the maximal discrepancy between both encoders which can not be higher than 20 mm. A discrepancy error is automatically ignored, if one of the encoders is bypassed.

The error codes are decimal representatives of a 1 byte word which describes the status of the system. The bit designation and the corresponding error codes are shown in table 7.2. The table allows to identify any error or error combination. It must be noted, that not all system parameters are monitored permanently during run-time. The high impedance (HiZ)

Error	Bit	Error code	Description	Bypass
Motor driver	0	1	onboard, H-Bridge module, no load (HiZ$^{(*)}$)	NO
Absolute encoder	1	2	stuck, not connected or invalid data	YES
Incremental encoder	2	4	stuck	YES
End-switch	3	8	stuck on init position or not connected$^{(*)}$	NO
Diff_Abs_Incr	4	16	discrepancy between absolute and incremental encoder $>$ 20 mm	YES
I^2C	5	32	onboard, system-wide	NO
24V	6	64	power supply, system-wide	NO
ADC	7	128	onboard, system-wide	NO

Table 7.2: Bit designation of the status byte to be used for the decimal error code reconstruction. Multiple errors result in combined error codes. Three of eight errors can be bypassed. $^{(*)}$ Tests performed only during power-up.

test and the end-switch test for example are performed only once, during system start-up. For this reason, error codes can change after switching off and on of the SIS control unit. Observing of the changes in the codes can be very helpful in the identification of a problem. The system status and the error codes are read explicitly on the LabView GUI or on the display of the control unit provided that the display debug mode has been switched on.

Apart the failure of one of the positioning systems, all other errors will fully block the functionality of the SIS. If the source is close to the parking position, it can be moved manually by overforcing the safety clutch. However, for the case the source is stuck close to the detector array, an external control box has been designed allowing to drive the motor of a string without the control unit and without the LabView GUI. The motor driver unit shown in figure 7.15 allows only for basic operation like moving the string up or down. Position monitoring must be performed on the control unit or on the LabView GUI if the position readout is still working. To operate a motor with the external motor driver, the motor must be explicitly connected to the driver as indicated in figure 7.15. Because this procedure overbridges the SIS control unit, all security measures are disabled and hence the operation must be performed with extreme carefulness.

Before using the motordriver, the last initialization position of the absolute encoder should be determined first by reading the last *Init.txt* file written to the hard disc of the SIS PC. Furthermore, the last source position should be determined by reading the *Positions.txt* file which is automatically saved to the PC. In both cases the multiturn value of the absolute encoder is the most important. If the absolute encoder is still operational and a

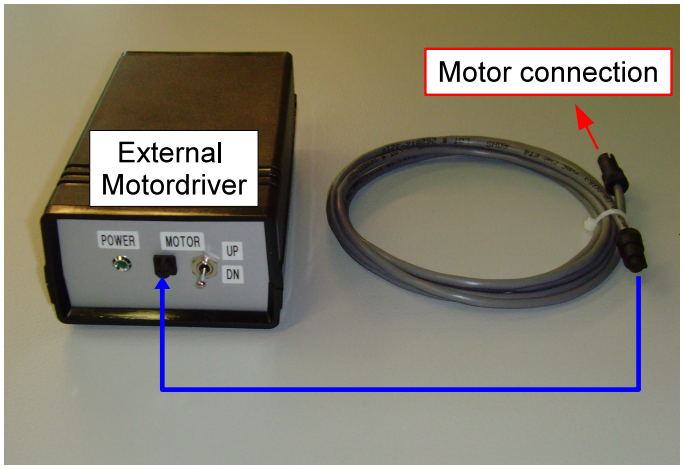

Figure 7.15: External motordriver unit allowing to move a string up or down. The unit has been designed with regard to error situations which can not be solved by error bypassing procedures.

reading of the position still possible, the driver should be used to move the source close to the parking position and stop the string about 2 multiturns before the last initialization position. This prevents the string to be driven to far, which possibly could damage the end-switch or mechanical parts of the system. After stopping, the source should be brought manually into the parking position by turning the motor gear and overforcing the safety clutch till the end-switch has been reached.

If the absolute encoder is not operational, the motor driver can also be used but the

full turns of the gear must be counted manually. If the last initialization position was at a multiturn value of 42 for example and the last measured position of the source was at a value of 20, the source will reach the last initialization position after 22 full turns. For safety reasons, operation of the motor driver should stop at least 2 turns before the supposed parking position. Moving the string into the final position should be than performed manually until the micro-switch has been reached.

In the following, the symptomatics of some possible error scenarios are described, including instructions about how to handle them. Realistic scenarios are for example blocking of the source due to oscillations, a clutch slipping or a positioning encoder failure. Errors of the absolute and incremental encoders and errors on the motor and the end-switch were simulated with an interface board allowing to disconnect or short circuit the components using onboard jumpers. In this section seven example error-scenarios performed on the system will be discussed. The errors were generated after system initialization and during a string movement. However it should be considered that errors patterns can change depending on the situation and conditions at which a failure took place. A failure of the incremental encoder for example will not appear at all if the system is not moving.

• **Failure of the incremental encoder:**
Errors: *Incremental* and *Absolute vs Incremental*, error code = 20.

If the incremental counter does not change its value while the string is supposed to move, an error on the incremental encoder will occur due to the run-time speed check. Furthermore, because the system controls the discrepancy between the positions of both encoder, a position discrepancy higher than 20 mm will trigger also the *Abs vs Incr* error.
The control unit should be switched off and on again. The incremental encoder has lost its positioning information and the source is not supposed to move. Hence, both errors will disappear.
The only function which can be called now is the initialization function which would calibrate the incremental encoder at the end-switch position. However, initialization will trigger again a speed check which will not be passed by the encoder and hence, the error code 4 will appear. The *Absolute vs Incremental* error will not be activated because it requires calibrated data from both encoders.

In order to operate the system, the incremental encoder must bypassed by activating the SW3 DIL switch on the mainboard of the control unit. This will allow to initialize the system and to bring the source back into the parking position.

• **Failure of the absolute encoder:**
Errors: *Absolute* and *Absolute vs Incremental*, error code = 18.

The functionality of the incremental encoder is controlled only during motion. In contrast, the status of the absolute encoder is monitored permanently. Therefore, a failure

of the absolute encoder will always result in the *Absolute* error. If the failure took place during string motion, additionally the *Absolute vs Incremental* error will appear due to the position discrepancy between both encoders.
Switching off and on of the control unit will change the error code from 18 to 2, which is an error only on the absolute encoder. The discrepancy error will not appear as long as the string is not in motion and the incremental encoder not calibrated.
Initializing of the system will not work unless the error on the absolute encoder has been bypassed. The unit should hence be switched off again and the SW2 DIL switch activated on the main board. After entering the LCD debug mode, initialization will be possible.

• No power on the motor:
Errors: *Absolute* and *Incremental*, error code = 6

The speed of a string is monitored permanently by the controller while in motion. If the measured string speed is above 40 mm/s or below 2 mm/s, the controller interprets the lost data integrity as a failure of both encoders.
Switching off and on of the controller always triggers a system selfcheck of the electronic components. The selfcheck includes the measurement of the motor impedance which will not pass the test (HiZ). Therefore, the error code will change to 1, indicating a failure of the motor driver.
Unless the motor can not be repaired (connectivity, power check), the system must be brought into the parking position fully manually by overforcing the safety clutch.

• Shortcircuit the motor:
Errors: *Motordriver*, error code = 1

The control unit monitors permanently the electrical current through the motors with the onboard ADC as well as shorts to GND and to the 24 V of the motor driver H-bridge. If the measured current exceeds 400 mA or if a short is detected, the control unit returns an error of the motor driver.
Switching on and off of the control unit will reset the error to zero, because the HiZ test will be passed. However, triggering the initialization procedure will immediately result again in error code 1, due to the high current.
To bring back the system into the parking position, the external motor driver should be used if possible, otherwise only manual operation is possible.

• Clutch slipping:
Errors: *Absolute* and *Incremental*, error code = 6

If the safety clutch is adjusted to sustain torsional momentums which are lower than the momentums occurring during the string movement and especially during acceleration, the clutch can slide, resulting in a speed feedback from both encoders which is not consistent with the acceptable speed range of 2-40 mm/s. The controller will return an error on both

encoders in consequence.
However, depending on the conditions, clutch slipping can also result in other errors like *Absolute* and *Absolute vs Incremental* or *Incremental* and *Absolute vs Incremental* with errors codes 18 and 20 respectively.
The errors will be reset after switching off and on the control unit. There is a chance, that triggering of the initialization process will not cause the errors to appear again depending on the mechanical and fractional conditions of the system. This can be an indicator for a clutch which should be tightened to increase the maximal torsional momentum.
However, if the errors appear again even after tightening the clutch, they can indicate for a source blocking. Such a scenario can happen for example if the source was in the vicinity of the parking tube neck while moving up. In this case, one should check manually for unexpected mechanical resistance or wait some minutes to reduce possible oscillations. Bypassing of both encoder errors will not allow to operate the system.

• **End-switch disconnected during movement:**
Errors: *Absolute* and *Incremental*, error code = 6

For safety reasons, the micro-switch used as a reference point for both encoders is always conductive and opens only if activated during the initialization process. Hence, a disconnected end-switch mimics the situation of an absorber which reached the reference point given by the end-switch. In this situation the code execution demands a stopping of the motor. However, this is in conflict with another instance of the code which monitors the actual source speed. In consequence, the system does not pass the speed check which results in an error on both encoders.
Switching off and on of the control unit triggers the selfcheck of the system which includes a plausibility check of the end-switch. Because this test will not be passed, the error code will change to 8 indicating a failure of the micro-switch functionality.
An error on the micro-switch can not be bypassed and hence if the reason for the failure can not be found, the only way to move a string into the parking position is to use the external motor driver or to move the string manually.

• **End-switch missed while initialization:**
Errors: *Absolute* and *Incremental*, error code = 6

During initialization, a piston mounted on the absorber activates the end-switch which entails a motor stopping, followed by the movement into the parking position. String oscillations in the ϕ-plane during the initialization process can in principle cause the piston to miss the end-switch. In this case the absorber will be forced to move further upwards than allowed by the mechanical design. The maximal resulting mechanical stress will be limited by the adjusted torsion moment of the safety clutch. However, if the measured speed is below 2 mm/s, the controller interprets the lost data integrity as a failure of both encoders resulting in the error code 6. The situation is equivalent to a source blocking.
Switching off and on of the control unit and triggering the initialization process will result

in the same error code. The problem can be resolved by moving down the source manually (few centimeters) and by restarting the initialization process.

In general, the errors occurring should be analyzed under the aspects of an overall picture of the system. The conditions under which the errors took place should be considered as well, as the errors occurring after switching off and on of the control unit. Further hints for the system debugging are given by calling the *Initialize* function and observing the system behavior. The external motor driver should be used as a last option to move a broken string into the parking position. The latter may be necessary in the case of errors which can not be bypassed for example.

7.5 SIS performance at LNGS

Extensive tests with all three strings were performed at the University of Zurich with the SIS arms mounted on a platform at a height of about 7 m. The tests included general functionality aspects of the control unit and of the LabView GUI. Furthermore, besides long term stability-, position discrepancy-, and vacuum- tests, errors were simulated and error handling procedures determined. Oscillation and rotation tests were performed by Francis Froborg and described in [57]. Additionally, cross check measurements were done in order to compare the positions given by the incremental encoder and the positions given by an independent measurement performed by a laser rangefinder. The maximal discrepancy found at a depth of 6 m was 3 mm and can be explained by a deviation of 2 μm in the distance between the band holes as described in [57].

After initialization, the incremental encoder becomes the first priority positioning system, because its position value is not affected by mechanical system parameters like the band thickness, band length or crank diameter. However, in the case the incremental encoder fails, the positioning will rely merely on the absolute encoder. For this reason it is important to correct for the position discrepancies between both encoders. The LabView GUI described in section 7.2 was designed to save all available positioning and status data automatically every 100 ms, once a system activity takes place. The saved data can be used to determine the position discrepancies between both encoders for each string. Although the three discrepancy data sets for each string could be fitted by a second order polynomial making a position discrepancy correction a straight forward procedure, the data revealed that each string has an individual discrepancy distribution. This indicates that the discrepancies observed are resulting from different mechanical conditions given in each string. The tolerance play of the mechanical components within a SIS arm can result for example in different band reeling conditions and in slightly different role diameters. Same effects can occur if a perfect system alignment is not assured or if the arms are not arranged in the horizontal plane. Before transporting the systems to LNGS for mounting, the *Infinite Loop* sequence of the LabView GUI, described in section 7.2 was used to run automatically the three string systems between 0 mm and 6500 mm for over 100 cycles.

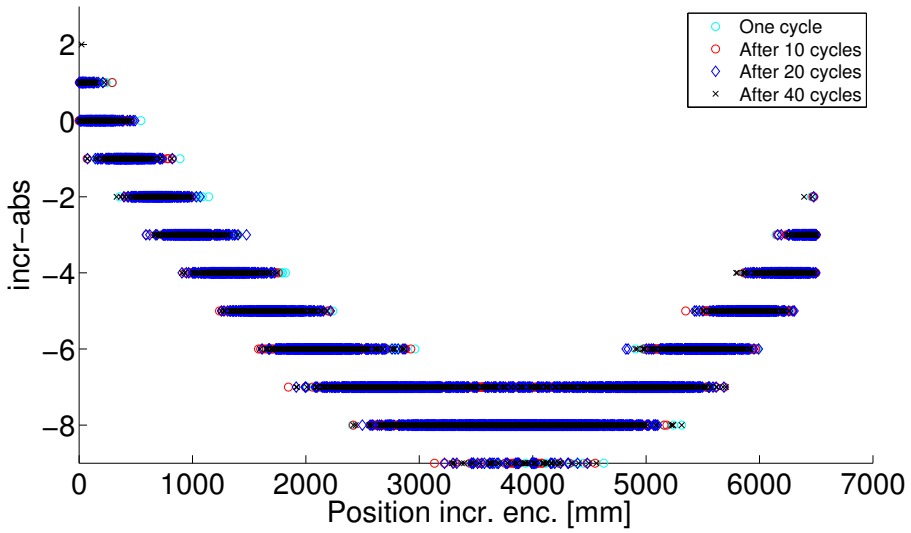

Figure 7.16: Incremental encoder data minus absolute encoder data plotted versus the position of the incremental encoder for one string. The discrepancy of up to 9 mm can be corrected using the WRITE.VI GUI described in section 7.2. No evolution in time of the discrepancies could be observed.

The goal of this run was to determine a possible instability or accumulation effects in the discrepancies. However, over the whole testing period, the discrepancy data stayed consistent with each other within ±1 mm. The cycling campaign at the University of Zurich included tests with and without positioning corrections. Figure 7.16 shows an example of the discrepancies distribution after 1, 10, 20 and 40 cycles as they resulted for string 1 without thermal and positioning corrections implemented. The plot indicates, that the discrepancies remain stable in the course of a string operation. For a better overview of the discrepancy evolution in time, the discrepancies have been fitted with a second order polynomial expressed by

$$D = \alpha \cdot pos_{incr}^2 + \beta \cdot pos_{incr} + \delta \tag{7.3}$$

where D is given by the difference between incremental and absolute encoder, pos_{incr} is the position given by the incremental encoder and α, β and δ are constants. Figure 7.17 shows the fits of the data shown in figure 7.16. All fits are consistent with each other in the full operational range of the string within ±1 mm. In conclusion, although each of the string shows a different discrepancy distribution as presented in figure 7.18, the correction procedure must be performed only once on each of the three strings. In addition, system data are always saved to the disc by the LabView GUI, and posterior discrepancy tests can be performed at any time in the future. After the tests at the University of Zurich, all three systems have been dismounted and the components cleaned in an ultrasonic bath. The mechanical components were partially reassembled and packed for transportation to the LNGS site.
Mounting of the three systems in the clean room of GERDA took place in June 2011.

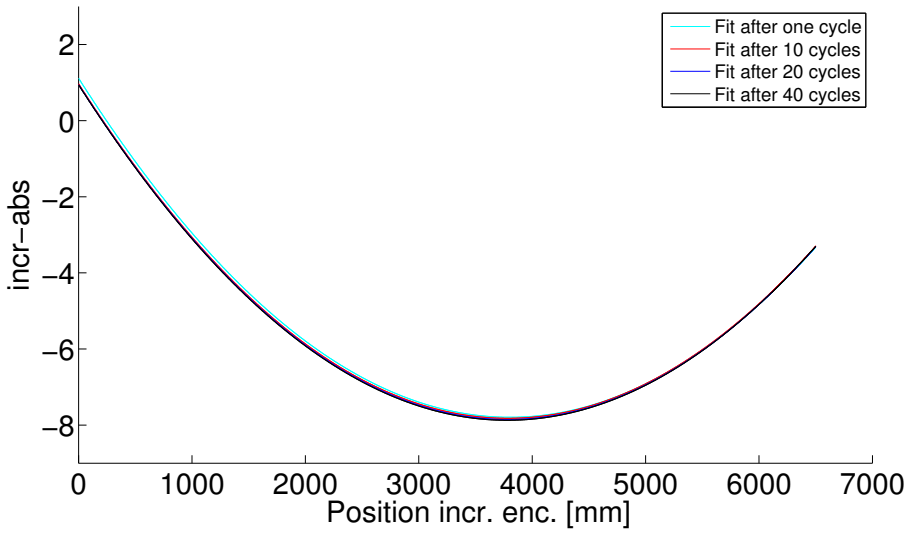

Figure 7.17: Second order polynomial fits of the discrepancies shown in figure 7.16. No evolution in time can be observed and hence, position corrections must be applied only once after a string has been mounted.

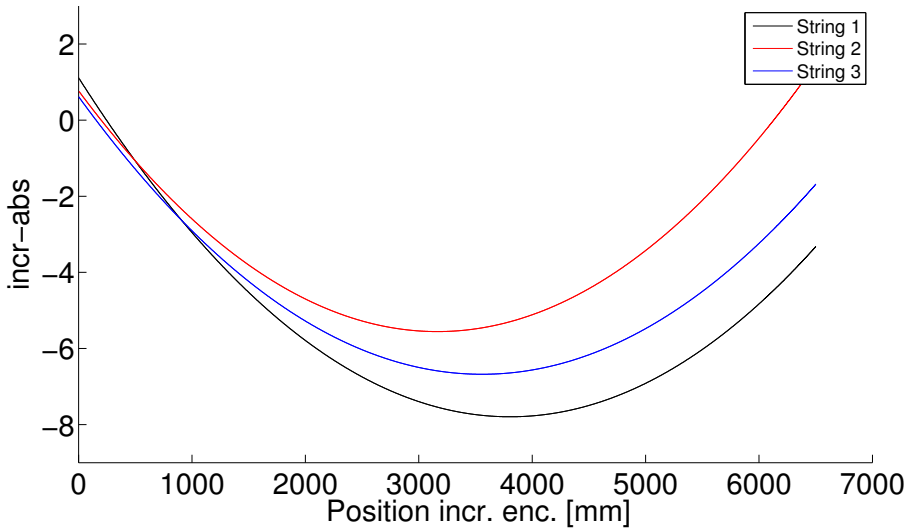

Figure 7.18: Discrepancy fits of the three strings. Although stable in time, correction tables to be implemented must be determined for each individual string.

At first, the torsional momentums of the three safety clutches have been adjusted using a variable set of weights mounted on each of the absorber. Each clutch has been adjusted to sustain an additional weight M_{add} of

$$M_{add} = 2.5 \text{ kg} \tag{7.4}$$

before starting to slip. This adjustment was found to be sufficient to sustain string acceleration under normal conditions and is expected to prevent serious damage on the mechanical components in the case of a source blocking. Furthermore, in the case the absorber misses to activate the end-switch during an initialization procedure, the end-switch should not be damaged.

Three ^{228}Th calibration sources were mounted on the absorber with the two custom sources on string 1 and string 2 and one commercial ^{228}Th source on string 3. Table 7.3 shows an overview of the sources and their activities. After assembling the mechanical components

String number	1	2	3
^{228}Th source	SV303, custom	SV304, custom	SK393, commercial
Activity [kBq] @ 1.1.2011	18.09±15%	12.81± 5%	19.02±3.1%

Table 7.3: ^{228}Th sources mounted on the SIS strings and their activities.

on the cluster flange of GERDA, leakage tests were performed in order to make sure the system is vacuum tight. Electronic components were connected to the control unit and the cabling for the shutter control assembled. The control unit, the LabView PC as well as the shutter control box were mounted within the PLC rack which is used to control the detector strings. The compact assembly in the direct vicinity to the glovebox allowed to avoid long cabling through the clean room. In particular, the RS422 cable with a length of 20 m could be replaced by a 10 cm long interface between the control unit and the RS422 to USB converter used for the connection to the PC.

Because the absolute encoders have been decoupled from the motor gear during transportation, all three strings had to be configured after the mounting took place. Different procedures for the first SIS configuration have been described in chapter 7.3. The system has been configured using the clutch overforcing at a depth of 6500 mm. To do so, the control unit had to be turned on and the absolute encoder decoupled. The multiturn value can be read on the SIS control display if in debug mode, or on the SIS LabView GUI without any intervention on the mainboard. After the multiturn value of the absolute encoder has been adjusted to a value of 50, it has been coupled back to the motor gear and fixed. After initialization, each of the string has been moved down to 6500 mm. From this point, the band was fully unrolled manually until the band fixation point on the crank was visible through the front window of the SIS arm. Bridging the reset pins on the mainboard, set the absolute encoder to zero. Initializing the system has completed the configuration process by moving the strings into their parking position.

The second part of the system configuration concerns the microcontroller settings and requires the two LabView GUI's READ.VI and WRITE.VI which can read and write the microcontroller settings used for the position calculation. To allow for parameter over-

writing, the SW4 DIL switch on the mainboard must be activated. The input consists of three position correction tables, four hardware parameters and two parameters for the liquid argon level and the thermal expansion coefficient of the band. Unless mechanical components in the SIS units have been changed, the hardware parameters stay always the same with

- Wheel diameter = 46 mm
- Tape length = 6500 mm
- Tape thickness = 0.1054 mm
- Tape hole pitch = 4 mm
- Liquid level = 1200 mm

The liquid level defines the position at which thermal corrections start to apply. The value should be only changed, if the argon level in GERDA has changed. Although in principle correlated, this level should not be mixed up with the liquid argon level adjustable on the LabView GUI. The GUI level serves only as the position at which a string stops for oscillation dumping. It has no influence on the position calculations of the microcontroller. In the ideal case, the LabView GUI level is a couple of centimeters below the actual liquid argon level for a more effective oscillation dumping.

The CTE parameter refers to the linear 'Coefficient of Thermal Expansion' and is given by

- CTE = - 0.002735

for the stainless steel band. The thermal contraction of the band in the liquid argon is taken into account by calculating the room temperature length of the band immersed into the liquid, according to

$$dL = CTE \times L_{imm} \times dT \tag{7.5}$$

where dL expresses the contraction of the band, L_{imm} is the length of the band immersed in the liquid and dT is the temperature difference between the room- and liquid argon temperatures given by 209 K.

Thermal corrections are applied only to the incremental encoder data while the position correction tables apply merely to the absolute encoder data. Therefore, in order to perform a final position correction, first the parameters described above are written to the controller together with the three positioning correction tables CT_0. At this stage, the tables consist of 64 dimensional zero vectors

$CT_0(\text{String [1-3]}) = \vec{0}$, $\dim(CT_0) = 64$.

With the settings described above, the strings are ready to take discrepancy data. Because the systems have been deassembled for transportation and mounted from scratch in a new environment, all three strings were first subject to a start-up cycling procedure of more than ten full cycles between 0 mm and 6500 mm. In order to simplify the position correction, additionally three full cycles were performed without the thermal corrections. This allows to fit the discrepancy data without thermal correction, using a second order polynomial and to add a linear thermal correction in posterior. Figure 7.19 shows the

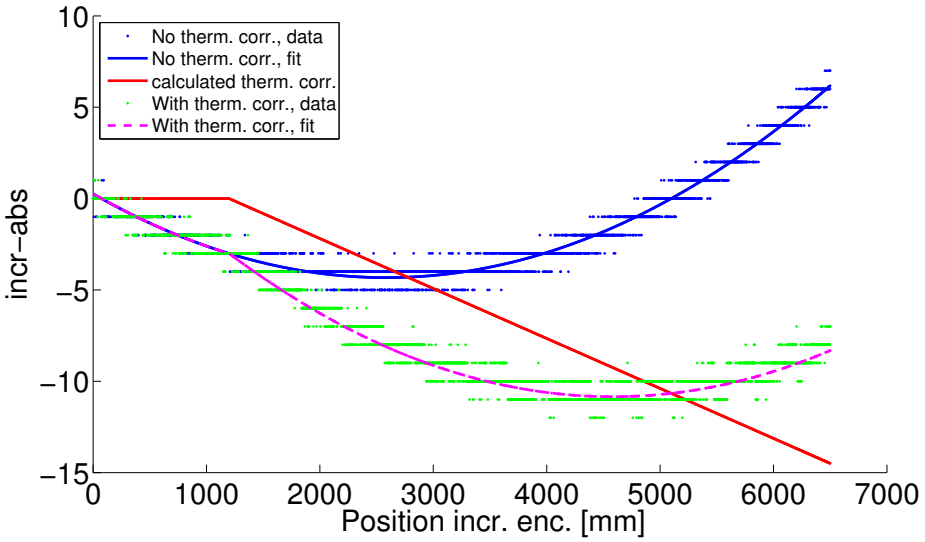

Figure 7.19: Discrepancies between incremental and absolute encoder before and after the implementation of thermal corrections. In order to create a position correction table, the acquired thermal-corrected data can be reconstructed by fitting the non-corrected data using a second order polynomial and by explicitly adding the calculated thermal corrections to the fit.

discrepancy data taken with string 1. The kink in the data at 1200 mm results from thermal corrections applied by the control unit at the liquid argon level. A contraction of the band expressed by the incremental data increases the discrepancy between both encoders. Linear thermal correction values calculated explicitly with the same parameters as used by the microcontroller can be added to the fit and applied to the data without thermal corrections. This allows to reproduce the discrepancy distribution as it results with the thermal corrections implemented. At this point, the fit which includes thermal corrections can be used to interpolate on the multiturn values of the absolute encoder.
The number of correction values is given by the range of the absolute encoder which is limited by the firmware to 64 multiturn values. Although the range of the absolute encoder is by far higher, 64 values are more than sufficient to cover the whole operational range

within the GERDA cryostat with a multiturn value of 0 at the full length of the band and a value of 42 in the parking position. Discrepancy corrections by the controller are not performed continuously but only at each of the 64 multiturn values of the absolute encoder. Therefore, a correction fit of the discrepancy data as a function of the multiturn values of the absolute encoder must be performed. An example of the final correction table determination is shown in figure 7.20. The discrepancies are plotted vs the 42 mul-

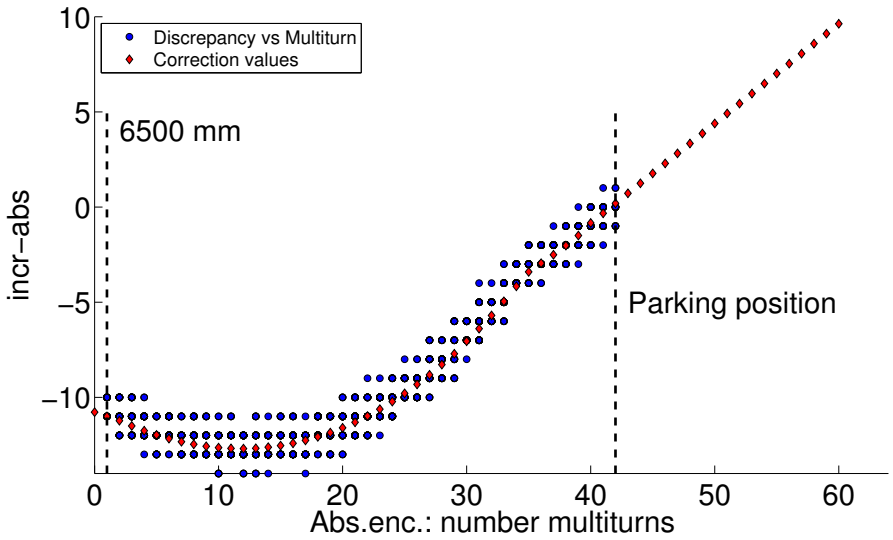

Figure 7.20: Discrepancies vs the multiturn values of the absolute encoder. The multiturn range is limited by the GERDA setup up to 42 values. Because 64 values are needed for the correction table, a linear interpolation up to a value of 64 has been performed. After implementation in the EEPROM of the controller, the values are used to correct for the discrepancies at each multiturn.

titurn values given by the operational range within the GERDA cryostat. Higher values than 42 represent positions above the end-switch and can not be reached with the system. Therefore, to complete the correction table, the discrepancies for higher values have been interpolated linearly. Because, those represent an inactive range, it is also possible to set this values to zero without any impact on the system functionality and precision. The thermal correction kink at 1200 mm shown in figure 7.19 can be observed at a multiturn value of 36 in figure 7.20.

To implement the corrections and configuration parameters, the SIS control LabView GUI must be stopped and the WRITE.VI opened. However, it is recommended to run the READ.VI first in order to save the old settings. After implementing all parameters into the WRITE.VI and importing the correction tables, the parameters can be written into the microcontroller using the WRITE TO MEMORY button. The new settings are adopted after switching off and on of the control unit and can be confirmed by using the READ.VI again. The control unit can be now switched off again in order to disable the DIL SW4

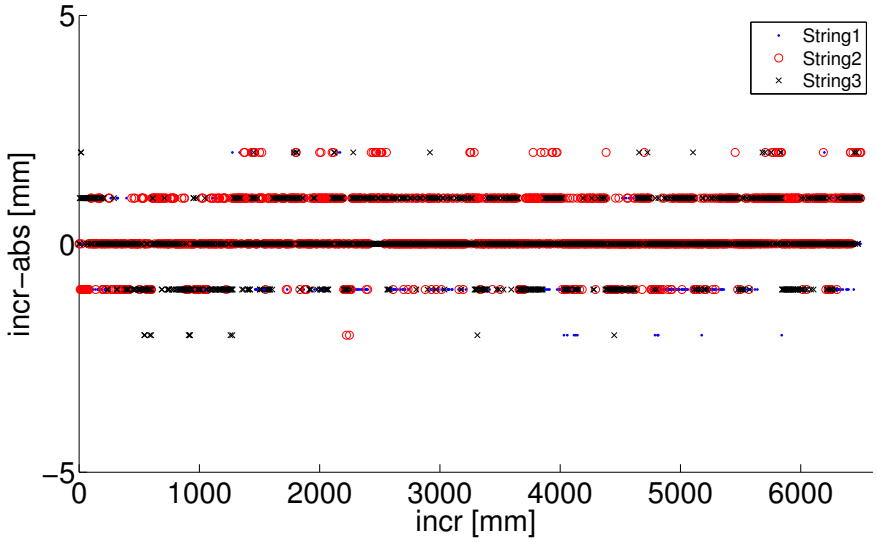

Figure 7.21: Disprepancies between incremental and absolute encoder, after the thermal- and position- corrections have been implemented. Most of the data can be found in a range of 0±1 mm. The plot shows deviations of up to ±2 mm. Values of up to 3 mm were observed but are extremely rare.

switch, which allowed for the parameter configuration. The red LED's on the front panel will stop blinking confirming a standard running mode of the control unit. The system is ready for operation after triggering the initialization function and can be monitored and controlled with the SIS LabView GUI. Figure 7.21 shows the discrepancies between the absolute and incremental encoder after the position and thermal corrections have been implemented. The distribution is flat with most of the points around zero mm. Although deviations of up to 3 mm were observed in the course of the SIS operation, more than 90% of the values lie within a range of ± 1 mm if the system is calibrated correctly. Figure 7.22 shows the histogrammed data of figure 7.21. More than 97% of all discrepancy data points for all three strings can be found within a range of 0±1 mm and only up to 3% in string 2 can be found at deviations reaching a value of 2 mm.

The discrepancy corrections are important to assure a reliable position reconstruction, if the incremental encoder fails. The first priority positioning system is the incremental encoder to which the thermal corrections are applied. Therefore, it is important to keep the liquid argon level updated.

Time-dependent broadening of the discrepancy distribution or a permanent drifting of the centroid can indicate problems with the mechanical components of the system and should never be ignored.

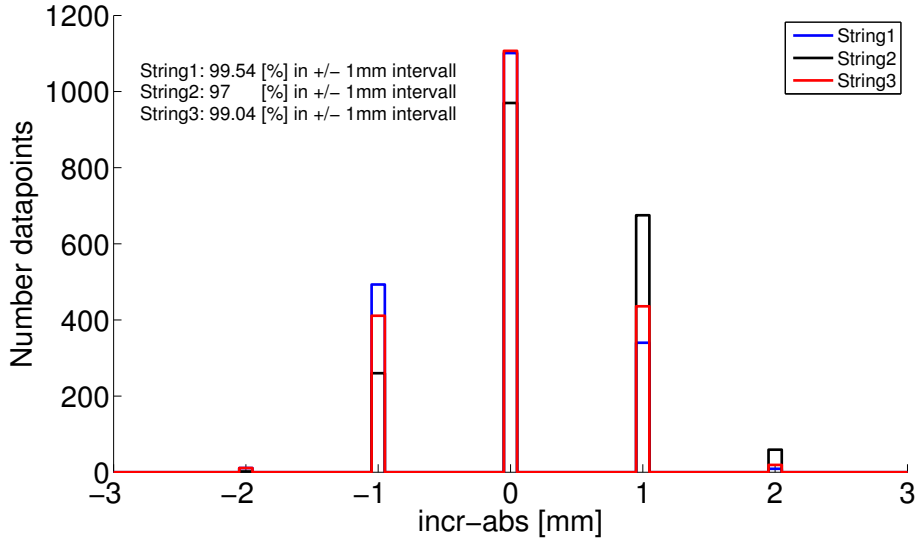

Figure 7.22: Histogrammed discrepancies at string 1 - 3 after implementing thermal and position corrections. More than 97% of the positions are consistent with each other within a range of 0 ±1 mm.

7.6 SIS online data base

Once a system activity takes place or an error occurs, the full set of system informations is written automatically by the LabView GUI on the SIS PC into text files. The data are saved locally and are not accessible to all collaboration members through a network. In order to allow a remote system monitoring, the LabView code has been modified providing an additional text file with the most relevant system data. The data were implemented into the slow control system in collaboration with R. Brugnera and A. Garfagnini from the Padova University. The file includes the following parameters:

AbsEncMulti: Multiturn value of the absolute encoder.

AbsEncSingle: Singleturn value of the absolute encoder.

AbsEncPos: The calculated position in mm, based on the raw data of the absolute encoder.

Discrep: Actual discrepancy between the incremental and absolute encoder.

IncrEncPos: Calculated position in mm, based on the data of the incremental encoder.

The GERDA slow control allows to monitor the status of the experiment and monitors system components like DAQ crates, cryostat, Rn concentration, temperatures and the

water loop system. To implement the SIS system into the slow control of GERDA, a sep-

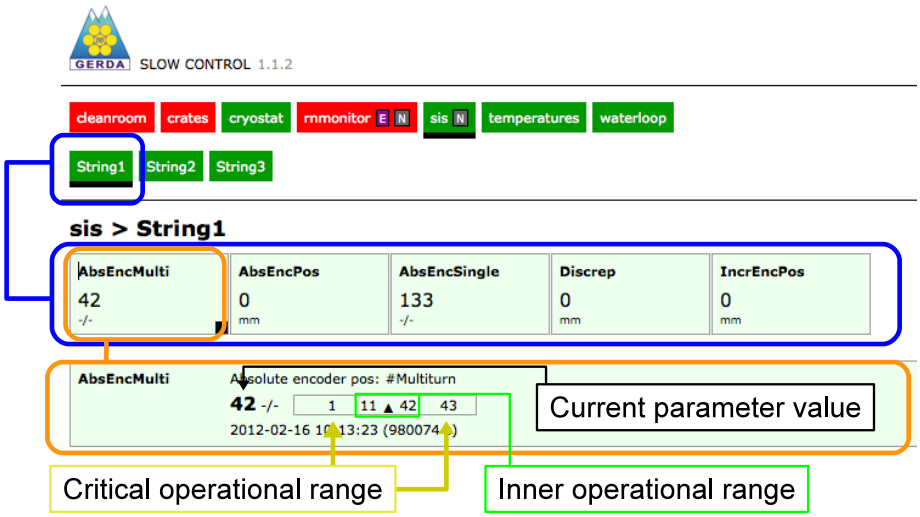

Figure 7.23: Layout of the online slow control of GERDA which allows to view and display five basic SIS parameters of the source strings.

arate text file containing the parameters to be monitored is saved on the harddrive in a suitable formate, which is required by the slow control system. The text file updates each 100 ms according to the loop frequency of the LabView GUI and overwrites the previously saved data. On the other hand, the data base of the slow control updates every ∼30 s, which drastically reduces the time resolution of the monitored data. However, if necessary exact information of the system and its history can be found in the files which are written permanently by the LabView GUI in 100 ms intervals. Figure 7.23 shows a part of the slow control with the information displayed for string 1. The parameters monitored and their current values are displayed in the table on top. Clicking on one of the parameters opens a second table below which shows again the current parameter value, and four numbers which define the operational range and a critical range. Figure 7.23 shows for example the value of 42 for the absolute encoder. The standard operational range has been defined between 11 and 42 which is equivalent to a range between 5000 mm and 0 mm. A multiturn value of 43 represents a source position above the end-switch and defines hence the upper limit for the alarm triggering. A multiturn value below 11 is still allowed, as the string can be moved down to 6500 mm. However, a critical state indicated by a yellow color will appear below a multiturn value of 11 to attract the users attention. Values below 1 occur at a depth which is equivalent to the band length and hence define the lower limit for the operation. Exceeding of the outer range values will trigger an alarm indicated by a red color. However, alarm triggering on the slow control will not have any active impact on the system. The correct error response is provided by the SIS control unit in the first order and by the LabView GUI in the second order. Table 7.4 shows the inner and outer alarm triggers as they have been set in the LabView code. The limits are hard-coded but can be changed at any time if necessary. Additionally, the five SIS parameters available

Parameter	Inner operational range	Critical operational range	Out of range
AbsEncMulti	[11 42]	[1 10] & >42	<1 & >42
AbsEncPos [mm]	[-10 5000]	[-12 -11] & [5001 6500]	>6500 & <-12
AbsEncSingle	[0 255]	< 0 & >255	<0 & >255
Discrep [mm]	[-10 10]	[-20 -10] & [10 -20]	<-20 & >20
IncrEncPos [mm]	[-10 5000]	[-12 -11] & [5001 6500]	>6500 & <-12

Table 7.4: Five parameters of the SIS system implemented in the slow control of GERDA. The system requires the definition of an inner operational range, a critical operational range and two absolute limits.

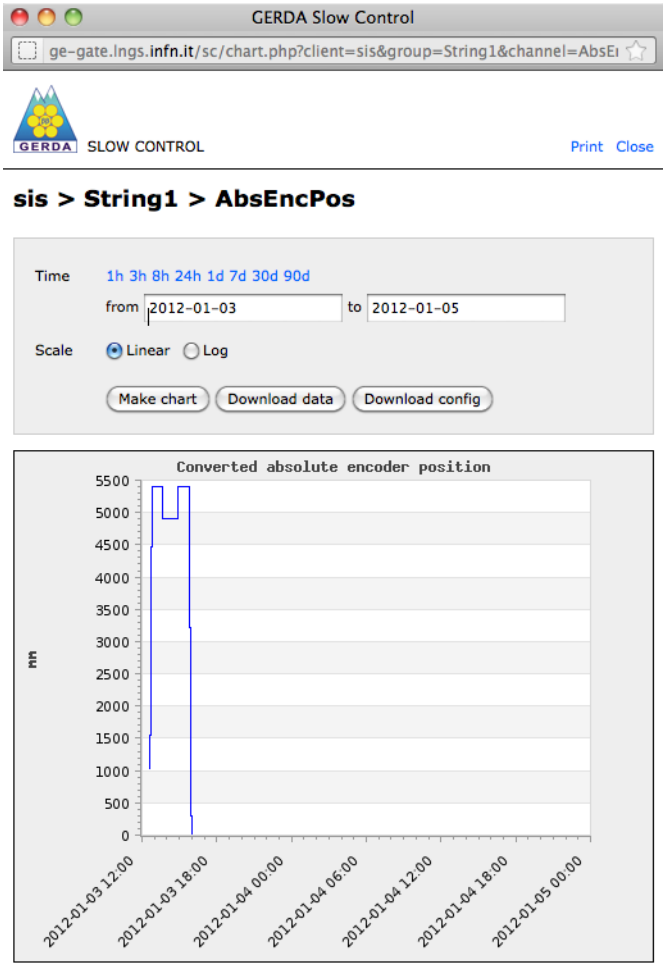

Figure 7.24: Example plot of historical absolute encoder data given by the slow control of GERDA. The plotted data can be also downloaded to extract a more exact timing and positioning information.

on the slow control can be plotted in a chart by choosing a time interval of interest. As an example, figure 7.24 shows a chart of the positions of string 1 given by the absolute encoder. The figure shows that the source has been moved on the 3.Jan. 2012 to a position of 5400 mm, moved up to 4900 mm and down again to 5400 mm before moving back to the parking position. The source was kept for about one hour at each position. For a more precise positioning and time determination, the plotted data can be also downloaded for further analysis.

7.7 Summary

The two custom ^{228}Th sources SV303 and SV304 and a commercial SK393 ^{228}Th source have been mounted in the Source Insertion System (SIS) of GERDA in 2011. The SIS system was designed and built at the University of Zurich and involves two redundant positioning devices consisting of an optical incremental encoder and a magnetic sampling absolute encoder. Besides the mechanical components, a control unit was developed allowing for source string operation and system monitoring. Onboard settings allow to bypass errors, reset the absolute encoder and to chose an interface allowing for the communication with a PC.

For the communication between computer and control unit, LabView driver have been developed and a Graphical User Interface (GUI) designed. The GUI allows to program string motion sequences with exact positioning. Furthermore, the system status including all available parameters, error flags and historical data are displayed graphically. Positioning data and error flags are saved on the hard disc automatically. Saving is triggered by any system activity or by a system error. Two additional LabView GUI's were developed to read and write configuration data of the EEPROM memory, which are used for the correct position reconstruction based on the hardware parameters of the SIS.

The system was tested in Zurich for functionality of the control unit and of the LabView GUI. Additionally, based on a digital I/O module, a shutter control unit was designed and implemented in the LabView GUI. Error scenarios were simulated and procedures determined to prevent a string to get stuck in the cryostat. For the case of a total system failure, an external motor driver has been designed, allowing for basic motor operation without the involvement of the control unit and the GUI.

Long term stability tests were performed by an implemented function allowing to operate the strings in an infinite loop. Error accumulation has not been found after more than 100 full cycles. Corrections of the position discrepancies between the absolute and incremental encoder were performed, resulting in deviations D of

$D = \pm 1$ mm

for more than 97% of the data acquired in 100 ms intervals.

Discrepancy and thermal corrections were explicitly performed again after mounting and configuring of the three SIS systems at LNGS. Finally, consecutive modification of the LabView code has been done to implement the most relevant data in the GERDA slow control. The latter allows to monitor the system history online.

Chapter 8

The Broad Energy Ge detector (BEGe) vs segmented Ge detectors

Although, the principle of semiconductor detectors is always the same, recent progress in germanium detector technology allows for different configurations making the technology more flexible in terms of individual experimental requirements. In GERDA phase I, closed-ended coaxial detectors are used which were operated in the past in the Heidelberg-Moscow [90] and in the IGEX experiments [91]. With a total mass of 18 kg and an isotopic enrichment in ^{76}Ge of 86%, the GERDA experiment is expected to reach a sensitivity of $> 2.2 \cdot 10^{25}$ years after one year of operation [92]. To reach this goal, the background index in the region of interest around $Q_{\beta\beta}$ must be below 10^{-2} counts/(keV·kg·y) . Besides passive shielding, the background can be also reduced actively by analyzing for example the topographic distribution of the events in the crystal. Due to the charge of β particles, their interactions are limited to a local range within couple of millimeters and are therefore called Single Site Events (SSE). In contrast, gamma paticles deposit their energy on a centimeter scale in several interactions. Multiple energy depositions distributed on a macro scale are called Multi Site Events (MSE). Effective discrimination methods to distinguish between SSE and MSE are crucial in order to reduce the gamma background and increase the $0\nu\beta\beta$ detectivity limit. Pulse shape analysis (PSA) methods can in principle identify MSE's by analyzing the time distribution of a signal. However, due to the homogenous electrical field, PSA methods applied to coaxial detectors allow only for a radial event separation. Furthermore, typical pulse rise times of about 100 ns require a high time resolution of the data acquisition modules and result usually in insufficient discrimination efficiencies with PSA methods.

Segmented detectors consist of several sensitive germanium segments. Although unified in one volume, the segments are separated by an isolating layer allowing to treat each of the segment as an independent detector. Crystal segmentation allows to map the distribution of an event within the detector and hence the technique is an effective tool to discriminate between SSE and MSE. However, the spatial resolution of an event depends on the number and size of the segments. Furthermore, the production of segmented detec-

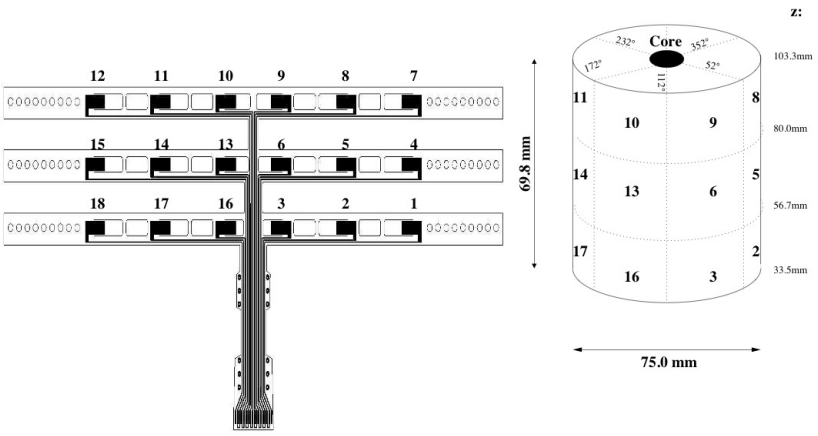

Figure 8.1: Scheme of a 18-fold segmented detector and its contacting array. The contacts are located on a capton support structure which can be mounted around the crystal to perform contacting of the segments. Picture from [93].

tors is complex and expensive and the operation of a segmented detector requires each of the segments to be read out explicitly. This implies more cabling, more DAQ capacity and a higher analysis effort. In addition, the higher cabling and electronic effort must be considered under additional background and noise aspects. For the second phase of GERDA, 18-fold segmented n-type detectors were considered as candidates to perform an effective SSE/MSE discrimination. The detectors were tested mainly by the group from the Max Planck Institut füer Physik in Munich. Figure 8.1 shows a scheme of a germanium detector in a true coaxial configuration with three folds along the z-axis and six folds in the ϕ plain. Signal readout of the eighteen segments has been performed by low radioactivity capton cables with snap contacts, which are described in [94] for example. In combination with additional pulse shape analysis methods, the detector segmentation allowed to reject more than 80% of MSE in the tested setup [95].

Especially with regard to the signal readout effort as required by segmented detectors, an alternative detector design has been developed in the past years which allows to operate the detector in the same way as a single crystal, simultaneously offering the possibility of an efficient SSE/MSE discrimination. BEGe (Broad Energy Germanium) detectors also known as P-PC detectors (p-type point contact) are consisting of a high purity germanium p-type crystal with a Li-drifted n+ contact covering the whole surface. In contrast to typical coaxial detectors, the bore hole electrode in the center of the crystal is completely removed. Instead, the central electrode consists of a point-contact as indicated in figure 8.2 with typical dimensions of several millimeters. The small p+ contact, drastically reduces the capacitance of a BEGe detector compared with bore hole contact detectors. As a consequence of the lower capacitance, the electronic noise is reduced and the resolution improved in BEGe configurations. Furthermore, the electrical field within the detector is not homogenous and has the highest gradient and potential in the vicinity of the point

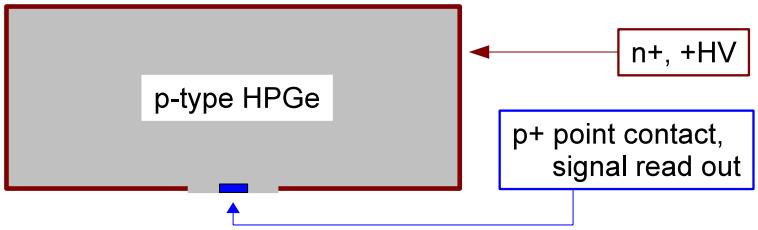

Figure 8.2: Scheme of a p-type BEGe detector. The small contact on the bottom reduces the capacitance of the crystal. Furthermore, the contact causes an inhomogeneous field within the crystal with a sharp jump of the potential in the vicinity of the contact.

contact. Charge collection processes on the electrode and the generated pulse shapes can be numerically simulated if the weighting potential distribution within the sensitive volume is known. Detailed studies of charge drifting and signal reconstruction of charge clusters within a BEGe detector were described in [59] and [96]. Due to the inhomogeneous field in the crystal with a sharp jump of the weighting potential at the electrode, the drift time interval for charges, propagating through the volume is increased allowing to distinguish between local charge clouds generated by single site events and multi site events which are characterized by a wide charge distribution in the crystal. Because no segmentation is needed, BEGe detectors are easier to produce, which directly translates into cost-effectivness.

8.1 SSE/MSE discrimination studies with BEGe detectors

A method to identify single site events and multi site events in BEGe detectors was developed by Dusan Budjas and is extensively described in [59]. The principle of the method bases on the pulse shape analysis which takes advantage of the increased drift times of the charges induced during an energy deposition. The charges induced by a single site event have a narrow spatial distribution with up to a few millimeters and are therefore exposed to an equal electrical field. The charges propagate in formation through the crystal and are collected on the p+ electrode simultaneously which results in one single peak in the differential signal. In contrast, multi site events as illustrated in figure 8.3 are characterized not only by different charge trajectories in the crystal, but furthermore the charges induced at each point of an energy deposition are exposed to different electrical fields resulting in considerably different propagation times. While the potential in the bulk is almost constant and the drift times comparable long, charges in the vicinity of the p+ electrode are subject to high propagation speeds and short drift times. In consequence, the differentiated signal from a MSE can distribute over a time interval of up to 1μs. Several peaks are appearing within the time interval of charge collection, each of them representing charges from a partial energy deposition within the crystal. The signature from a SSE and a MSE in a BEGe detector is shown in figure 8.4. The energy of an event is given by

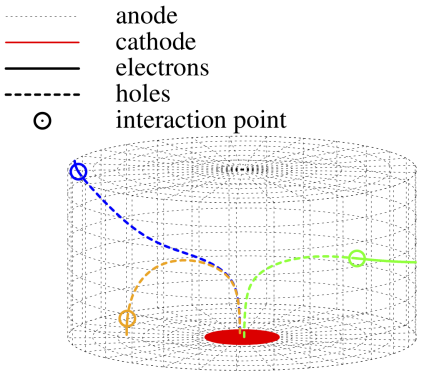

Figure 8.3: Simulated charge propagation trajectories of a multi site event in a BEGe detector. Figure from [97].

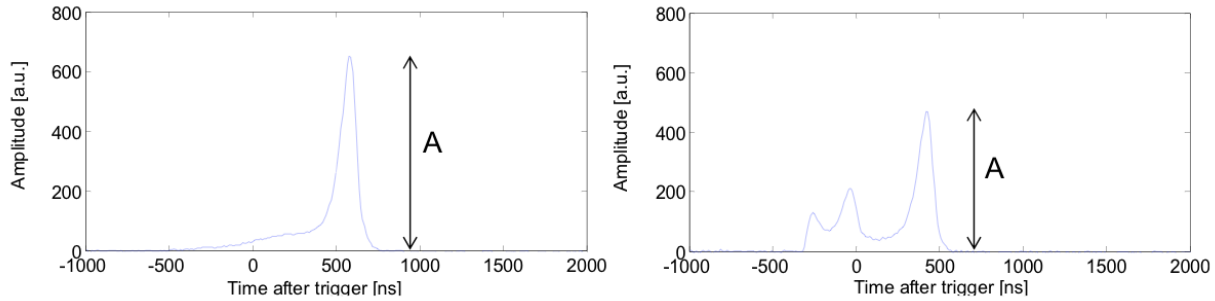

Figure 8.4: Differential signal characteristics of a single site event (left) and a multi site event (right) in a BEGe detector. Figure from [98].

the integral of the current signal, and therefore the maximal amplitude of a MSE pulse is lower with respect to a SSE pulse of the same energy. The MSE signature of the BEGe detectors allows for a variety of pulse shape analysis methods for the event discrimination. The method described in [59] uses the ratio of the current signal amplitude A vs. the integral of the signal which is equivalent to the event energy E. The A/E discrimination parameter has been successfully tested in [59]. Figure 8.5 shows the spectrum of a ^{228}Th source, a background spectrum and a density diagram of the acquired A/E parameter for all events. Single site events are characterized by a maximal amplitude in relation to the total energy of an event. Therefore the upper edge of the density diagram contains mainly single site events. A very good example of single site events is given by the double escape peak (DEP) of the 2.6 MeV line of ^{228}Th . The DEP peak arises as a consequence of e^-e^+ pair production within the detector triggered by the 2.6 MeV γ of ^{228}Th. The positron annihilates almost instantly emitting two γ particles with a total energy of 1.02 MeV. If both of the γ's escape the detector, the energy deposition is limited locally to the point of the initial pair production and can be classified as a SSE. The energy of such event is given by

$$E_{DEP} = 2.6 \text{ MeV} - 2m_e = 1.592\text{MeV}. \tag{8.1}$$

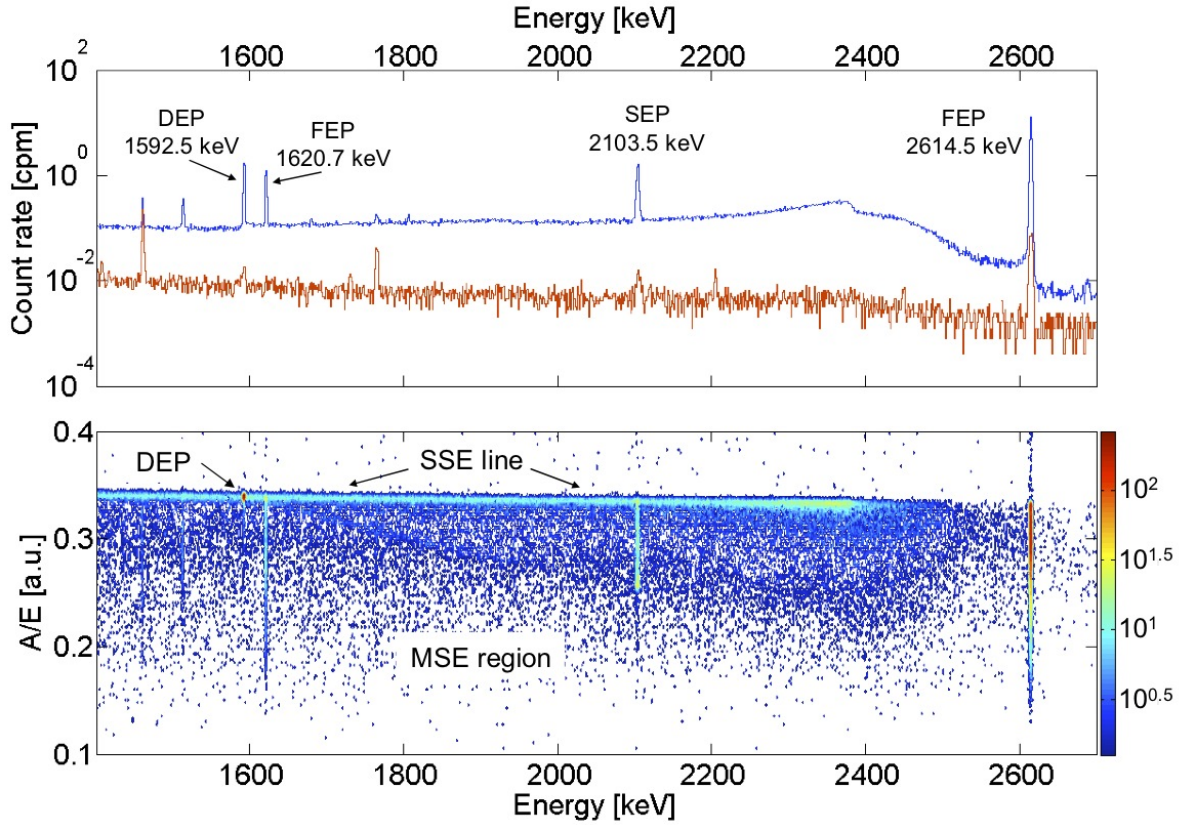

Figure 8.5: Top: ^{228}Th spectrum and the background taken with a BEGe detector. Bottom: Event density distribution of the A/E discrimination parameter for the acquired data. Single site events can be identified by the upper edge of the distribution. [59]

As shown on the bottom part of figure 8.5, an event accumulation takes place on the upper A/E border at the DEP energy of 1592.5 keV indicating the SSE characteristic of such events. As reported in [98], the A/E cut set to 97.7 % acceptance for an ideal SSE, yielded an acceptance of (89.2 ± 0.9)% for the DEP events and (10.1 ±0.7)% for the 2.6 MeV full energy peak which is expected to consist of MSE events. Furthermore, Monte Carlo simulations have been performed and an acceptance level of (89.4 ± 1.4)% determined for the $0\nu\beta\beta$ events.

To conclude, besides the excellent BEGe performance given by the detector resolution and efficiency, BEGe's require a minimal cabling effort which allows to keep the background low. Furthermore background suppression techniques based on pulse shape analysis can be efficiently applied. Finally, the detectors can be produced more cost effective than segmented detectors. Therefore, it has been decided by the GERDA collaboration to use BEGe detectors in the phase II of the experiment.

8.2 BEGe acceptance tests

The first phase of the GERDA experiment operates in total 18 kg of germanium detectors. In addition, up to four HPGe reference detectors consisting of natural germanium can be deployed in the cryostat. The goal for the maximal background index with this configuration is $< 10^{-2}$ counts/(keV·kg·y) . With the BEGe detectors implemented in phase II of GERDA, a better noise performance is expected but also an effective $0\nu\beta\beta$ signal identification using for example the pulse shape analysis method introduced in chapter 8.1.

With regard to a future implementation of the BEGe detectors in GERDA, a test campaign has been started with the goal to test the full production chain of the detectors. This entails the isotopic enrichment, crystal pulling, and assembling of the final BEGe configuration. Besides testing of the production chain, the acceptance test campaign covered also the detector characterization in terms of noise, resolution and long term stability. Furthermore, dead layers thicknesses and active volumes have been measured. In contrast to commercially available BEGe detectors, the GERDA crystals are not subject to additional machining of the lithium drifted n+ electrode. While dead layers are kept usually as thin as possible in order to avoid energy losses of incident particles on the surface, they are advantageous for the search of $\beta\beta$ decay. This is given by the fact that the $\beta\beta$ decay process takes place within the crystal. Thick dead layers provide an additional shield against background given by environmental α and β particles but also against low-energy γ particles. In total, four BEGe detectors were produced and tested in the first campaign. The crystals were pulled from depleted germanium, which is a byproduct of the isotopic enrichment of ^{76}Ge. After crystal pulling, the detector volumes have been cut out of the

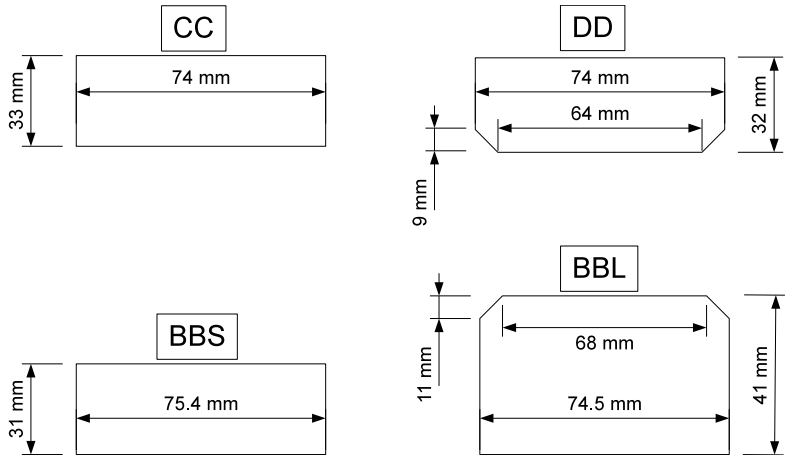

Figure 8.6: BEGe crystal geometries of the detectors used in the first acceptance test campaign. The crystals are made of depleted germanium.

precursor germanium. Crystals originating from the top part of the precursor are therefore not fully cylindrical and have a conical section on one of their side. The four crystals used so far, their designation and their dimensions are shown in figure 8.6. For the operation,

the crystals were mounted in standard vacuum cryostats from Canberra and equipped with charge sensitive amplifiers. Besides the measurements concerning the dead layer and the active volume of the crystals, depletion characteristics have been investigated, the resolution determined and long term stability tests performed. The test campaign was performed in collaboration of several groups from INFN, Heidelberg, Munich, Tübingen, Zurich and Padova and was coordinated by Dusan Budjas.

8.3 BEGe Monte Carlo simulations

For the dead layer and active volume determination, data were taken with ^{241}Am, ^{133}Ba and ^{60}Co sources and the rates compared with Monte Carlo simulations. In analogy to the acceptance tests, the Monte Carlo simulations were performed in collaboration of the groups involved in the project and implemented in the MaGe framework used by the GERDA and Majorana collaborations [99]. In order to determine the thickness of the dead layer of each crystal, the simulations were performed using a variable dead layer which was defined as a non-sensitive volume. Comparing the measured rates with the simulated rates at each dead layer allowed to characterize the crystals. Based on the information provided by Canberra, the exact geometries and materials were implemented, including the point contacts, the crystal holder and the endcaps. In order to simulate several dead layers per detector, a pearl script written by S. Georgi has been used, which automatically changes the dead layer geometry and restarts the simulation with the new parameters, once a simulation run has been completed. Figure 8.7 shows the geometry of the BBL detector

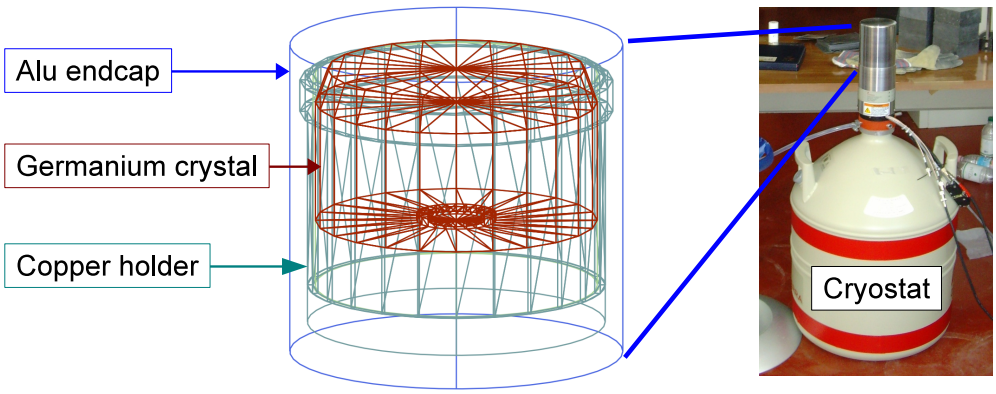

Figure 8.7: BBL detector geometry implemented in the Monte Carlo simulations for the dead layer and active volume determination. The simulated part of the detector is indicated on the right.

as it has been implemented in the Monte Carlo simulation. The geometry includes the aluminum endcap, the BBL germanium crystal and a copper holder. Furthermore, a teflon cylinder is placed between the copper holder and the crystal (the teflon spacer is not shown

in the picture). The crystal consists of natural germanium with an outer non-sensitive lithium drifted region defined as the dead layer. For the lithium content within the dead

Material	Component	Density [g/cm^3]	Composition
Germanium	Crystal, sensitive volume	5.32	natural
Lithium/Germanium	Crystal, dead layer	5.32	10% lithium
Teflon	Spacer	2.16	natural
Copper	Holder	8.96	natural
Alumina	Endcap	2.70	natural

Table 8.1: Materials used in the Monte Carlo simulation of the BEGe detectors. The lithium drifted germanium dead layer contains a mass fraction of 10% lithium.

layer a mass fraction of 10% has been assumed. Because radioactive sources were either used on top of the detector or on the side, the cryostat has not been simulated, as it plays an insignificant role for the results. Table 8.1 shows the materials, their function, density, and the chemical composition implemented in the simulation. All materials besides the dead layer were chemically defined according to their natural isotopic abundance.

8.4 Dead layer determination

Interactions of γ particles in germanium can be described by three energy dependent processes. As shown in figure 8.8, high energy γ interactions above 10 MeV are dominated by pair production, while low energy γ's are involved in Compton scattering or interactions based on the photoelectric effect. Given the fact that the absorption probability in the crystal increases with decreasing γ energies, low energy γ particles and their energy deposition in the detector are most sensitive to variations of the dead layer. Two γ sources, ^{241}Am and ^{133}Ba were used to determine the dead layer of the BEGe crystals. The γ lines used in the measurements and in the Monte Carlo simulations are shown in table 8.2. In

Source	Lines used [keV]	Branching [%]	Ratio
^{241}Am	60, 99, 103	35.92, 0.02, 0.019	$R_{60}/(R_{99}+R_{103})$
^{133}Ba	79, 81, 356	2.65, 32.9, 62.05	$(R_{79}+R_{81})/R_{356}$

Table 8.2: Gamma sources and their low energy lines used for the dead layer determination. Comparing the ratios of the lines allows to measure the dead layer independently of the source activities.

order to perform the measurements independently of the gamma activity of the sources, the ratios of the rates between a lower and a higher energetic line have been compared together with the ratios obtained by Monte Carlo simulations. The ratio sensitivity on the

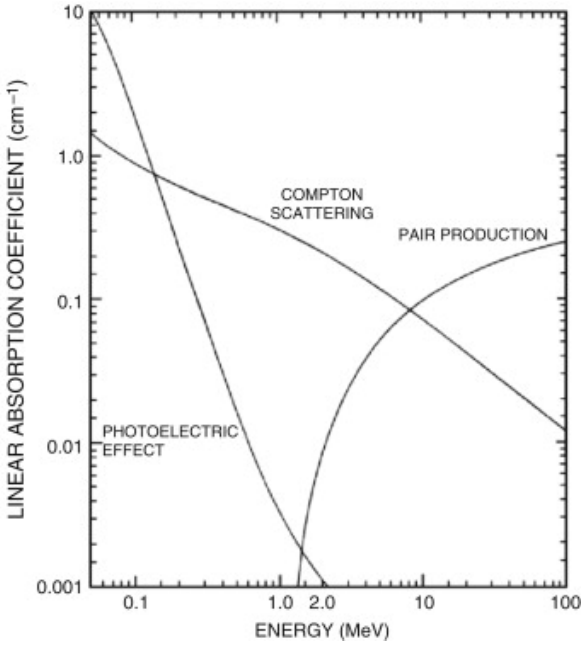

Figure 8.8: Gamma attenuation in germanium resulting from Compton scattering, photo effect and pair production, [100].

dead layer increases with an increasing energy difference between the two lines. To assure sufficient statistics, only prominent lines with a high branching fraction in the decay chain have been used.

Due to their energetic vicinity and comparable cross sections, the two 99 keV and 103 keV lines from ^{241}Am have been considered together. The same applies to the 79 keV and the 81 keV line from ^{133}Ba as indicated in figure 8.9. Data acquisition was performed using a charge amplifier from Canberra, a shaping amplifier and a multi channel analyzer with 8k resolution. For dead layer determination, the sources were located above the endcap on the z-axis of the crystal. The determined values represent therefore a mean value of the top dead layer. Table 8.3 shows an overview of the runs performed with the low energy γ sources. Data analysis of the two CC and DD detectors was extensively described in the Bachelor Thesis of S. Georgi [101].

In the following, only the measurements and the data analysis of the BBS and BBL detectors will be described as the measurements and analysis methods were comparable for all setups. A summary of the results for all four tested BEGe detectors will be presented at the end of this section. Figure 8.10 shows a zoom-in of the three ^{241}Am lines considered for the dead layer measurement. In order to determine the rates in the peaks, the background has been modeled using equation (6.23) which expresses a smoothed step function. For the determination of an integration interval I_1, the peaks were fitted with a gaussian which

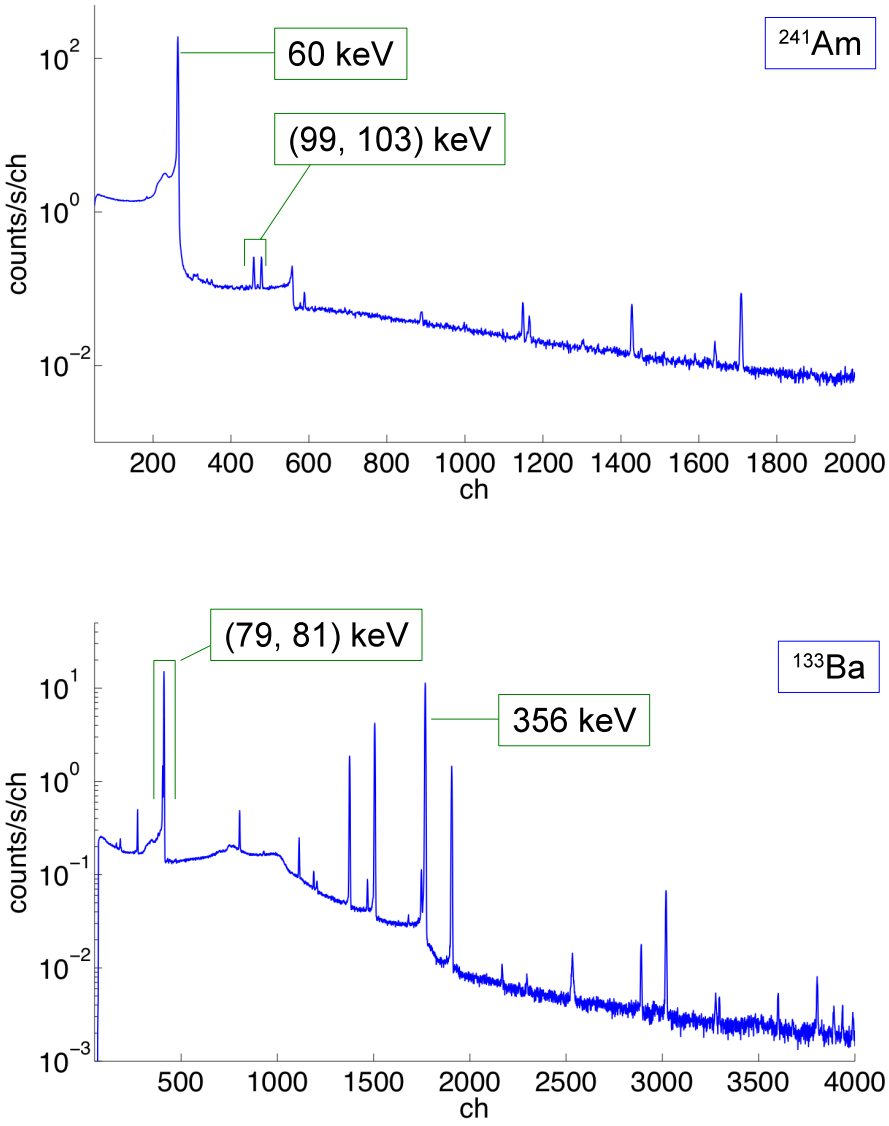

Figure 8.9: Top: ^{241}Am spectrum and the lines used for the dead layer determination. The 99 keV and the 103 keV lines were both summed up. Bottom: ^{133}Ba spectrum. The 79 keV and the 81 keV lines were summed up and compared with the 356 keV line.

was used to define a range of

$$I_1 = [\mu - 6\sigma,\ \mu + 6\sigma] \tag{8.2}$$

where μ is the peak position given by the gaussian and σ is the peak width. In the case of two adjacent peaks which were considered as one single contribution, the integration interval I_2 has been defined according to

$$I_2 = [\mu_1 - 6\sigma_1,\ \mu_2 + 6\sigma_2]. \tag{8.3}$$

Source	Detector	Distance [cm]	Lifetime [s]
^{241}Am	BBS	12	12484
^{133}Ba	BBS	44	30000
^{241}Am	BBL	16	14177
^{133}Ba	BBL	70	10564
^{241}Am	CC	16.2	16086
^{133}Ba	CC	35.1	1646
^{241}Am	DD	16.2	46176
^{133}Ba	DD	35.1	1000

Table 8.3: Overview of the dead layer measurements with the four BEGe detectors.

Figure 8.10 shows the 60 keV line and the two adjacent 99 keV and 103 keV lines from ^{241}Am together with the applied background model and the determined integration intervals. The net rate R_{Net} in the ^{241}Am data has been determined according to

$$R_{Net60} = \sum(R_{Data}) \mid_{ROI_{60}} - \sum(Bckg_{fit}) \mid_{ROI_{60}} \tag{8.4}$$

for the 60 keV line. While the 60 keV line is a stand-alone line, a small peak at 101 keV appears between the 99 keV and the 103 keV line. For the determination of the net rate in both lines, the 101 keV contribution has been cut out, assuming a flat distribution between both, the 99 keV and 103 keV lines given by the background model. The net rate for the two lines has been calculated by subtracting the 101 keV net contribution via

$$R_{Net(99,103)} = \sum(R_{Data}) \mid_{ROI_{(99,103)}} - \sum(Bckg_{fit}) \mid_{ROI_{(99,103)}} - (\sum(R_{Data}) \mid_{CUT} - \sum(Bckg_{fit}) \mid_{CUT}). \tag{8.5}$$

For the parameter representing the dead layer, the ratio $R_{DL_{Am}}$ has been defined as

$$R_{DL_{Am}} = \frac{R_{Net60}}{R_{Net(99,103)}}. \tag{8.6}$$

The ratio is given by the net rate of the 60 keV line R_{Net60} and the sum of the two net rates of the 99 keV line and the 103 keV line $R_{Net(99,103)}$. While $R_{DL_{Am}}$ has been used for the data taken with the ^{241}Am source, the ^{133}Ba data were analyzed according to an analogue parameter given by

$$R_{DL_{Ba}} = \frac{R_{Net(79,81)}}{R_{Net356}} \tag{8.7}$$

where $R_{Net(79,81)}$ is the sum of the net rates in the 79 keV and the 81 keV lines and R_{Net356} is the net rate given by the 356 keV line. The net ratios for the ^{133}Ba data were determined in full analogy to the ^{241}Am data by modeling a background, which has been subtracted

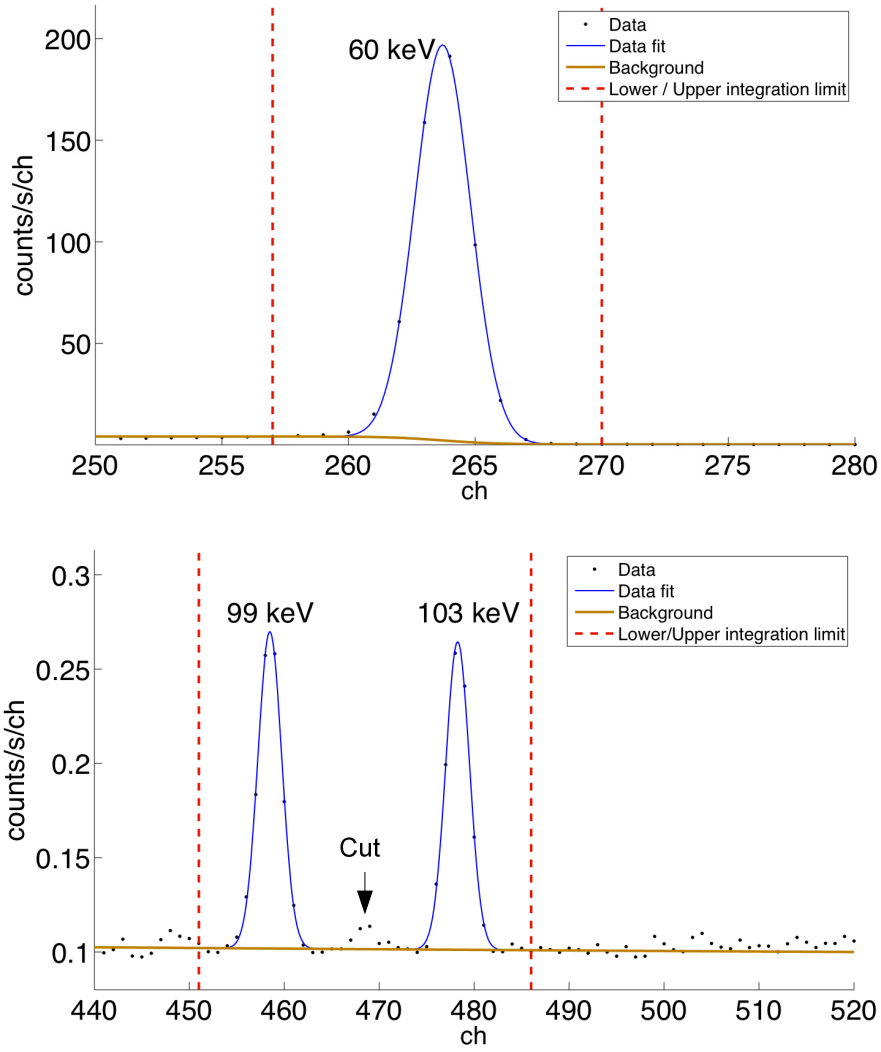

Figure 8.10: Top: the 60 keV line from ^{241}Am. No further peaks in the vicinity of the line must be considered in order to determine the net rate. Bottom: the 99 keV and the 103 keV line from ^{241}Am. The background line at 101 keV has been considered in the net rate calculation.

from the data.

Energy calibration of the MCA data was performed using a linear approximation in order to analyze the Monte Carlo data in an equivalent energy interval. To determine the counts in the Monte Carlo data, an analogue procedure has been used as applied before on the measured data. Besides using the same energy intervals, the background has been modeled equivalently in order to calculate the Monte Carlo rates in the peaks . The two dead layer

parameters,

$$R^{MC}_{DL_{Am}} = \frac{R^{MC}_{Net60}}{R^{MC}_{Net(99,103)}} \text{ and } R^{MC}_{DL_{Ba}} = \frac{R^{MC}_{Net(79,81)}}{R^{MC}_{Net356}}, \tag{8.8}$$

both resulting from the Monte Carlo data performed with variable dead layers between 0 mm and 1 mm were compared with the measured values. Figure 8.11 shows the dead

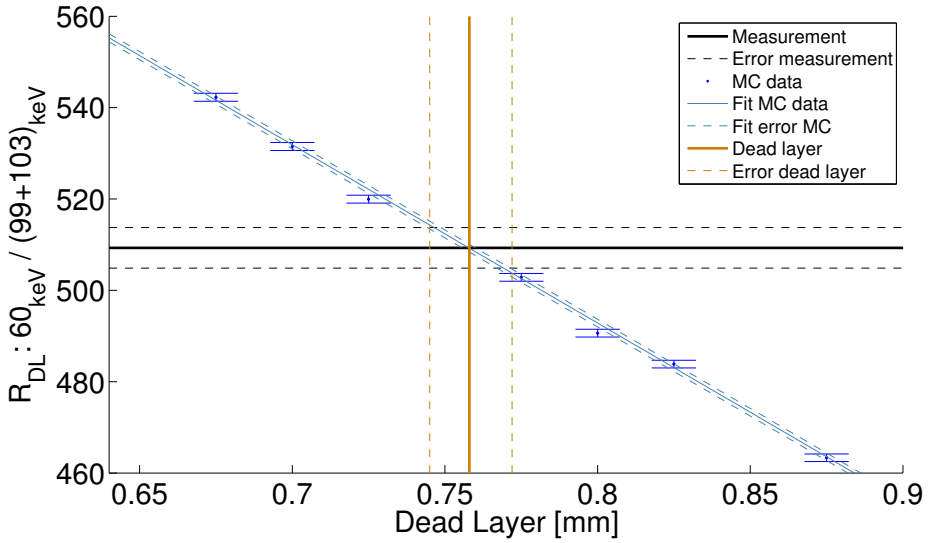

Figure 8.11: Dead layer determination using the ^{241}Am data and equivalent Monte Carlo simulations at different simulated dead layer values. The intersection between the measurement and the Monte Carlo data defines the dead layer.

layer determination with the ^{241}Am source as acquired with the BBS detector. For the measured $R_{DL_{Am}}$ parameter a value of

$$R_{DL_{Am}} = 509.3 \pm 4.4 \tag{8.9}$$

has been determined. The equivalent dead layer parameter found with the ^{133}Ba data was

$$R_{DL_{Ba}} = 0.97 \pm 0.001 \tag{8.10}$$

as shown in figure 8.12. The values obtained by Monte Carlo simulations at different dead layer thicknesses were fitted linearly in the region of interest in order to find the intersection point of the measured value and the Monte Carlo data. The determined intersection values define the mean dead layer of the crystal. Error estimation was performed by considering the intersection points of the error fits of the Monte Carlo data with the errors resulting from the data. The lower error on the dead layer is defined by the intersection point between the upper error of the data and the lower error fit of the simulated data. In full analogy, the upper error is defined by the intersection point of the lower data error and the upper error fit of the Monte Carlo data. Table 8.4 shows the determined dead layers

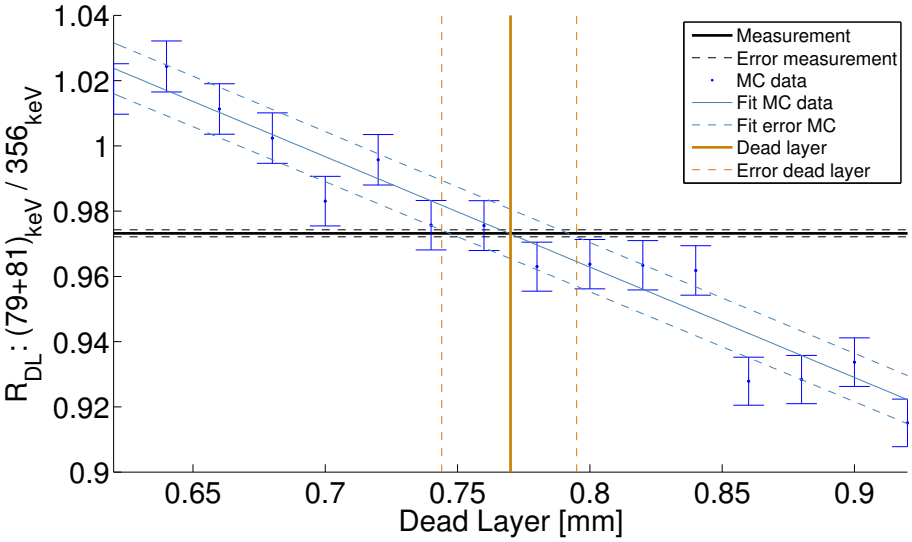

Figure 8.12: Dead layer determination using the ^{133}Ba data. Monte Carlo data are fitted linearly in order to determine the dead layer and the errors.

Detector	Source	R_{DL}	Dead layer [mm]	Dead layer (Canberra) [mm]
BBS	^{241}Am	509±4	0.758±0.014	0.5
BBS	^{133}Ba	0.97±0.001	0.770±0.026	0.5
BBL	^{241}Am	619±5	0.441±0.020	0.4
BBL	^{133}Ba	0.5±0.002	>1	0.4
CC	^{241}Am	531±4	0.679±0.012	0.7
CC	^{133}Ba	1.1±0.005	0.593±0.025	0.7
DD	^{241}Am	659±3	0.405±0.007	0.45
DD	^{133}Ba	1.2±0.006	0.378±0.023	0.45

Table 8.4: Summary of the dead layer values determined for the four BEGe detectors. Results for the CC and DD detectors are taken from [101]. The gray BBL measurement with the ^{133}Ba source must be repeated and is not taken into account in further considerations.

for the BBS and the BBL detectors. Furthermore, the dead layers for the CC and the DD detectors resulting from the analysis in [101] are shown. Values provided by Canberra are also presented in the table for comparison, although the latter are given without errors. While the BBS values determined in this section are consistent within 1σ, the ^{133}Ba data taken with the BBL detector, show an unexpected low R_{DL} value which results in a dead layer higher than 1 mm. The measurement was performed with the source located 70 cm above the endcap which could give rise to a shift with respect to the z-axis of the detector. It can be also assumed that the source positioning in height was performed incorrectly

resulting in a discrepancy between the real and the Monte Carlo setups. For this reason, this measurement should be repeated in future and will not be considered anymore in further discussion.

8.5 Active volume determination

Based on the dead layers determined in section 8.4, the active volumes can be calculated if the full crystal geometry is known which includes also the region of the p+ electrode. However, active volume calculations based on the dead layer determined on the top surface of the crystal can only be representative by assuming the layer to be homogeneously distributed over the whole surface of the detector. The active volumes resulting from such calculations will be presented at the end of this section. In order to measure the active volume explicitly, independent measurements were performed which were also used to cross check the dead layer values obtained so far.

Measuring of the active volume was performed using two high energetic lines of a ^{60}Co source. The source emits high energy γ lines at 1173,2 keV and 1332,5 keV with a branching ratio of $\sim$100% as shown in table 8.5. Due to their energy, the absorption of the γ's takes place preferably within the volume of the detector rather than on its surface. The

Source	Lines used [keV]	Branching [%]	Activity (BBS) @ 27.Sept.2010	Activity (BBL) @ 5.Oct.2010
^{60}Co	1173.2, 1332.5	99.85, 99.98	13.13±1.5%	12.77±1.5%

Table 8.5: High energy ^{60}Co lines used for the active volume determination. The measurement requires the activity of the source to be considered.

high energy γ particles from ^{60}Co penetrate the volume of the crystal without relevant energy losses in the dead layer. Therefore, the total count rate of a high energy γ line in the detector can be used as a representative parameter for the active volume. The energetic vicinity of the two ^{60}Co lines, does not allow to define an activity independent volume parameter like in the case of the dead layer determination. For this reason, the measurement requires the consideration of absolute count rates in both, data and Monte Carlo simulations, which can only be performed if the source activity is known. Furthermore, to allow for a direct comparison between data and Monte Carlo simulations, the data cts_{Dat} must be normalized on the lifetime and the source activity according to

$$[R_{Dat}] = [\frac{1}{\mathrm{s} \cdot \mathrm{kBq}}] \tag{8.11}$$

Because, time distributions of radioactive decays can not be simulated with Geant4, an equivalent normalization of the Monte Carlo data can only be achieved by assuming a

simulated source activity of A_0=1 kBq for example. Such an assumption translates into a simulated lifetime of

$$T_{MC} = \frac{N_{tot}}{A_0} \tag{8.12}$$

where N_{tot} is the total number of simulated decays and A_0 is the norm activity. Therefore, dividing the Monte Carlo data cts_{MC} by T_{MC} leads to a rate R_{MC} which is equivalently normalized to R_{Dat}

$$R_{Dat} = \frac{cts_{Dat}}{T_L \cdot A[\text{kBq}]} \mid_{ROI} \equiv \frac{cts_{MC}}{T_{MC}} \mid_{ROI} \tag{8.13}$$

where cts_{Dat} are the counts in the data, T_L is the lifetime of the measurement and A is the activity of the source. ROI is the region of interest, which is given by the energy integration interval around a peak. It must be the same in both data sets after energy calibration of the MCA. The data sets, normalized according to equation (8.13) are compared with each other in full analogy to the dead layer determination. Monte Carlo simulations were performed for different dead layers in order to find the value of best agreement. Table 8.6 shows an overview of the measurements done with the ^{60}Co source for the active volume determination. The Monte Carlo simulations were performed with a variable dead

Source	Detector	Distance [cm]	Activity [kBq]	Lifetime [s]
^{60}Co	BBS	23	131.13±1.5%	12484
^{60}Co	BBL	30	12.77±1.5%	30000
^{60}Co	CC	23	13.58±1.5%	7554
^{60}Co	DD	23	13.57±1.5%	6075

Table 8.6: Overview of the active volume determination with the four BEGe detectors.

layer equally distributed over the whole surface of the crystal. The data allow therefore determination of the mean active volume in the crystal. Furthermore, because the absolute rates are compared, only one of the two high energy ^{60}Co γ lines is sufficient to determine the active volume. Both ^{60}Co lines can be used independently to measure the active volume allowing simultaneously to cross check the method of the determination of the rates. The lines were fitted with a gaussian in order to determine the integration interval of $\pm 6\sigma$, following the same procedure as applied for the dead layer measurements. Because the data do not exactly follow a gaussian distribution, the rates have been determined by integration of the data after background subtraction. Errors on the measured rates R_{Dat} as defined in equation (8.13) were calculated considering both, statistical errors and the activity uncertainty. Using error propagation, the uncertainty $\sigma_{R_{Dat}}$ is given by

$$\sigma_{R_{Dat}} = \frac{\sqrt{(\frac{\sigma_{stat}}{A})^2 + (\frac{\sum cts_{Dat}}{A^2})^2 \cdot \sigma_A^2}}{T_L} \tag{8.14}$$

where σ_{stat} and σ_A are the statistical error and the activity uncertainty respectively. Figures 8.13 and 8.14 show the dead layers determined for the BBS and the BBL detectors, using

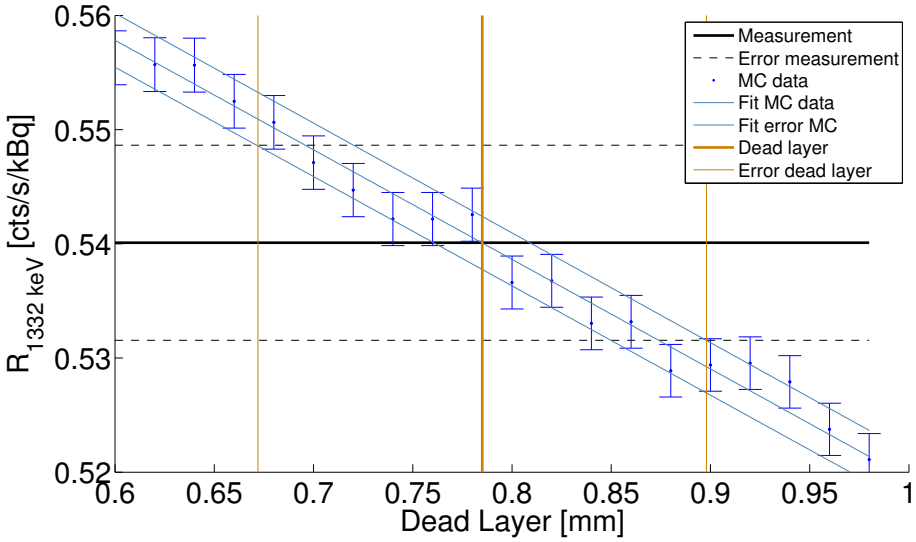

Figure 8.13: Normalized rates of the 1332 keV line acquired with the BBS detector. The error on the measured rate includes the uncertainty of the source activity which results in a broadening of the determined dead layer uncertainty obtained by Monte Carlo simulations.

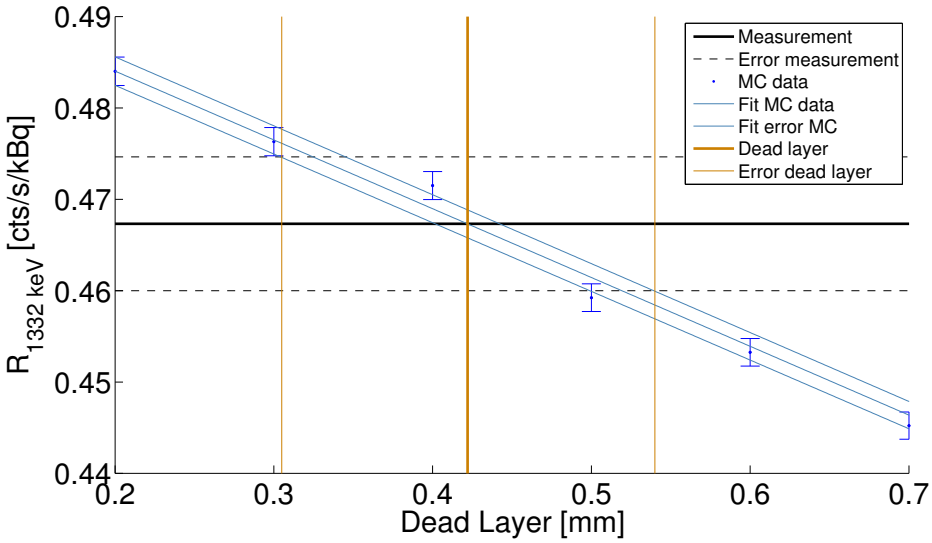

Figure 8.14: Normalized rates of the 1332 keV line acquired with the BBL detector. Although the dead layer error reaches an uncertainty of about 30%, the measured value confirms a drastically reduced dead layer compared to the the BBS detector.

the 1332 keV line of ^{60}Co. The additional uncertainties in the gamma activity of the sources, translate into relatively high errors on the normalized rates R_{Dat}. In consequence, the error on the dead layer is broader than in section 8.4 where an activity independent

method has been used. The numbers agree with the results obtained in section 8.4 however, confirming in particular a smaller mean dead layer of the BBL detector with respect to the BBS detector. Table 8.7 summarizes the dead layer values obtained with all three gamma sources for the BBS and the BBL detector. The agreement between the dead layer values

Detector	Source	Dead layer [mm]
BBS	^{241}Am	0.758±0.014
BBS	^{133}Ba	0.770±0.026
BBS	^{60}Co, 1173 keV	0.803±0.110
BBS	^{60}Co, 1332 keV	0.785±0.113
BBL	^{241}Am	0.441±0.020
BBL	^{133}Ba	>1 (value not considered)
BBL	^{60}Co, 1173 keV	0.458±0.139
BBL	^{60}Co, 1332 keV	0.422±0.118

Table 8.7: Summary of the dead layer values determined for the BBS and BBL detectors with three gamma sources. Besides the BBL outlier taken with a ^{133}Ba source, the values obtained for each detector are consistent within 1σ.

obtained with the ^{241}Am, ^{133}Ba, and ^{60}Co sources indicates that the measured mean dead layer on top of the crystal represents also the mean dead layer distribution of the whole crystal. As shown in figure 8.15, BEGe crystals have a cylindrical ditch in order to separate

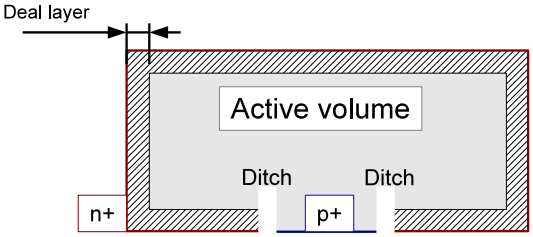

Figure 8.15: Schematic of the dead layer distribution in the crystal used for the active volume determination. The cylindrical ditch has been taken into acount for the calculations of the active volume.

physically the two p+ and n+ electrodes. The height and thickness of the groove as well as the size of the p+ contact are individual for each detector and has been taken into account for the active volume determination. Table 8.8 shows the active volumes for the BBS and BBL detectors as they result from the ^{60}Co measurements. Furthermore, assuming that the dead layer values determined with ^{241}Am and ^{133}Ba are representative for the whole crystal, active volumes based on the latter two sources were calculated for comparison. Besides one ^{133}Ba measurement, which has been considered as invalid, all values for the BBS and the BBL detectors are consistent in terms of dead layer thicknesses and active volumes.

Detector	Source, line	Active volume [mm^3]
BBS	^{60}Co, 1173 keV	125430±1652
BBS	^{60}Co, 1332 keV	125700±1700
BBS	^{241}Am	126110±211 based on mean top dead layer
BBS	^{133}Ba	125930±391 based on mean top dead layer
BBL	^{60}Co, 1173 keV	175000±2119
BBL	^{60}Co, 1332 keV	174980±1803
BBL	^{241}Am	174990±305 based on mean top dead layer
BBL	^{133}Ba	–

Table 8.8: Summary of the active volumes determined with the ^{60}Co source. For comparison, the analogue results based on the mean top dead layer determination are presented. All values, besides the BBL ^{133}Ba measurement are consistent for each detector.

8.6 Summary

In June 2011, the first enriched phase I detectors were deployed in GERDA starting with physics runs. The first detectors were produced in a closed-end coaxial configuration and therefore, pulse shape analysis methods could not be applied efficiently in order to discriminate against multi site events.

To improve the SSE/MSE discrimination efficiency, segmented and BEGe detectors were considered as candidates for the phase II of GERDA. However, in contrast to segmented Ge detectors, the BEGe configuration is more cost effective and simpler in terms of cabling and data acquisistion. Furthermore, BEGe detectors have a better noise- and resolution-performance and allow for efficient SSE/MSE discrimination by pulse shape analysis techniques. Based on the considerations concerning the benefits of the BEGe configuration, it has been decided to operate BEGe detectors in phase II of GERDA. The implementation

Detector	Dead layer [mm]	Active volume [mm^3]
BBS	0.76±0.01	126060±183
BBL	0.44±0.02	174990±297
CC	0.67±0.06	131000±2300
DD	0.40±0.02	120900±1200

Table 8.9: Weighted mean values for the deadlayers and active volumes for four BEGe detectors. Results for the CC and the DD detectors are taken from [101].

of the detectors requires to test the full production chain and to characterize prototype detectors in terms of their performance. The test campaign entailed the determination of the dead layer values and active volumes, which was done with four prototype detectors made from depleted germanium. Data acquired with ^{241}Am, ^{133}Ba and ^{60}Co were compared with Monte Carlo simulations which were performed at different dead layer thicknesses in order to determine the value of best agreement. Active volumes were explicitly measured using the two high energy ^{60}Co lines. Table 8.9 summarizes the weighted mean values for the dead layers thicknesses and the active volumes. The table includes the results for the CC and the DD detector described in [101]. The values given for the BBL and the BBS detectors were calculated considering data taken with all three sources.

Chapter 9

Conclusions & Outlook

The calibration of GERDA requires three ^{228}Th sources, which are located about 5 m above the detector array during physics runs. Besides the emission of γ-rays, the ^{228}Th and its daughters emit also α particles which can undergo (α, n) reactions with low-Z materials within the source encapsulation. Because, commercial encapsulations contain a ceramic which is saturated with the activity, the ceramic pellets are considered as the materials which play the dominant role in neutron production through the (α, n) channel.

Given the unknown chemical composition of the ceramics, two representative examples, $NaAlSiO_2$ and Al_2O_3 were discussed in the context of neutron production. Estimations of the neutron fluxes given by (α, n) reactions in the two example materials were performed with SOURCES4A. The calculated production rates of

$$R > 1 \cdot 10^{-2} \text{ neutrons/s/kBq} \tag{9.1}$$

and the calculated neutron spectra were considered in Monte Carlo simulations in order to estimate the neutron background in GERDA in the $Q_{\beta\beta}$ region of interest. With a value of

$$B_n = (2.97 \pm 0.2) \cdot 10^{-5} \text{ counts/(keV·kg·y·kBq)} \tag{9.2}$$

[57], the neutron background induced by (α, n) reactions within the calibration sources was found to be potentially dangerous for the second phase of GERDA.

In order to suppress the (α, n) channel in the calibration sources, a new technique has been developed in collaboration with PSI, Villigen, Switzerland. The method uses a liquid $ThCl_4$ precursor and a chemical and thermal treatment to produce a ThO_2 layer deposited on gold. α particles emitted by the ^{228}Th chain are absorbed in the gold which has an (α, n) threshold energy of about 10 MeV. Because the threshold energy is higher than the maximal α energy emitted by ^{228}Th , no (α, n) reactions are expected to take place in the ideal case.

Neutrons can be still produced in combination with the bound oxygen in the ThO_2 compound and with impurity materials present in the precursor solution or introduced during

the source preparation. For ThO_2, a neutron flux has been calculated which is two orders of magnitudes lower with respect to the fluxes calculated for a ceramic.

The produced custom sources were characterized in terms of their γ activity and neutron emission. For the γ measurements, a germanium detector has been setup at the University of Zurich. Further γ measurements were performed at IRMM in Geel, Belgium.

Neutron measurements were performed with a ^{3}He and a LiI(Eu) detector and demonstrated a neutron reduction of up to about a factor of 5. The mean neutron reduction value was found to be

$$\overline{G}_{nRed} = 4.09 \pm 0.69. \tag{9.3}$$

The measured neutron flux reduction indicates an overestimation of the calculated neutron fluxes for a commercial source and an underestimation of the neutron flux calculated for the custom ThO_2 source. The discrepancy can be a result of unknown impurities in the precursor $ThCl_4$ solution and of wrong assumptions concerning the unknown chemical composition of the ceramics.

However, although the achieved neutron reduction yield is about 20 times lower than expected, the developed technique has demonstrated its functionality and high potential for low background experiments. Furthermore, it is not restricted to ^{228}Th sources and can be in principle applied to any α emitting source. Although the custom sources are not free of impurities, the process drastically reduces the uncertainties given by the unknown chemical composition of the ceramics used by the manufacturer. Furthermore, the process can be further optimized by a chemical analysis of the involved materials. The latter allows to exactly determine the elements contributing to the remaining neutron production and to introduce further processing steps to eliminate the most relevant target materials. Especially with regard to the ultimate one-ton scale $0\nu\beta\beta$ experiment, the developed neutron reduction technique can be very interesting.

In the second part of this work the source insertion system (SIS) has been discussed under technical and software aspects. Tests performed at the University of Zurich concerned the system functionality, system configuration and error handling. The system was mounted and configured in the GERDA cleanroom in June 2011. Discrepancy and thermal corrections were implemented resulting in positioning uncertainties of ± 1 mm for more than 97% of the values acquired. Furthermore, the system was implemented in the slow control of GERDA, allowing for an online system monitoring.

Finally, with regard to the second phase of GERDA, BEGe detectors made of depleted germanium were tested in terms of their dead layer thicknesses and active volumes. The methodology for the dead layer and active volume measurement can be also applied during the characterization of future BEGe detectors made of enriched germanium. The results obtained will be important for further Monte Carlo simulations and data analysis.

Acknowledgment

First of all I would like to thank my supervisor Prof. Laura Baudis who gave me the opportunity to join her group at the University of Zurich and to work on a very exciting project like the GERDA experiment. I appreciate very much her support, guidance and patience over the last years which were in particular very helpful for this work.
Many thanks also to my colleagues from the Paul Scherrer Institute, Rugard Dressler, Robert Eichler and Dorothea Schumann who were extremely inspiring during the development of the neutron reduction process and who finally made the production of the custom sources possible. I would also like to thank Roberto Santorelli for his suggestions and technical support concerning the neutron reduced sources and Serena Fattori for the very first neutron flux measurements. Furthermore I appreciate a lot the contribution to the neutron measurements given by Carla Cattadori, Enrico Bellotti and Roberto Santerolli who provided the ^{3}He detector and who performed additional neutron measurements of the sources. In this context, I wish furthermore to thank Alfredo Davide Ferella who was always very helpful in keeping the measurements running at LNGS and who performed the screening measurements with GATOR. It was also a pleasure to collaborate with Mikael Hult and his group who performed precise γ activity measurements at IRMM, which made the neutron reduction measurements possible.
The hardware and software aspects of the SIS system could be only solved with the expertise of Kurt Boesiger, Daniel Florin and Achim Vollhardt who were always very flexible and open for discussions to find optimal solutions. I wish also to thank the whole BEGe acceptance test team for the nice and funny time we had together at LNGS and in particular Dusan Budjas for his project guidance and support. Furthermore, I would like to thank the whole GERDA collaboration for a very nice and productive atmosphere and the whole group of Laura Baudis for lots of support, discussions and suggestions concerning this work. In particular many thanks to Marc Schumann, Aaron Manalaysay, Alfredo Davide Ferella, Sebastian Arrenberg, Alexander Kish and Francis Froborg. Finally, I would also like to thank my family for their encouragement and patience during the past years.

Bibliography

[1] F. Reines and C. L. Cowan, "The neutrino," *Nature*, vol. 178, pp. 446–449, 1956.

[2] S. Abe *et al.*, "Precision Measurement of Neutrino Oscillation Parameters with KamLAND," *Phys.Rev.Lett.*, vol. 100, p. 221803, 2008. arXiv: hep-ex/0801.4589.

[3] P. Adamson *et al.*, "Measurement of the neutrino mass splitting and flavor mixing by MINOS," *Phys.Rev.Lett.*, vol. 106, p. 181801, 2011. arXiv: hep-ex/1103.0340.

[4] F. An *et al.*, "Observation of electron-antineutrino disappearance at Daya Bay," 2012. arXiv: hep-ex/1203.1669.

[5] T. Schwetz, M. Tortola, and J. Valle, "Global neutrino data and recent reactor fluxes: status of three-flavour oscillation parameters," *New J.Phys.*, vol. 13, p. 063004, 2011. arXiv: hep-ph/1103.0734.

[6] A. Osipowicz *et al.*, "KATRIN: A next generation tritium beta decay experiment with sub-eV sensitivity for the electron neutrino mass," 2001. arXiv: hep-ex/0109033.

[7] A. Strumia and F. Vissani, "Neutrino masses and mixings and...," 2006. arXiv: hep-ph/0606054.

[8] P. Vogel, "Neutrinoless double beta decay," 2006. arXiv: hep-ph/0611243.

[9] M. G. Inghram and J. H. Reynolds, "Double Beta-Decay of Te^{130}," *Phys. Rev.*, vol. 78, pp. 822–823, Jun 1950.

[10] S. R. Elliott, A. A. Hahn, and M. K. Moe, "Direct evidence for two-neutrino double-beta decay in ^{82}Se," *Phys. Rev. Lett.*, vol. 59, pp. 2020–2023, Nov 1987.

[11] A. Balysh *et al.*, "Double beta decay of ^{48}Ca," *Phys. Rev. Lett.*, vol. 77, pp. 5186–5189, 1996. arXiv: nucl-ex/9608001.

[12] V. B. Brudanin *et al.*, "Search for double beta decay of Ca-48 in the TGV experiment," *Phys. Lett.*, vol. B495, pp. 63–68, 2000.

[13] R. L. Flack, "Results from NEMO 3," *J. Phys. Conf. Ser.*, vol. 136, p. 022032, 2008. arXiv: hep-ex/0810.5497.

[14] F. T. Avignone, "Double-beta decay: Some recent results and developments," *Prog. Part. Nucl. Phys.*, vol. 32, pp. 223–245, 1994.

[15] A. Morales, "Review on double beta decay experiments and comparison with theory," *Nucl. Phys. Proc. Suppl.*, vol. 77, pp. 335–345, 1999. arXiv: hep-ph/9809540.

[16] C. Dorr and H. V. Klapdor-Kleingrothaus, "New Monte-Carlo simulation of the HEIDELBERG-MOSCOW double beta decay experiment," *Nucl. Instrum. Meth.*, vol. A513, pp. 596–621, 2003.

[17] R. Arnold *et al.*, "First results of the search of neutrinoless double beta decay with the NEMO 3 detector," *Phys. Rev. Lett.*, vol. 95, p. 182302, 2005. arXiv: hep-ex/0507083.

[18] S. R. Elliott, A. A. Hahn, M. K. Moe, M. A. Nelson, and M. A. Vient, "Double beta decay of ^{82}Se," *Phys. Rev. C*, vol. 46, pp. 1535–1537, Oct 1992.

[19] R. Arnold *et al.*, "Double beta decay of Se-82," *Nucl. Phys.*, vol. A636, pp. 209–223, 1998.

[20] R. Arnold *et al.*, "Double beta decay of Zr-96," *Nucl. Phys.*, vol. A658, pp. 299–312, 1999.

[21] J. Argyriades *et al.*, "Measurement of the two neutrino double beta decay half- life of Zr-96 with the NEMO-3 detector," *Nucl. Phys.*, vol. A847, pp. 168–179, 2010. arXiv: nucl-ex/0906.2694.

[22] D. Dassie *et al.*, "Two neutrino double beta decay measurement of Mo-100," *Phys. Rev.*, vol. D51, pp. 2090–2100, 1995.

[23] A. S. De Silva, M. K. Moe, M. A. Nelson, and M. A. Vient, "Double beta decays of Mo-100 and Nd-150," *Phys. Rev.*, vol. C56, pp. 2451–2467, 1997. arXiv: nucl-ex/9706005.

[24] H. Ejiri *et al.*, "Double beta decays of Cd-116," *J. Phys. Soc. Jap.*, vol. 64, pp. 339–343, 1995.

[25] F. A. Danevich *et al.*, "Search for 2 beta decay of cadmium and tungsten isotopes: Final results of the Solotvina experiment," *Phys. Rev.*, vol. C68, p. 035501, 2003.

[26] R. Arnold *et al.*, "Double-beta decay of Cd-116," *Z. Phys.*, vol. C72, pp. 239–247, 1996.

[27] C. Arnaboldi *et al.*, "A Calorimetric Search on Double Beta Decay of 130Te," *Phys. Lett.*, vol. B557, pp. 167–175, 2003. arXiv: hep-ex/0211071.

[28] V. I. Tretyak, "Recent results of the NEMO 3 experiment," *AIP Conf. Proc.*, vol. 1180, pp. 135–139, 2009.

[29] N. Ackerman *et al.*, "Observation of Two-Neutrino Double-Beta Decay in Xe-136 with EXO-200," *Phys. Rev. Lett.*, vol. 107, p. 212501, 2011. arXiv: nucl-ex/1108.4193.

[30] KamLAND-Zen Collaboration, "Measurement of the double-β decay half-life of ^{136}Xe with the KamLAND-Zen experiment," *Phys. Rev.*, vol. C85, p. 045504, 2012. arXiv: hep-ex/1201.4664.

[31] J. Argyriades *et al.*, "Measurement of the Double Beta Decay Half-life of 150-Nd and Search for Neutrinoless Decay Modes with the NEMO-3 Detector," *Phys. Rev.*, vol. C80, p. 032501, 2009. arXiv: hep-ex/0810.0248.

[32] W. H. Furry, "On transition probabilities in double beta-disintegration," *Phys. Rev.*, vol. 56, pp. 1184–1193, Dec 1939.

[33] I. Avignone, Frank T., S. R. Elliott, and J. Engel, "Double Beta Decay, Majorana Neutrinos, and Neutrino Mass," *Rev.Mod.Phys.*, vol. 80, pp. 481–516, 2008. arXiv: nucl-ex/0708.1033.

[34] O. Chkvorets, *Search for Double Beta Decay with HPGe Detectors at the Gran Sasso Underground Laboratory*. PhD thesis, University of Heidelberg, 2008.

[35] J. Schechter and J. W. F. Valle, "Neutrinoless double-β decay in SU(2) $\times$ U(1) theories," *Phys. Rev. D*, vol. 25, pp. 2951–2954, Jun 1982.

[36] F. Boehm and P. Vogel, *Physics of Massive Neutrinos*. Cambridge University Press, 1992.

[37] H. V. Klapdor-Kleingrothaus, A. Dietz, H. L. Harney, and I. V. Krivosheina, "Evidence for Neutrinoless Double Beta Decay," *Mod. Phys. Lett.*, vol. A16, pp. 2409–2420, 2001. arXiv: hep-ph/0201231.

[38] F. T. Avignone, G. S. King, and Y. G. Zdesenko, "Next generation double-beta decay experiments: metrics for their evaluation," *New Journal of Physics*, vol. 7, no. 1, p. 6, 2005.

[39] H. V. Klapdor-Kleingrothaus, A. Dietz, and I. V. Krivosheina, "Critical View to 'The IGEX neutrinoless double beta decay experiment....' published in Phys. Rev. D, Volume 65 (2002) 092007," *Phys. Rev.*, vol. D70, p. 078301, 2004. arXiv: hep-ph//0403056.

[40] C. Aalseth, I. Avignone, F.T., A. Barabash, F. Boehm, R. Brodzinski, *et al.*, "Comment on 'Evidence for neutrinoless double beta decay'," *Mod.Phys.Lett.*, vol. A17, pp. 1475–1478, 2002. arXiv: hep-ex/0202018.

[41] D. Gonzalez *et al.*, "Pulse shape discrimination in the IGEX experiment," *Nucl. Instrum. Meth.*, vol. A515, pp. 634–643, 2003. arXiv: hep-ex/0302018.

[42] F. Alessandria *et al.*, "Sensitivity of CUORE to Neutrinoless Double-Beta Decay," 2011. arXiv: nucl-ex/1109.0494.

[43] J. Argyriades *et al.*, "Measurement of the background in the NEMO 3 double beta decay experiment," *Nucl. Instrum. Meth.*, vol. A606, pp. 449–465, 2009. arXiv: nucl-ex/0903.2277.

[44] R. Ardito, C. Arnaboldi, D. Artusa, I. Avignone, F.T., M. Balata, *et al.*, "CUORE: A Cryogenic underground observatory for rare events," 2005. arXiv: hep-ex/0501010.

[45] C. M. Cattadori, "Gerda status report," in *12th International Conference on Topics in Astroparticle and Underground Physics (TAUP 2011)*, 2011.

[46] MAJORANA Collaboration, "The MAJORANA Experiment," 2011. arXiv: hep-ex/1109.4790.

[47] NEXT Collaboration, "The NEXT-100 experiment for neutrinoless double beta decay searches (Conceptual Design Report)," *ArXiv e-prints*, 2011. arXiv: 1106.3630.

[48] C. Kraus and S. J. M. Peeters, "The rich neutrino programme of the SNO+ experiment," *Prog. Part. Nucl. Phys.*, vol. 64, pp. 273–277, 2010.

[49] A. Wright, *Robust Signal Extraction Methods and Monte Carlo Sensitivity Studies for the Sudbury Neutrino Observatory and SNO+ Experiments*. PhD thesis, Queens University, 2009.

[50] J. Gomez-Cadenas, J. Martin-Albo, M. Mezzetto, F. Monrabal, and M. Sorel, "The Search for neutrinoless double beta decay," *Riv.Nuovo Cim.*, vol. 35, pp. 29–98, 2012. arXiv: hep-ex/1109.5515.

[51] G. F. Knoll, *Radiation Detection and Measurement*. Wiley, 1999.

[52] E. M. Pell, "Diffusion Rate of Li in Si at Low Temperatures," *Phys. Rev.*, vol. 119, pp. 1222–1225, Aug 1960.

[53] G. S. Hubbard, E. E. Haller, and W. L. Hansen, "Zone Refining High-Purity Germanium," *Nuclear Science, IEEE Transactions on*, vol. 25, pp. 362 –370, feb. 1978.

[54] F. Gao, L. Campbell, Y. Xie, R. Devanathan, A. Peurrung, and W. Weber, "Electron-Hole Pairs Created by Photons and Intrinsic Properties in Detector Materials," *Nuclear Science, IEEE Transactions on*, vol. 55, pp. 1079 –1085, june 2008.

[55] I. Abt, M. F. Altmann, A. Bakalyarov, I. Barabanov, C. Bauer, *et al.*, "A New Ge-76 double beta decay experiment at LNGS: Letter of intent," 2004. arXiv: hep-ex/0404039.

[56] H. Klapdor-Kleingrothaus, L. Baudis, A. Dietz, G. Heusser, B. Majorovits, *et al.*, "GENIUS-TF: A Test facility for the GENIUS project," *Nucl.Instrum.Meth.*, vol. A481, pp. 149–159, 2002. arXiv: hep-ex/0012022.

[57] F. Froborg, *Calibration of Phase I of the GERDA Double Beta Decay Experiment*. PhD thesis, University of Zurich, 2012.

[58] P. Peiffer, *Liquid argon as active shielding and coolant for bare germanium detectors: A novel background suppression method for the Gerda $0\nu\beta\beta$ experiment*. PhD thesis, University of Heidelberg, 2007.

[59] D. Budjas, *Germanium detector studies in the framework of the GERDA experiment*. PhD thesis, University of Heidelberg, 2009.

[60] P. Belli, R. Bernabei, S. d'Angelo, M. de Pascale, L. Paoluzi, R. Santonico, N. Taborgna, N. Iucci, and G. Villoresi, "Deep underground neutron flux measurement with large BF_3 counters," *Il Nuovo Cimento A (1971-1996)*, vol. 101, pp. 959–966, 1989. 10.1007/BF02800162.

[61] L.Pandola, "Evaluation of neutron background due to natural radioactivity in GERDA." GERDA Scientific / Technical Report: GSTR-08-022.

[62] W. Stolz, *Radioaktivitaet, Grundlagen-Messung-Anwendungen*. Teubner Verlag, 2005.

[63] Karlsruhe Nuclide Chart, URL http://www.nucleonica.net/nuclidechart.aspx.

[64] S. S. K. P. Santhosh, R. K. Biju, "The systematic study of spontaneous fission versus alpha decay of superheavy nuclei," *J. Phys. G*, vol. 36, p. 115101, 2009.

[65] C. Xu, Z. Ren, and Y. Guo, "Competition between α decay and spontaneous fission for heavy and superheavy nuclei," *Phys. Rev. C*, vol. 78, p. 044329, Oct 2008.

[66] W. Demtroeder, *Experimentalphysik 4, Kern-, Teilchen- und Astrophysik*. Springer Verlag, 2004.

[67] W. Wahl, "Table of commonly used radionuclides, version: 2.3," 1996.

[68] G. Audi, A. Wapstra, and C. Thibault, "The Ame2003 atomic mass evaluation: (II). Tables, graphs and references," *Nuclear Physics A*, vol. 729, no. 1, pp. 337 – 676, 2003.

[69] W. Wilson, R. Perry, W. Charlton, and T. Parish, "Sources: A code for calculating (alpha, n), spontaneous fission, and delayed neutron sources and spectra," *Progress in Nuclear Energy*, vol. 51, no. 4-5, pp. 608 – 613, 2009.

[70] Eckert & Ziegler Nuclitec GmbH, URL http://www.ezag.com/home.html.

[71] W. H. BRAGG and K. R, "On the alpha particles of radium and their loss of range in passing through various atoms and molecules," *Phil. Msg.*, vol. 10, p. 318, 1905.

[72] URL http://www.webelements.com.

[73] URL http://www.nndc.bnl.gov/qcalc/qcalcr.jsp.

[74] URL http://physics.nist.gov/PhysRefData/Star/Text/ASTAR.html.

[75] W. R. Leo, *Techniques for Nuclear and Particle Physics Experiments*. Springer Verlag, 1994.

[76] URL http://www-nds.iaea.org/exfor/exfor.htm.

[77] URL http://www-nds.iaea.org/empire/.

[78] E.K. Hyde, The radiochemistry of Thorium, University of California, Berkeley, California, NAS-NS 3004 (1960).

[79] W. Maneschg, *Low-energy solar neutrino spectroscopy with Borexino: Towards the detection of the solar pep and CNO neutrino flux*. PhD thesis, University of Heidelberg, 2011.

[80] W. Maneschg, L. Baudis, R. Dressler, K. Eberhardt, R. Eichler, H. Keller, R. Lackner, B. Praast, R. Santorelli, J. Schreiner, M. Tarka, B. Wiegel, and A. Zimbal, "Production and characterization of a custom-made 228Th source with reduced neutron source strength for the Borexino experiment," 2011. arXiv: 1110.1217.

[81] A. Ljubicic, A. L. Carter, and R. L. Clarke, "Positron annihilation in Ge(Li) detector from line shape of single-escape peak," *Phys. Rev. B*, vol. 10, pp. 31–35, Jul 1974.

[82] L. Baudis *et al.*, "Gator: a low-background counting facility at the Gran Sasso Underground Laboratory," *JINST*, vol. 6, p. P08010, 2011. arXiv: astro-ph/1103.2125.

[83] URL http://www.canberra.com/products/449.asp.

[84] URL http://atom.kaeri.re.kr/cgi-bin/endfplot.pl.

[85] S. Fattori, *Study of Radioactive Background Minimization for a 1 Ton Module of the XENON Experiment*. PhD thesis, University of L'Aquila, 2010.

[86] E. Crivelli, *Neutron Background Monitoring for XENON100*. Bachelor thesis, University of Zurich, 2012.

[87] URL http://radiopurity.in2p3.fr/.

[88] URL http://www.scionix.nl/.

[89] E. Aprile *et al.*, "Material screening and selection for XENON100," *Astropart. Phys.*, vol. 35, pp. 43–49, 2011. arXiv: astro-ph/1103.5831.

[90] M. Günther, J. Hellmig, G. Heusser, M. Hirsch, H. V. Klapdor-Kleingrothaus, B. Maier, H. Päs, F. Petry, Y. Ramachers, H. Strecker, M. Völlinger, A. Balysh, S. T. Belyaev, A. Demehin, A. Gurov, I. Kondratenko, D. Kotel'nikov, V. I. Lebedev, and A. Müller, "Heidelberg-moscow $\beta\beta$ experiment with^{76}Ge: Full setup with five detectors," *Phys. Rev. D*, vol. 55, pp. 54–67, Jan 1997.

[91] C. Aalseth, F. Avignone, R. Brodzinski, S. Cebrian, D. Gonzles, E. Garca, W. Hensley, I. Irastorza, I. Kirpichnikov, A. Klimenko, H. Miley, A. Morales, J. Morales, A. rtiz de Solrzano, S. Osetrov, V. Pogosov, J. Puimedn, J. Reeves, M. Sarsa, S. Scopel, A. Smolnikov, A. Starostin, A. Tamanyan, A. Vasenko, S. Vasiliev, and J. Villar, "Recent results of the IGEX ^{76}Ge double-beta decay experiment," *Physics of Atomic Nuclei*, vol. 63, pp. 1225–1228, 2000. 10.1134/1.855774.

[92] H. Simgen, "Status of the GERDA experiment," in *10th Int. Conf. on Topics in Astroparticle and Underground Physics (TAUP2007)*, 2007.

[93] K. Kroeninger, *Techniques to distinguish between electron and photon induced events using segmented germanium detectors*. PhD thesis, Technische Iniversitaet Muenchen, 2007.

[94] I. Abt, A. Caldwell, D. Gutknecht, K. Kroninger, M. Lampert, *et al.*, "Characterization of the first true coaxial 18-fold segmented n-type prototype detector for the GERDA project," *Nucl.Instrum.Meth.*, vol. A577, pp. 574–584, 2007. arXiv: nucl-ex/0701004.

[95] X. Liu, "Workshop on germanium-based detectors and technologies," in *UC Berkeley*, 2010.

[96] M. Agostini, "Characterization of a Broad Energy Germanium detector through advanced pulse shape analysis techniques for the GERDA double-beta decay experiment," Master's thesis, University Padova, 2009.

[97] M. Agostini, C. Ur, D. Budjas, E. Bellotti, R. Brugnera, *et al.*, "Signal modeling of high-purity Ge detectors with a small read-out electrode and application to neutrinoless double beta decay search in Ge-76," *JINST*, vol. 6, p. P03005, 2011. arXiv: 1012.4300.

[98] D. Budjas, M. Barnabe Heider, O. Chkvorets, N. Khanbekov, and S. Schonert, "Pulse shape discrimination studies with a Broad-Energy Germanium detector for signal identification and background suppression in the GERDA double beta decay experiment," *JINST*, vol. 4, p. P10007, 2009. arXiv: nucl-ex/0909.4044.

[99] M. Bauer, S. Belogurov, Y. Chan, M. Descovich, J. Detwiler, M. D. Marco, B. Fujikawa, D. Franco, V. Gehman, R. Henning, K. Hudek, R. Johnson, D. Jordan, K. Kazkaz, A. Klimenko, M. Knapp, K. Kroeninger, K. Lesko, X. Liu, M. Marino, A. Mokhtarani, L. Pandola, M. Perry, A. Poon, D. Radford, C. Tomei, and C. Tull, "MaGe: a Monte Carlo framework for the Gerda and Majorana double beta decay experiments," *Journal of Physics: Conference Series*, vol. 39, no. 1, p. 362, 2006.

[100] J. Eberth and J. Simpson, "From Ge(Li) detectors to gamma-ray tracking arrays 50 years of gamma spectroscopy with germanium detectors," *Progress in Particle and Nuclear Physics*, vol. 60, no. 2, pp. 283 – 337, 2008.

[101] S. Georgi, *Untersuchungen zur Totschicht von BEGe-Detektoren im Rahmen des GERDA Experiments*. Bachelor thesis, University of Heidelberg, 2010.